

An international journal devoted to all branches of analytical chemistry

ANALYTICA CHIMICA ACTA

Aims and Scope

Analytica Chimica Acta provides a forum for the rapid publication of original research, and critical reviews dealing with all aspects of fundamental and applied modern analytical science. The journal welcomes the submission of research papers which report studies concerning the development of new and significant analytical methodologies. In determining the suitability of submitted articles for publication, particular scrutiny will be placed on the degree of novelty and significance of the research and the extent to which it adds to existing knowledge in analytical chemistry.

Manuscripts detailing fundamental research on all aspects of analytical theory and methodology (including chemometric techniques), such as innovative instrumental, chemical and biological approaches, detectors and sensors, sample treatment methods and data treatment are especially encouraged. On the other hand, papers describing the use of routine analytical methods or straightforward extension of these methods to new sample matrices will normally not be published unless new developments are described which can be demonstrated to give very clear and quantifiable advantages over existing methods. In all submissions to the journal, authors must address the question of how their proposed methodology compares with previously reported methods.

It will normally be expected that where new analytical methodologies and developments are described these will be applied to a sample matrix of suitable analytical complexity. In such cases appropriate validation of the method should be provided, together with proper statistical treatment of data. Analytical performance characteristics of new methods should be given, including sensitivity, detection limits, accuracy, precision, and interferences.

Reviews are normally written by prior agreement of the editors. Potential authors are encouraged to discuss the subject matter of a proposed review with either the editorial office or with individual editors and will be asked to provide a brief outline of the subject matter of the proposed review. Review articles should be sufficiently broad in scope to appeal to a wide cross-section of the journal's readership, but should be specific enough to permit discussion to be made at an appropriate depth. Basic methodology and principles should not be included in reviews, but suitable reference should be made to sources of this information. Above all, reviews should be critical rather than enumerative and should provide the reader with expert opinion regarding the relative merits of the various published approaches to the topic under review. Figures and Tables are encouraged in review articles.

Further details can be found on the ACA website at www.elsevier.com/locate/aca

Submission of Papers: It is a condition of publication that all manuscripts must be written in clear and grammatical English and be submitted to the *Analytica Chimica Acta* Web site at <http://ees.elsevier.com/aca>. Authors are requested to transmit the text and art of the manuscript in electronic form to this address. Each manuscript must also be accompanied by a cover letter outlining the basic findings of the paper and their significance. If you are unable to provide an electronic version, please contact the editorial office prior to submission at e-mail: aca@elsevier.com; telephone: (619) 699-6391; or fax: (619) 699-6801.

Analytica Chimica Acta

Editorial Office
525 B Street
Suite 1900, San Diego, California 92101-4495
U.S.A.
Telephone: (619) 699-6391
Fax: (619) 699-6801
E-mail: aca@elsevier.com

Authors may suggest an Editor appropriate for the paper; however, assignment to that Editor is not assured. In addition, authors are encouraged to identify at least three (and preferably five) persons who are qualified to serve as reviewers.

Publication information: *Analytica Chimica Acta* (ISSN 0003-2670). For 2004 volumes 501–526 are scheduled for publication. Subscription prices are available upon request from the Publisher or from the Regional Sales Office nearest you or from this journal's website (<http://www.elsevier.com/locate/aca>). Further information is available on this journal and other Elsevier products through Elsevier's website: (<http://www.elsevier.com>). Subscriptions are accepted on a prepaid basis only and are entered on a calendar year basis. Issues are sent by standard mail (surface within Europe, air delivery outside Europe). Priority rates are available upon request. Claims for missing issues should be made within six months of the date of dispatch.

Author enquiries

For enquiries relating to the submission of articles (including electronic submission where available) please visit Elsevier's Author Gateway at <http://authors.elsevier.com>. The Author Gateway also provides the facility to track accepted articles and set up e-mail alerts to inform you of when an article's status has changed, as well as detailed artwork guidelines, copyright information, frequently asked questions and more.

Contact details for questions arising after acceptance of an article, especially those relating to proofs, are provided after registration of an article for publication.

Orders, claims, and journal enquiries: please contact the Customer Service Department at the Regional Sales Office nearest you:

Orlando: Elsevier, Customer Service Department, 6277 Sea Harbor Drive, Orlando, FL 32887-4800, USA; phone: (+1) (877) 8397126 [toll free number for US customers], or (+1) (407) 3454020 [customers outside US]; fax: (+1) (407) 3631354; e-mail: usjcs@elsevier.com

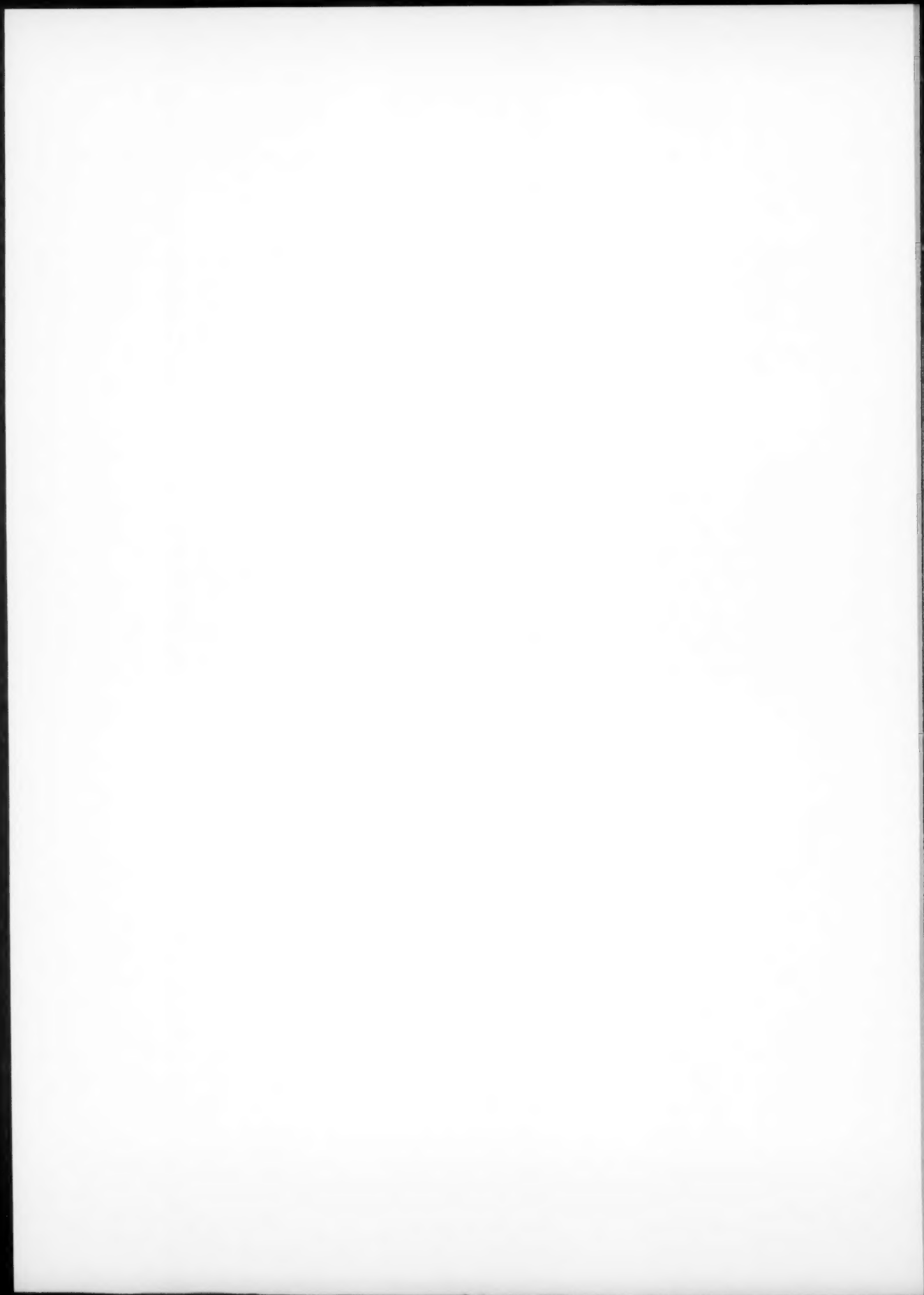
Amsterdam: Elsevier, Customer Service Department, PO Box 211, 1000 AE Amsterdam, The Netherlands; phone: (+31) (20) 4853757; fax: (+31) (20) 4853432; e-mail: ninfo-f@elsevier.com

Tokyo: Elsevier, Customer Service Department, 4F Higashi-Azabu, 1-Chome Bldg, 1-9-15 Higashi-Azabu, Minato-ku, Tokyo 106-0044, Japan; phone: (+81) (3) 5561 5037; fax: (+81) (3) 5561 5047; e-mail: jp.info@elsevier.com

Singapore: Elsevier, Customer Service Department, 3 Killiney Road, #08-01 Winsland House I, Singapore 239519; phone: (+65) 63490222; fax: (+65) 67331510; e-mail: asiainfo@elsevier.com

ANALYTICA CHIMICA ACTA

VOL. 519 (2004)



ANALYTICA CHIMICA ACTA

An international journal devoted to all branches of analytical chemistry

Editors: Alan Townshend (Hull, Great Britain)
Paul J. Worsfold (Plymouth, Great Britain)
Lutgarde Buydens (Nijmegen, Netherlands)
Paul R. Haddad (Hobart, Australia)
Ulrich J. Krull (Toronto, Canada)
Richard P. Baldwin (Louisville, KY, USA)
Purnendu K. Dasgupta (Lubbock, TX, USA)

Editorial Advisers:

F.C. Adams, Antwerp
N.W. Barnett, Geelong, Vic.
F.V. Bright, Buffalo, NY
W.W. Buchberger, Linz
C.S. Creaser, Nottingham
R. Dams, Ghent
Z. Fang, Shenyang
C. Gooijer, Amsterdam
B.D. Hammock, Davis, CA
P.de.B. Harrington, Athens, OH
P.C. Hauser, Basel
K. Jinno, Toyohashi
B. Karlberg, Stockholm
W.R. La Course, Baltimore, MD
H.K. Lee, Singapore
R. Lobinski, France
C.A. Lucy, Alberta
D.L. Massart, Brussels
V. McGuffin, East Lansing, MI

M.E. Meyerhoff, Ann Arbor, MI
A. Michael, Pittsburgh, PA
P.N. Nesterenko, Moscow
H.L. Pardue, West Lafayette, IN
C.J. Patton, Denver, CO
D. Pérez-Bendito, Córdoba
E. Pretsch, Zürich
F.X. Rius, Tarragona
S.C. Rutan, Richmond, VA
M.R. Smyth, Dublin
R. Tauler, Barcelona
T. Toyo'Oka, Shizuoka
C.M.G. van den Berg, Liverpool
W.E. van der Linden, Delden
J. Wang, Las Cruces, NM
O.S. Wolfbeis, Regensburg
R.-Q. Yu, Changsha
E. Zagatto, Piracicaba
J. Zupan, Ljubljana



ELSEVIER

Amsterdam • Boston • Jena • London • New York • Oxford • Paris • Philadelphia • San Diego • St. Louis

Anal. Chim. Acta, Vol. 519 (2004)

© 2004 Elsevier B.V. All rights reserved.

This journal and the individual contributions contained in it are protected under copyright by Elsevier B.V., and the following terms and conditions apply to their use:

Photocopying

Single photocopies of single articles may be made for personal use as allowed by national copyright laws. Permission of the Publisher and payment of a fee is required for all other photocopying, including multiple or systematic copying, copying for advertising or promotional purposes, resale, and all forms of document delivery. Special rates are available for educational institutions that wish to make photocopies for non-profit educational classroom use.

Permissions may be sought directly from Elsevier's Rights Department in Oxford, UK: phone: (+44) 1865 843830; fax: (+44) 1865 853333; e-mail: permissions@elsevier.com. Requests may also be completed on-line via the Elsevier homepage (<http://www.elsevier.com/locate/permissions>).

In the USA, users may clear permissions and make payments through the Copyright Clearance Center, Inc., 222 Rosewood Drive, Danvers, MA 01923, USA; phone: (+1) (978) 7508400; fax: (+1) (978) 7504744, and in the UK through the Copyright Licensing Agency Rapid Clearance Service (CLARCS), 90 Tottenham Court Road, London W1P 0LP, UK; phone: (+44) 20 7631 5555; fax: (+44) 20 7631 5500. Other countries may have a local reprographic rights agency for payments.

Derivative Works

Subscribers may reproduce tables of contents or prepare lists of articles including abstracts for internal circulation within their institutions. Permission of the Publisher is required for resale or distribution outside the institution.

Permission of the Publisher is required for all other derivative works, including compilations and translations.

Electronic Storage or Usage

Permission of the Publisher is required to store or use electronically any material contained in this journal, including any article or part of an article.

Except as outlined above, no part of this publication may be reproduced, stored in a retrieval system or transmitted in any form or by any means, electronic, mechanical, photocopying, recording or otherwise, without prior written permission of the Publisher.

Address permissions requests to: Elsevier Rights Department, at the fax and e-mail addresses noted above.

Notice

No responsibility is assumed by the Publisher for any injury and/or damage to persons or property as a matter of products liability, negligence or otherwise, or from any use or operation of any methods, products, instructions or ideas contained in the material herein. Because of rapid advances in the medical sciences, in particular, independent verification of diagnoses and drug dosages should be made.

Although all advertising material is expected to conform to ethical (medical) standards, inclusion in this publication does not constitute a guarantee or endorsement of the quality or value of such product or of the claims made of it by its manufacturer.

♻ The paper used in this publication meets the requirements of ANSI/NISO Z39.48-1992 (Permanence of Paper).

CONTENTS

(Full texts are incorporated in CJESEVIER, a file in the Chemical Journals Online database available on STN International; Abstracted, indexed in: Aluminium Abstracts; Anal. Abstr.; Biol. Abstr.; BIOSIS; Chem. Abstr.; Curr. Contents Phys. Chem. Earth Sci.; Engineered Materials Abstracts; Excerpta Medica; Index Med.; Life Sci.; Mass Spectrum. Bull.; Material Business Alerts; Metals Abstracts; Sci. Citation Index)

Chemometrics

- Quantitative determination of the catalysed asymmetric transfer hydrogenation of 1-methyl-6,7-dimethoxy-3,4-dihydroisoquinoline using in situ FTIR and multivariate curve resolution
S. Richards, M. Ropic, D. Blackmond and A. Walmsley (Hull, UK) 1
- Genetic algorithms (GA) applied to the orthogonal projection approach (OPA) for variable selection
S. Gourvénec, X. Capron and D.L. Massart (Brussel, Belgium) 11
- Liquid chromatography and chemometric methods for determination of rofecoxib in presence of its photodegradate and alkaline degradation products
M.A. Shehata, A. Ashour, N.Y. Hassan, A.S. Fayed and B.A. El-Zeany (Cairo, Egypt) 23

Sensors and electroanalytical chemistry

- Electrochemistry and biosensing reactivity of heme proteins adsorbed on the structure-tailored mesoporous Nb₂O₅ matrix
X. Xu, B. Tian, S. Zhang, J. Kong, D. Zhao and B. Liu (Shanghai, PR China) 31
- Multivariate optimisation of electrochemically pre-treated electrodes used in a voltammetric electronic tongue
S. Holmin, C. Krantz-Rülcker and F. Winquist (Linköping, Sweden) 39
- Steady-state oxidation of cholesterol catalyzed by cholesterol oxidase in lipid bilayer membranes on platinum electrodes
M.P. Bokoch, A. Devadoss, M.S. Palencsar and J.D. Burgess (Cleveland, OH, USA) 47
- Simultaneous determination of nickel(II) and cobalt(II) by square wave adsorptive stripping voltammetry on a rotating-disc bismuth-film electrode
M. Morfobos, A. Economou and A. Voulgaropoulos (Thessaloní, Greece) 57

Micellar electrokinetic chromatography

- Determination of neutral and cationic herbicides in water by micellar electrokinetic capillary chromatography
M.-I. Acedo-Valenzuela, T. Galeano-Díaz, N. Mora-Díaz and A. Silva-Rodríguez (Badajoz, Spain) 65
- Separation and selectivity in micellar electrokinetic chromatography using sodium dodecyl sulfate micelles or Tween 20-modified mixed micelles
M. Wang, D. Wu, Q. Yao and X. Shen (Hangzhou, China) 73

Isotope dilution inductively coupled plasma mass spectrometry

- Certification measurement of the cadmium, copper and lead contents in rice using isotope dilution inductively coupled plasma mass spectrometry
E. Vassileva and C.R. Quétel (Geel, Belgium) 79

Solid phase extraction

- Determination of bismuth and cadmium after solid-phase extraction with chromosorb-107 in a syringe
N. Tokman and S. Akman (Maslak-Istanbul, Turkey) 87
- Micro-solid phase extraction with helical-solid-sorbent in the presence of organic solvent for gas chromatography-mass spectrometry analysis of per-O-methylated mono- and disaccharides
I. Ciucanu, K.C. Swallow and R. Căpriță (Timisoara, Romania) 93

Archaeometry

- Study and characterization of the ancient bricks of monastery of "San Filippo di Fragalà" in Frazzanò (Sicily)
P. Cardiano (Messina, Italy), S. Ioppolo (Catania, Italy), C. De Stefano, A. Pettignano, S. Sergi and P. Piraino (Messina, Italy) 103

Chemiluminescence

- New flow-multicommutation method for the photo-chemiluminometric determination of the carbamate pesticide asulam
A. Chivulescu, M. Catalá-Icardo, J.V. García Mateo and J. Martínez Calatayud (Valencia, Spain) 113

Gas chromatographic detection

- Improved micro-flame detection method for gas chromatography
K.B. Thurbide and T.C. Hayward (Calgary, Canada) 121

- Calendar of forthcoming meetings N1

CONTENTS
direct

This journal is part of **ContentsDirect**, the *free* alerting service which sends tables of contents by e-mail for Elsevier books and journals. You can register for **ContentsDirect** online at: <http://contentsdirect.elsevier.com>

SCIENCE  DIRECT®

Full text of this journal is available, on-line from **ScienceDirect**. Visit www.sciencedirect.com for more information.

Quantitative determination of the catalysed asymmetric transfer hydrogenation of 1-methyl-6,7-dimethoxy-3,4-dihydroisoquinoline using in situ FTIR and multivariate curve resolution

Selena Richards, Melanie Ropic, Donna Blackmond, Anthony Walmsley*

Department of Chemistry, The University of Hull, Hull HU6 7RX, UK

Received 6 April 2004; received in revised form 11 May 2004; accepted 11 May 2004

Available online 17 July 2004

Abstract

Multivariate Curve Resolution with Alternating Least Squares (MCR–ALS) has been successfully applied to in situ infrared measurements of rhodium catalysed asymmetric transfer hydrogenation (CATHy) reaction of 1-methyl-6,7-dimethoxy-3,4-dihydroisoquinoline to provide an alternative to the traditional method of HPLC analysis. The pure spectra and concentration profile of the imine, amine and carbon dioxide (an intermediate component) were resolved without previous calibration information regarding the reaction. The root mean square prediction error (RMSPE) of the imine and amine were 0.02 and 0.04, respectively. The FTIR method developed enabled the reaction to be monitored in situ, which eliminated the need for constant sampling, required of HPLC analysis, and facilitated the quantitation of components not identified in the chromatographic analysis (CO₂).

© 2004 Published by Elsevier B.V.

Keywords: Multivariate Curve Resolution; Chemometrics; Catalysed Asymmetric Transfer Hydrogenation; Imine

1. Introduction

The reduction of carbonyl or nitrogen containing groups is usually catalysed by either microsomal or cytosolic reductases in nature [1]. These reactions are highly stereo-selective and as such their use is limited [2]. Catalytic asymmetric transfer hydrogenation (CATHy) has been shown to be a beneficial generic method both economically and technically for the reduction of C=N and the saturation of C=C and C=O linkages [3,4]. It is operationally very simple and requires non-hazardous organic molecules. It has been shown to be a powerful alternative to asymmetric hydrogenation using molecular hydrogen with chiral Ru(II)-bisphosphane catalysts due to its practical simplicity and the possibility of using accessible and robust ligands [5]. Noyori and coworkers [3,4] found that CATHy reactions were particularly useful for the asymmetric enantioselective reduction of cyclic imines giving amines with

90–97%ee (using Ru-CATHy), which opened a new general route to natural and synthetic isoquinoline alkaloids as well as a convenient preparation for chiral amines [3,4].

Nevertheless, the complete mechanism of catalytic asymmetric transfer hydrogenation reactions has not been solved. Yet, it is required (from an industrial perspective) to monitor and predict the evolution of specific chemical constituents within the reaction to aid control. Uematsu et al. [3] proposed the most feasible and detailed mechanism for this reaction (Fig. 1) with Casey [6] and Yi [7] affirming the likelihood of steps 3, 5 and 6 of the stepwise hydrogen transfer.

Multivariate curve resolution is a technique used for resolving data sets into spectra and concentration profiles. This technique has been applied to obtain the concentration and spectral profiles of strongly coeluted organophosphorus pesticides from liquid chromatography diode array detection (LC–DAD) [8], and to resolve complex and strongly overlapping infrared spectra to determine the behaviour of the reactive sites of humic acids in the binding with heavy metals [9]. Imbedded kinetic constraints has been used to predict the rate constants for the reaction pathway for the degradation of ally using liquid chromatography diode array

* Corresponding author.

E-mail address: a.d.walmsley@hull.ac.uk (A. Walmsley).

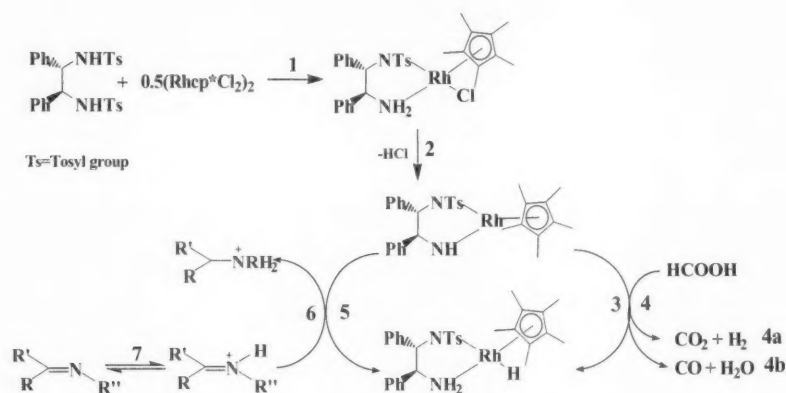


Fig. 1. Noyori and Hashiguchi's [4] proposed reaction mechanism for the asymmetric hydrogenation of imines.

detection [10] and to resolve overlapped NMR spectra from the hydrolysis of sulfonylurea (SU) herbicide [11]. The kinetic constraint was applied during the iteration which improved the accuracy of the rate constant in comparison to the use of separate MCR followed by kinetic fitting [12].

In this work, the CATHy reduction of 1-methyl-6,7-dimethoxy-3,4-dihydroisoquinoline was monitored using in situ Fourier transform infrared (FTIR) and multivariate curve resolution using alternating least squares (MCR-ALS) to generate the concentration and spectral profiles of the imine, amine, (1-methyl-6,7-dimethoxy-1,2,3,4-tetrahydroisoquinoline) and carbon dioxide (the intermediate species) within the CATHy reaction from overlapped FTIR spectra, in attempts to provide an alternative quantitative method to HPLC. This is essential as the HPLC method took 6 months to develop and is time consuming. The HPLC workup is approximately twice as long as the reaction. For explorative analysis, the HPLC method was limited to target analytes, as intermediates and by-products were frequently lost in the work-up procedure. Therefore, MCR-ALS is required to characterise the chemical process without using explicitly the underlying chemical model linked to it. This avoids error caused by the assumption of a wrong model and allows the presence and modelling of chemical components, which are not realised from prior quantitative analysis such as HPLC and univariate analysis.

The reaction was completed using the TsDPEN ligand as it is recognised to be the optimal ligand for the rhodium(III) catalysed asymmetric hydrogenation [13]. Formic acid was used as the hydrogen source to reduce the need for high pressure, which may affect the enantio-selectivity and reduce the threat of an explosion. FTIR was used as the detection method because it allows bond changes to be continuously observed during the reaction. The high information content in FTIR and broad applicability are merited to the speed of the method, both for the analysis itself and the time window that can be observed [14]. HPLC was used as a quantitative reference to validate the chemometric results for 1-methyl-3,4-dihydroisoquinoline

and 1-methyl-1,2,3,4-tetrahydroisoquinoline. The root mean standard prediction error (RMSPE) was used to qualify the error of prediction for each chemical constituent.

2. Theory

2.1. Multivariate curve resolution–alternating least squares

MCR-ALS was applied to spectral data acquired as a function of time to reveal pure concentration and spectral profiles of individual chemical constituents. The pre-requisite for the decomposition is that the total response is a linear additive signal of each component. For multi-component spectroscopic systems, the total response at a specific wavenumber (at a constant light pathlength) is a linear additive signal of each chemical constituent, Eq. (1).

$$A_{\lambda} = \varepsilon_{\lambda 1}c_1 + \varepsilon_{\lambda 2}c_2 + \dots + \varepsilon_{\lambda m}c_m = \sum_{j=1}^m \varepsilon_{\lambda j}c_j \quad (1)$$

where A_{λ} is the absorbance at wavelength λ ; ε_{λ} is the molar absorptivity, $\text{mol dm}^{-3} \text{cm}^{-1}$ and c is the concentration, mol dm^{-3} . Therefore, it was possible to employ MCR to determine the pure concentration C and spectra S , of individual components, by minimising the residual matrix E . Where n is the number of rows (samples) and p is the number of columns (wavenumbers)

$$X_{n \times p} = C_{n \times m}^* S_{m \times p}^{*T} + E_{n \times p} \quad (2)$$

Initially, factor analysis was applied to reduce the measurement matrix to the lowest dimensionality, Eq. (3).

$$X_{n \times p} = U_{n \times m}^* V_{m \times p}^{*T} + E_{n \times p} \quad (3)$$

where U is the scores matrix (abstract concentration profiles) and shows the variation between the samples and V is the loadings matrix (abstract spectra) and describes the variation

between the variables. Each row of the data matrix X are linear combinations of all the principle factors in the loadings matrix, the multiplicative factor of the linear combination for a particular row of x_i , are given by the corresponding row u_i in the scores matrix $x_i = u_i V^T$ [15]. The symbol (*) denotes the nc significant columns of V and U that are retained. The reduced factors are called abstract factors, as the orthogonal relationship of the factors is determined by the magnitude of the variance in the data, which is based on a purely mathematical relationship. The measurement matrix was reconstructed by taking the first nc significant principal factors. The number of significant components (principle factors) was determined using Malinowskis F -test, although there are a number of different methods which can be used to determine the number of components. [15–17]. If the correct number of components are chosen, then, the residual matrix E is close to the experimental error, Eq. (3). To calculate the real concentration and spectral profiles, it was necessary to solve Eq. (4), however, for an arbitrary transformation of matrix R , rotational and intensity ambiguity in C and S often result because there are an infinite number of solutions, and thus, it is impossible to transform U and V into C and S matrices without additional information.

$$\hat{X} = UV^T = URR^{-1}V^T = CS^T \quad (4)$$

The objective of curve resolution is to constrain the numbers of possible solutions which can give chemically meaningful solutions for C and S . Using initial estimates of either the pure concentration or spectral profiles, which can be determined from EFA (see next section), SIMPLISMA, T-SMPLISMA, OPA or prior knowledge of the system [18–23]. Alternating least squares regression was applied using the initial estimates to solve for S and C , respectively.

2.1.1. Alternating least squares procedure

The initial estimate from EFA, and the pre-treated measurement matrix X were used to provide the unknown species spectra, using least squares (Eq. (5)):

$$S = C^+ \hat{X} \quad (5)$$

where \hat{X} is the reproduced data matrix for the considered number of species and C^+ is the pseudo-inverse of C . The matrix S gives the current least squares estimation of the unit spectra.

$$C = \hat{X} S^+ \quad (6)$$

In the second step, the concentration profiles were constrained using the non-negativity constraint, which sets any negative values to zero and the kinetic constraint (which solves the differential rate equation numerically and determines the optimal rate constants for representing the kinetic profiles [10–12]). The corrected C profiles were used to calculate S , using least squares. These steps were repeated until the error matrix, E , had been minimised sufficiently within the experimental error. Other constraints which can be applied include closure, equality, selectivity and shape con-

straints, see [25] for an extensive review. The lack of fit in the ALS optimisation was calculated according to Eq. (7), where x_{np} is the experimental absorbance at the sampled time n and the wavenumber p , and x_{np}^* is the ALS calculated absorbance at the sampled time n , and the wavenumber p .

$$\% \text{ lack of fit} = 100 \sqrt{\frac{\sum (x_{np} - x_{np}^*)^2}{(\sum x_{np})^2}} \quad (7)$$

2.1.2. Evolving factor analysis (EFA)

Evolutionary analysis of the raw data matrix was used to provide initial estimates of the concentration profiles for MCR. Data sets can either be factor analysed according to their row or columns (depending on the information required). The rows tend to follow a logical sequence, such as response according to time; this property can be exploited to locate the pure rows or variables in the matrix. By plotting the log of the singular value, variance described by each singular vector against the number of rows added (from singular value decomposition of subsequent submatrices in the forward direction then repeating in the reverse direction), it is possible to derive the rank of the successive submatrices [18–20]. Since evolutionary analysis identifies independent factors and not chemical constituents, it is important to realise that an evolutionary profile may comprise of a summation of various chemical compounds, such that analysis of consecutive sub-windows may yield the same number of independent variables, although the chemical components of those sub-windows may be different, i.e. reactants that co-vary may not be split out as separate factors [15].

2.1.3. Root mean square prediction error

To assess the prediction error of the concentration profiles obtained from MCR–ALS, the root mean square prediction error [15] was used. This sums the residual between the reference and predicted curves and gives the root mean square value or prediction error for the concentration profile. The best prediction is determined by the lowest RMSPE value.

$$\text{PRESS} = \sum (c_i - \hat{c}_i)^2 \quad (8)$$

$$\text{RMSPE} = \left(\frac{\text{PRESS}}{n_t} \right)^{1/2} \quad (9)$$

2.1.4. Standard normal variate (SNV)

SNV was used to correct for baseline offsets by subtracting the mean spectral reading. This corrects for differences affecting the overall variation. The standardisation was completed by considering each spectrum x_i as a set of observations and calculating their z -scores [15].

$$z_i = \frac{x_i - \bar{x}}{s} \quad (10)$$

3. Experimental

The reaction solvent acetonitrile [17.34 M; Fisher Chemicals], hydrogen donating reagent TEAF [distilled formic acid, 1.0 M; distilled triethylamine, 0.4 M; both, Fisher Chemicals] and the HPLC internal standard phenanthrene [0.01 M; Aldrich] were placed in the ReactIR background spectrum. A sample spectra of 1-methyl-6,7-dimethoxy-3,4-dihydroisoquinoline [0.25 M; Acros Organics] was taken and the reaction initiated by the addition of the pre-catalyst components. Regular samples were taken and quenched [2 M sodium hydroxide (BDH GPR) and dichloromethane (Fisher Chemicals)] during the reaction for analysis by HPLC [Daicel Chemical Industries Ltd.; Chiralcel OD Analytical column, 0.46 cm i.d. \times 25 cm].

The reaction was monitored for an hour using ASi ReactIR 1000. The resolution of the instrument was 8 cm^{-1} such that a total of 869 points were recorded in the X direction.

Sample spectra were recorded every 30 s for the first 5 min, followed by every 2 min for the remaining time, a total of 39 samples were recorded. Each spectrum was recorded at a predefined time using the average of 32 scans. The data was converted from SPA format using the REACTIR software to JCAMP-DX, then to MATLAB.MAT. MATLAB6p5[®] (The Math Works Inc.) was used to complete all data processing.

The reference spectra of formic acid, distilled triethylamine mixed and separate, 1-methyl-6,7-dimethoxy-3,4-dihydroisoquinoline and carbon dioxide, were taken prior to data acquisition (acetonitrile in the background). 1-Methyl-6,7-dimethoxy-1,2,3,4-tetrahydroisoquinoline spectrum was acquired from a previous synthesis (Fig. 2). The reference spectra of these components were taken, as preliminary curve resolution analysis (results and discussion), revealed that these components were present in the measurement matrix.

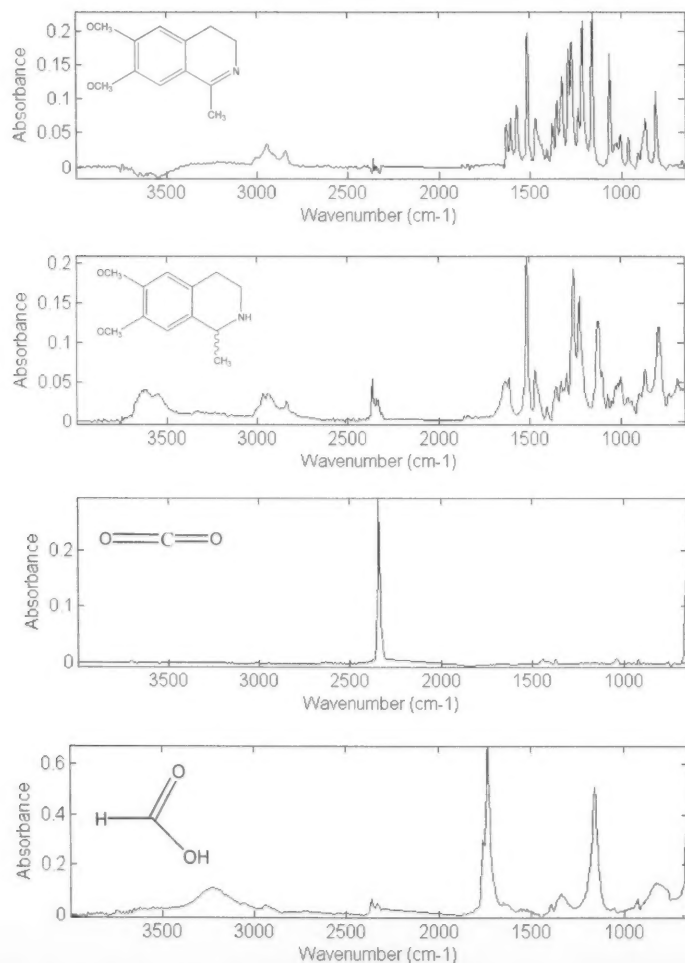


Fig. 2. Reference spectra of 1-methyl-6,7-dimethoxy-3,4-dihydroisoquinoline, 1-methyl-6,7-dimethoxy-1,2,3,4-tetrahydroisoquinoline, carbon dioxide and formic acid.

Table 1

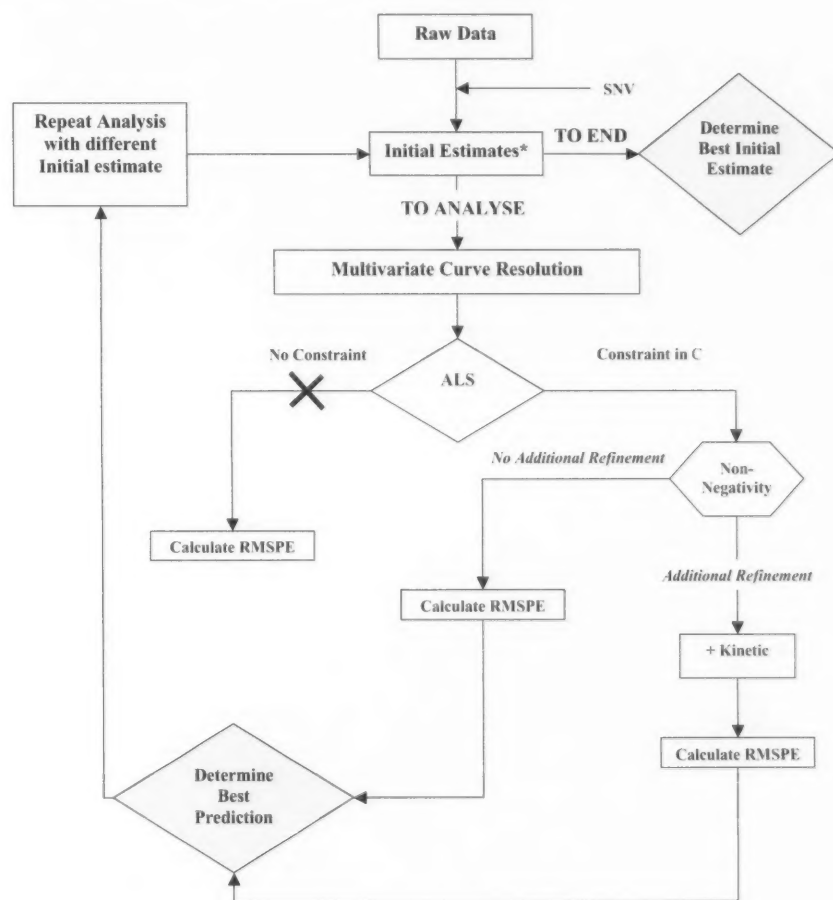
Common group frequencies for 1-methyl-6,7-dimethoxy-3,4-dihydroisoquinoline and 1-methyl-1,2,3,4-tetrahydroisoquinoline

Functional group	Bond movement	Frequency range (cm ⁻¹)
Ether or alkyl	CH ₃ -O-H/CH ₃ -C/-CH ₂ -/CH stretch	3200–2800/3000–2840/2950–2800/3300–2700
Substituted aromatics	C=C	1590–1575, 1465–1440
Alkyl	-CH ₂ -	1475–1425
Alkyl	CH bends	1475–1300
Ether/2° amine	C-O stretch/C-N stretch	1300–900
Substituted aromatics	CH out of plane deformations	900–860/860–800 if 1,2,4-substituted

Common group frequencies for the imine and amine were identified and tabulated (Table 1).

Characteristic group frequencies for 1-methyl-6,7-dimethoxy-3,4-dihydroisoquinoline are 1657–1600 cm⁻¹ for >C=N-C and 1700–1575 cm⁻¹ for C=N stretch in substituted imine. For secondary amines, characteristic group frequencies are 3700–3000 cm⁻¹ for N-H stretch, 3500–3100 cm⁻¹

for CH-NH-CH stretch and 1650–1500 cm⁻¹ for NH bend in secondary amine. The characteristic bands in formic acid are 3300–2500 cm⁻¹ for O-H stretch, the peak ~1730 cm⁻¹ is due to C=O stretch in saturated carboxylic acid, the peaks 1340–1150 cm⁻¹ are due to C=O stretch and 830–670 cm⁻¹ is due to OH deformation.



*Initial Estimates

- EFA estimates of concentration profiles
- Reference spectra of imine, amine and carbon dioxide

Fig. 3. Flow chart of multivariate analysis.

3.1. Multivariate analysis

The multivariate analysis was completed stepwise according to the flowchart (Fig. 3). Standard normal variate (SNV) was used to correct the raw spectral data for baseline variation. The initial estimates used were (a) the singular values calculated from EFA and (b) the reference spectra of these components. The unconstrained solution, the solution with non-negativity constraint in the concentration profiles and the solution with non-negativity and imbedded kinetic constraints in the concentration profiles were calculated to assess the accuracy of the fit. A consecutive first order estimate of the kinetic parameters of the overall CATHy of 1-methyl-6,7-dimethoxy-3,4-dihydroisoquinoline was incorporated. Due to the rank deficiency of the data set, three components were incorporated in the kinetic rate equation, which were representative of the imine, amine and carbon dioxide concentration profiles.

$$\begin{aligned} \text{imine} &\xrightarrow{k_1} \text{carbon dioxide} \xrightarrow{k_2} \text{amine} \quad \frac{d[\text{imine}]}{dT} = -k_1[\text{imine}] \\ \frac{d[\text{carbon dioxide}]}{dT} &= -k_1[\text{imine}] - k_2[\text{carbon dioxide}] \\ \frac{d[\text{Amine}]}{dT} &= k_2[\text{carbon dioxide}] \end{aligned} \quad (11)$$

The initial rate constants estimates were $k_{1,2} = 1$. The root mean standard prediction error was used to qualify the error of prediction for the concentration profiles of the imine and amine using the reference HPLC measurements. The data

points chosen were the closest timed IR sample to the reference measurement sample. The assay data and the ALS resolved concentration profiles were scaled between zero and one for the RMSPE calculation. No reference information was available for CO₂.

4. Results and discussion

Initial observations of the spectral variations shown in Fig. 4, show several regions of interest, the first is the negative response emanating from regions A, B and C: 660.9–718.2 cm⁻¹, 1141.4–1225.1 cm⁻¹ and 1692.4–1767.3 cm⁻¹, respectively. These frequencies were comparable to the reference spectrum of formic acid taken prior to the analysis. The negative response intensified as the reaction proceeded, which is due to the decomposition of formic acid to carbon dioxide and hydrogen. Peak D increased as CO₂ was produced and decreased as CO₂ was removed from the solution, possibly due to partitioning between the liquid and air phase.

4.1. Number of components

Three independent variables were realised although at least six chemical components were expected, which were imine, amine, triethylamine, formic acid and carbon dioxide (Fig. 1, step 4a) or carbon monoxide and water (Fig. 1, step 4b) substantiated from the proposed Noyori and Hashiguchi [4] reaction, Fig. 1. The catalyst components were unlikely to be resolved as the molecular changes occurred at con-

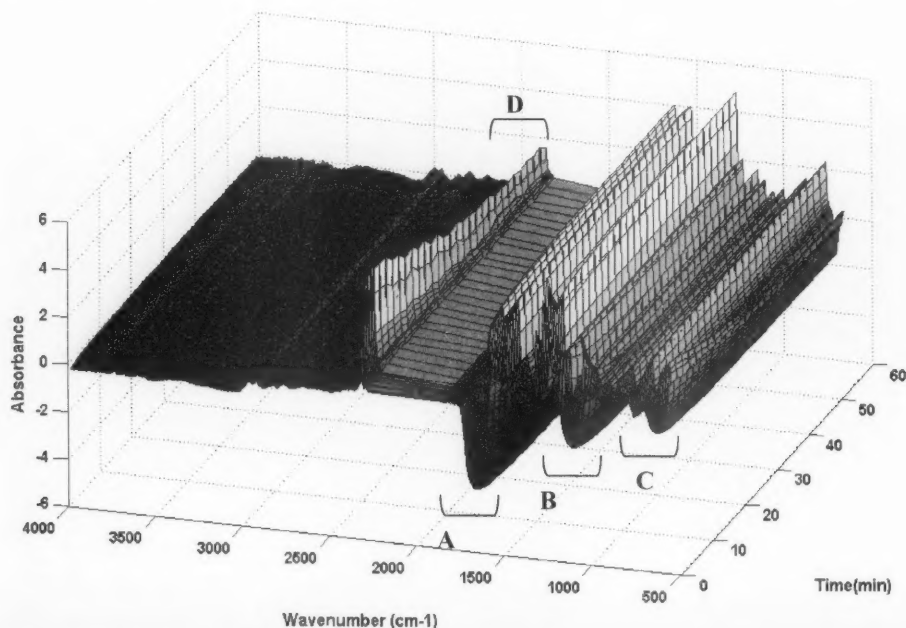


Fig. 4. Reaction profile of CATHy of 1-methyl-6,7-dimethoxy-3,4-dihydroisoquinoline. Regions A, B and C are representative of formic acid. Region D is representative of C=O stretch in carbon dioxide.

centrations lower than the limit of detection of the FTIR spectrophotometer. The chemical rank, i.e. the number of reacting chemical components differed to the rank of the matrix because of linear dependency amongst chemical constituents.

4.2. Preliminary analysis: MCR-ALS with EFA

The results from the analysis with no constraints applied showed that the predicted imine and amine spectrum contained the characteristic formic acid peaks, which were $660.9\text{--}718.2\text{ cm}^{-1}$, $1141.4\text{--}1225.1\text{ cm}^{-1}$ and $1692.4\text{--}1767.3\text{ cm}^{-1}$. The predicted carbon dioxide profile contained characteristic vibrational frequencies from both formic acid and amine. The predicted spectral profiles tended to be highly correlated to the formic acid component because of linear dependency amongst the constituents. The ALS concentration profiles of imine and amine were not comparable to the reference data. The application of

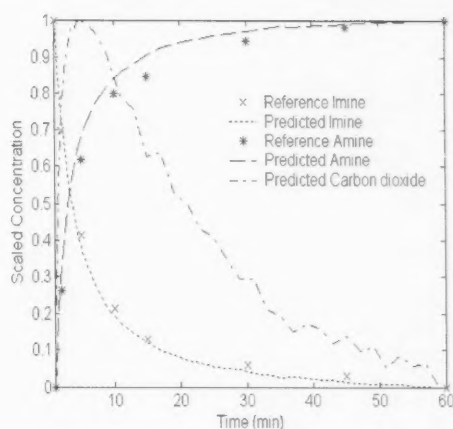


Fig. 5. MCR-ALS resolved concentration profile of 1-methyl-6,7-dimethoxy-3,4-dihydroisoquinoline, 1-methyl-6,7-dimethoxy-1,2,3,4-tetrahydroisoquinoline and carbon dioxide; non-negativity constraint in concentration profile.

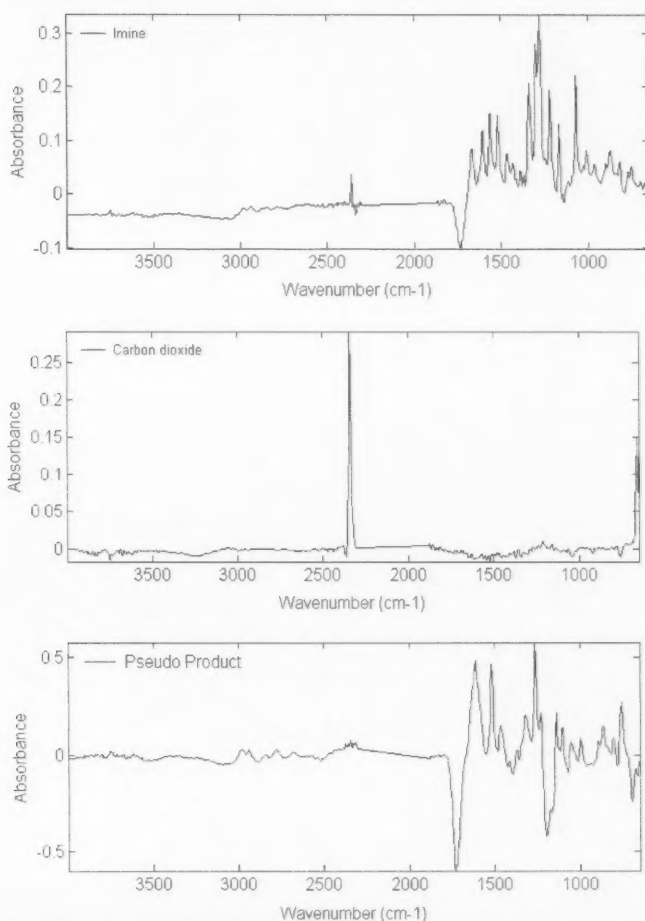


Fig. 6. MCR-ALS resolved spectral profiles of 1-methyl-6,7-dimethoxy-3,4-dihydroisoquinoline, 1-methyl-6,7-dimethoxy-1,2,3,4-tetrahydroisoquinoline and carbon dioxide; no constraints applied in spectral dimension.

Table 2
RMSPE values of imine, amine and carbon dioxide concentration profiles

	EFA (a)	EFA (b)	EFA (c)	SPEC (a)	SPEC (b)
Imine	0.34	0.35	0.27	0.04	0.04
Amine	0.13	0.12	0.12	0.02	0.02

(a) No constraint; (b) non-negativity in concentration and (c) non-negativity and kinetic constraint in concentration.

non-negativity constraint showed no improvements in the results, as this constraint was not active, i.e. the concentration profiles already fulfilled the non-negativity criterion. The addition of the kinetic gave smoother concentration profiles and the RMSPE were slightly improved, although the rate of loss for the imine was much faster in the kinetic profile than the reference data and the rate of formation was much slower for amine than the reference data. The most probable reasons why the kinetic law was not fulfilled is because the evolution of the concentration profile of carbon dioxide does not obey a kinetic law due to the additional gas liquid equilibrium. The kinetic constraint was not implemented for any further analysis, as CO₂ could not be constrained appropriately (Table 2).

The reference spectra of imine, amine and carbon dioxide were used as the initial estimates to improve the ALS solution, as they were partially resolved from the initial analysis.

4.3. MCR-ALS using reference spectra

The predicted amine spectrum resolved from MCR-ALS is a pseudo-spectrum formed from amine and formic acid. The pseudo-product spectrum contains negative peak contributions at 1739, 1148.5 and 648 cm⁻¹ from formic acid and the characteristic group frequencies from amine. Formic acid and amine are collinear as formic acid is consumed (increased negative signal as the reaction proceeds) at the same rate that amine is produced, as a result the concentration profiles could not be mathematically separated. Despite this, the concentration profile of amine is comparable to the assay data collected, Figs. 5 and 6. The predicted imine spectrum was slightly inaccurate (rotational ambiguity) due to the carbonyl stretch of formic acid being present in the spectrum. However, the calculation of the imine concentration profile were in excellent agreement with the HPLC data at the sampled time intervals. There was no difference between using no constraints and non-negativity constraints in the concentration profile, as the non-negativity constraints was not active (Table 2). Additionally, the pure spectra and concentration profiles of carbon dioxide (Figs. 5 and 6) was resolved using the reference spectra and non-negativity constraint. As stipulated previously, no reference information was available to validate the concentration profile of carbon dioxide, however, the additional information could be used to determine dangerous levels of CO₂ in the reactor.

Thus, using MCR-ALS, it was possible to successfully resolve the concentration profiles of imine, amine and car-

bon dioxide to provide an alternative approach to HPLC analysis.

5. Conclusion and future work

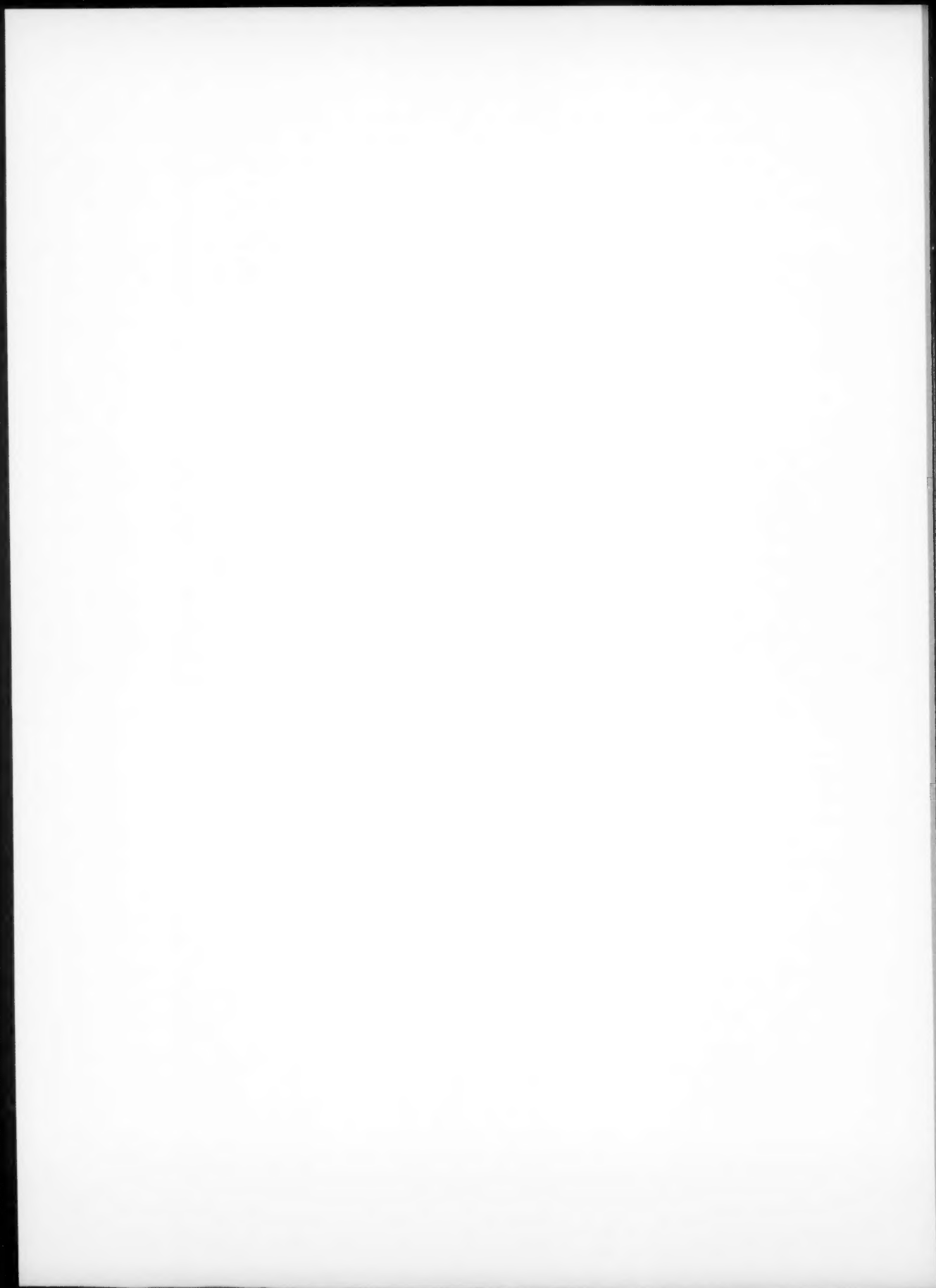
The combination of in situ FTIR with multivariate curve resolution has been used successfully to determine the spectral and concentration profiles of imine, amine and carbon dioxide in the complex CATHy reaction. The resolved pure spectra and concentration profiles of the analytes of interest ensured that this technique could be used as an economically viable and convenient replacement to the currently used HPLC method. The additional information content from MCR with respect to the carbon dioxide concentration and spectral profiles was advantageous to notify batch operators of dangerous levels of CO₂ in the reactor. The FTIR method developed enables reaction to be monitored in situ and eliminates need for constant sampling. The combined approach offers significant advantages in cases where viewing complex experimental data by eye is problematic.

Future work includes breaking the rank deficiency of the data set through chemical perturbation of the system and partial kinetic modelling of the data will be applied to give clues about the reaction mechanism.

References

- [1] J.A. Timbrell, *Introduction to Toxicology*, 2nd ed., Taylor & Francis, London, 1995, pp. 38–43.
- [2] D. Anderson, D.M. Conning, *Experimental Toxicology: The Basic Issues*, Royal Society of Chemistry, Cambridge, 1993, pp. 135–150.
- [3] N. Uematsu, A. Fujii, S. Hashiguchi, T. Ikariya, R. Noyori, *J. Am. Chem. Soc.* 118 (1996) 4916–4917.
- [4] R. Noyori, S. Hashiguchi, *Acc. Chem. Res.* 30 (1997) 97–102.
- [5] B. Mohar, A. Valleix, J.-R. Desmurs, M. Felemez, A. Wagner, C. Mioskowski, *Chem. Commun.* 1 (2001) 2572–2573.
- [6] C.P. Casey, S.W. Singer, D.R. Powell, R.K. Hayahi, M. Kavava, *J. Am. Chem. Soc.* 123 (2001) 1090–1100.
- [7] C.S. Yi, Z. He, *Organometallics* 20 (2001) 3614–3643.
- [8] R. Tauler, E. Lacorte, D. Barceló, *J. Chromatogr. A* 730 (1996) 177–183.
- [9] P. Gossart, A. Semmoud, C. Ruckebusch, J.-P. Huvenne, *Anal. Chim. Acta* 477 (2003) 201–209.
- [10] E. Bezemer, S. Rutan, *Chemom. Intell. Lab. Syst.* 59 (2001) 19–31.
- [11] E. Bezemer, S. Rutan, *Anal. Chim. Acta* 459 (2002) 277–289.
- [12] A. de Juan, M. Maeder, M. Martínez, R. Tauler, *Chemom. Intell. Lab. Syst.* 54 (2000) 123–141.
- [13] D.J. Cross, J.A. Kenny, I. Houson, L. Campbell, T. Walsgrove, M. Wills, *Tetrahedron: Asymmetry* 12 (2001) 1801–1806.
- [14] P. von Ragué Schleyer, in: N.L. Allinger, P.A. Kollman, T. Clark, H.F. Schaefer III (Eds.), *Encyclopaedia of Computational Chemistry*, Wiley, Chichester, 1998, pp. 1299–1312.
- [15] B.G.M. Vandeginste, in: D.L. Massart, L.M.C. Buydens, S. de Jong, P.J. Lewi, J. Smeyers-Verbeke (Eds.), *Data Handling in Science and Technology, Handbook of Chemometrics and Qualimetrics: Part B*, vol. 20B, Elsevier, Amsterdam, 1997, pp. 243–306.
- [16] E.R. Malinowski, *Factor Analysis in Chemistry*, 2nd ed., Wiley, New York, 1991.

- [17] R. Marine, *Chemom. Intell. Lab. Syst.* 27 (1995) 89–94.
- [18] H. Gampp, M. Maeder, C.J. Myer, A.D. Zuberbuhler, *Talanta* 32 (1985) 1133–1139.
- [19] H. Gampp, M. Maeder, C.J. Myer, A.D. Zuberbuhler, *Anal. Chim. Acta* 193 (1987) 293–297.
- [20] M. Maeder, A.D. Zuberbuhler, *Anal. Chim. Acta* 181 (1986) 287–291.
- [21] W. Windig, J. Guilment, *Anal. Chem.* 63 (1991) 1425–1432.
- [22] B.G.M. Vandegiste, W. Derks, G. Kateman, *Anal. Chim. Acta* 173 (1985) 253–264.
- [23] F. Cuesta-Sanchez, J. Toft, V.D. Bogaert, D.L. Massart, *Anal. Chem.* 68 (1996) 79–85.
- [24] A. de Juan, R. Tauler, *Anal. Chim. Acta* 500 (2003) 195–210.





Genetic algorithms (GA) applied to the orthogonal projection approach (OPA) for variable selection

S. Gourvénec, X. Capron, D.L. Massart*

ChemoAC, Pharmaceutical Institute, Vrije Universiteit Brussel, Laarbeeklaan 103, B-1090 Brussel, Belgium

Received 13 January 2004; received in revised form 13 May 2004; accepted 13 May 2004

Available online 13 July 2004

Abstract

Multivariate curve resolution (MCR) and especially the orthogonal projection approach (OPA) can be applied to spectroscopic data and were proved to be suitable for process monitoring. To improve the quality of the on-line monitoring of batch processes, it is interesting to get as many as possible spectra in a given period of time. Nevertheless, hardware limitations could lead to the fact that it is not possible to acquire more than a certain number of spectra in this given period of time. Wavelength selection could be a good way to limit this problem since it decreases size, and consequently the acquisition time, of each recorded spectrum. This paper details an industrial application of genetic algorithms (GA) coupled with a curve resolution method (OPA) for such purpose.

© 2004 Elsevier B.V. All rights reserved.

Keywords: Genetic algorithms (GA); Orthogonal projection approach (OPA); Curve resolution; Variable selection

1. Introduction

In order to monitor chemical reactions, more and more manufacturers acquire a lot of data, which are often multivariate. Nowadays, spectroscopy, and especially near infrared (NIR) spectroscopy, is commonly used to monitor chemical processes [1,2], particularly batch processes. Chemometrics is applied to reduce and compress to a low number of variables the information present in the many wavelengths that constitute a spectrum. Curve resolution is a group of chemometric methods that is very helpful to extract information from complex mixtures in batches. Several curve resolution methods are available, and the orthogonal projection approach (OPA) [3–6] was shown to be consistent in certain cases to monitor batch processes [7]. After development of a model based on OPA results, concentration profiles can be predicted at any time of a process and the evolution of different chemical species can be followed in function of time. One of the limitations of this technique for process monitoring in plants is the time that is necessary to acquire one spectrum and to transfer it to the database. Due to multiple hardware limitations,

acquiring many absorbances at several wavelengths could indeed decrease the number of available spectra during a certain period of time. It is then very interesting to make a variable selection on these spectra in order to keep only those that produce the best results from a curve resolution point of view. The elimination of variables that do not bring much information for resolution of the data matrix (leading to concentrations profiles) or the elimination of variables that are highly correlated between themselves (leading to redundant information) would give smaller spectra. It would be then possible to acquire more of such spectra in a certain period of time. Genetic algorithms (GA) [8–10] are used in this application to select certain variables, i.e. NIR wavelengths, that yield similar results as the complete spectrum would.

2. Theoretical part

2.1. OPA on single matrices

Monitoring a batch process with NIR spectroscopy produces for each batch a data matrix \mathbf{X} ($m \times n$) where m is the number of spectra (obtained at different times) and n the number of variables (e.g. wavelengths). The OPA is based

* Corresponding author. Tel.: +32 2 477 47 34; fax: +32 2 477 47 35.
E-mail address: fabid@vub.vub.ac.be (D.L. Massart).

on the bilinearity of the data matrix \mathbf{X} , which means that it can be decomposed into the product of the concentration profiles (\mathbf{C}) and pure compound spectra (\mathbf{S}), and a remaining residual matrix (\mathbf{E}).

$$\mathbf{X} = \mathbf{CS}^T + \mathbf{E} \quad (1)$$

OPA is a self-modelling curve resolution method and allows recovery of pure spectra and/or concentration profiles after estimation of the right number of components. OPA looks for the most dissimilar variables (columns) or spectra (rows) in \mathbf{X} . Although OPA can be applied in both directions of the matrix, OPA will be applied here in the time direction since the aim is to monitor a batch process by recording the evolution of spectra over time. The dissimilarity of each spectrum is defined as the determinant of the dispersion matrix ($\mathbf{Y}_i \mathbf{Y}_i^T$) of \mathbf{Y}_i , which initially contains the mean spectrum of the data matrix as a reference, normalized to length equal to 1, and the measured spectrum i (forming $m \times 2$) matrices).

$$d_i = \det(\mathbf{Y}_i^T \mathbf{Y}_i) \quad \text{for } i = 1 \dots m \quad (2)$$

The dissimilarity values are plotted as a function of time and the spectrum with the highest dissimilarity (and therefore the least correlated with this reference) is selected (\mathbf{x}_{s1}). \mathbf{x}_{s1} substitutes the mean spectrum as reference in \mathbf{Y}_i and each matrix \mathbf{Y}_i contains now the first selected spectrum \mathbf{x}_{s1} (normalized to length equal to 1) and spectrum i . This procedure is iteratively repeated step by step, by comparing each spectrum of \mathbf{X} with the spectra that have already been selected, and including the most dissimilar one into the matrix \mathbf{Y}_i for the next step. At each step, the dissimilarity of the newly selected spectrum is plotted as a function of time. A random behaviour of the dissimilarity plot indicates that a number of spectra equal to the number of components present has been selected in the step before, and that dissimilarity values represent only noise. The evaluation of the dissimilarity plots is often visual and depends on the judgement of the analyst but some other criteria like the Durbin–Watson criterion on dissimilarity plots [11] can be to make the decision more objective.

After the selection of these components, which are often called “pure” although they are not, multivariate curve resolution–alternating least squares (MCR–ALS) is applied to resolve the data matrix \mathbf{X} into the pure component spectra and their related individual concentration profiles. The procedure starts by calculating the concentration profiles (\mathbf{C}) by least squares as:

$$\mathbf{C} = (\mathbf{XS})(\mathbf{S}^T \mathbf{S})^{-1} \quad (3)$$

where \mathbf{S} is the matrix containing in the columns the selected spectra in OPA.

With the new matrix \mathbf{C} , a new set of spectra (matrix \mathbf{S}) is calculated by least squares as:

$$\mathbf{S} = (\mathbf{X}^T \mathbf{C})(\mathbf{C}^T \mathbf{C})^{-1} \quad (4)$$

The sum of squares of the residuals, SSR, is calculated by:

$$\text{SSR} = \sum_{i=1}^m \sum_{j=1}^n r_{ij}^2$$

where r_{ij} are elements of \mathbf{R} , defined by:

$$\mathbf{R} = \mathbf{X} - \mathbf{CS}^T \quad (5)$$

Eqs. (3) and (4) are repeated iteratively until the relative difference in the SSR values of two consecutive iterations is lower than a pre-defined convergence limit.

When \mathbf{X} is decomposed into \mathbf{C} and \mathbf{S} , which are both unknown, an infinite number of possible combinations for the correct reproduction of the data matrix \mathbf{X} can be found. The matrices \mathbf{C} and \mathbf{S} obtained from the MCR–ALS procedure are subjected to two sources of ambiguities: rotational and intensity ambiguity [12]. The rotational ambiguity results in \mathbf{C} and \mathbf{S} matrices, which contain linear combinations of the real profiles, while the intensity ambiguity does not affect the shape of the profiles but only the magnitude. Constraints can be used to break these ambiguities [13]. Several constraints are available. Unimodality, closure and non-negativity are used in this particular application.

A constraint derived from the unimodality concept that allows only one maximum in a profile is applied to the concentration and spectral profiles. It consists in comparing consecutive values two by two (starting from the maximum of a profile) and by equalizing consecutive values that are not significantly different. It does not allow minor noise peaks for concentration profiles and spectra and has a smoothing effect in each iteration of the ALS procedure. Closure is applied to the concentration profiles. The total concentration of the species involved in the reaction is considered to be constant at each time of the reaction (closed reaction system). The concentrations related to the species involved are modified proportionally to make their sum equal to the closure constant (which is set to 1). The last constraint used is the non-negativity constraint. In each step of the ALS procedure, a negative value of a concentration profile is set to zero for the next iteration. As the spectra that are used are second derivative spectra, no non-negativity constraint was applied in the spectral dimension.

2.2. OPA on several matrices

OPA and MCR–ALS can also be applied to three-dimensional data matrices. It is indeed possible to study several matrices (e.g. several batches from the same process) by building an augmented matrix by column wise matrix augmentation. This augmented (three-way) data matrix

$X_{\text{augmented}}$ follows the same rules of decomposition as a single matrix:

$$X_{\text{augmented}} = \begin{bmatrix} X_1 \\ X_2 \\ \vdots \\ X_{n-1} \\ X_n \end{bmatrix} = \begin{bmatrix} C_1 \\ C_2 \\ \vdots \\ C_{n-1} \\ C_n \end{bmatrix} S + \begin{bmatrix} E_1 \\ E_2 \\ \vdots \\ E_{n-1} \\ E_n \end{bmatrix} \quad (6)$$

$$= C_{\text{augmented}} S + E_{\text{augmented}}$$

The right number of components was determined with OPA applied on different single batches. The pure spectra obtained from these single-OPA analyses are input as initial estimates in the ALS optimisation to recover the concentration profiles ($C_{\text{augmented}}$) and spectra (S). According to the same principles as explained above, the following equations are applied:

$$C_{\text{augmented}} = X_{\text{augmented}} S^T (S^T S)^{-1} \quad (7)$$

$$S = (C_{\text{augmented}}^T C_{\text{augmented}})^{-1} C_{\text{augmented}}^T X_{\text{augmented}} \quad (8)$$

The same constraints as for the two-way matrix are applied for this augmented matrix and, because of the structure of the augmented matrix, additional constraints are used. The first one is that common species have the same spectrum in all appended matrices. This constraint is inherent to the decomposition of the column wise augmented matrix, and the possibility to have only one spectrum for each compound in all matrices makes the rotational ambiguity less severe than in the case of single matrices. The scale and intensity ambiguities are removed in this way. The second additional constraint is the correspondence between species, which attributes the first column of the augmented concentration matrix to the first species, the second column to the second species and so on.

2.3. Genetic algorithms

Holland [8] introduced GA [13–18] as problem-solving methods that simulate a natural evolution process. GA are well fitted to solve subset selection problems, such as variable selection. The natural evolution process simulated by the GA follows Darwin's classical rules about natural evolution, and uses random steps to converge to a non-random optimal solution. Since in this study the aim of the genetic algorithm is to optimise the selection of ranges of NIR wavelengths, a solution is a set of continuous wavelengths grouped in a certain number of ranges. The wavelengths selected from the 201 available wavelengths will constitute a reduced NIR spectrum that can deliver the same information as the full spectrum. The fact that the selected wavelengths have to be grouped in ranges is a constraint that the GA has to take into account. The flow chart of the genetic algorithm is shown in Fig. 1. The different steps of GA are listed below.

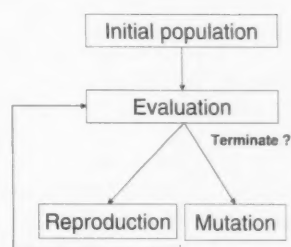


Fig. 1. Flow chart representing the genetic algorithm.

2.3.1. Mathematical representation of the solutions

A mathematical representation of the solutions is needed. They are encoded as a string of binary, integer or real numbers. In this case solutions to the problem are encoded as strings of integers, a string standing for a range of wavelengths. One solution can be seen as a continuous series of strings of zeros and strings of ones the total number of integers being equal to the total number of variables. Strings of zeros indicate that the solution does not include these variables while strings of ones indicate the selected wavelengths. Each string n_i of a solution (coded as a string of ones) contains a free number m_i of wavelengths, with the constraint that the total number of wavelengths selected (i.e. $\sum m_i$) should not be larger than p , the maximum number of wavelengths allowed. Initially, each string n_i contains m_i randomly chosen wavelengths respecting the constraint. The total number of ranges of selected variables in a solution is n . An example of a solution is shown in Fig. 2. It has to be noticed that the total number of genes in a valid individual is not necessary p , but could be less. Solutions are allowed to overlap: the same wavelengths can belong to two or more solutions.

2.3.2. Initial population

A number of possible candidate solutions is randomly generated. As the solution space has to be well spanned, the number of initial candidates should be large enough. In this case the initial population consists of 100 solutions.

2.3.3. Evaluation

A fitness function has to be defined. This function computes a criterion, the fitness, which evaluates the quality of candidate solutions.

Here, the fitness function is a measure of the dissimilarity between concentration profiles obtained with all variables (C_{real}) on the one hand, and those obtained with a subset of selected variables (C_{new}) on the other. The optimal

000011000000111100001111111100

Fig. 2. Example of a solution coded with 30 integers (representing 30 wavelengths) with n ranges ($n = 3$) and m selected wavelengths ($m = 14$, $m_1 = 2$, $m_2 = 4$, $m_3 = 8$).

solution is the one with the lowest value for this criterion, meaning that, in this case the dissimilarity has here to be minimized. Several concentration profiles corresponding to different chemical species are obtained with OPA. The fitness function can be calculated for all concentration profiles together or for only one of them that is judged to be the most important. In this study, different fitness functions were tried. They are all based on the comparison between C_{real} and C_{new} , but through different approaches. Four main approaches were retained and are, respectively, related to correlation (function 1), Euclidean distance (function 2), difference between curves (function 3) and Hausdorff's distance (function 4). Wavelength selection was performed on different batches with all fitness functions. Based on the results, it was established that the four fitness functions all yield similar results. Function 3 was chosen as the reference function for the rest of the paper because of its simplicity and is consequently the only one described here.

Fitness function: for one chemical species based on the difference between curves:

$$\text{Diff}_i = \sum |C_{\text{real}_i} - C_{\text{new}_i}| \quad (9)$$

Fitness function: for q chemical species based on the difference between curves:

$$\text{Diff} = \sqrt{\frac{\sum_{i=1}^q \text{Diff}_i^2}{q}} \quad (10)$$

Once the initial population has been evaluated, it evolves to give new solutions. For this purpose, two genetic operators are used: reproduction and mutation.

2.3.4. Reproduction

It consists in using cross over in the recombination of fractions of two candidates (the parent strings) to obtain two new solutions (the child strings). Individuals are first grouped in pairs according to their fitness, i.e. individuals with best fitness have higher probability to recombine between each other. The two individuals that give the best fitness constitute the first pair. The two next ones constitute the second pair and so on. Then a cross-over point is randomly selected. At this point, strings are recombined to obtain the child strings, which are new solutions to the problem. In the algorithm applied here, the cross-over point is not a real cross-over point because of the constraint of wavelengths that are necessarily grouped in ranges. A range is chosen randomly on each parent, and the reproduction consists in exchanging these ranges between parents

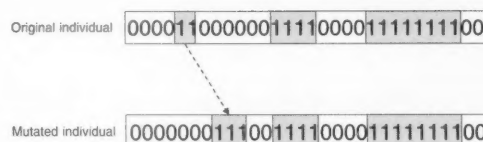


Fig. 4. Scheme of mutation of the GA of the study.

(Fig. 3). Once the reproduction is performed, the validity of the children is checked, i.e. it is verified that the child means respects the maximum number of allowed wavelengths and that the wavelengths within a range are continuous. In case one child is not valid, its parent replaces it, parent 1 replacing child 1 for instance. If a child is valid, its fitness is compared to the fitness of the worst individual in the population. If better, the child is kept, if not, it is discarded. It has to be mentioned that reproduction as performed in this GA is quite different from what is usually done in standard GA.

2.3.5. Mutation

When all strings in a population share an identical part, the reproduction is not able to explore the whole solution space. Therefore, the mutation is used to randomly introduce new variability in the population of solutions. The mutation operator used here does not change a single wavelength as it would in classical GA but a range to respect the constraints of the problem, i.e. continuous wavelengths grouped in ranges with a maximum total number allowed. Otherwise each generation of the algorithm would yield many non-valid individuals that would have to be discarded during the evaluation step, resulting in an inefficient genetic algorithm. The mutation consists in modifying one range of a solution, both its location in the spectrum (i.e. the wavelength that characterizes the beginning of the range) and size (i.e. the number of wavelengths of the range). It means that a mutated range results in a range that is larger or smaller than the original one (Fig. 4).

At each generation of the algorithm, the evolution operator applied is chosen randomly, with the same probability 0.5 to occur, i.e. both the reproduction and the mutation operator have the same probability to occur.

Cross over and mutation are here performed as two independent steps, measuring the fitness function after each of them. This is a major difference with standard GA, in which the evaluation is performed after the offspring obtained by a cross over has undergone mutation.

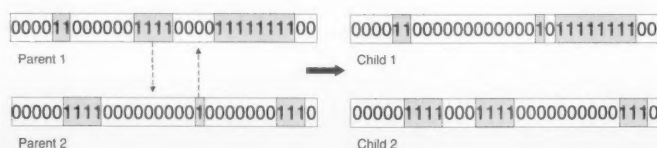


Fig. 3. Scheme of reproduction of the GA of the study.

2.3.6. Termination of the algorithm

The presented algorithm terminates after a predefined number of generations, equal to 75 000 iterations.

3. Experimental section

3.1. Data

The dataset consists of NIR spectra of polymerisation recorded as a function of time. These spectra are pre-treated using the second derivation of Savitsky and Golay [19]. Thirty-three batches are available. The spectra were measured from 900 to 1700 nm with a gap of 4 nm. For convenience the wavelengths will be called here from 1 to 201.

3.2. Software

All programs were run under the Matlab (The MathWorks, Natick, MA) computing environment. The genetic algorithm was written in-house. The OPA program was originally written by Sánchez et al. for chromatographic peak purity assessment and mixture analysis. This mfile is part of the ChemoAC toolbox, downloadable at <http://minf.vub.ac.be/~fabl/>. The ALS program used for the augmented matrix was written by Tauler and de Juan and is freely accessible on the Internet at <http://www.ub.es/gesq/mcr/mcr.htm>.

4. Results and discussion

OPA was applied to several batches in earlier work and it was found that the best results are obtained with three components [7] using non-negativity and closure constraints for the concentration profiles and the unimodality constraint for the spectral and concentrations profiles. OPA yields concentration profiles for three different chemical species which will be denoted as “3 curves” in what follows. For the process engineers only the third one is really important and therefore only the concentration profile of the third species, representing the concentration evolution of the final product of the process, was used for wavelength selection.

The p value (maximum of wavelengths allowed) was set between 50 and 80.

The q value (maximum number of ranges allowed in a solution) was set between 2 and 4. It was established in agreement with the process engineers that this number of ranges and wavelengths should be sufficient to obtain correct results.

Several successive runs for four different combinations of q and p values were made to be able to compare results, to have an idea of the reproducibility of the results and the interpretation of the selected variables. Some wavelengths are indeed known to be important for the specific studied process.

Table 1

Results of the selection of 2 ranges with a maximum number of 50 wavelengths for batch 1

	Ranges selected	Fit
Fitness function 3		
Run 1	53–73/175–201	0.0311
Run 2	60–74/166–201	0.0461
Run 3	51–73/174–201	0.0347
Run 4	52–73/175–201	0.0303
Run 5	52–73/175–201	0.0303
Run 6	52–73/175–201	0.0303
Run 7	52–73/175–201	0.0303

The results of a GA optimisation can depend on the randomly chosen original population and for this reason several runs were made.

4.1. Wavelength selection on batch 1

To start with, only one batch representative for the process was studied. Several runs for four different pairs of values of q (from 2 to 4) and p (from 50 to 80) were made to perform wavelength selection. For the reasons explained higher only curve 3 was studied. The results for the selection of maximum $q = 2$ ranges with a maximum of $p = 50$ wavelengths are shown in Table 1. In six cases of seven the first range obtained for this batch is from 51, 52 to 53–73 and the second from 174 to 175–201. Only one solution is somewhat different (and shows somewhat higher dissimilarity), but it still comes from the same region in the spectrum.

For 3 ranges with a maximum of 60 wavelengths, for 3 ranges with a maximum of 80 wavelengths and 4 ranges with a maximum of 80 wavelengths, the results are also displayed in Tables 2–4.

For the four different cases tested here, except for one run, the selection always leads to 2 ranges which can therefore be considered to be the best number of ranges for this batch. Fig. 5 shows wavelengths that were the most often selected during all runs. These wavelengths are important to obtain correct OPA results and are visualised with second derivative NIR spectra of the concerned batch. The two

Table 2

Results of the selection of 3 ranges with a maximum number of 60 wavelengths for batch 1

	Ranges selected	Fit
Run 1	48–72/173–201	0.0354
Run 2	49–70/179–200	0.0381
Run 3	58–73/170–200	0.0305
Run 4	57–75/175–199	0.0270
Run 5	48–72/175–199	0.0243
Run 6	56–74/172–201	0.0350
Run 7	56–73/175–201	0.0327
Run 8	58–76/175–200	0.0262
Run 9	55–77/173–199	0.0248
Run 10	45–73/179–198	0.0357
Run 11	47–75/175–198	0.0235

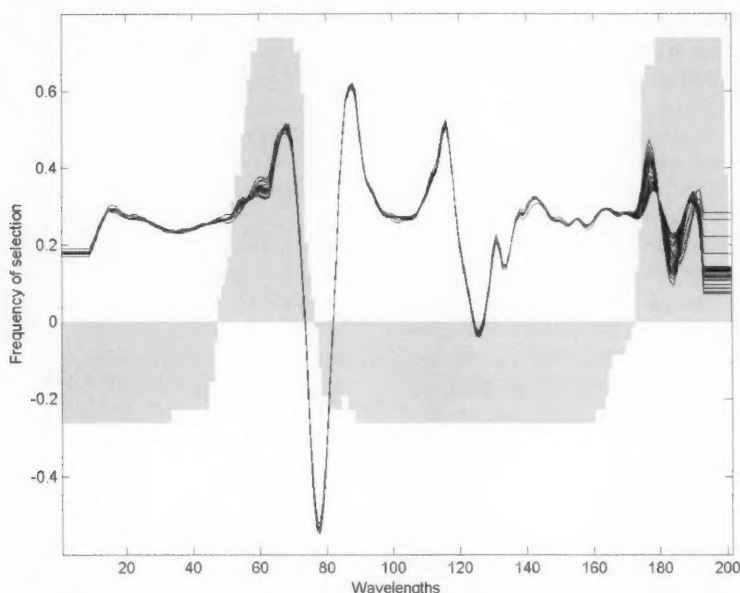


Fig. 5. Bar plot of the cumulative frequency of selection of each wavelength for batch 1, with the corresponding second derivative NIR spectra. To make differences more evident, the average value has been subtracted.

most important regions can be identified as region 1:48–76 and region 2:173–201. It can also be noticed that the fit is not very different from run to run and even from case to case. Obviously, the more wavelengths are selected the better is the obtained fit. However, in the studied case, the fit does not change significantly for different combinations of q and p . It seems that a local optimum of fitness is rapidly obtained and that afterwards, adding wavelengths does not further improve the results to an appreciable extent (Tables 1–4).

Table 3

Results of the selection of 3 ranges with a maximum number of 80 wavelengths for batch 1

	Ranges selected	Fit
Run 1	47–77/165–199	0.0247
Run 2	50–78/174–200	0.0251
Run 3	47–77/165–199	0.0247
Run 4	55–73/176–200	0.0313
Run 5	45–76/161–198	0.0222

Table 4

Results of the selection of 4 ranges with a maximum number of 80 wavelengths for batch 1

	Ranges selected	Fit
Run 1	57–78/175–199	0.0244
Run 2	55–80/164–201	0.0278
Run 3	53–86/173–199	0.0309
Run 4	34–72/173–200	0.0275
Run 5	48–73/85–88/174–200	0.0132

4.2. Wavelength selection on other batches

In order to check if wavelengths selected by GA for one batch are similar to those selected for different batches of the same process, two other batches were studied. Batch 2 is a production batch prepared at industrial scale and batch 3 was obtained at pilot plant scale in the research center. Wavelength selection is still performed batch per batch, meaning that the selection is done within a batch and not for all batches together. The four, same combinations of q and p as previously are studied and from 2 to 4 ranges are searched for a maximum number of wavelengths varying from 50 to 80. The results of the selections are shown in Tables 5 and 6. Figs. 6 and 7 show the frequency with which each wavelength was selected and reveal that the selected wavelengths are from the same regions as for batch 1. For batch 2, the selected regions are 50–92 and 174–201, while for batch 3, the selected regions are 61–91 and 172–200. Analysis of separate results leads to the conclusion that one region is always selected (173–201 for batch 1, 174–201 for batch 2 and 172–200 for batch 3). The second selected region is less constant and seems to be of smaller importance (48–76 for batch 1, 50–92 for batch 2 and 61–91 for batch 3). Inspection of this second region leads to the conclusion that the wavelengths that are chosen are parts of the same peak but they can be either on the ascendant or the descendant part.

4.3. Wavelength selection on several batches analysed together

In order to have variable selection for one grade of product for the same process and not only for one batch, GA was

Table 5

Results of four selections for batch 2: 2 ranges with maximum 50 wavelengths, 3 ranges with maximum 60 wavelengths, 3 ranges with maximum 80 wavelengths and 4 ranges with maximum 80 wavelengths

	$q = 2, p = 50$		$q = 3, p = 60$		$q = 3, p = 80$		$q = 4, p = 80$	
	Ranges selected	Fit	Ranges selected	Fit	Ranges selected	Fit	Ranges selected	Fit
Run 1	59–82/175–201	0.0161	54–71/79–87/174–201	0.0076	44–89/173–199	0.0110	67–89/176–199	0.0169
Run 2	58–76/179–198	0.0249	53–76/79–84/175–201	0.0068	52–89/174–198	0.0178	1–13/61–92/174–200	0.0062
Run 3	67–88/176–201	0.0250	41–75/90–95/181–199	0.0224	55–71/79–109/170–201	0.0073	47–92/175–199	0.0057
Run 4	47–74/180–200	0.0247	58–72/79–95/174–201	0.0081	44–74/79–98/172–201	0.0044	53–70/78–95/160–197	0.0060
Run 5	62–77/179–200	0.0331	49–77/179–196	0.0027	50–72/77–105/175–200	0.0080	51–90/179–197	0.0020

Table 6

Results of four selections for batch 3: 2 ranges with maximum 50 wavelengths, 3 ranges with maximum 60 wavelengths, 3 ranges with maximum 80 wavelengths and 4 ranges with maximum 80 wavelengths

	$q = 2, p = 50$		$q = 3, p = 60$		$q = 3, p = 80$		$q = 4, p = 80$	
	Ranges selected	Fit	Ranges selected	Fit	Ranges selected	Fit	Ranges selected	Fit
Run 1	63–84/173–198	0.0031	62–84/119–127/174–199	0.0019	61–95/158–198	0.0016	57–75/130–143/170–201	0.0010
Run 2	63–83/174–198	0.0029	63–85/171–200	0.0019	49–91/128–138/174–200	0.0014	59–81/119–129/175–200	0.0019
Run 3	62–85/173–199	0.0025	64–84/115–122/173–198	0.0026	62–93/118–135/173–200	0.0013	64–92/116–123/161–199	0.0018
Run 4	61–84/174–199	0.0021	59–91/174–198	0.0019	61–95/158–198	0.0018	57–102/172–200	0.0015
Run 5	63–83/174–199	0.0029	57–75/172–200	0.0017	39–54/63–91/165–199	0.0018	42–55/61–96/172–197	0.0015

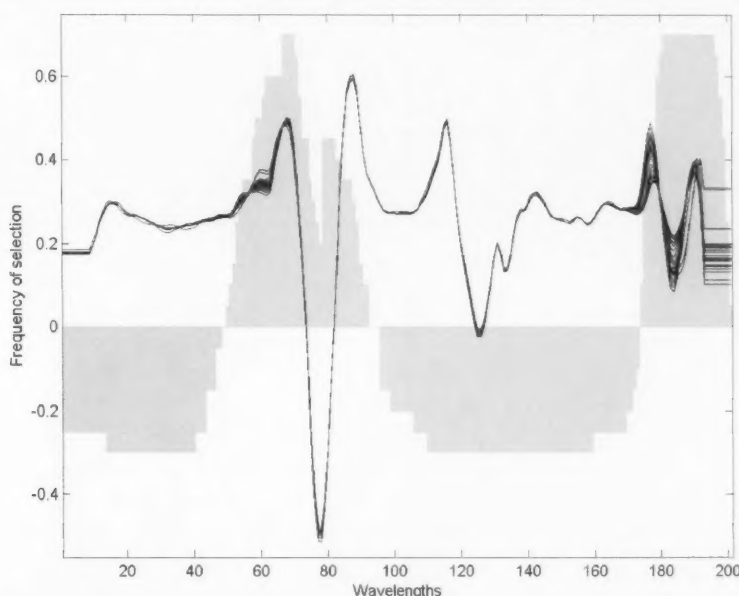


Fig. 6. Bar plot of the cumulative frequency of selection of each wavelength for batch 2, with the corresponding second derivative NIR spectra. To make differences more evident, the average value has been subtracted.

Table 7

Results of four selections for 5 batches analysed simultaneously: 2 ranges with maximum 50 wavelengths, 3 ranges with maximum 60 wavelengths, 3 ranges with maximum 80 wavelengths and 4 ranges with maximum 80 wavelengths

	$q = 2, p = 50$		$q = 3, p = 60$		$q = 3, p = 80$		$q = 4, p = 80$	
	Ranges selected	Fit	Ranges selected	Fit	Ranges selected	Fit	Ranges selected	Fit
Run 1	73–97/176–193	0.183	53–66/75–113/185–190	0.149	42–90/183–191	0.154	69–76/82–123/177–199	0.177
Run 2	73–97/176–193	0.183	35–42/67–99/177–194	0.216	61–84/113–139/175–198	0.126	72–91/101–119/177–197	0.144
Run 3	84–114/177–193	0.232	67–79/129–148/175–193	0.183	75–84/113–136/176–201	0.189	40–81/158–164/176–196	0.189
Run 4	71–86/165–193	0.179	19–38/76–89/178–196	0.196	60–88/120–129/158–197	0.137	54–84/121–131/165–196	0.139
Run 5	73–86/165–193	0.187	21–30/73–83/167–193	0.199	65–78/86–128/175–197	0.175	56–97/174–194	0.136

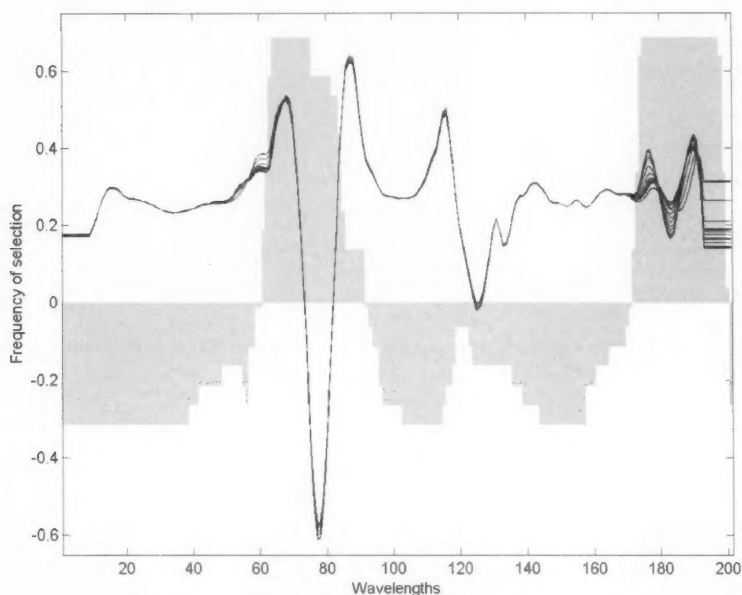


Fig. 7. Bar plot of the cumulative frequency of selection of each wavelength for batch 3, with the corresponding second derivative NIR spectra. To make differences more evident, the average value has been subtracted.

performed on five representative batches together. Batches 1, 2 and 4 are production batches, 3 and 5 are from the pilot plant. The results of these selections are shown in Table 7. They confirm the results obtained on batches separately: the wavelengths selected correspond to those selected when separate batches were studied.

Obviously, as new variability was introduced by the two new batches and as OPA performed on several batches simultaneously brings additional constraints, results could not be compared exactly with results on single batches (details about these additional constraints are given in Section 2.2 about OPA on several matrices). However, as can be seen on

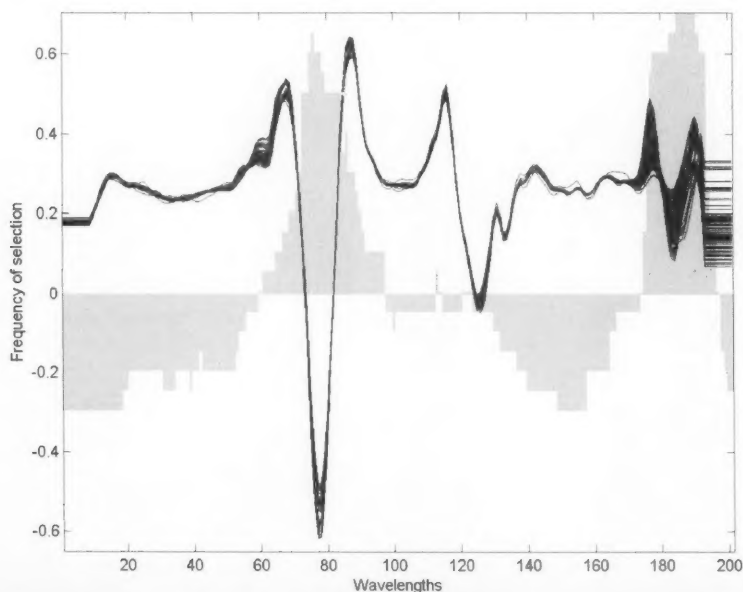


Fig. 8. Bar plot of the cumulative frequency of selection of each wavelength for the 5 batches analysed simultaneously, with the corresponding second derivative NIR spectra. To make differences more evident, the average value has been subtracted.

Fig. 8, two regions of NIR spectra are needed to obtain good OPA results. These two regions are 61–97 and 175–196, corresponding to 1140–1284 and 1596–1680 nm for a total of 59 wavelengths. They were selected as the optimal ones according to the researched aim in this study.

It can be added that although repeatability and reproducibility are not perfect, the results reveal that the ranges that are selected are always in the same spectral domain (between approximately 50–100 and 160–200). Even if the GA does not reach exactly the same fitness each time, the second range (160–200) is always selected and is quite reproducible. This selection confirms the knowledge that we have from the process and from the products.

4.4. Evaluation of the results: comparison with full spectrum results

The comparison between the concentration profiles obtained with OPA with complete spectra (201 wavelengths)

and with only 59 wavelengths is shown in Fig. 9. This comparison is performed on the five tested batches separately, for the three concentration profiles, although only the third one is of interest for the process engineers. The Fig. 9 shows that the concentration profiles calculated with both complete and incomplete spectra are very similar, and that no clear difference is observed between the two.

4.5. The use of the selected wavelengths in the plant

Engineers from the plant were interested to have smaller spectra to be able to record a larger number of them. The ranges selected are about 3.5 times smaller than the original spectra. One problem remains. Only second derivative spectra were available and the wavelength selection was therefore performed on these spectra. When the reduced spectra will be measured and subjected to derivatisation not exactly the same spectra will be obtained. Two possible solutions are considered. The first consists of working with

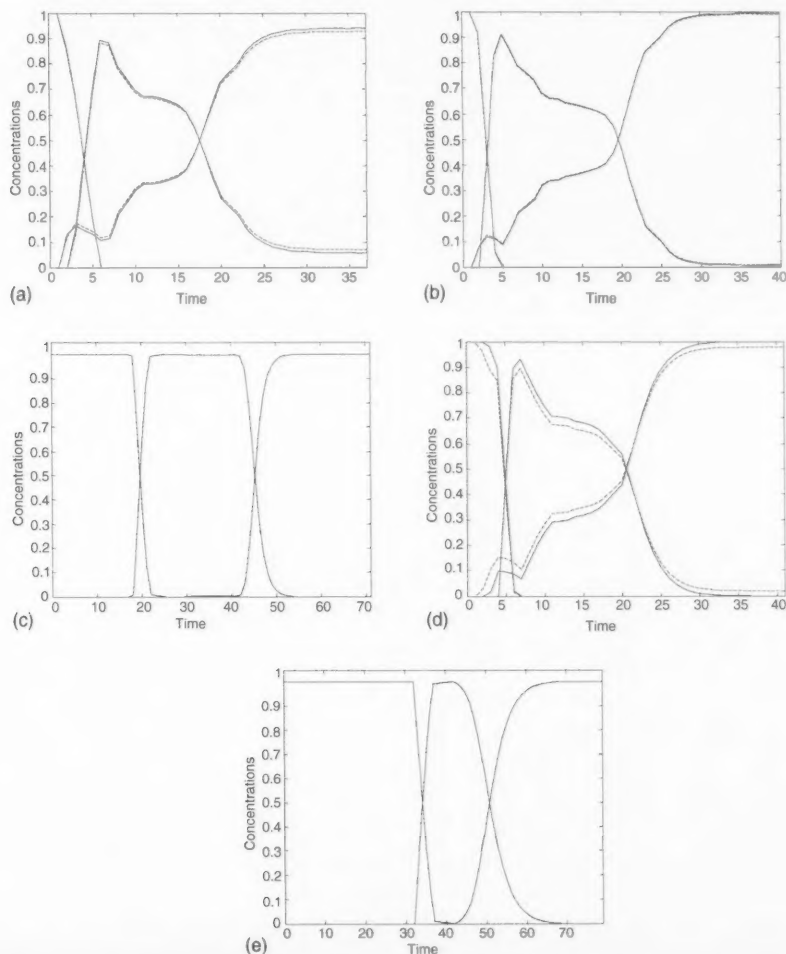


Fig. 9. Comparison of results of OPA with second derivative spectra composed of 201 wavelengths (—) and of 59 selected wavelengths (---) for (a) batch 1, (b) batch 2, (c) batch 3, (d) batch 4 and (e) batch 5.

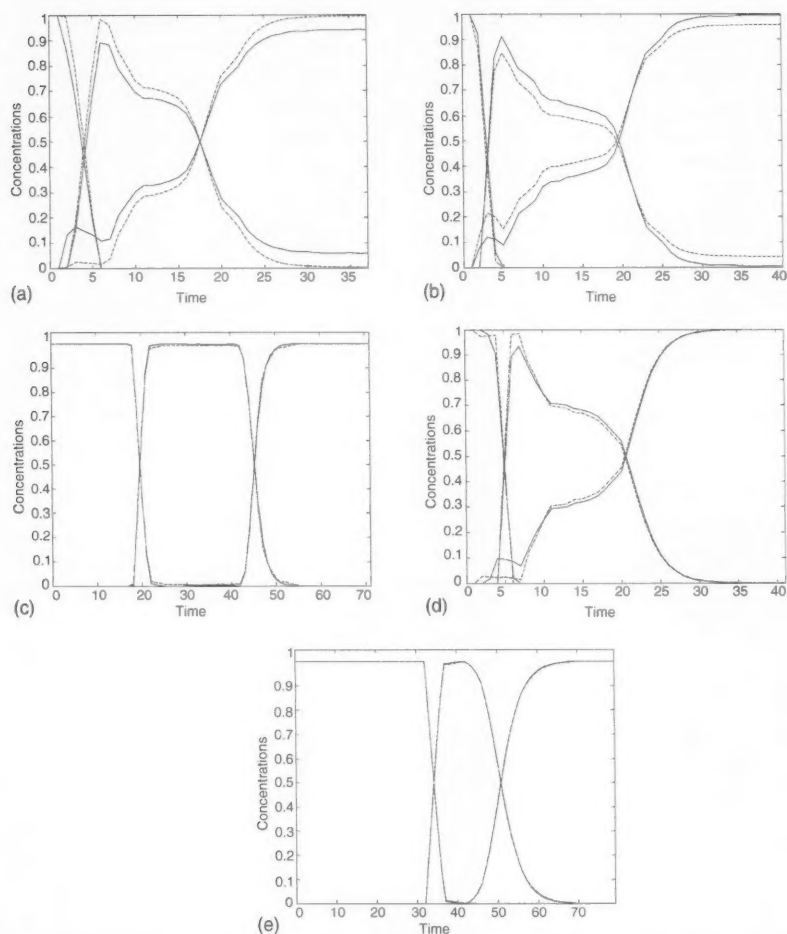


Fig. 10. Comparison of results of OPA with second derivative spectra composed of 201 wavelengths (—) and with raw NIR spectra with 59 selected wavelengths (---) for (a) batch 1, (b) batch 2, (c) batch 3, (d) batch 4 and (e) batch 5.

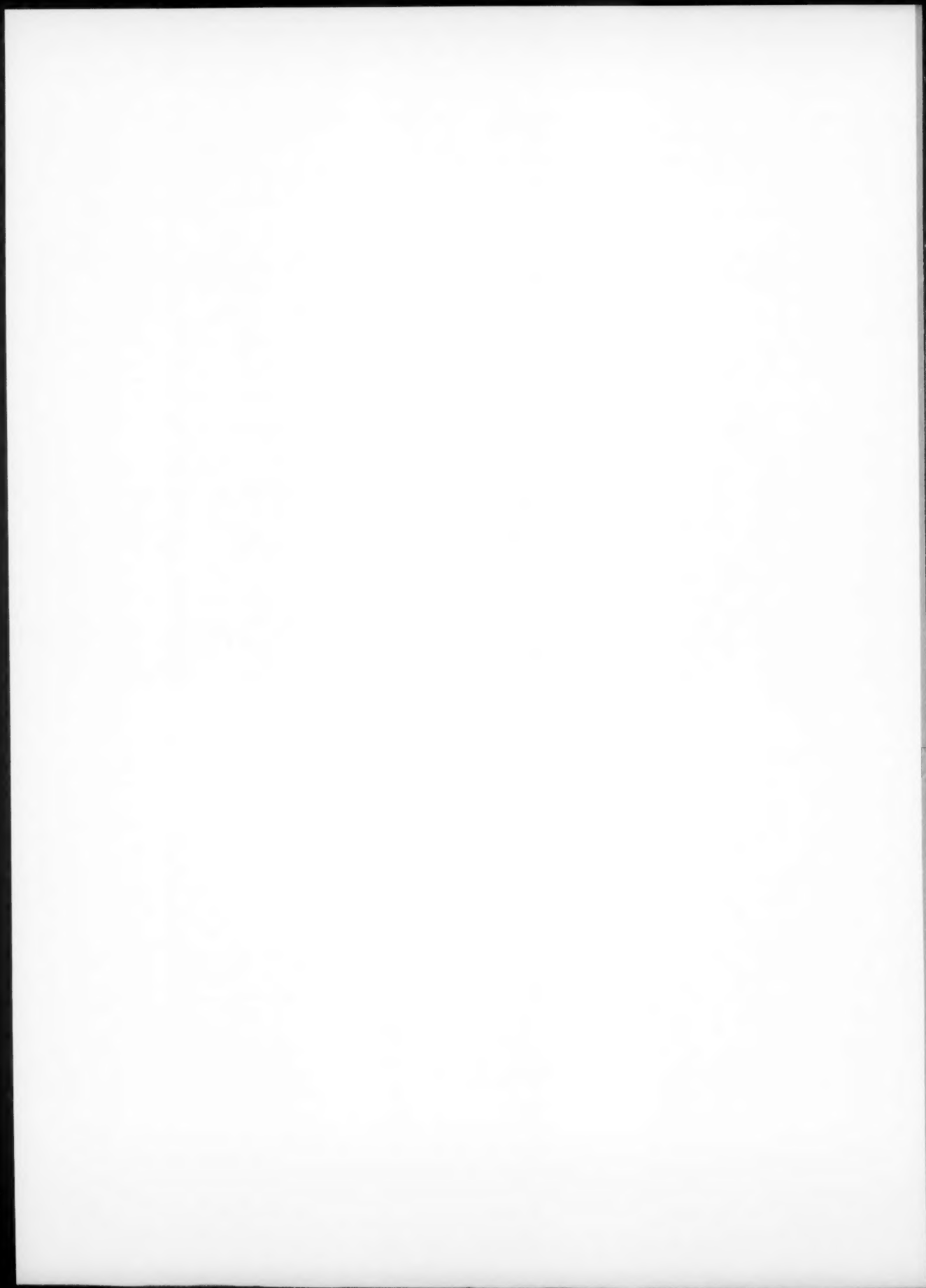
the underivatised spectra. The selected wavelengths provide the most important information in the spectra, and since the rest of the spectrum was eliminated the use of derivatives is not as necessary as with complete spectra. Indeed one of the goals of the derivatives is to enhance differences between spectra and this is less necessary after feature selection because only the really informative part of spectra is kept. Moreover, working with raw spectra would also increase somewhat the number of spectra that can be recorded in a given time span. The second possibility is to enlarge the 2 ranges of selected wavelengths. To be able to obtain the same derivative values as with complete spectra and to consequently avoid border effects, the selected ranges have to be a little bit extended. Since the window size was 17 in this study, eight extra wavelengths have to be recorded at the lower border of this range to be able to calculate the derivative value of the first point of the range (that corresponds to the center of a 17-size window). The same rule applies to the upper border of the first range and to both borders of the

second one. This second solution would lead to 2 ranges of 53–105 and 167–201 instead of 61–97 and 175–196 originally. On the “new” selection, second derivatisation can be performed, and only parts of spectra with original selected wavelengths can be kept for exploitation with OPA. These two selections, although we have 29 wavelengths more, are not so different, and the number of wavelengths is still decreased by around 2.2 compared to the original spectra, which allows gaining some time. In the present case, the first solution was retained, since the idea is to have as less wavelengths as possible. As can be seen on Fig. 10, even if this first solution seems to be more restrictive, concentration profiles are well recovered and differ from the references profiles (i.e. the ones that are obtained with derivative data) mostly in intensity but not in shape. It should be added that concentrations profiles of batches (a), (b), (d) that are from production plant are not completely equivalent to profiles of batches (c) and (e) coming from a pilot plant. This can be easily explained by the fact that in the pilot plant both quality

of raw products and process conditions are constant and well controlled, leading to smooth profiles and plateaus. In contrary, in the production plant, several perturbations can occur (evolving process conditions, quality of raw products, noise on data . . . , etc) giving profiles that are more “imperfect” but that represent the process as it is in reality. In the study, it was decided to keep both pilot and production data because they represent the same process and provide both very interesting and useful information in term of curve resolution.

References

- [1] R. de Maesschalck, F. Cuesta Sanchez, D.L. Massart, P. Doherty, P. Hailey, *Appl. Spectrosc.* 52 (1998) 725–731.
- [2] H.W. Ward, S.D. Sekulic, M.J. Wheeler, G. Taber, F.J. Urbanski, F.E. Sistare, T. Norris, P.K. Aldridge, *Appl. Spectrosc.* 52 (1998) 17–21.
- [3] F.C. Sánchez, J. Toft, B. Van den Bogaert, D.L. Massart, *Anal. Chem.* 68 (1996) 79–85.
- [4] F.C. Sánchez, B.G.M. Vandeginste, T.M. Hanczewicz, D.L. Massart, *Anal. Chem.* 69 (1997) 1477–1484.
- [5] R. Tauler, D. Barcelo, *Trends Anal. Chem.* 12 (1993) 319–327.
- [6] F.C. Sánchez, S.C. Rutan, M.D. Gil Garcia, D.L. Massart, *Chemom. Intell. Lab. Sys.* 36 (1997) 153–164.
- [7] S. Gourvénec, C. Lamotte, P. Pestiaux, D.L. Massart, *Appl. Spectrosc.* 57 (2003) 80–87.
- [8] J.H. Holland, *Adaptation in Natural and Artificial Systems*, University of Michigan Press, Ann Arbor, MI, 1975 (Revised Print: MIT Press, Cambridge, MA, 1992).
- [9] D.E. Goldberg, K. Deb, A comparative analysis of selection schemes used in genetic algorithms, in: G.J.E. Rawlins (Ed.), *Foundations of Genetic Algorithms*, Morgan Kaufmann, San Mateo, 1991, pp. 69–93.
- [10] L. Davis, A genetic algorithms tutorial, in: L. Davis (Ed.), *Handbook of Genetic Algorithms*, Van Nostrand Reinhold, New York, 1991, pp. 1–101.
- [11] S. Gourvénec, D.L. Massart, D.N. Rutledge, *Chemom. Intell. Lab. Syst.* 61 (2002) 51–61.
- [12] R. Tauler, A. Smilde, B. Kowalski, *J. Chemom.* 9 (1995) 31–58.
- [13] A. De Juan, Y. Vander Heyden, R. Tauler, D.L. Massart, *Anal. Chim. Acta* 346 (1997) 307–318.
- [14] C.B. Lucasius, G. Kateman, *Chemom. Intell. Lab. Syst.* 19 (1993) 1–33.
- [15] C.B. Lucasius, G. Kateman, *Chemom. Intell. Lab. Syst.* 25 (1994) 99–146.
- [16] D. Jouan-Rimbaud, D.L. Massart, R. Leardi, O. De Noord, *Anal. Chem.* 67 (1995) 4295–4301.
- [17] R. Leardi, A. Lupianez Gonzalez, *Chemom. Intell. Lab. Sys.* 41 (1998) 195–207.
- [18] R. Leardi, R. Boggia, M. Terrile, *J. Chemom.* 6 (1992) 267–281.
- [19] A. Savitsky, M.J.E. Golay, *Anal. Chem.* 36 (1964) 1627–1639.



Liquid chromatography and chemometric methods for determination of rofecoxib in presence of its photodegradate and alkaline degradation products

Mostafa A. Shehata^{a,*}, Ahmed Ashour^b, Nagiba Y. Hassan^a,
Ahmad S. Fayed^a, Badr A. El-Zeany^a

^a Analytical Chemistry Department, Faculty of Pharmacy, Cairo University, Kasrel Aini Street, 11562 Cairo, Egypt

^b Pharmaceutical Analytical Chemistry Department, Faculty of Pharmacy, Ain Shams University, Cairo, Egypt

Received 13 April 2004; received in revised form 6 May 2004; accepted 6 May 2004

Available online 10 July 2004

Abstract

Rofecoxib (I) has been determined in presence of its photodegradate (II) and alkaline degradation products (III) and (IV) by liquid chromatography method using a Shimpak ODS C₁₈ column (150 mm × 4.5 mm i.d.) and acetonitrile/0.05% phosphoric acid (35:65) at pH 2.6. The method could determine (I) in the range of 0.3–28 µg ml⁻¹ with mean percentage recovery of 100.29 ± 0.979%. Also, two chemometric methods were developed using partial least square (PLS) and concentration residual augmented classical least square method (CRACLS). The methods could determine (I) in presence of (II), (III) and (IV) with linearity range of 2–36 µg ml⁻¹ and with mean percentage recovery of 99.53 ± 1.613 and 99.31 ± 1.42% for PLS and CRACLS, respectively. The PLS method was used to carry out a kinetic study of the alkaline degradation. The reaction rate constant was found to be $k = 0.051 \text{ min}^{-1}$ and the $t_{1/2} = 13.5 \text{ min}$ using 0.051 M sodium hydroxide at 25 °C, other kinetic data were also presented. The three methods were applied to the analysis of pharmaceutical dosage forms and bulk powder.

© 2004 Elsevier B.V. All rights reserved.

Keywords: Rofecoxib; Photodegradates; Alkaline degradates; HPLC; Chemometrics; Kinetics

1. Introduction

Non steroidal anti-inflammatory drugs (NSAIDs) are widely used for the treatment of pain and for management of oedema and tissue damage resulting from inflammatory joint diseases. Some of these drugs may cause gastric ulcers and hemorrhagia upon chronic use due to inhibiting both cox-1 and cox-2 enzymes such as aspirin and ketoprofen [1]. The development of selective cox-2 inhibitors minimizes the gastrointestinal toxicity caused by these drugs. Rofecoxib (I) was found to be a highly selective cox-2 inhibitor, the selectivity ratio is more than 800 [2]. Also, rofecoxib toxicity in patients with rheumatoid arthritis was found to be one-fourth that of naproxen [3]. Few methods

were mentioned for the determination of (I). These methods include HPLC [4–7], solid phase extraction [8], colorimetric [9] and fluorimetric methods [10]. LC–MS methods have been reported for studying the bioavailability and pharmacokinetics [11,12]. Determination of (I) by HPLC in presence of its related compounds has been mentioned [13]; also examination of (I) solution decomposition under alkaline and photolytic stress conditions by HPLC method has been reported [14]. Two stability indicating methods for determination of (I) in presence of its photodegradate (II) by derivative spectrophotometry were also previously reported [10].

Most of the previously reported HPLC methods aimed to determine (I) in biological fluids without referring to its separation from different degradates, while the others, including the spectrophotometric methods, determine it in pure form, in presence of related compounds, in presence photodegradate or in pharmaceutical formulations. The aim

* Corresponding author. Fax: +202 3628426.

E-mail address: mostafa1960@yahoo.com (M.A. Shehata).

of this work is to develop sensitive, rapid and stability indicating methods for simultaneous determination of (I) in presence of both its photodegrade and alkaline degradation products. This was achieved by developing an HPLC and two chemometric methods. In the chemometric methods, a quantitative, multivariate, spectral analysis by classical least squares (CLS) requires that the concentrations of all spectrally active constituents to be known and included in the calibration samples before a stable prediction model can be developed. Because of this critical limitation, the use of principle component regression (PCR) and partial least square (PLS) methods have been popular during the past 20 years. PCR and PLS methods can achieve excellent predictions for data sets even when some of the constituents have not been included in the calibration. However, PCR or PLS do not have the qualitative capabilities of CLS as they do not generate explicit estimated pure-component spectra. It was until the year 2000 when Haaland and Melgaard developed a family of augmented CLS techniques that have many advantages over PCR and PLS [15–17]. Concentration residual augmented classical least squares (CRACLS) is a new algorithm that allows updating the model during prediction without recalibration. The CRACLS algorithm is based on CLS so it retains the qualitative benefits of CLS and the flexibility of PLS modeling when spectrally active components are not explicitly included in the calibration. The components may be unknown, components with unknown concentrations, or other unidentified sources of spectral variation that are present in the calibration spectra. The developed methods were applied for the analysis of (I) in some pharmaceuticals.

2. Experimental

2.1. Instrumentation

Spectrophotometric measurements were carried out using a double beam UV-Visible spectrophotometer (SHIMADZU, Japan) Model UV 1601 PC, connected to an IBM compatible computer and an HP 800 inkjet printer. The bundled software was a UVPC personal spectroscopy software version 3.7. The spectra bandwidth was 2 nm and wavelength scanning speed was 2800 nm min^{-1} . A "La-Chrom" HPLC instrument (Hitachi-Merck) Germany, pump model L-7150, connected with a photodiode array detector model L-7455, was used for HPLC analysis. The injector was a manual Rheodyne injector (Model 7161, Catati, California, USA) equipped with a 20- μl injector loop and a 100- μl Hamilton syringe. The instrument was connected to an IBM compatible PC bundled with Merck-Hitachi Model D-7000 chromatography Data Station software HPLC septum manager and an HP 800 inkjet printer. A Shimpak VP-ODS C18 column (150 mm \times 4.6 mm i.d.) particle size 5 μm was used for the analysis. The photodegradation was performed using

a UV lamp (4 W) from UVP company, Cambridge UK model UVGL 25. For alkaline degradation kinetic studies a Memert (24) thermostatically controlled water bath, UK was used to control the temperature. A SOI Stuart shaker, UK was used for extraction of drug from pharmaceutical formulations. A Software for chemometric study: all computations were performed in Matlab for WindowsTM version 5.3 Mathworks Inc. 1999 with our own written codes. The PLS procedure was taken from PLS Toolbox 2.1, Eigenvector Research Inc. 2001 created by B.M. Wise, N.B. Gallagher for use with Matlab.

2.2. Materials and reagents

Rofecoxib standard material was kindly supplied by Global Napi Pharmaceuticals-EGYPT and was certified to have a purity of 99.98%. Vioxx[®] tablets (12.5 mg) batch number A/29701 and (25 mg) batch number 39801 manufactured by Global Napi Pharmaceuticals-EGYPT under license from: Merck & Co. Inc., Whitehouse Station, NJ, USA. were purchased from local market. Acetonitrile, water and phosphoric acid used were HPLC grade (Merck, Germany). Phosphoric acid 0.05%, 2% and 5% aqueous solutions were prepared by suitable aqueous dilution of phosphoric acid. Calculated weights of sodium hydroxide (Merck, Germany) were dissolved in water to obtain 0.25, 0.5 and 1.0 M solutions for alkaline degradation study.

2.3. Standard solutions

All glassware must be actinic or wrapped with aluminum foil. A stock standard solution of rofecoxib (I) $800 \mu\text{g ml}^{-1}$ was prepared by transferring accurately weighed 20 mg of (I) into a 25-ml volumetric flask, dissolved in 15 ml of acetonitrile, then the volume was completed with the same solvent; while the working standard solution of (I) $80 \mu\text{g ml}^{-1}$ was prepared by transferring 10 ml of the stock solution into a 100-ml volumetric flask and the volume was completed with acetonitrile/water (35:65). To prepare working standard photodegrade (II) solution $40 \mu\text{g ml}^{-1}$, 5 ml of stock standard solution of (I) were transferred into a 100-ml volumetric flask, diluted to the mark with acetonitrile/water (50:50). The solution was transferred into quartz cuvettes and tightly covered then subjected to a UV lamp (4 W) at a 15 cm distance for 45 min. To prepare working standard solution of alkaline degradates (III, IV) $40 \mu\text{g ml}^{-1}$, 5 ml of stock solution of (I) were transferred into a 100-ml volumetric flask, 5 ml of 0.5 M sodium hydroxide were added and the solution was left for 30 min at room temperature, then 5 ml of 5% phosphoric acid were added (calculated amount so that the pH was 6.0 ± 0.5). The volume was then completed with mixture of acetonitrile/water so as the final ratio will be (35:65). Both photo- and alkaline degradation working solutions were tested for complete degradation by the proposed HPLC method.

2.4. Procedures

2.4.1. Calibration for HPLC method

A series of standard solutions of (I) in the concentration range of 0.3–28 $\mu\text{g ml}^{-1}$ was prepared by suitably diluting aliquots of the working standard solution of (I) using acetonitrile/water (35:65). The solutions were subjected to HPLC analysis under the following conditions:

The mobile phase was prepared by mixing acetonitrile and 0.05% phosphoric acid in the ratio of (35: 65). The solvent was allowed to equilibrate, degassed and the column was conditioned for at least 30 min before injection. Mobile phase pH was 2.6. The samples were filtered using 0.45 μm PTFE[®] filter before use. The flow rate was 1 ml min^{-1} . All measurements were performed at wavelength 220 nm and ambient temperature. Triplicate 20- μl injections were done for each concentration and chromatographed. The average peak areas were calculated and plotted against concentration and the regression equation was computed.

2.4.2. Calibration for chemometric methods

For CRACLS and PLS methods, training set of 19 synthetic mixtures with different concentrations ratios of (I), (II) and (III, IV) containing intact drug in the range of 2–36 $\mu\text{g ml}^{-1}$ were prepared by mixing different aliquots of working standard solutions in 25-ml volumetric flasks, then the volumes were completed with acetonitrile/water (35:65). Table 1 shows the concentrations of the prepared mixtures solutions. The UV spectra of the prepared solutions were recorded over the range 200–400 nm. The data points of the spectra were exposed to Matlab version 5.3.

Table 1
Concentration ($\mu\text{g ml}^{-1}$) of rofecoxib (I), its photodegrade (II) and its alkaline degradates (III and IV) in the training set for CRACLS and PLS chemometric methods

Mixture number	(I)	(II)	(III and IV)
1	5	18	18
2	7	12	12
3	7	3	4
4	7	2	2
5	14	1	3
6	10	0.5	1
7	12	2	2
8	2	0.4	0.2
9	2	0.3	0.3
10	2	0.2	0.4
11	3	0.3	0.2
12	3	0.2	0.3
13	3	0.4	0.4
14	4	0.4	0.2
15	4	0.2	0.3
16	4	0.3	0.4
17	19	0.5	0.6
18	20	0.5	0.6
19	28	1	0.8

Multivariate calibration models were applied to these mixtures to calculate the concentration of (I) in presence of (II) and (III, IV).

2.4.3. Pharmaceutical formulations

Into a 250-ml volumetric flask, four tablets were transferred; 10 ml of water were added and swirled for 15 min. 175 ml of acetonitrile were added, sonicated for 30 min, and then shaken for 1 h on an orbital shaker at 250 rpm. The volume was completed with acetonitrile, filtered and aliquots were transferred into 50-ml volumetric flasks to obtain a concentration of 10 $\mu\text{g ml}^{-1}$ upon dilution to mark with acetonitrile/water (35:65). The procedures under HPLC and chemometric methods were followed.

2.4.4. Kinetic studies

Two different series, each of seven tubes were prepared by transferring 3 (series 1) and 4 ml (series 2) of (I) working solutions 40 $\mu\text{g ml}^{-1}$ in a Pyrex 20-ml test tubes. 0.4 ml of 0.5 M sodium hydroxide was added to each tube and allowed to stand in a thermostatically controlled water bath at 25 °C. The degradation was stopped at 5-min intervals by adding 1.5 ml of 2% phosphoric acid (calculated amount) in succession to the test tubes of each series. The volume was completed to 10 ml with acetonitrile/water (35: 65) and the absorption spectra were scanned in the range of 200–400 nm.

For studying the effect of sodium hydroxide concentration on the reaction rate, the above procedure was followed using two of solutions 0.25 and 1.0 M sodium hydroxide and 3.5 ml of (I) working solution (80 $\mu\text{g ml}^{-1}$). The study was performed at 25 °C.

For studying the temperature effect on the reaction rate, the above procedure was followed at 40 °C using 6 ml of (I) working solution (80 $\mu\text{g ml}^{-1}$) and 0.35 ml of 0.5 M sodium hydroxide solution.

3. Results and discussion

3.1. Liquid chromatography

Rofecoxib is a highly photosensitive drug and it also undergoes base promoted hydrolysis of the lactone moiety followed by oxidation to yield the dicarboxylate degradate (III), hydroxy furanone degradate (IV) and also the dicarboxylate anhydride can be produced [14]. Fig. 1 shows the structures of (I), (II), (III) and (IV). These structures were identified and elucidated by mass spectrometry [14]. Separation of photodegrade and alkaline degradates was achieved via step gradient elution on a C8 column [14], this method did not aim to quantify the intact drug in presence of its degradates, thus no quantitative or validation parameters were mentioned for the method. In our study, a simpler isocratic method was developed using C18 column with a mobile phase consisting of acetonitrile/0.05% phosphoric acid (35:65) as a stability indicating method for quantitative determination of (I)

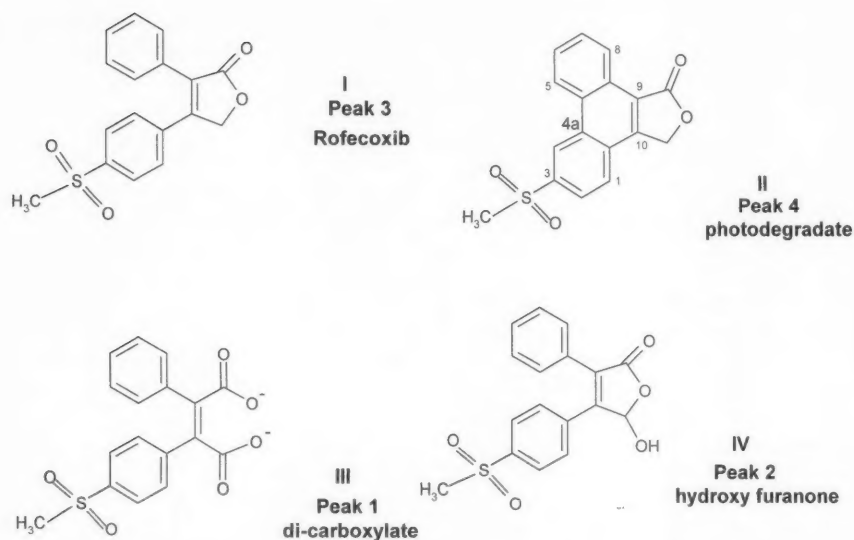


Fig. 1. Structures of rofecoxib (I), its photodegradate (II) and its alkaline degradates (III and IV) (peak number indicates the sequentially separated peaks by HPLC method).

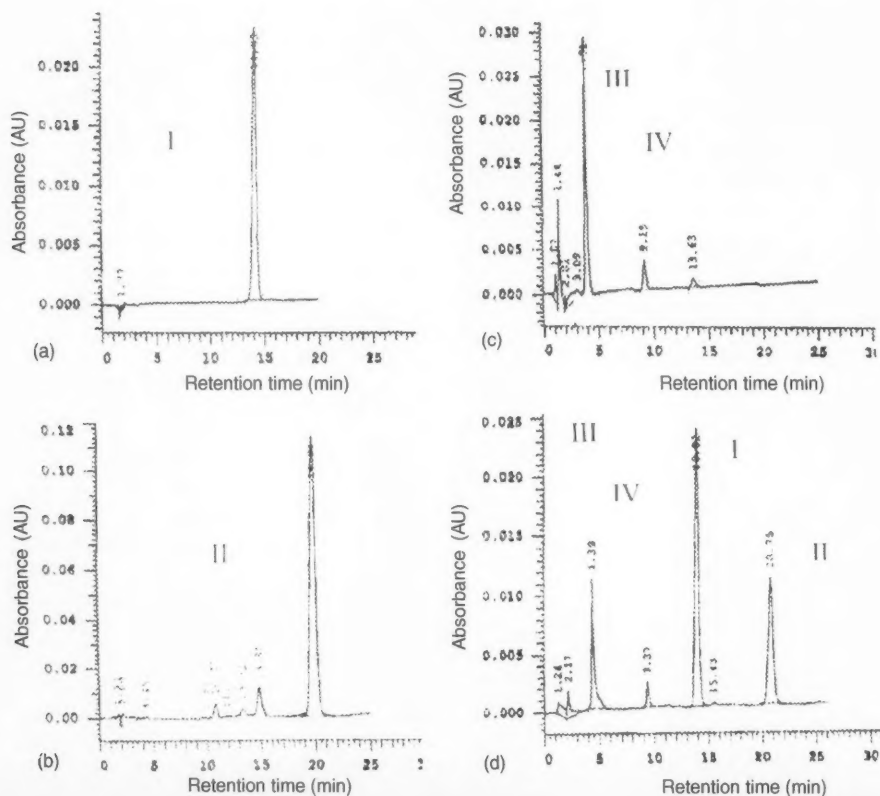


Fig. 2. HPLC chromatogram of: (a) rofecoxib (I) $6 \mu\text{g ml}^{-1}$, (b) rofecoxib photodegradate (II) $30 \mu\text{g ml}^{-1}$, (c) rofecoxib alkaline degradates (III and IV) $8 \mu\text{g ml}^{-1}$ and (d) mixture of (I) $7 \mu\text{g ml}^{-1}$, (II) $2 \mu\text{g ml}^{-1}$ and (III and IV) $2 \mu\text{g ml}^{-1}$ in acetonitrile: water (35:65).

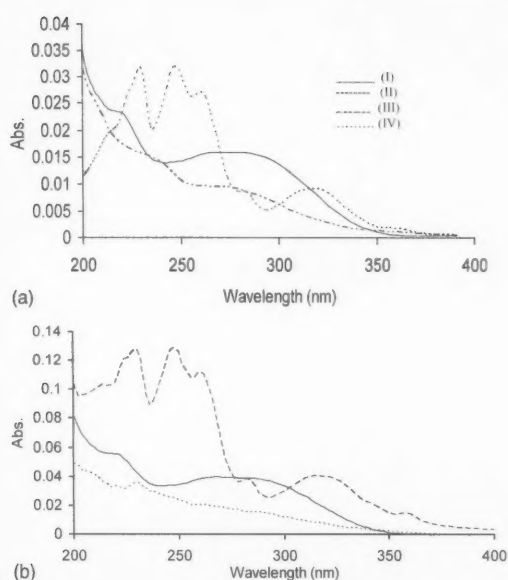


Fig. 3. (a) UV spectra of rofecoxib (I), its photodegradate (II) and its alkaline degradates (III and IV) as extracted from photodiode array HPLC detector, (b) UV spectra of rofecoxib (I), its photodegradate (II) and its alkaline degradates (III and IV) as estimated by PLS.

in presence of its degradates. The method does not need regeneration of column from run-to-run, which is time consuming and decreases the lifetime of the column, this offer advantages over gradient elution.

3.1.1. Peak identification

The identification of peaks was performed by carrying out separate chromatographic analysis for each of drug and its degradation products using the suggested chromatographic method. The analysis revealed the production of one photodegradate and two major alkaline degradates as shown in Fig. 2. Identification of the peaks was carried out by extracting the spectrum of each peak stored in the photodiode array detector data using the instrument software (Fig. 3a). The spectra were identical to those mentioned by Mao et al. [14] for (I), (II), (III) and (IV). The purity of (I) was confirmed by developing the three-dimensional (3D) spectrum of the separated peak.

Table 2

Peak information of the separated rofecoxib (I), its photodegradate (II) and its alkaline degradates (III and IV)

Separated compounds	Rofecoxib	Photodegradate	Alkaline degradate	Alkaline degradate
Structure number	I	II	III	IV
R_t (min)	13.92	19.90	4.38	9.04
Purity	1.00	0.99	0.98	0.99
Asymmetry factor	1.12	1.06	2.90	1.29
K'	1391.0	2073.0	437.0	936.0
W	0.57	0.85	0.29	0.42
R_s (relative to I)	–	8.40	22.10	9.85
Selectivity factor (α) (relative to I)	–	1.50	3.20	1.50

Table 3

Statistical comparison between the suggested methods and a reported method for the determination of Rofecoxib

Concentration ($\mu\text{g ml}^{-1}$)	Method			
	HPLC	CRCLS	PLS	Reported ^a
0.5	100.80	–	–	–
1	98.60	–	–	–
4	101.40	–	–	–
7.1	101.80	–	–	102.60
8	99.40	101.49	97.67	99.60
10	–	100.70	–	–
11.5	100.20	99.04	96.34	100.90
13.5	100.00	98.59	98.66	–
20	100.50	98.75	98.95	100.00
28	99.90	98.71	99.30	100.60
36	–	100.04	101.14	–
Mean	100.29	99.31	99.53	100.74
S.D.	0.98	1.14	1.61	1.16
R.S.D. (%)	0.98	1.15	1.64	1.15
V	0.96	1.30	2.60	1.34
n	9	7	6	–
t (tabulated)	2.178	2.228	2.262	–
t	0.775	1.671	2.386	–
F (tabulated)	3.838	4.534	6.256	–
F	1.388	1.026	1.944	–

^a Reported HPLC method [6].

3.1.2. System suitability

Trials to use other ratios of the mobile phase were done. Using acetonitrile/0.05% phosphoric acid in the ratio of (40:60) results in an increase of the retention time (R_t) of all peaks from 8–10 min, which is accompanied by peak broadening. When the pH of mobile phase was raised to 3.5 using sodium hydroxide, distortion of peaks was observed. Table 2 gives the R_t values of the separated peaks, together with other chromatographic parameters. The calculated resolution (R_s) values for each of the three degradate's peaks relative to (I) were more than 1.5; while the selectivity factor (α) was also more than 1, which ensures complete or 100% separation of (I) from all of its degradation products. The asymmetry factor of (I) peak was 1.15, which also reveals linear isotherm peak elution without tailing. Assessment of the system suitability by changing the concentration of phosphoric acid using 0.1% (pH 2.4) and 0.025% (pH 2.7) did not alter the retention times of the separated peaks. The separation also was performed under the same conditions using

Table 4
Assay validation sheet of the proposed methods for the determination of rofecoxib

Parameter	Method		
	HPLC	CRACLS	PLS
Accuracy (mean \pm R.S.D. (%))	100.08 \pm 0.78	99.31 \pm 1.14	99.53 \pm 1.61
Precision			
Repeatability	99.7 \pm 0.53	98.96 \pm 1.05	99.57 \pm 1.09
Reproducibility	99.3 \pm 0.48	99.2 \pm 1.12	99.15 \pm 1.03
Range ($\mu\text{g ml}^{-1}$)	0.3–28	2–36	2–36
Linearity			
Slope	36743	0.9999	1.017
R.S.E.% of the slope	0.3	–	–
Intercept	538	–0.1	–0.396
Correlation coefficient	0.99995	–	–

Table 5
Results of laboratory prepared mixtures of rofecoxib (I) and its photodegrade (II) and alkaline degradation products (III, IV) by the three suggested methods

Mixture number	Ratio			Recovery (%) for (I)		
	(I)	(II)	(III) and (IV)	HPLC	CRACLS	PLS
1	36	34	30	101.10	98.19	100.67
2	72	8	20	99.90	98.19	102.40
3	82	6	12	100.90	100.41	102.28
4	88	4	8	100.57	100.20	101.80
5	95	2	3	98.72	100.69	102.28
6	93	3.5	3.5	100.62	99.33	100.30
Mean				100.29	99.77	101.62
S.D.				0.66	0.91	0.91

a Hypersil BDS C18 column (250 mm \times 4.6 mm i.d.) 5 μm particle size. R_f for all peaks was slightly retarded.

3.1.3. Accuracy and precision

The accuracy was assessed by analyzing different samples and also by comparing the results with those obtained when a reported method was applied (Table 3). No significant difference was observed between the two methods. The repeatability was assessed by assaying freshly prepared solutions in triplicates at concentrations of 8, 20 and 28 $\mu\text{g ml}^{-1}$. The results are shown in Table 4. The inter-day precision was performed by assaying freshly prepared solutions in triplicates for three successive days.

3.1.4. Specificity and selectivity

The specificity of the method was tested by analyzing mixtures of the drug with both the photodegrade and alkaline degradates, which showed excellent recoveries (Table 5). This demonstrated the ruggedness of the method for determination of (I) in presence of (II) and (III, IV) and its suitability for routine analysis and quality control of the mentioned drug in bulk powder and pharmaceutical formulations as presented in Table 6.

3.2. Chemometric methods

The analysis of mixture composed of (I), (II), and (III, IV) by conventional spectrophotometry is not feasible, because

Table 6
Application of the proposed methods for determination of rofecoxib in pharmaceutical formulations

Preparation	Method recovery ^a % \pm R.S.D.			
	HPLC	PLS	CRACLS	Reported ^b
Vioxx [®] tablets (12.5 mg) B.N. A/29701				
Mean	99.23 \pm 0.79	99.42 \pm 1.58	99.67 \pm 1.21	100.03 \pm 1.65
Vioxx [®] tablets (25 mg) B.N. 39801				
Mean	99.19 \pm 0.81	99.31 \pm 1.44	99.58 \pm 1.34	99.92 \pm 1.72

^a Mean of at least four determinations.

^b Reported HPLC method [6].

of the overlapping of the broad absorption spectral bands as shown in Fig. 3a.

In this work, the new chemometric method namely CR-ACLS and the PLS were applied on experimental data obtained from UV spectra of a mixture composed of (I), (II), and (III, IV), for the resolution of this mixture. A calibration set was designed with 19 calibration samples containing (I), (II), and (III, IV) in the ranges and concentrations shown in Table 1. Validation set was composed of another six samples. Spectra were digitized each at 0.2 nm that 1001 experimental points were used in the calculations. In order to determine the correct number of latent variables to be used for modeling of the data, a cross-validation calculation for all the samples in the training set was performed to calculate the cumulative prediction residual error sum of squares (PRESS). Three latent variables were found optimum for the mean centered data. The mean recovery of the samples in the validation set was about 98.5%. The high similarity between the absorption spectrum of (I) and (III, IV) was suspected for the reduced accuracy of the developed PLS model, accordingly the training set was enriched with pure spectra of (I). The mean recovery was improved to about 99.5%.

CRACLS models were built for (I). Good recovery was obtained from model built with the training set without enrichment with pure spectra of (I). The estimated pure components spectra that resulted by including only (I) concentration and augmenting 14 times are shown in Fig. 3b. The model estimated the (III and IV) to be one component. The estimated pure components spectra were found to be improved by including all components concentration or increasing the number of augmentations.

3.2.1. Specificity and selectivity

To test the prediction ability of the new method, the model was challenged with the spectra of the validation set. Excellent recoveries were obtained (Table 5). The produced models were used for the analysis of pharmaceutical tablets. The results are shown in Table 6. The indicated values are the mean of five independent determinations of the same commercial batch. To test the accuracy of the developed methods, they were compared with a reported HPLC method for the mean and the standard deviation using the *t*-test and *F*-test, respectively. There were no significant differences (Table 3).

3.2.2. Method validation

The results obtained by both the HPLC and chemometric methods were compared with a reported HPLC method

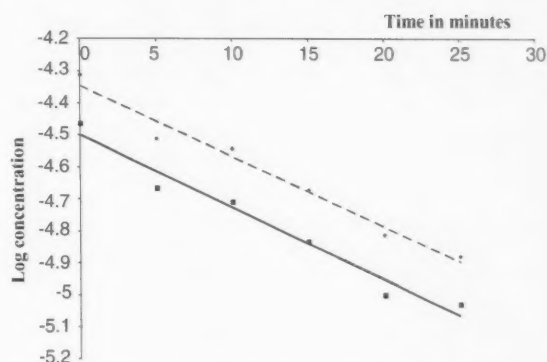


Fig. 4. Kinetic plots of alkaline degradation for (—) 3.44×10^{-5} M and (---) 4.86×10^{-5} M rofecoxib solutions in acetonitrile/water (35:65) using 0.051 M sodium hydroxide at 25 °C.

(used for determination of the intact drug) for validation (Table 3). Other validation parameters are given in Table 4, which shows the considerably small relative standard error (R.S.E.%) of the slope of HPLC regression equation (0.3%) indicating the high reproducibility of the method. The confidence interval of the intercept obtained was -3321 to $+4397$ which contained zero value indicating that the intercept is not statistically different from zero. The linearity given for the chemometric methods in Table 4 is obtained by plotting the true value of the concentration of (I) against the predicted values resulted by applying the CRACLS and PLS methods. The slope values of both methods are nearly one which proves their accuracy.

3.2.3. Kinetic studies

Kinetics of the base promoted hydrolysis of (I) was studied by following the concentration of the remaining drug within 30 min at 5-min interval at 25 °C. Fig. 4 shows a plot of log two different concentrations of the remaining drug against time. In comparison to the drug concentrations (3.44×10^{-5} and 4.86×10^{-5} M) the hydrolysis was performed in large excess of sodium hydroxide (0.051 M). The linear relationship obtained indicates a pseudo-first order reaction kinetics. Table 7 shows the observed rate constant and the $t_{1/2}$. To determine the rate constant of the second order kinetics of the reaction, a plot of the observed rate constant against different sodium hydroxide concentrations has to be carried out [18]. A plot of this curve gave a linear relationship and the regression equation showed a positive intercept value of

Table 7
Kinetic data of rofecoxib (I) alkaline degradation

Rofecoxib (molar concentration)	Sodium hydroxide (molar concentration)	Temperature (°C)	k_{observed} (min^{-1})	$t_{1/2}$ (min)
3.44×10^{-5}	0.051	25	0.051	13.6
4.86×10^{-5}	0.051	25	0.051	13.6
1.4×10^{-4}	0.026	40	0.059	11.8
8.3×10^{-5}	0.026	25	0.032	21.6
8.7×10^{-5}	0.103	25	0.083	8.3

0.016, which suggests the presence of two reacting species, one involving the sodium hydroxide and the other does not. However, the second order reaction rate constant was calculated by plotting $\log k_{\text{observed}}$ against \log sodium hydroxide concentration. A slope \approx unity was obtained and an intercept of 0.397 which indicates the value of second order rate constant which was found to be $0.403 \text{ L min}^{-1} \text{ mol}^{-1}$. The activation energy of the reaction was determined by calculating the rate constant at 25 and 40°C using 0.026 M sodium hydroxide and then applying the equation [19];

$$\log \frac{k_2}{k_1} = \frac{E_a(T_2 - T_1)}{2.303RT_1T_2}$$

Where " E_a " is the activation energy, " T_1 " and " T_2 " are the two temperature degrees in Kelvin, " R " is the gas constant and " k_1 ", " k_2 " are the rate constant at the two temperature degrees used. The calculated " E_a " was found to be $7.455 \text{ kcal mol}^{-1}$, which is comparatively a low value for esters and suggests the instability of the drug in alkaline medium.

4. Conclusion

A simple isocratic HPLC method and newly developed CRCLS and PLS chemometric methods are presented as stability indicating methods for determination of rofecoxib in presence of its photodegradate and alkaline degradation products. They were applied to bulk powder, pharmaceutical formulations and mixtures of rofecoxib and its degradation products. The CRCLS has prediction abilities comparable to PLS and yet has better qualitative characteristics than PLS. The three suggested methods can be applied for quality control and routine analysis.

References

- [1] M.C. Allison, M.G. Howatson, C.I. Torrance, F.D. Lee, R.I. Russel, *New Engl. J. Med.* 327 (1992) 749–754.
- [2] F.L. Lanza, M.F. Rack, D.A. Callison, et al., *Gastroenterology* 42 (1997) A 194.
- [3] C. Bombardier, L. Laine, A. Reicin, VIGOR Study Group, *New Engl. J. Med.* 343 (2000) 1520–1528.
- [4] E. Woolf, I. Fu, B. Matulski, *J. Chromatogr. B* 730 (1999) 221–227.
- [5] F. Jamali, S. Sattari, *J. Pharm. Pharm. Sci.* 3 (2000) 307–312.
- [6] T. Radhakrishna, D. Sreeniva, G. Om Reddy, *J. Pharm. Biomed. Anal.* 26 (2001) 617–628.
- [7] A. Savašer, Y. Özkan, C.K. Özkan, C. Taş, S.A. Özkan, *Anal. Lett.* 37 (2004) 81–97.
- [8] C.Z. Matthews, E.J. Woolf, B.K. Matuszewski, *J. Chromatogr. A* 949 (2002) 83–89.
- [9] M.N. Reddy, T.K. Murthy, S.M. Shanta Kumar, *Indian Drugs* 39 (1) (2002) 39–40.
- [10] M.A. Shehata, N.Y. Hassan, A.S. Fayed, B.A. El-Zeany, *Il Farmaco* 59 (2004) 139–145.
- [11] C.M. Chavez-Eng, M.L. Constanzer, B.K. Matuszewski, *J. Chromatogr. B* 767 (2002) 117–119.
- [12] U. Werner, D. Werner, R. Mondkowsky, M. Gillich, K. Brune, *J. Chromatogr. B* 760 (2002) 83–90.
- [13] K.V. Krishna, J.B. Moses, P.K. Dubey, B.S. Chandra, G. Om Reddy, K. Vyas, *J. Pharm. Biomed. Anal.* 29 (2002) 355–360.
- [14] B. Mao, A. Ibrahim, Z. Ge, D. Ellison, R. Hartman, S. Prabhu, et al., *J. Pharm. Biomed. Anal.* 28 (2002) 1101–1113.
- [15] D.M. Haaland, D.K. Melgaard, *Appl. Spectrosc.* 54 (9) (2000) 1303–1312.
- [16] D.M. Haaland, W.B. Chambers, M.R. Keenan, D.K. Melgaard, *Appl. Spectrosc.* 54 (9) (2000) 1291–1302.
- [17] D.K. Melgaard, D.M. Haaland, C.M. Wehlburg, *Appl. Spectrosc.* 56 (5) (2002) 615–624.
- [18] P.L. Houston, *Chemical Kinetics and Reaction Dynamics*, first ed., McGraw-Hill, (2001), p. 46.
- [19] A. Martin, J. Swarbrick, A. Cammarata, *Physical Pharmacy*, third ed., Lea and Febiger, Philadelphia, 1983, pp. 359–360.

Electrochemistry and biosensing reactivity of heme proteins adsorbed on the structure-tailored mesoporous Nb₂O₅ matrix

Xin Xu, Bozhi Tian, Song Zhang, Jilie Kong, Dongyuan Zhao, Baohong Liu*

Department of Chemistry, Fudan University, Shanghai 200433, PR China

Received 31 March 2004; received in revised form 24 May 2004; accepted 24 May 2004

Abstract

The highly ordered mesoporous niobium oxides fabricated by self-adjusted synthesis have been used as immobilization matrices of heme proteins including Cytochrome *c* (Cyt *C*) and horseradish peroxidase (HRP) for their large surface areas, narrow pore size distributions and good biocompatibility. The assembling process was investigated by cyclic voltammetry, amperometry and potential step chronoamperometry in details. Niobium oxide matrices with different structural features were templated with the surfactants and the selectivity of these hosts to specific protein characteristics was determined. It was observed that proteins could be readily assembled onto the mesoporous films with detectable retention of bioactivity. The Nb₂O₅ matrix with a tailored pore size and counterpoised surface charge to that of hemes allowed for a maximum adsorption capacity of biomolecules. The adsorbed redox molecules exhibited direct electrochemical behavior and gave a pair of well-defined quasi-reversible cyclic voltammetric peaks, indicating that the mesoporous niobium oxide matrix could effectively promote the direct electron transfer between the protein redox site adsorbed and the electrode surface. The midpoint redox potentials of adsorbed Cyt-*c* and HRP were 14 and –122 mV versus SCE, respectively. Furthermore, the immobilized HRP onto Nb₂O₅ derived electrode presented good bioactivity and thus was fabricated as an amperometric biosensor for the response of hydrogen peroxide in the range from 0.1 μM to 0.1 mM. © 2004 Elsevier B.V. All rights reserved.

Keywords: Heme protein; Mesoporous niobium oxides; Biosensor; Electrochemistry

1. Introduction

Currently immobilization of biomolecules onto electrode surfaces has attracted considerable interest both in the fundamental research of protein properties and in the development of novel biosensors without mediators [1,2]. Electron transfer reactions of immobilized redox proteins have been widely studied while up to now there are limited reports of the direct electron transfer between the electrode surface and the protein redox sites because of the inaccessibility of the electroactive center. Therefore, it is expected to find a simple, reliable and effective immobilization strategy to retain high activity of the immobilized biomolecules and allow efficient electron transfer between the electrode and a redox protein [1,3]. Some approaches have been used to construct a protein film electrode for electrochemical studies, such as self-assembled monolayers. In recent years, several nanoporous materials such as titanium oxide and zinc oxide

films have been applied as attractive candidates for the immobilization of redox proteins such as Cytochrome *c* and hemoglobin, also as electrodes for such proteins [4]. These films are of interest due to their high surface area, optical transparency, electrochemical activity and ease of fabrication. While those materials may promote electron transfer directly to a certain extent, the electrochemical reduction currents of the redox proteins adsorbed on such films were observed but only few quasi-reversible cyclic voltammograms were presented. To improve the reduction–oxidation kinetics of the protein adsorbed, some advanced materials were desirably used to functionalize the electrode for direct electrochemistry studies of redox proteins [5–8]. Durrant and coworkers recently extended the study to nanocrystalline SnO₂ electrodes, which allowed both the electrochemical and spectroelectrochemical researches of the protein redox function [5]. The electrodes modified with single-walled carbon nanotube and layer-by-layer assembly of hemoglobin and clay nanoparticles have been used to study the electrochemistry of proteins [6,7]. The nanofilm deposits of titania nanoparticle phytates have also been reported on the accu-

* Corresponding author.

E-mail address: bhliu@fudan.edu.cn (B. Liu).

mulation and reactivity of biomolecule [8]. Here an ordered mesoporous Nb_2O_5 film has been considered in the present work for biomolecule immobilization, direct electrochemical studies of redox proteins and biosensor application.

Nanoporous niobium oxide or doped niobium oxide exhibits good photocatalytic and electronic properties, hence expected to be applicable in electronic and magnetic devices, and biotechnology [9,10]. Its certain electrical conductivity at potentials above the conduction band edge can be expected to provide good possibility of nanoporous niobium oxide to promote direct electron transfer of redox proteins. Compared with those nanoporous metal oxide substrates composed of irregular nanocrystallites reported, the currently prepared nanoporous Nb_2O_5 exhibits highly ordered pore structures and very narrow pore size distributions [9] that make it possible to design the selectivity of these substrates for biomolecule immobilization, such as structure and charge, by varying the pore diameter and by functionalizing the substrate. We have firstly reported the biocapsulation of Cyt-*c* with the mesoporous Nb_2O_5 films and its application to direct electrochemical study, which demonstrated that the ability to readily tailor the pore size by design has provided them unique properties for the study of diverse biomolecules immobilization [11].

In this paper, we further extend the study to electrochemical enzyme biosensors with the highly ordered, pore size tunable mesoporous niobium oxides which were prepared via to "acid-base pairs" route reported in our lab [12]. Herein such nanoporous niobium oxide film was used to investigate the adsorption process of heme proteins, including Cytochrome *c* and horseradish peroxidase, monitored by cyclic voltammetry and potential step chronoamperometry. We also studied the direct electrochemical behavior of the proteins assembled on such films. Several niobium oxides with different pore size and pore geometries were tuned to compare the adsorption of biomolecules and amperometric response of biosensors. Moreover, hydrogen peroxide could be catalytically reduced at both Cyt-*c*/ Nb_2O_5 and HRP/ Nb_2O_5 biocomposites. Such modified electrodes present good characteristics and supply a promising approach to fabricate amperometric biosensors using mesoporous niobium oxide matrices with tailored pore size. The research of Nb_2O_5 -based biosensors would provide a new tool for enzyme studies and biomolecular analysis.

2. Experimental

2.1. Reagents and materials

Anhydrous niobium(V) chloride (NbCl_5) and niobium(V) ethoxide ($\text{Nb}(\text{OC}_2\text{H}_5)_5$) were purchased from Acros. Horse heart Cytochrome *c* (Cyt-*c*) and horseradish peroxidase (E.C.1.11.1T, >250 units/mg) were obtained from Sigma. Anhydrous ethanol and hydrogen peroxide (30%) were purchased from Shanghai Chemical Reagent Company (Shang-

hai, China). Indium tin oxide (ITO) glass (the electrode area of ca. 1 cm^2) was purchased from Nanbo Electrical Co. (Shenzhen, China). All of the other chemicals used were reagent grade.

2.2. Preparation and characterization of mesoporous Nb_2O_5 film

Nb_2O_5 was prepared as previously described [12]: 0.007 mol of NbCl_5 and 0.003 mol of $\text{Nb}(\text{OC}_2\text{H}_5)_5$ were mixed and diluted by 20 ml of ethanol, then 1 g of amphiphile was added to the solution. The mixture was further stirred for 2 h at room temperature and aged for 24 h at 50°C . The as-made film was deposited on the ITO glass slides by dip-coating procedure. The hollowed out inorganic framework was obtained via calcination at 350°C . The amphiphiles used here are triblock copolymer P123, oligomeric alkyl-ethylene oxide surfactant Brij 97, triblock copolymer B50-6600, which correspond to the 2D-hexagonal Nb_2O_5 -1 (6.0 nm, for detailed investigation in current work), 2D-hexagonal Nb_2O_5 -2 (2.0 nm) and 3D-hexagonal Nb_2O_5 -3, respectively. The amorphous niobium oxide film was also prepared by direct film deposition without any amphiphiles addition for comparison. XRD patterns were recorded with a Bruker D4 diffractometer with $\text{Cu K}\alpha$ radiation; the surface area and pore characteristics of the samples were measured using the BET and BJH method by N_2 adsorption and desorption curves at 77 K in a Micrometitics Tri-star 3000 analyzer; transmission electron microscopy (TEM) images of the mesoporous niobium oxide films were taken with a Hitachi H-800, using an accelerating voltage of 200 kV (Hitachi Ltd., Tokyo, Japan).

2.3. Protein assembling and biosensor construction

Protein immobilization was achieved by immersing mesoporous Nb_2O_5 films in $(1-5) \times 10^{-6}\text{ M}$ Cyt-*c* and HRP solutions (pH 7.0) at ambient condition. The process of protein adsorption onto the Nb_2O_5 film was monitored by electrochemical measurements. Prior to all measurements, the protein-embedded electrodes were rinsed with buffer solution and kept in blank buffer solution at 4°C . Protein adsorption was generated by putting the Nb_2O_5 materials (final concentration 2 mg mL^{-1}) into protein solutions ($0.5\text{ }\mu\text{M}$) at room ambient condition for 20 h. The adsorbed amounts were determined by solution analysis before and after adsorption using UV absorption at 407 nm ($\epsilon_{\text{molar}} = 100,000\text{ M}^{-1}\text{ cm}^{-1}$) [13] by a SM-240 CCD spectrophotometer (CVI spectral instruments, Putnam, CT, USA) at room temperature. As the comparison, $\text{Nb}_2\text{O}_5/\text{ITO}$ electrode without proteins was also prepared.

2.4. Electrochemical procedures

Electrochemical measurements including amperometry, cyclic voltammetry and chronoamperometry were

performed with a CHI 660 electrochemical workstation (CHI, USA). All measurements were carried out using a three-electrode system, employing platinum wire as the counter electrode, saturated calomel electrode (SCE) as the reference, and either Nb₂O₅/ITO or heme/Nb₂O₅/ITO electrode as the working electrode in a thermostated, stirred electrochemical glass cell containing phosphate buffer solutions (pH 7.0). All experimental solutions were de-oxygenated by bubbling nitrogen through the solution for 30 min before measurement. A holding potential of -0.25 V versus SCE was applied to the working electrode and the background current was allowed to a steady state. Aliquots of hydrogen peroxide standard solution were added to the cell and the current–time curves were recorded.

3. Results and discussion

3.1. Characterization of proteins adsorbed onto the mesoporous Nb₂O₅ matrices

Ordered mesoporous Nb₂O₅ was prepared adopting the reported concept of “acid–base pairs”, which takes a different perspective to address the influence of inorganic–inorganic interplay on the synthesis of mesoporous materials. By employing metal alkoxide as the main inorganic precursor and anhydrous metal chloride as the pH adjuster and hydrolysis–condensation controller, the ordered nonsiliceous mesoporous Nb₂O₅ has been easily and effectively synthesized. As shown in Fig. 1, N₂ adsorption–desorption isotherm curve of the calcined mesoporous niobium oxide materials templated by P123 featured a steep rise in adsorption at the relative pressure (P/P_0) region of 0.4–0.7. The hysteresis at the high pressure of N₂ adsorption–desorption isotherms of all these niobium oxide materials strongly suggested the presence of mesopores. The pore size distribution calculated by Barrett–Joyner–Halanda

(BJH) model was centered at 6.0 nm and the surface area was 190 m² g⁻¹ by applying Brunauer–Emmett–Teller (BET) equation [14,15]. The high resolution electron microscopy experiment indicated that the mesoporous niobium oxide film was basically amorphous [11]. Transmission electron microscopy images (Fig. 1) display regular ordered patterns recorded along (110) direction of the *p6m* structure and further confirmed that the nanoporous niobium oxide exhibited high mesoscopic structural quality. The pore size and the wall thickness of the porous film viewed from the TEM images are about ca. 6 and 2.5–3 nm, respectively. Those structural features make the mesoporous niobium oxide film a good matrix for immobilization of the biomolecules.

As to the adsorption of biomolecules onto the nanoporous materials, the surface charge species and the pore properties of the materials are two factors [4,13] besides the intermolecular interactions between the functional groups of the enzymes (e.g. -COOH or -NH₂) and some specific sites on the pore internal surface of oxides reported in our previous experiments [16]. For effective adsorption, the surface charges of the protein and metal oxide matrix must be complementary. We have shown that the immobilization of enzymes on inorganic matrices such as modified zeolites is controlled by the pH of buffer solution [16]. The isoelectric points (IEP) of Cyt-*c* and HRP are 10.5 [17] and 8.9 [18], respectively, while the zero point of charge of Nb₂O₅ is 4.1 [19]. At physiological pH solutions, electrostatic charges should be counterpoised and the strong electrostatic interactions would occur between negatively charged Nb₂O₅ matrix and positively charged heme molecules. Therefore proteins adsorption is expected under such conditions.

On the other hand, by varying the molecular mass of the nonionic amphiphiles, the pore size, mesoporous volume and BET surface area of the niobium oxide can be easily tuned. The mesoporous Nb₂O₅ films with different structural topologies were prepared, namely Nb₂O₅-1, Nb₂O₅-2 and Nb₂O₅-3 represented 2D-hexagonal (pore size of 2.2 and

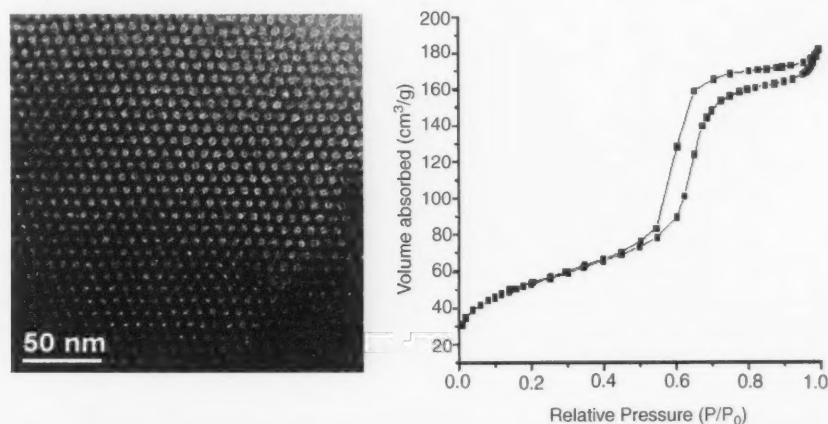


Fig. 1. TEM image viewed from (110) direction of the 2D hexagonal Nb₂O₅ and N₂ adsorption–desorption isotherm curve of the calcined mesoporous niobium oxide templated by P123.

Table 1
Physicochemical properties of Nb₂O₅ matrices and the amounts of protein adsorbed

Nb ₂ O ₅ ^a	<i>S</i> _{BET} (m ² g ⁻¹)	<i>S</i> _{ave} (nm)	<i>V</i> _{meso} (cm ³ g ⁻¹)	<i>A</i> _{Cyt-c} (μmol g ⁻¹) ^b	<i>A</i> _{HRP} (μmol g ⁻¹) ^b
Nb ₂ O ₅ -1	114	2.0	0.0608	1.8	1.8
Nb ₂ O ₅ -2	190	6.0	0.206	2.4	2.4
Nb ₂ O ₅ -3	105	4.3	0.117	1.4	1.4

*S*_{BET}, *S*_{ave}, *V*_{meso} and *A*_{Cyt-c} are the BET surface area, average pore size, mesopore volume and the amount of Cyt-c and HRP adsorbed, respectively.

^a Nb₂O₅-1, Nb₂O₅-2 and Nb₂O₅-3 represent 2D, 2D and 3D-hexagonal Nb₂O₅, tuned by the nonionic amphiphiles.

^b *A*_{Cyt-c} and *A*_{HRP} are the average values calculated with three measurements, and the R.S.D. was 4.3–8.1%.

6 nm) and 3D-hexagonal Nb₂O₅ (cage size of 4.3 nm and entrance size of below 2 nm), respectively. Here, 3D-hexagonal Nb₂O₅ was prepared and further used as the comparison. The three materials exhibited different binding capacities for Cyt-*c* and HRP with the amount of molecules adsorbed determined before and after adsorption by UV-Vis spectrum curves. Table 1 lists the comparison of the amounts of proteins adsorbed on these materials. As shown herein, 2D-hexagonal Nb₂O₅-2 exhibited the largest adsorption of Cyt-*c* and HRP (diameters, ca. 3.3 and ca. 4.8 nm [20], respectively) because of its maximum values of pore size, mesopore volume and BET surface area. N₂ sorption data showed that the matrix after biomolecular immobilization exhibited low BET surface areas less than 2 m² g⁻¹, suggesting that biomolecules can fill or plug the Nb₂O₅ pores or pore entrances with high capacities [11]. As for 3D caged structured Nb₂O₅-3, due to the small entrance size that preclude the successful infiltration of large biomolecules, protein adsorption mainly occurred on the external surfaces and yielded little unstable protein adsorption as well as Nb₂O₅-1 and nonporous one, on which no obvious redox peaks were observed in electrochemical studies. Therefore it is evident that the pore size and mesoscopic topology (such as tubular, caged or nonporous) are important for the adsorption of biomolecules. This result was in accord with the following discussion on the response of biosensors that were fabri-

cated by immobilization of proteins onto mesoporous matrices with tailored pore size.

3.2. Entrapment and electrochemistry of proteins assembling onto Nb₂O₅ modified electrode

The electrochemical behavior of native heme proteins such as Cyt-*c* onto mesoporous Nb₂O₅ derived electrode was investigated previously. When the niobium oxide modified ITO electrode was immersed in aqueous Cyt-*c* solutions, well-defined oxidation and reduction peaks appeared (Fig. 2) but no peak was observed in the Nb₂O₅-modified electrode in protein-free buffer solution, which were attributed to heme oxidation and reduction. The formal redox potential of adsorbed Cyt-*c* was determined from the reduction and oxidation peaks potential to be 14 mV versus SCE, which was close to the midpoint potential of that in a solution [21,22]. The cathodic and anodic currents were found to be linearly proportional to the scan rates from 0.02 to 0.2 V s⁻¹, characteristic of a thin film adsorption redox behavior (Fig. 2B). As a semiconductor, Nb₂O₅ can effectively promote electron transfer between the protein redox site adsorbed and the electrode surface, which was often very slow at most of the unmodified electrodes [23].

The protein assembling process was studied in details. Fig. 3 shows the dependence of the charge density obtained

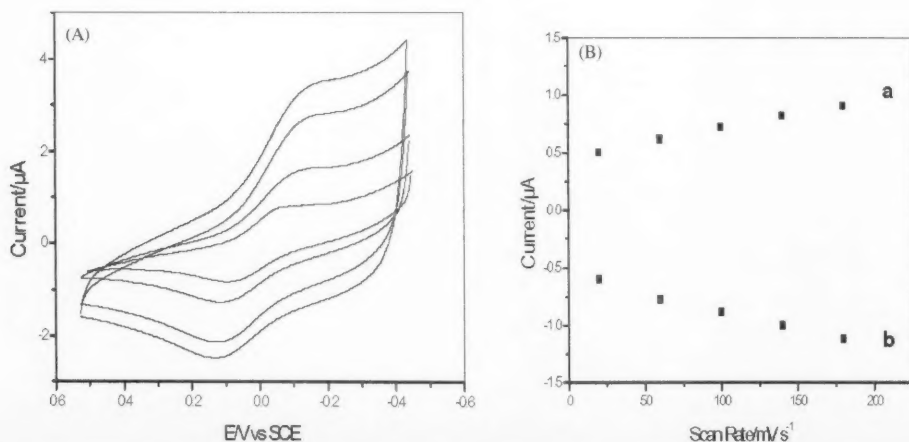


Fig. 2. (A) Cyclic voltammograms of nanoporous niobium oxide film in 2.5 μM Cyt-*c* solution at different scan rates. From inner to outer: 20, 50, 80, 100 mV s⁻¹, respectively. (B) Plot of cathodic (a) and anodic (b) peak current vs. scan rate for Nb₂O₅-derived electrode, respectively.

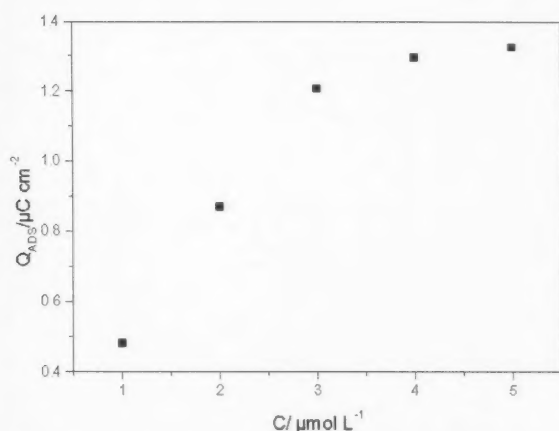


Fig. 3. Plot of surface charge density of Nb_2O_5 -derived electrode obtained from cyclic voltammograms as a function of different Cyt-*c* concentrations.

from cyclic voltammograms against the Cyt-*c* concentration in the bulk solution. With increase of the Cyt-*c* content, Q_{ADS} initially increased and finally reached plateau level at ca. $1.3 \mu\text{C cm}^{-2}$, meaning that saturated amount of Cyt-*c* molecules were adsorbed from the bulk solution onto the film surfaces. Potential-step chronoamperometry technique was further applied to investigate the processes that occurred on the surfaces of Nb_2O_5 film in the presence of protein molecules. Fig. 4 shows the chronoamperometric current transients recorded for nanoporous Nb_2O_5 films in Cyt-*c* solution. The current transient after a potential step is attributed to capacitive charging of the film (and substrate)

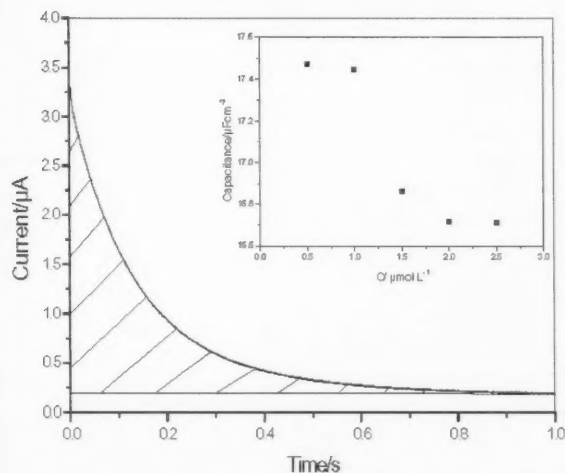


Fig. 4. Chronoamperometric transients for Nb_2O_5 film in $0.5 \mu\text{M}$ Cyt-*c* solution after a potential jump from 0 to -25 mV . Capacitance was obtained by integration of the exponential components of the chronoamperometric traces (see the hatched area). Prior to voltage step, the film was equilibrated at the starting potential for 5 min. Inset line is the plot of the film capacitances obtained as a function of different Cyt-*c* concentration by numerical integration over time of the chronoamperometric data.

and can be modeled by a single-exponential decay, as expected for standard RC behavior [24,25]. Film capacitances obtained as a function of different protein concentration by numerical integration over time of the chronoamperometric data are presented in Fig. 4 inset line. For this measurement, a potential step (25 mV) was applied from 0 V , and the resulting current transients were recorded. This base potential (0 V) was selected because the pseudo capacitance arising from redox reaction of Cyt-*c* molecules was absent in this potential range. The protein molecules adsorbed onto the Nb_2O_5 surface would form a new capacitor that was cascaded with the capacitor for bare mesoporous Nb_2O_5 layer. The new build-up of two capacitors in series would cause the decrease of the total capacitance compared to that for only Nb_2O_5 layer. With increase of the Cyt-*c* concentration in the bulk solution, the capacitance measured also rapidly decreased and finally leveled off, agreeing with the results of CV experiment.

The electroactive protein surface concentration, Γ in mol cm^{-2} , can be determined from Q_{ADS} using Eq. (1), where Q_{ADS} is the surface charge density in C cm^{-2} , n the number of electrons transferred (in the case, one electron for the redox reaction of each Cyt-*c* molecule), and F the Faraday constant in C mol^{-1} :

$$\Gamma = \frac{Q_{\text{ADS}}}{nF} \quad (1)$$

According the charge density Q_{ADS} obtained from cyclic voltammograms, an electroactive saturating protein loading of ca. 14 pmol cm^{-2} for the 500 nm thick film was obtained. Assuming Cyt-*c* molecule approximately as a solid sphere of 3.3 nm diameter [20], this value was close to the theoretical maximum coverage, suggesting that the electroactive protein molecules formed a full coverage of the film surface.

The electrochemical performance of the as-prepared Cyt-*c*/ Nb_2O_5 film derived electrode was carried out in protein-free buffer solution. The peak currents of cyclic voltammograms exhibited no observable decay comparing with that in protein solution. However, after the protein-modified electrode was kept in PBS buffer solution for 12 h, a redox potential shift was observed in cyclic voltammograms. The mid-point potential of anodic and cathodic peaks was observed at -150 mV versus SCE, which suggested that there might be some interaction occurred between the adsorbed Cyt-*c* and niobium oxide matrix [11,26]. Fig. 5A shows the cyclic voltammograms of the Cyt-*c*/ Nb_2O_5 electrode at various scan rates. The redox process was a typical quasi-reversible electrochemical behavior involving an active substance attached onto the Nb_2O_5 -modified electrode [27]. From cyclic voltammograms, the electroactive protein surface concentration, Γ in mol cm^{-2} , was well consistent with the full coverage value of the Nb_2O_5 films obtained above, indicating that the assembled protein molecules did not leak off from the Nb_2O_5 surface though the formal potential changed. The electrochemical behaviors were stable for more than two weeks

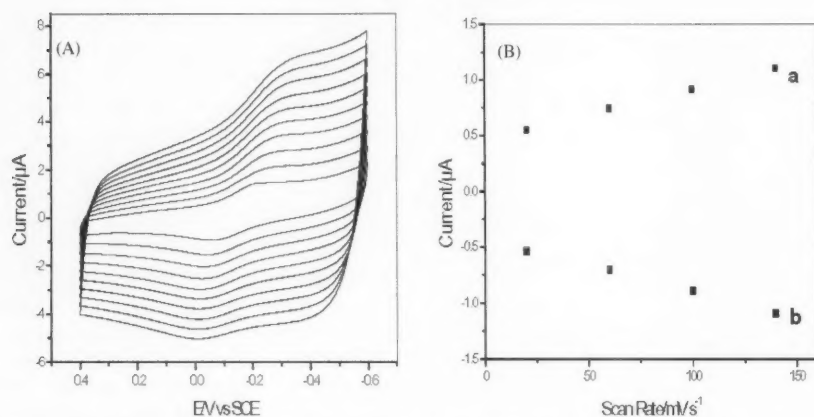


Fig. 5. (A) Cyclic voltammograms of Cyt-*c*/Nb₂O₅ film in pH 7.0 blank buffer solution at different scan rates. From inner to outer: 20, 40, 60, 80, 100, 120, 140, 160, 180 and 200 mV s⁻¹, respectively. (B) Plot of cathodic (a) and anodic (b) peak current vs. scan rate for Cyt-*c*/Nb₂O₅-derived film electrode, respectively.

during the experiments. The kinetic of the heterogeneous electron transfer for the Cyt-*c*/Nb₂O₅ film was calculated to be 0.28 s⁻¹ [28]. Despite the fact that the value of k_{et}^0 seems to be lower than that reported in literature such as SnO₂ [5], it may be the conductive diversity between such materials and different distance between protein redox sites adsorbed and electrode surface that cause the difference of the electron transfer rate.

To investigate that not only was direct reduction of the FeIII-heme to FeII-heme of the Cytochrome-*c* possible but that the immobilized protein in the film was electroactive, such Cyt-*c*/Nb₂O₅ derived electrodes with different pore size were used for electrocatalysis of hydrogen peroxide. The amperometric response to H₂O₂ was observed with a detection limit of 0.01 mM for the matrix of pore size 6.0 nm, indicating that the adsorbed Cyt-*c* still kept its catalytic activity. In comparison, its response characterization and stability were better than those of Cyt-*c*/Nb₂O₅ derived electrodes with smaller pore diameters because the protein molecules adsorbed onto the external surfaces were easily and rapidly inactivated due to direct exposure to the environmental change, which implied the dimension matching effect.

3.3. Biosensor applications based on assembling of HRP onto Nb₂O₅ modified electrodes

As one of the readily available and versatile enzymes, HRP is a heme containing glycoprotein with molecular weight of ca. 42,000, a more complicated heme protein than Cyt-*c*. Here, HRP can be successfully immobilized onto the mesoporous Nb₂O₅ modified electrodes by tailoring pore structures. Fig. 6A(a) depicts the cyclic voltammogram of the HRP/Nb₂O₅-derived electrode in buffer solution and shows a pair of oxidation and reduction peaks at the midpoint potential of about -0.122 V versus SCE.

The enzymatic biosensing activity is expected to be depending on the film thickness and pore size of matrices as well as the surface charge and pore geometries discussed above. The effect of mesoporous Nb₂O₅ film thickness on protein immobilization and the biosensor response was investigated (Fig. 7A). It showed that the response of the biosensor became greater with increasing film thickness from 200 nm to 1 μm due to increasing protein adsorption. But the response time increased and the direct electrochem-

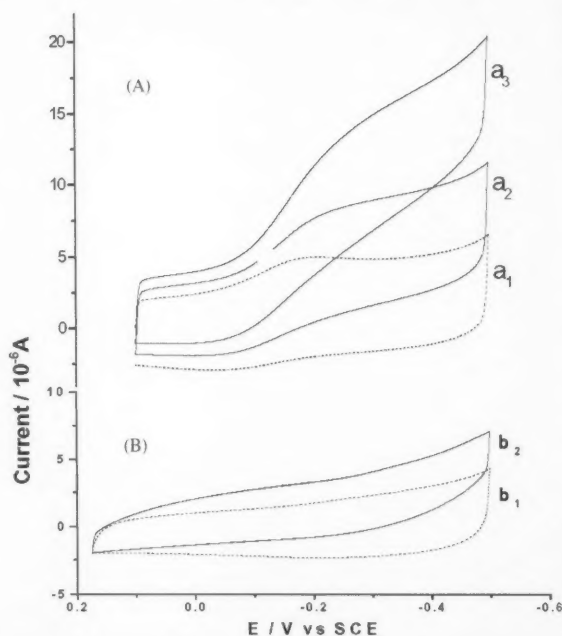


Fig. 6. Cyclic voltammograms of the HRP/Nb₂O₅-derived biosensor (A) and blank Nb₂O₅-modified electrode (B) in the absence (a₁, b₁), in the presence of 0.05 mM H₂O₂ (a₂), 0.3 mM H₂O₂ (a₃) and 1 mM H₂O₂ (b₂) at a scan rate of 100 mV s⁻¹, respectively.

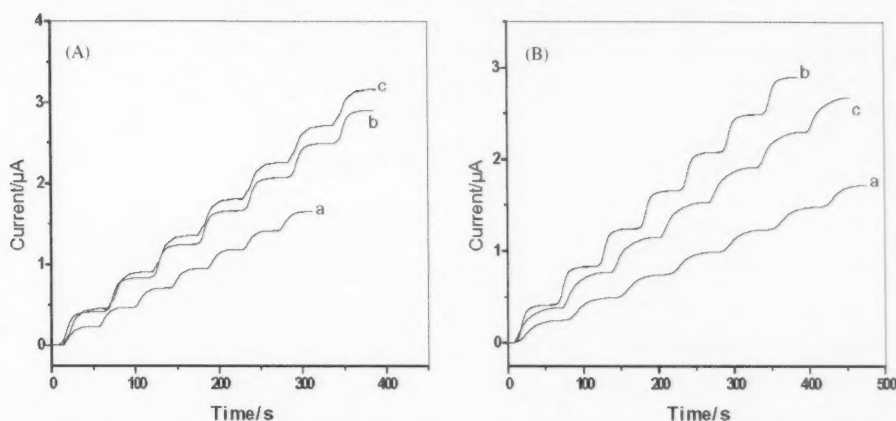


Fig. 7. Typical steady-state response of the HRP/Nb₂O₅-derived biosensor, (A) with different thickness of Nb₂O₅ film (pore size of 6 nm) (a) 20 nm; (b) 500 nm; (c) 1 μ m, and (B) with different pore size of Nb₂O₅ film (500 nm thickness) (a) 2 nm; (b) 6 nm; (c) 10 nm on successive injection of 5 μ M H₂O₂. Applied potential of -250 mV vs. SCE. The time required to reach 95% of the steady-state current is about 20, 15 and 25 s for different film thickness, respectively.

ical behavior lowered when the film thickness was up to 1 μ m. So we selected 500 nm thick mesoporous Nb₂O₅ film for this study.

The effect of 2D-hexagonal mesoporous Nb₂O₅ film with different pore diameters from 2 to 10 nm was tested (Fig. 7B). The response of the biosensor made from the mesoporous Nb₂O₅ film with 6 nm pore size arrived at a maximum value, suggesting the highest bioactivity of protein remained onto this matrix. The HRP molecule is an elongated object, and the average of molecule diameter is ca. 4.8 nm [20]. So the mesoporous Nb₂O₅ (pore diameter 6 nm) derived biosensor showed high sensitivity when the pore size of these films matched the molecular diameters of HRP. These matching pores of mesoporous Nb₂O₅ films would prevent increased conformational flexibility of enzyme. On the other hand, if the pore diameters (such as 10 nm) were much larger than the diameters of an enzyme, the enzyme would leach from supports or even increased conformational flexibility of enzyme that might cause protein denaturation. While the pore diameter (such as 2 nm) was smaller than the spherical molecular size of the enzyme, the enzymes were just adsorbed on the outer surface, resulting in easily inactivation to the environmental exposure. Thus it can be seen that, with respect to the protein immobilization on the nanoporous metal oxide films, surface characteristics of the mesoporous films and matching of sizes between the biomolecules and the mesoporous substrates are of essential importance.

Fig. 6 shows the electrochemical response of the HRP/Nb₂O₅-derived biosensor (A) and Nb₂O₅-derived electrode without enzyme (B) for hydrogen peroxide. The addition of H₂O₂ to the solution resulted in a dramatic increase in the reductive current and a concomitant decrease in the oxidation current (Fig. 6A, a₁–a₃), while a little current response for higher concentration H₂O₂ was observed on the blank Nb₂O₅ electrode (Fig. 6B, b₁ and b₂).

From Fig. 8, the linear response of the biosensor to H₂O₂ was from 0.1 μ M to 0.1 mM and R^2 was calculated to be 0.99. The biosensor reproducibility was estimated at four electrodes that were prepared under the same conditions and the relative standard deviation was about 10%. When not in use, the biosensor was stored in the refrigerator at 4 $^{\circ}$ C and retained 90% of its initial current response after one month. In the previous research of HRP assembled in DNA films, HRP tended to lose its catalytic function for a fairly high concentration of H₂O₂ (the upper linear range was up to 1 μ M) in case the electroactive site was exposed to the electrode for direct electron transport [26]. Compared with free enzymes, the immobilized enzymes

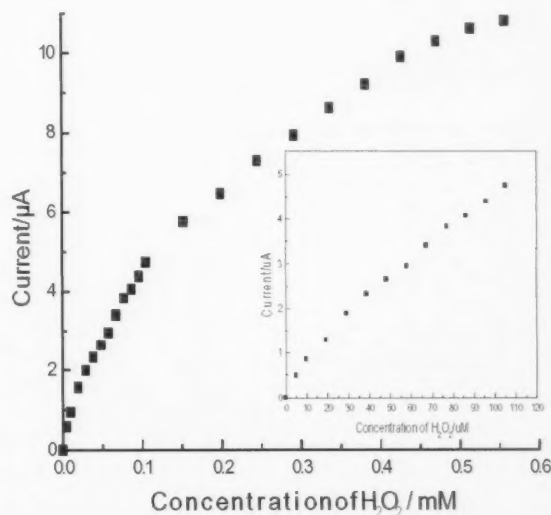


Fig. 8. The calibration curve of HRP/Nb₂O₅-derived biosensor to H₂O₂ response. The inset shows the linear range of the biosensor response. Applied potential of -250 mV vs. SCE.

can lose some activities for the certain interaction occurred between the biomolecules and matrix. However, the current results show that HRP can be effectively immobilized onto the mesoporous Nb₂O₅ film and retain its response activity with good stability. Nb₂O₅ can directly promote or mediate electrode transfer between the protein redox site and the electrode surface.

4. Conclusions

The highly ordered mesoporous niobium oxide films readily prepared with tailored pore size and topology were employed to immobilize biomolecules. With complementary surface charges, the protein molecules such as Cyt-c and HRP were readily assembled and allowed for a maximum adsorption when the pore size of such mesoporous niobium oxides was matched for proteins to diffuse properly into the channels. The process of protein assembling was investigated by cyclic voltammetry and chronoamperometry, exhibiting a full surface coverage with the electroactive molecules. The direct electrochemical behaviors for protein assembled on such films were measured and the reactivity of adsorbed protein was still remained, characterized by amperometric response. Furthermore, an amperometric biosensor was successfully fabricated by immobilizing HRP onto the mesoporous Nb₂O₅ modified electrode with tailored pore size and film thickness for the electrochemical response of hydrogen peroxide. With the property of promoting the direct electron transfer between proteins and electrodes without addition of electron transfer mediators, such nanoporous niobium oxide materials have potential application for the development of novel biosensors.

Acknowledgements

The authors acknowledge National Nature Science Foundation of China (30270386, 20299030, 20335040) and NanoSciTech Promote Center (0144nm067) for support of this research.

References

- [1] H.A. Heering, J.H. Weiner, F.A. Armstrong, *J. Am. Chem. Soc.* 119 (1997) 11628.
- [2] G. Reach, G.S. Wilson, *Anal. Chem.* 64 (1992) 381A.
- [3] Y.M. Lvov, Z. Lu, J.B. Schenkman, X. Zu, J.F. Rusling, *J. Am. Chem. Soc.* 120 (1998) 4073.
- [4] (a) E. Topoglidis, A.E.G. Cass, G. Gilardi, S. Sadeghi, N. Beaumont, J.R. Durrant, *Anal. Chem.* 70 (1998) 5111;
(b) E. Topoglidis, T. Lutz, R.L. Willis, C.J. Barnett, A.E.G. Cass, J.R. Durrant, *Faraday Discuss.* 116 (2000) 35;
(c) E. Topoglidis, C.J. Campbell, A.E.G. Cass, J.R. Durrant, *Langmuir* 17 (2001) 7899.
- [5] E. Topoglidis, Y. Astuti, F. Duriaux, M. Gratzel, J.R. Durrant, *Langmuir* 19 (2003) 6894.
- [6] J.X. Wang, M.X. Li, Z.J. Shi, N.Q. Li, Z.N. Gu, *Anal. Chem.* 74 (2002) 1993.
- [7] Y.L. Zhou, N.F. Hu, Y.H. Zeng, J.F. Rusling, *Langmuir* 18 (2002) 211.
- [8] K.J. McKenzie, F. Marken, *Langmuir* 19 (2003) 4327.
- [9] P. Yang, D. Zhao, D.I. Margolese, B. Chmelka, G. Stucky, *Nature* 396 (1998) 512.
- [10] (a) S. Murray, M. Trudeau, D.M. Antonelli, *Adv. Mater.* 12 (2000) 1339;
(b) B. Ye, M. Trudeau, D.M. Antonelli, *Adv. Mater.* 13 (2001) 29;
(c) M. Vetrano, X. He, M. Trudeau, J.E. Drake, D.M. Antonelli, *Adv. Funct. Mater.* 12 (2002) 174.
- [11] X. Xu, B. Tian, J. Kong, S. Zhang, B. Liu, D. Zhao, *Adv. Mater.* 15 (2003) 1932.
- [12] B. Tian, X. Liu, B. Tu, C. Yu, J. Fan, L. Wang, S. Xie, G.D. Stucky, D. Zhao, *Nat. Mater.* 2 (2003) 159.
- [13] (a) J. Deere, E. Magner, J.G. Wall, B.K. Hodnett, *J. Phys. Chem. B* 106 (2002) 7340;
(b) E. Laurenti, G. Suriano, E.M. Ghibaudi, R.P. Ferrari, *J. Inorg. Biochem.* 81 (2000) 259.
- [14] E.P. Barrett, L.G. Joyner, P.P. Halenda, *J. Am. Chem. Soc.* 73 (1951) 373.
- [15] S. Brunauer, P.H. Emmett, E. Teller, *J. Am. Chem. Soc.* 60 (1938) 309.
- [16] B. Liu, R. Hu, J. Deng, *Anal. Chem.* 69 (1997) 2343.
- [17] M. Collinson, E.F. Bowden, *Langmuir* 8 (1992) 2552.
- [18] K.G. Welinder, *Eur. J. Biochem.* 96 (1979) 483.
- [19] M. Kosmulski, *Langmuir* 13 (1997) 6315.
- [20] (a) X. Chen, R. Ferrigno, J. Yang, G.A. Whitesides, *Langmuir* 18 (2002) 7009;
(b) H. Takahashi, B. Li, T. Sasaki, C. Miyazaki, T. Kajino, S. Inagaki, *Micropor. Mesopor. Mater.* 44 (2001) 755.
- [21] A.S. Haas, D.L. Pilloud, K.S. Reddy, G.T. Babcock, C.C. Moser, J.K. Blasie, P.L. Dutton, *J. Phys. Chem. B* 105 (2001) 11351.
- [22] A. Avila, B.W. Gregory, K. Niki, T.M. Cotton, *J. Phys. Chem. B* 104 (2000) 2759.
- [23] D.D. Schlereth, W. Manrele, *Biochemistry* 32 (1993) 1118.
- [24] P. Hoyer, J. Weller, *J. Phys. Chem.* 99 (1995) 14096.
- [25] R.L. Willis, C. Olson, B. O'Regan, T. Lutz, J. Nelson, J.R. Durrant, *J. Phys. Chem. B* 106 (2002) 7605.
- [26] X. Chen, C. Ruan, J. Kong, J. Deng, *Anal. Chim. Acta* 412 (2000) 89.
- [27] R.W. Murray, A.J. Bard, *Electroanalytical Chemistry*, vol. 13, Marcel Dekker, New York, 1984, p. 191.
- [28] A. El Kasmi, M.C. Leopold, R. Galligan, R.T. Robertson, S.S. Saavedra, K. El Kacemi, E.F. Bowden, *Electrochem. Commun.* 4 (2002) 177.

Multivariate optimisation of electrochemically pre-treated electrodes used in a voltammetric electronic tongue

Susanne Holmin*, Christina Krantz-Rülcker, Fredrik Winquist

S-SENCE (Swedish Sensor Centre) and Laboratory of Applied Physics, Department of Physics and Measurement Technology, Linköping University, SE-581 83 Linköping, Sweden

Received 15 February 2001; received in revised form 11 July 2002; accepted 18 March 2004

Available online 17 July 2004

Abstract

The use of experimental design as a tool to optimise electrochemically cleaned electrodes applied in a voltammetric electronic tongue is described. A simple and quick activation of electrode surfaces is essential for this type of device, especially for on-line applications in industrial processes. The electronic tongue consisted of four metal electrodes, e.g. Au, Ir, Pt, and Rh in a three-electrode configuration. Current was measured as a function of large potential pulses of decreasing amplitude applied to each electrode. Preliminary results showed that electrochemical cleaning activated the electrode surfaces to similar extent as polishing. Settings of potential and time for each electrode was determined with experimental design in a solution containing 1.0 mM $K_4[Fe(CN)_6]$ in 0.1 M phosphate buffer (pH 6.8). Electrode surfaces were deactivated in-between measurements in a complex liquid, like tea. Optimal settings for potential and time in the electrochemical cleaning procedure at each electrode were chosen at recoveries of 100% (compared to polished electrodes). The recoveries were larger than 100% when too large potentials and times were applied. This could be explained by the fact that the electrode areas increased and therefore also the current responses. Principal component analysis (PCA) was used to investigate the stability of the electrode settings at 100% recoveries. No obvious trends of drift in the signals were found.

© 2004 Elsevier B.V. All rights reserved.

Keywords: Electrode pre-treatment; Electronic tongue; Experimental design; Optimisation; Principal component analysis and voltammetry

1. Introduction

During the last two decades, interest in using sensor array techniques, such as “electronic noses” and “electronic tongues” has increased in the field of analytical chemistry. The word “electronic tongue” and “electronic nose” [1] was coined to establish a new concept, when an array of non-specific sensors with overlapping response signals was combined with multivariate data analysis (e.g. principal component analysis, partial least squares, artificial neural networks, etc.). These techniques were supposed to mimic human sensing mechanisms and subsequently developed to measure in complex gases or liquids. With these devices, attributes (odour, taste, quality, status, etc.) are determined rather than single parameters.

In the beginning of the 1990s, a potentiometric taste sensor based on various lipid polymers was developed to determine human taste sensations such as bitterness, saltiness, sourness, sweetness, etc. [2]. This device has also been commercialised (Anritsu Corporation, Japan). Other types of electronic tongues and taste sensors using potentiometric [3] or optical sensors [4,5] have also been reported. So far there exist only one electronic tongue based on voltammetry, but similar concepts using multisensing voltammetric devices have recently been presented [6,7]. Winquist et al. developed a voltammetric electronic tongue at Linköping University in 1997 [8]. It consisted of two metal working electrodes (Au and Pt) in a three-electrode configuration (working electrodes, an Ag/AgCl reference electrode and an auxiliary electrode of stainless steel). This sensor array was able to classify complex solution, like fruit juices. It has later been used in various applications, such as monitoring of freshness in milk [9] and monitoring of water quality in a water plant [10]. In addition, a hybrid electronic tongue of

* Corresponding author. Tel.: +46-13-28-13-72; fax: +46-13-28-89-69.
E-mail address: susho@ifm.liu.se (S. Holmin).

voltammetric, potentiometric and conductometric electrodes was used to discriminate between different fermented milk samples [11]. Current is measured as a function of potential, which is applied to one metal electrode at a time as a series of large pulses of decreasing or increasing amplitude. Transient responses are obtained, which are combinations of charging and faradic currents. To simplify the interpretation of complicated response patterns, which consist of hundreds or thousands of variables, the data are treated with multivariate data analysis. For example, principal component analysis (PCA) is a popular pattern recognition tool often used to find relations or non-relations between different groups of objects when a data set contains lots of variables [12]. By reducing the dimensionality of the original data set the interpretation is simplified. Samples are projected on to new uncorrelated dimensions (principal components, PCs) and the largest variation or difference between objects is extracted. This method can also be used to monitor changes in a process of typical interest, like drift in sensor responses. Furthermore, experimental design has become a powerful tool in many different research areas when experimental conditions are to be optimised [13]. For example, it has been used in adsorptive stripping voltammetry when various parameters (accumulation time, pulse amplitude, scan rate, etc.) were optimised [14,15].

Electrochemical reactions in solutions taking place on metal electrode surfaces have been investigated thoroughly with voltammetry. It is well known that the faradic response obtained when species in a solution are oxidised or reduced in the vicinity of an electrode is dependent on the state of the electrode surface [16]. The surface should be reproducible to achieve accurate results. However, fouling of electrodes caused from accumulation of adsorbed species on to electrode surfaces may occur. Different species, like halide ions [17] and organic molecules [18] can change the surface states. Poisoning of metal electrodes due to sulphur compounds have also been reported [17,19]. In addition, metal electrodes are oxidised at higher anodic potentials, forming thin layers of metal oxides and hydroxyl radicals. This oxide film may inhibit [18] or catalyse [20] electrochemical reactions of interest. To activate electrode surface states, some kind of electrode pre-treatment has been suggested. There exist different methods, such as heating, polishing, laser, ultrasound, microwaves, chemical, electrochemical pre-treatment, etc. which has been reviewed by Stulik [16].

Since the electronic tongue based on voltammetry is usually applied in complex liquid media, electrode surfaces are most likely to deteriorate when no pre-treatment is performed. This will result in drift in responses, which was found in earlier papers [11,21]. Recently, it was possible to remove drift in voltammetric signals by using mathematical algorithms [22]. Even if they may be successful in reducing drift, the proper use and development of stable sensors is still essential. This is especially important for on-line monitoring when quick and simple cleaning procedures are required for

the voltammetric electronic tongue. A method called electrochemical cleaning has been thoroughly used in liquid chromatography to regenerate a electrode surface in a quick and reproducible way in an electrochemical detection procedure [23–30]. Therefore, this method is also interesting to apply to the electrodes in the voltammetric electronic tongue. In the electrochemical procedure, a positive anodic potential is usually applied to oxidise the electrode surface and to desorb oxidised species. A negative cathodic potential is then used to reduce the surface oxide, which regenerates the electrode surface prior to analysis. In the papers above, the settings of each potential and time were optimised usually by one parameter at a time. This procedure is often time-consuming and it is well known that a local optimum is sometimes found instead of a global one. In addition, interaction effects between different parameters can be lost. A reasonable solution to this is to use multivariate experimental design instead.

In this article, different pre-treatments like electrochemical cleaning and polishing of metal electrodes were investigated with multivariate data analysis, like PCA. A model experiment containing three complex liquids and two other solutions were used to study activation/deactivation of electrodes. For the reasons described above, multivariate experimental design was used to optimise the electrochemical cleaning steps of each electrode when factors as potential and time were alternated.

2. Experimental

2.1. Electronic tongue

Experiments were conducted with an electronic tongue consisting of working electrodes of various metals, such as gold, iridium, platinum, and rhodium of 99.9% purity (Johnson Matthey, Sweden). Potentials were referred to a single junction reference electrode (Ag/AgCl, 3 M KCl, Beta Sensor, Sweden) and current was measured between the working electrode of interest and an auxiliary electrode of stainless steel (Fig. 1). Wires of the different metals were encapsulated in a ceramic material, exposing a geometric surface of 0.79 mm² of each electrode. An ISKRA 5410 potentiostat (Chemel AB, Sweden) was used to apply a series of large potential pulses with decreasing amplitude to each electrode, e.g. large amplitude pulse voltammetry (LAPV). A relay box was used to consecutively measure the working electrodes and resulting transient currents were collected and stored by a computer. The responses consist of a combination of charging and faradic currents. Charging current is obtained when a potential pulse is applied to an electrode and charged species in the solution of opposite sign are arranged at the metal surface. Faradic current is due to the oxidation or reduction of electrochemically active compounds in the solution. The measurement principle is described elsewhere [8].

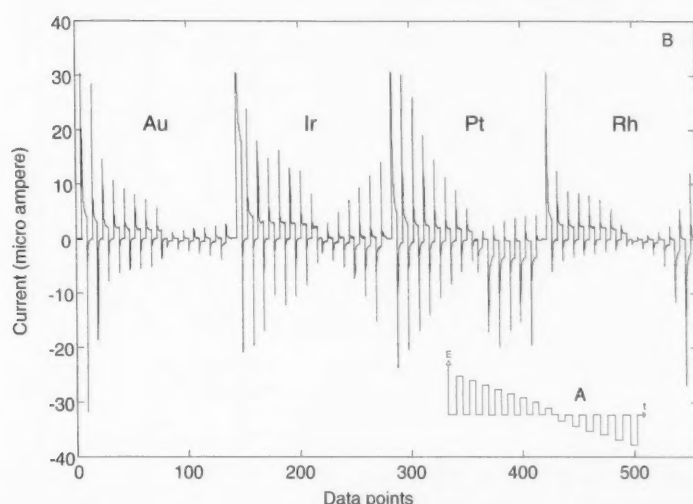


Fig. 1. (A) Potential pulse sequence applied to each electrode used in the electronic tongue; (B) typical current response patterns at four electrodes.

2.2. Sample preparation and chemicals

Different complex liquids (apple juice, tea and process water from a paper industry), and two "well-defined" solutions, with/without 1.0 mM $K_4[Fe(CN)_6]$ in 0.1 M phosphate buffer, were used in the model experiment. The apple juice was bought from a local dealer. Since the juice was already diluted, no extra sample pre-treatment was conducted. Sixteen gram black tea (Ceylon) was extracted in 2 l boiled tap water and mechanically stirred for 5 min. A sieve was used to remove the tealeaves. The solution was then cooled to +22 °C. Two litres of process water from a paper making industry was also used. It was obtained from the wet-end of a paper machine, when fibres were separated from water. An aqueous solution ("white water") was received containing fines, starch and process chemicals. The process water was filtered before use. A solution of 5 l 0.1 M

phosphate buffer (pH 6.8) using KH_2PO_4 and K_2HPO_4 was prepared and diluted to volume by distilled water. Two litres of the buffer solution was also used to prepare a solution containing 1.0 mM $K_4[Fe(CN)_6]$ in 0.1 M phosphate buffer (pH 6.8). The chemicals were of analytical grade (p.a.) and obtained from Kebo Lab (Spånga, Sweden). Each solution was divided into 40 sub-samples, each containing 50 ml. The samples were stored at -80 °C to avoid deterioration of the samples. For the optimisation of electrochemically cleaned electrodes, samples were not refrigerated because the experiments were performed during 1 day.

2.3. Measurement procedure

A series of large potential steps with decreasing amplitude (-0.1 V per step) were applied consecutively to each electrode (Fig. 1A). The potential range was applied be-

Table 1
Measurement order of five solutions using different electrode pre-treatments

Measurement occasion	Measurement order					Pre-treatment
	Apple juice measurement order	1.0 mM $K_4[Fe(CN)_6]$ in 0.1 M phosphate buffer (pH 6.8)	Process water	Tea	0.1 M phosphate buffer (pH 6.8)	
1	4	5	2	1	3	Polishing
2	3	1	2	5	4	Polishing
3	5	3	2	1	4	No ^a
4	1	5	4	3	2	No ^a
5	4	2	3	5	1	Ec ^b
6	3	1	2	5	4	Ec ^b
7	1	2	4	5	3	Ec ^b
8	4	5	1	2	3	Ec ^b
9	3	1	4	2	5	No
10	2	4	1	3	5	No
11	3	2	—	—	1	Polishing

^a The gold electrode was polished with a sand cloth, but not the others.

^b Ec = electrochemical cleaning of electrodes using the following potential sequence: +2 V (2.5 s), -2 V (5 s), and 0 V (10 s).

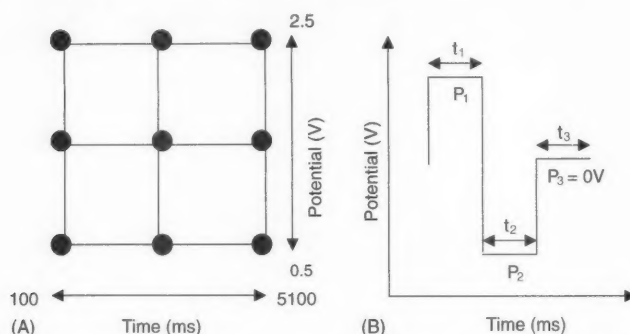


Fig. 2. (A) A model of central composite face design (CCF). Two factors in electrochemical cleaning of electrode surfaces were used. (B) Electrochemical cleaning with an applied potential sequence of P_1 , $P_2 = -P_1$ and time $t_1 = t_2$ for one experiment. The rest potential (P_3) was set to 0 V ($t_3 = 5$ s).

tween 0.8 and -0.6 V, and a base potential at 0 V was used between the pulses. Each potential step was applied during 0.5 s. Transient current responses were collected from 48 evenly distributed data points over a potential step. This resulted in altogether 48 data points per step \times 29 steps per electrode \times 4 electrodes = 5568 data points for each sample (Fig. 1B). Each sample was measured three times, and the average of the replicates was used in the data evaluation. The experiments were performed in a water bath at 22 ± 0.1 °C. Each sample was thawed 1 h prior to analysis in the water bath.

In the first model experiment, different electrode pretreatment techniques were investigated. Random measurements were performed on five different solutions as described in Table 1, when no pre-treatment, polishing, or electrochemical cleaning was conducted. A sand cloth was used to polish the electrodes, which were then rinsed with distilled water. When electrochemical cleaning was used, the following potential sequence was applied to each electrode: +2 V (2.5 s), -2 V (5 s), and 0 V (10 s). Electrochemical cleaning of the electrodes was performed in each sample to be measured. The same potential program and settings was used as described above. Four repetitive measurements were conducted on each sample, and the average of the repetitions was used in the data evaluation.

Experimental design was used to optimise the method of electrochemical cleaning (see Section 3.2). Electrochemical cleaning of the electrodes was conducted in each sample to be measured with variable settings determined by the experimental design. Data was collected as described above. The following measurement sequence was conducted to each sample:

- 10 repetitive measurements were performed in tea to deactivate the electrodes;
- one measurement was conducted in 1 mM $K_4[Fe(CN)_6]$ in 0.1 M phosphate buffer (pH 6.8) to follow the deactivation of electrodes previously conducted in tea;
- electrochemical cleaning of electrodes was performed in 1 mM $K_4[Fe(CN)_6]$ in 0.1 M phosphate buffer (pH 6.8) with variable settings determined by the experimental

design;

- three repetitive measurements of 1 mM $K_4[Fe(CN)_6]$ in 0.1 M phosphate buffer (pH 6.8) with electrochemical cleaning of electrodes conducted as described in point 3.

Three experiments were performed with polished electrodes to be able to compare and determine the efficiency of electrochemical cleaning versus polishing. An amount of 1 mM $K_4[Fe(CN)_6]$ in 0.1 M phosphate buffer (pH 6.8) was used.

3. Data analysis

3.1. Principal component analysis

Principal component analysis [12] was performed using software Sirius 6.0 (Pattern Recognition Systems A/S, Bergen, Norway).

3.2. Experimental design

Experimental design is used to systematically determine important factors (screening) and to optimise a measurement system with as few experiments conducted as possible [13]. Central composite face (CCF) design was used in this study (Fig. 2A). It was a full factorial design with star points placed on the faces of the sides. The experimental domain was determined by two factors, potential, P and time, t . The relation between the main (linear), interaction and quadratic (non-linear) terms and the response, *recovery* in the model is described with the following equation:

$$\text{recovery (\%)} = b_0 + b_1P + b_2t + b_{12}Pt + b_{11}P^2 + b_{22}t^2 + \varepsilon \quad (1)$$

where b_0 is the mean value, $b_{n>0}$ the effect of the n th parameter, and ε is the pure error (residual) not explained by the model. In order to obtain a clean and active metal surface, a positive potential is applied to produce a metal oxide film and to desorb species, then a negative potential

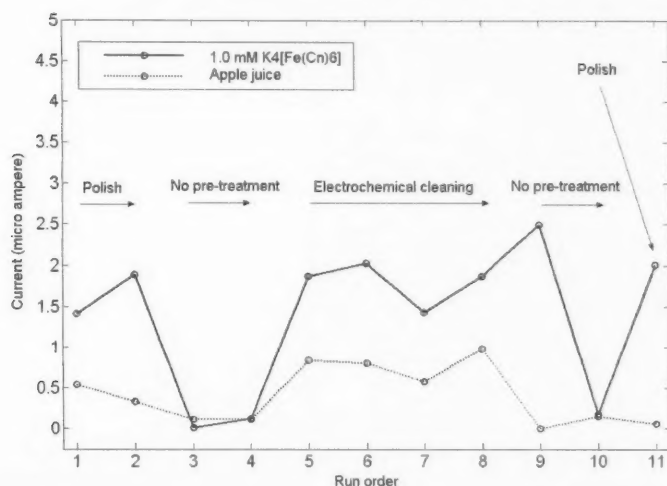


Fig. 3. Activation/deactivation of a Pt electrode using different pre-treatment techniques. Faradic current at 0.4 V of 1.0 mM $K_4[Fe(CN)_6]$ /0.1 M phosphate buffer (pH 6.8) and apple juice at different run orders according to Table 1.

is used to strip the oxide film [23]. Hence, electrochemical cleaning was applied using a potential sequence of three potential steps, P_1 – P_3 (Fig. 2B). The second applied potential, P_2 was used with the same potential amplitude but of a negative sign as P_1 . A rest potential ($P_3 = 0$ V) was applied for 5 s. Time, t was identical during the first two potential steps ($t_1 = t_2$). P_1 and subsequently P_2 was varied in three levels between 0.5 and 2.5 V (centre point: 1.5 V), and t was varied between 100 and 5100 ms (centre point: 2600 ms). Three levels were chosen in order to simplify the detection of non-linear relationships between the parameters and the response. Two experiments at each point in the experimental domain and six centre-point measurements were conducted, making altogether 22 experiments. The experiments were randomised in order to eliminate systematic variations. The experimental design was performed in Model 5.0 (Umetrics, Umeå, Sweden). Partial least squares (PLS) was applied as a regression tool to fit the variables with the responses. To evaluate each model, estimates of R^2 (explained variation) and Q^2 (prediction variation) was used. $Q^2 > 0.7$ is considered as good predictive power of the model.

4. Results and discussion

4.1. Activation/deactivation of electrodes

Drift was found earlier in current responses when the voltammetric electronic tongue was applied in complex liquids. It was obtained since the electrodes were not polished, but was successfully removed with mathematical algorithms [22]. To increase the long-term stability of the sensors it is also important to use physical methods to prevent deterioration of electrode surfaces. In this

model experiment, two electrode pre-treatment techniques, e.g. polishing and electrochemical cleaning were investigated. To study the efficiency of these methods different complex liquids were used like apple juice, tea and process water from a paper industry. They were compared to more well-defined solutions, e.g. with/without 1.0 mM $K_4[Fe(CN)_6]$ in 0.1 M phosphate buffer (pH 6.8). Potassium hexacyanoferrate(II) is often used as a model substance in voltammetric studies. The faradic current of this compound was collected at 0.4 V where oxidation occurs. The influence of these two methods on the faradic current of 1.0 mM $K_4[Fe(CN)_6]$ /0.1 M phosphate buffer (pH 6.8) and apple juice is displayed for the Pt electrode in Fig. 3. When the electrode was not pre-treated a significant loss in current responses for the two liquids were obtained. During each measurement occasion the electrode surfaces were treated as described in Table 1. It was also shown that the currents were recovered when electrochemical cleaning was applied. Similar trends were found for the other liquids and electrodes (data not shown). Depending on the liquid run order in each measurement occasion (Table 1), the effect of activation or deactivation of electrode surfaces from a previous experiment was found. For example, no loss in current response was obtained for potassium hexacyanoferrate(II) during measurement occasion 9. According to Table 1, this sample was measured first during this occasion. This implies that the electrode surface was still active after measurement occasion 8, when electrochemical cleaning was used as a pre-treatment method. For the Ir electrode, the charging and faradic current increased (data not shown), indicating that an increased electrode area due to a porous metal oxidation growth was obtained. The method of electrochemical cleaning showed promising abilities but the applied positive potential must be chosen carefully so that drift is not induced instead of being

prevented.

4.2. Optimisation of electrochemical cleaning

The previous experiment showed that the procedure of electrochemical cleaning is a possible alternative to activate electrode surfaces. Sometimes it is also important to use as short measurement times as possible during an experiment. Thus, it can be useful to reduce the time for the pre-treatment procedure as well. Experimental design was investigated as a tool to optimise the method of electrochemical cleaning. The variable settings of potential and time are described in Section 3.2. Before each experiment the electrode surfaces were deactivated with tea. In order to determine the efficiency of the electrochemical cleaning step, recovery (%) was calculated. Faradic currents obtained with electrochemically cleaned electrodes in 1.0 mM $K_4[Fe(CN)_6]/0.1$ M phosphate buffer (pH 6.8) at potential 0.4 V were compared to polished electrodes. Influence of main, interaction and quadratic terms on the response was studied in regression coefficient plots. Large regression coefficients (positive or negative) mean that the parameters have large impacts on the model. In this study, individual designs were conducted for each electrode, which were later refined by excluding non-significant terms (95% c.f.). Regression coefficients from each model are displayed in Fig. 4. It was generally found that *potential* had more influence on the response (recovery, %) than *time*. Smaller negative quadratic terms, e.g. *pot* × *pot* and/or *time* × *time* were obtained for the electrodes, except for Ir (positive effect). In addition, Ir was the only electrode that obtained a positive interaction

Table 2

Validation of refined regression models for each electrode using multivariate experimental design

Electrode	Experimental data	According to model (%)
Au	107 ± 25% (82, 132)	97
Ir	90 ± 9% (81, 99)	81
Pt	109 ± 13% (96, 122)	110
Rh	113 ± 14% (99, 127)	118

The deviation is determined with 95% c.i. ($n = 3$).

between the main factors. The prediction variation, Q^2 was 0.87, 0.88, 0.77 and 0.62 for the Au, Ir, Pt, Rh electrode, respectively. This indicates that the prediction ability of each regression model was good, except for the Rh electrode. Regression variation, R^2 (response variation explained by the model) was calculated as well; 0.90, 0.94, 0.86 and 0.84 for the Au, Ir, Pt and Rh, respectively. These estimates are in agreement with Q^2 for each electrode.

Contour response plots of refined models for each electrode are shown in Fig. 5. Different results were obtained for each electrode, indicating that different settings of potential and time in the electrochemical cleaning step should be used. True global optima's were not found; instead recoveries larger than 100% were obtained at certain potentials and times, except at the Ir electrode. Too largely applied potentials and times have a tendency to increase the electrode areas as described above. It should be mentioned that potentials used in the contour plots are expressed only as P_1 (see Fig. 2B). Subsequently, a negative potential of the same amplitude, $P_2 = -P_1$, was also applied during the ex-

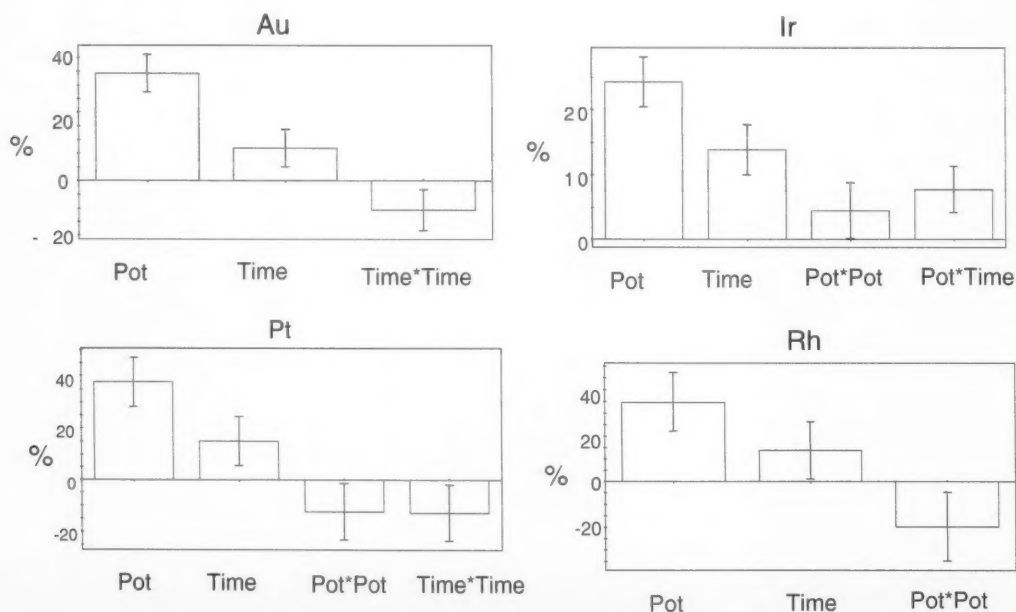


Fig. 4. Regression coefficient plots of each electrode. The bars represent the deviation with 95% c.i.

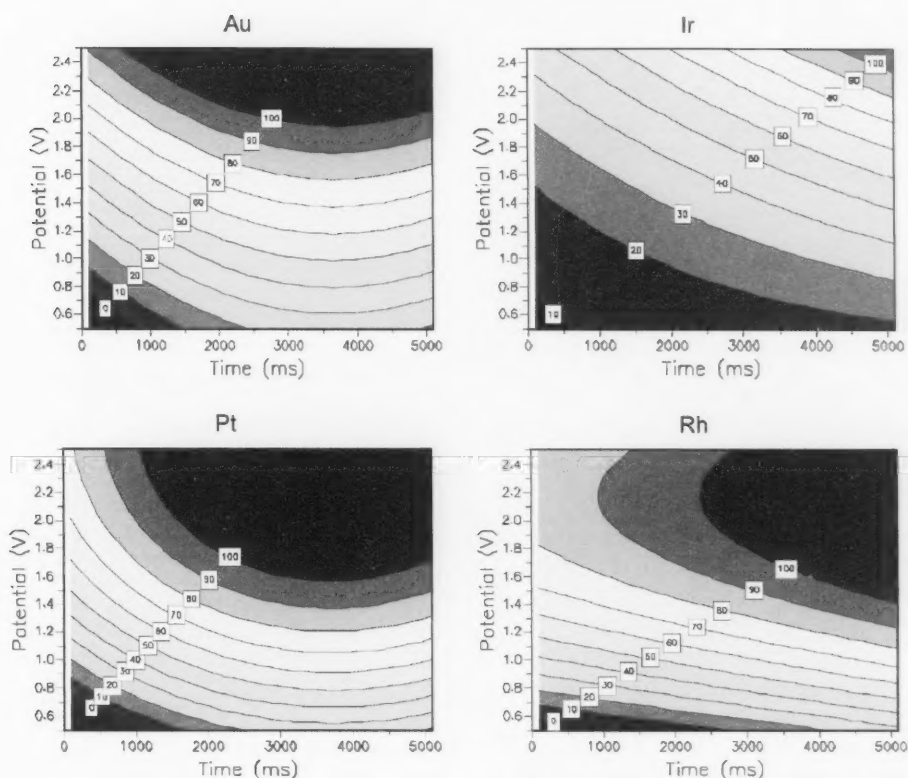


Fig. 5. Response contour plots of different electrodes when potential and time is varied. The response is recovery in percentage (compared to polished electrodes).

periments. To validate the regression models for each electrode, the same potential ($P_1 = 2\text{ V}$, $P_2 = -2\text{ V}$) and time (5000 ms) in the electrochemical cleaning step was used. According to the surface plots different recoveries were expected. The results are shown in Table 2. The accuracy of the experimental data for the Pt and Rh electrode agreed well with the model values. Less satisfying results, but still approvable, was obtained for the other electrodes. In addition, response deviation for the Au electrode was twice as large compared to the other electrodes.

The stability of the electrodes after electrochemical cleaning was studied with multivariate data analysis, like PCA. The measurements were performed 30 times in 1.0 mM $\text{K}_4[\text{Fe}(\text{CN})_6]/0.1\text{ M}$ phosphate buffer (pH 6.8). The electrodes were deactivated with tea between measurements as described earlier. Optimal settings of potential and time in the electrochemical cleaning step were chosen from the response surface plots for each electrode at 100% recoveries, in order to minimise the risk of increasing the electrode areas. Minimum potentials in the 100% recovery curves were used. Thus, different times were also applied (see Table 3). All current responses obtained during a whole potential scan (0.8 to -0.6 V , see also Section 2) were used in the data evaluation, which was not the

case in earlier experiments when only the faradic current at 0.4 V was used. The data set for each electrode was of size (30×1392). A larger data set was obtained by consecutively arranging the measurements from each electrode in rows, making altogether (120×1392). A score plot is displayed in Fig. 6. It shows that there are no obvious trends in time (drift) for the electrodes. To summarise, to achieve 100% recovery and no drift in the data, the optimal settings of potential and time in the electrochemical cleaning step for each electrode (see Table 3) was successfully determined using multivariate experimental design. Care must be taken though; too large applied potentials may increase the electrode area and then induce drift into the system.

Table 3

Settings of potential and time obtained from contour surface plots at 100% recovery

Electrode	Potential, P_1 (V)	Potential, P_2 (V)	Time $t_1 = t_2$ (ms)
Au	2.0	-2.0	3000
Ir	2.5	-2.5	5000
Pt	1.6	-1.6	3000
Rh	1.6	-1.6	4000

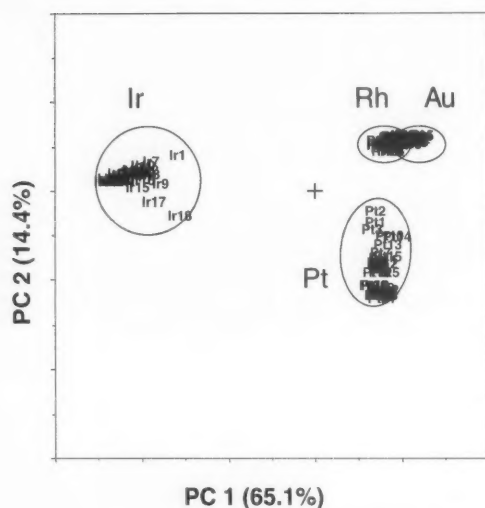


Fig. 6. PCA score plot of electrochemically cleaned electrodes with settings described in Table 3.

5. Conclusions

Different electrode pre-treatment techniques were investigated when various aqueous solutions were measured with an electronic tongue based on voltammetry. Electrochemical cleaning as a pre-treatment method showed similar performance compared to polished electrodes. A simple and quick activation of electrodes is essential when the electronic tongue is used in complex liquids and for on-line applications. It was found that complex liquids were responsible for the loss of current responses when no pre-treatment was used. Fouling of electrodes due to adsorbed species likely caused this behaviour. Multivariate experimental design showed to be a promising tool to investigate and optimise the different parameters (potential and time) in the electrochemical cleaning procedure, which minimised the amount of experiments to perform and considered the main and interaction effects between the parameters that could not be neglected. The electrodes were contaminated with a complex liquid (tea) between the measurements. Settings of potential and time were incorporated in a potential program to be used. Optimal settings for the parameters in the electrochemical cleaning procedure were chosen at 100% recoveries (compared to polished electrodes) when no drift in signals was found. Too largely applied potentials showed a tendency to increase the electrode areas and subsequently the current responses. Of course, other settings are expected and must be considered compared to what was obtained in this article when the voltammetric electronic tongue is applied to other applications.

Acknowledgements

The Swedish Sensor Centre, S-SENCE, supported with grants from the Swedish Agency for Innovation Systems, VINNOVA and Swedish Industry is greatly acknowledged. Support from the graduate school Forum Scientium (S.H.) is also acknowledged.

References

- [1] K. Persaud, G. Dodd, *Nature* 299 (1982) 352.
- [2] K. Toko, *Electroanalysis* 10 (1998) 657.
- [3] C. Di Natale, A. Macagnano, F. Davide, A. D'Amico, A. Legin, Y. Vlasov, A. Rudnitskaya, B. Selezenev, *Sens. Actuators B* 44 (1997) 423.
- [4] J.J. Lavigne, S. Savoy, M.B. Clevenger, J.E. Ritchie, B. McDoniel, S. Yoo, E.V. Anslyn, J.T. McDevitt, J.B. Shear, D. Neikirk, *J. Am. Chem. Soc.* 120 (1998) 6429.
- [5] S. Yamakawa, A. Yamaguchi, *Sens. Mater.* 7 (1995) 271.
- [6] C.-C. Hsueh, Y. Liu, M. Henry, M.S. Freund, *Anal. Chim. Acta* 397 (1999) 135.
- [7] S.K. Schreyer, S.R. Mikkelsen, *Sens. Actuators B* 71 (2000) 147.
- [8] F. Winquist, P. Wide, I. Lundström, *Anal. Chim. Acta* 357 (1997) 21.
- [9] F. Winquist, C. Krantz-Rülcker, P. Wide, I. Lundström, *Meas. Sci. Technol.* 9 (1998) 1937.
- [10] C. Krantz-Rülcker, M. Stenberg, F. Winquist, I. Lundström, *Anal. Chim. Acta* 426 (2000) 217.
- [11] F. Winquist, S. Holmin, C. Krantz-Rülcker, P. Wide, I. Lundström, *Anal. Chim. Acta* 406 (2000) 147.
- [12] S. Wold, K. Esbensen, P. Geladi, *Chemom. Intell. Lab. Syst.* 2 (1987) 37.
- [13] G.E.P. Box, W.G. Hunter, J.S. Hunter, *Statistics for Experimenters*, Wiley, 1978.
- [14] S. Furlanetto, S. Pinzauti, P. Gratterer, E. La Porta, G. Calzeroni, *J. Pharm. Biomed. Anal.* 15 (1997) 1585.
- [15] S. Pinzauti, P. Gratterer, S. Furlanetto, P. Mura, E. Dreassi, R. Phan-Tan-Luu, *J. Pharm. Biomed. Anal.* 41 (1996) 881.
- [16] K. Stulik, *Electroanalysis* 4 (1992) 829.
- [17] M. Gerlache, G. Girousi, G. Quarin, J.-M. Kauffmann, *Electrochim. Acta* 43 (1998) 3467.
- [18] R.N. Adams, *Electrochemistry at Solid Electrodes*, Marcel Dekker, New York, 1969.
- [19] E. Lamy-Pitara, J. Barbier, *J. Electroanal. Chem.* 416 (1996) 47.
- [20] K. Kano, K. Takagi, K. Inoue, T. Ikeda, T. Ueda, *J. Chromatogr. A* 721 (1996) 53.
- [21] P. Ivarsson, S. Holmin, N.-E. Höjer, C. Krantz-Rülcker, I. Lundström, F. Winquist, *Sens. Actuators B* 76 (2001) 449.
- [22] S. Holmin, C. Krantz-Rülcker, I. Lundström, F. Winquist, *Meas. Sci. Technol.* 12 (2001) 1348.
- [23] D.S. Austin-Harrison, D.C. Johnson, *Electroanalysis* 1 (1989) 189.
- [24] L.E. Welch, W.R. LaCourse, D.A. Mead Jr., D.C. Johnson, T. Hu, *Anal. Chem.* 61 (1989) 555.
- [25] D.C. Johnson, W.R. LaCourse, *Anal. Chem.* 62 (1990) 589.
- [26] D.C. Johnson, W.R. LaCourse, *Electroanalysis* 4 (1992) 367.
- [27] W.R. LaCourse, D.C. Johnson, *Anal. Chem.* 65 (1993) 50.
- [28] M.B. Jensen, D.C. Johnson, *Anal. Chem.* 69 (1997) 1778.
- [29] R.D. Rocklin, A.P. Clarke, M. Weitzhandler, *Anal. Chem.* 70 (1998) 1496.
- [30] P. Jandik, A.P. Clarke, N. Avdolic, D.C. Andersen, J. Cacia, *J. Chromatogr. B* 732 (1999) 193.

Steady-state oxidation of cholesterol catalyzed by cholesterol oxidase in lipid bilayer membranes on platinum electrodes

Michael P. Bokoch, Anando Devadoss, Mariela S. Palencsár, James D. Burgess*

Department of Chemistry, Case Western Reserve University, 10900 Euclid Avenue, Cleveland, OH 44106-7078, USA

Received 12 December 2003; received in revised form 25 February 2004; accepted 9 March 2004

Available online 13 July 2004

Abstract

Cholesterol oxidase is immobilized in electrode-supported lipid bilayer membranes. Platinum electrodes are initially modified with a self-assembled monolayer of thiolipid. A vesicle fusion method is used to deposit an outer leaflet of phospholipids onto the thiolipid monolayer forming a thiolipid/lipid bilayer membrane on the electrode surface. Cholesterol oxidase spontaneously inserts into the electrode-supported lipid bilayer membrane from solution and is consequently immobilized to the electrode surface. Cholesterol partitions into the membrane from buffer solutions containing cyclodextrin. Cholesterol oxidase catalyzes the oxidation of cholesterol by molecular oxygen, forming hydrogen peroxide as a product. Amperometric detection of hydrogen peroxide for continuous solution flow experiments are presented, where flow was alternated between cholesterol solution and buffer containing no cholesterol. Steady-state anodic currents were observed during exposures of cholesterol solutions ranging in concentration from 10 to 1000 μM . These data are consistent with the Michaelis–Menten kinetic model for oxidation of cholesterol as catalyzed by cholesterol oxidase immobilized in the lipid bilayer membrane. The cholesterol detection limit is below 1 μM for cholesterol solution prepared in buffered cyclodextrin. The response of the electrodes to low density lipoprotein solutions is increased upon addition of cyclodextrin. Evidence for adsorption of low density lipoprotein to the electrode surface is presented.

© 2004 Elsevier B.V. All rights reserved.

Keywords: Cholesterol oxidase; Electrode; Lipid bilayer; Lipoprotein

1. Introduction

The formation and characterization of lipid bilayer membranes on solid supports such as electrode surfaces has been the subject of numerous publications [1–42], with increased attention over the last decade [1–3,5,8–20,22,29–43]. Supported lipid bilayer membranes have been shown to accommodate a variety of proteins and enzymes in controlled orientations and in active conformations. In an earlier report we have demonstrated that cholesterol oxidase can be immobilized in a functional conformation by lipid bilayer membranes on tin-doped indium oxide electrodes [44]. In this initial study, turnover of cholesterol was monitored by electrochemical reduction of hydrogen peroxide generated by the enzyme. This detection scheme suffered from nonzero baseline currents due to reduction of molecular

oxygen at the electrode surface. This paper describes the use of platinum electrodes that allow hydrogen peroxide to be electrochemically oxidized, thus avoiding a large background current from oxygen reduction. This step also regenerates molecular oxygen, which oxidizes cholesterol in the enzyme-catalyzed reaction. Other research groups have demonstrated electrochemical oxidation of hydrogen peroxide at platinum as a detection scheme for reactions catalyzed by cholesterol oxidase [45–52], as well as other oxidase enzymes [53–55]. This paper reports the use of the supported lipid bilayer membrane to sequester cholesterol from solution and immobilize cholesterol oxidase near the electrode surface. This electrode architecture exhibits steady-state responses allowing characterization of enzyme activity under discrete levels of lipid bilayer membrane cholesterol content.

The idealized model of the electrode architecture with cholesterol oxidase partially inserted in the thiolipid/lipid bilayer membrane is shown in Fig. 1. The enzyme immobilization scheme is supported by structural studies of cholesterol

* Corresponding author.

E-mail address: jdb22@po.cwru.edu (J.D. Burgess).

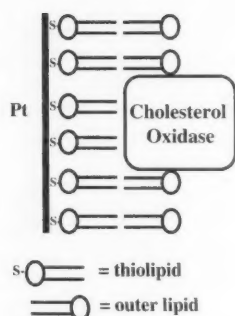


Fig. 1. Idealized structure of the electrode-supported lipid bilayer membrane containing cholesterol oxidase.

oxidase, as well as reports indicating that the enzyme associates with lipid bilayer vesicles and cell plasma membranes during oxidation of membrane-resident cholesterol [56–61].

It is proposed that cholesterol partitions into the electrode-supported lipid bilayer membrane from solution. This is consistent with literature describing the use of lipid bilayer vesicles as solution phase cholesterol acceptors in cellular cholesterol efflux experiments [62,63]. Based on these studies, it is reasonable to assume that cholesterol partitions into the electrode-supported lipid bilayer membrane from solution. Lateral diffusion of cholesterol (diffusion coefficient of $10^{-8} \text{ cm}^2 \text{ s}^{-1}$ at 20°C in a bilayer of 6:4 dipalmitoylphosphatidylcholine:cholesterol) [64–66], and possibly of the enzyme within the membrane [5], allows binding between cholesterol and the enzyme.

Enzymatic oxidation of cholesterol proceeds with the two electron reduction of the cholesterol oxidase flavin adenine dinucleotide (FAD) prosthetic group to FADH_2 . Most cholesterol oxidases catalyze both the oxidation of cholesterol to an intermediate (cholest-5-en-3-one) and the subsequent isomerization to cholest-4-en-3-one [67]. However, the cholesterol oxidase produced by *Pseudomonas* sp. (the enzyme used in the work reported here) yields different prod-

ucts. As shown in Fig. 2, the *Pseudomonas* enzyme produces 6β -hydroperoxycholest-4-en-3-one as the major initial product of cholesterol oxidation (Fig. 2) [68,69]. This intermediate spontaneously reacts to form two stable products, cholest-4-ene-3,6-dione and 6β -hydroxycholest-4-en-3-one. FAD, the redox active center of cholesterol oxidase, is regenerated through reduction of molecular oxygen to hydrogen peroxide.

Various detergents and surfactants have been used to solubilize cholesterol during kinetic experiments, and all have been shown to affect the activity of cholesterol oxidase [70]. A number of Michaelis–Menten constants (K_m) have been reported for cholesterol oxidase in solution, ranging from 3.0 to $800 \mu\text{M}$ [50,57,71–76]. The values for K_m vary depending on the genera of bacterial enzyme used, the method used to measure reaction rate (including electrochemical methods [50,76]), pH, ionic strength, and the concentration and type of detergent used for the studies. Sampson et al. [57] have reported initial rates for the cholesterol oxidase-catalyzed turnover of cholesterol contained in vesicle membranes. The rate of cholesterol oxidation in various cell plasma membranes upon exposure to cholesterol oxidase has also been investigated [77]. However, there is apparently no literature that reports K_m for cholesterol oxidase associated with a lipid bilayer or cell plasma membrane (the enzymes native environment).

Continuous solution flow experiments allow the cholesterol content of the electrode-supported lipid bilayer membrane to be held constant during steady-state enzymatic turnover of cholesterol. The anodic current observed at the electrode provides a measure of the steady-state rate of enzymatic turnover under discrete cholesterol concentrations. This is possible because the current responses are reasonably stable (e.g., over 2 h) during continuous flow of cholesterol solution. The cholesterol concentration dependence of steady-state current is analyzed with respect to Michaelis–Menten kinetic behavior. Data are presented for exposure of low density lipoprotein solution to the electrode.

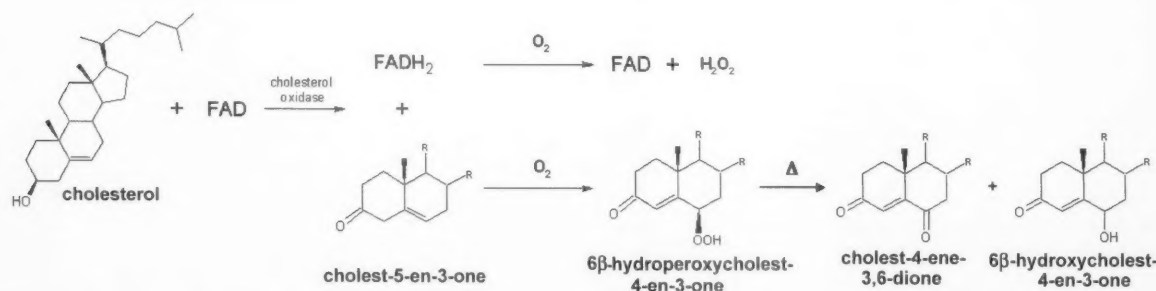


Fig. 2. Reaction sequence for oxidation of cholesterol as catalyzed by cholesterol oxidase from *Pseudomonas* sp. Cholesterol oxidase catalyzes the two electron oxidation of cholesterol through electron transfer to the FAD prosthetic group of the enzyme, yielding FADH_2 . FAD is regenerated through reduction of molecular oxygen to hydrogen peroxide. The enzyme also catalyzes further oxidation of the intermediate cholest-5-en-3-one to 6β -hydroperoxycholest-4-en-3-one, the major initial product. Over time the intermediate undergoes spontaneous conversion to more stable products (Δ indicates spontaneous reaction, R is used to abbreviate the remaining carbon skeleton that is unaffected by oxidation).

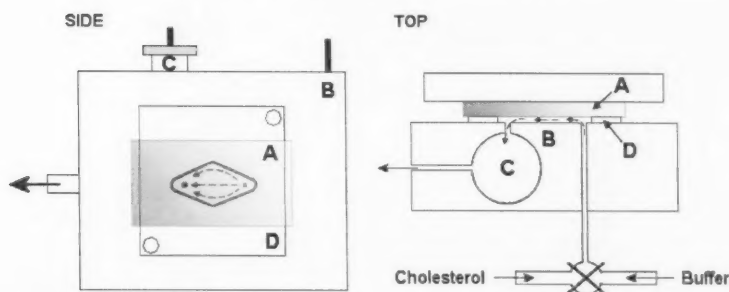


Fig. 3. Schematic diagram of the thin-layer electrochemical cell as viewed from the side and top. Dashed arrows represent flow of solution across the working electrode surface. (A) Bulk platinum sheet working electrode (shown cut-away in side view). (B) Platinum-plated auxiliary electrode and flow cell housing. (C) Ag/AgCl/KCl (1 M) reference electrode. (D) Teflon gasket that defines the shape and thickness of the fluid layer in contact with the working and auxiliary electrodes.

2. Experimental

2.1. Electrochemical cell

Amperometric data shown in Figs. 4, 7–9 were collected in a thin-layer type electrochemical flow cell. The cell (Fig. 3) was constructed using a modified liquid chromatography flow-injection apparatus (BAS, Model CC-5E). The working electrode (0.56 cm^2) is a bulk platinum sheet mounted in the flow-injection housing (Fig. 3A). The region of the cell housing that is adjacent to the working electrode is plated with platinum and serves as the auxiliary electrode (Fig. 3B). The reference electrode (Ag/AgCl/KCl (1 M), Fig. 3C) is threaded into a cavity downstream of the working electrode. A Teflon gasket ($30 \mu\text{m}$ thick) sandwiched between the platinum surfaces (Fig. 3D) defines the volume of the fluid layer in contact with the working electrode

(ca. $17 \mu\text{l}$). Liquid enters and exits the cell through two openings in the auxiliary electrode (Fig. 3, dashed arrows). The platinum working electrode was polished to a mirror finish using $1 \mu\text{m}$ diamond grit followed by rinsing, and sonicating for 10–15 min first in ethanol and then in water. The polished platinum was heated to red hot in a hydrogen flame and quenched in deionized water to remove adsorbed organic material from the electrode surface. Injection lines and cell components were flushed with ethanol and water

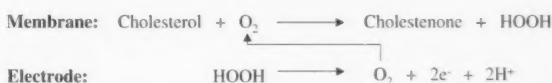


Fig. 5. Reactions for production of anodic current at the cholesterol oxidase-modified electrode. Membrane: membrane bound cholesterol oxidase catalyzes the two-electron oxidation of cholesterol by molecular oxygen producing hydrogen peroxide. Electrode: hydrogen peroxide is electrochemically oxidized at the platinum surface thus regenerating molecular oxygen.

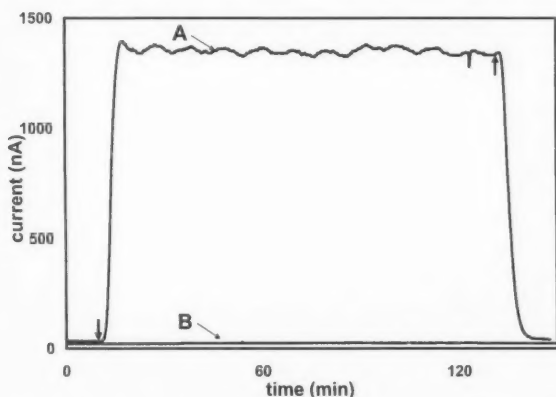


Fig. 4. Amperometric response at a cholesterol oxidase-modified electrode to $100 \mu\text{M}$ cholesterol containing 50 mM CD. (A) Trace of response for a cholesterol oxidase-modified electrode. The downward arrow (\downarrow) indicates change of flow from cholesterol-free buffer to buffer containing cholesterol. The upward arrow (\uparrow) indicates change of flow back to cholesterol-free buffer. (B) Trace of response of the same electrode before immobilization of cholesterol oxidase (control experiment).

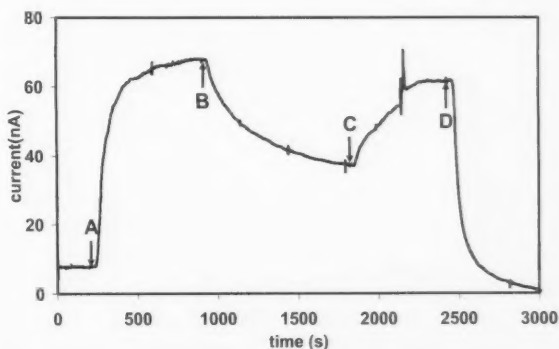


Fig. 6. Amperometric response at a cholesterol oxidase-modified electrode for exposure to aerobic (air saturated) cholesterol solution (A and C) and anaerobic (nitrogen purged) cholesterol solution (B). The current for reverting the flow to buffer containing no cholesterol is also shown (D). The cholesterol concentration is $100 \mu\text{M}$ containing 50 mM CD. The sharp noise spikes are due to changing the injection valve setting.

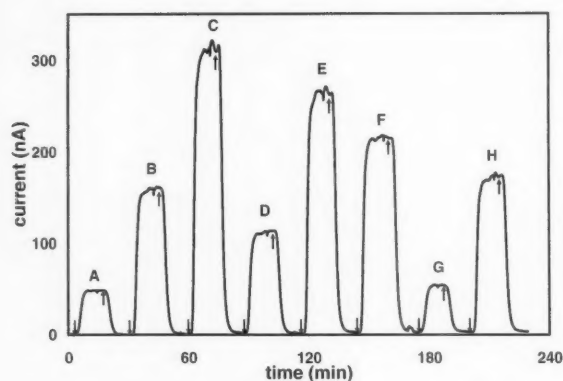


Fig. 7. Amperometric responses at a cholesterol oxidase-modified electrode to continuous flow exposure of various cholesterol concentrations containing 50 mM CD. A downward arrow (↓) indicates change of flow from buffer to cholesterol solution, and an upward arrow (↑) indicates change of flow back to buffer. (A) 10 μ M; (B) 30 μ M; (C) 60 μ M; (D) 20 μ M; (E) 50 μ M; (F) 40 μ M; (G) 10 μ M and (H) 30 μ M cholesterol. The trace was biased by -12.4 nA to zero the initial baseline.

before each set of experiments. Data shown in Fig. 6 for nitrogen purged solution were collected using a wall jet flow cell described elsewhere [35] which allowed a higher solution flow rate (0.5 ml/min). The working electrode (0.2 cm 2) was bulk platinum and the electrode cleaning procedure was that described above.

2.2. Lipid membrane preparation

Chloroform stock solutions of 1,2-dipalmitoyl-*sn*-glycero-3-phosphothioethanol (thiolipid) and 1,2-dipalmitoyl-*sn*-glycero-3-phosphocholine (DPPC) were obtained from Avanti Polar Lipids. In each case the stock was dried under nitrogen to evaporate the chloroform solvent. Lipids were dissolved in 100% ethanol and again dried under nitrogen to remove any trace chloroform. Thiolipid was dissolved in ethanol to a final concentration of 5.5 mM. This relatively high thiolipid concentration was used to minimize the time required to modify the electrode with a monolayer of thiolipid. DPPC lipid vesicles were prepared according to a procedure reported by Plant [5]. In brief, dried DPPC (2 μ moles) was dissolved in isopropanol (50 μ l) and this solution was diluted with buffer (50 mM sodium phosphate, pH 6.5) to yield to a final DPPC concentration of 2 mM.

The lipid membrane was formed on the platinum working electrodes by injecting lipid solution directly into the flow cell. The cell was filled with thiolipid (5.5 mM) and incubated for 2 h to form a self-assembled monolayer of thiolipid on the platinum working electrode (i.e., the inner lipid leaflet of the electrode-supported lipid bilayer). The cell was subsequently flushed with buffer. The DPPC vesicle solution (2 mM DPPC) was injected into the cell and incubated for 2 h to deposit the outer leaflet of the lipid bilayer membrane by vesicle spreading [5]. Electrode capacitance was

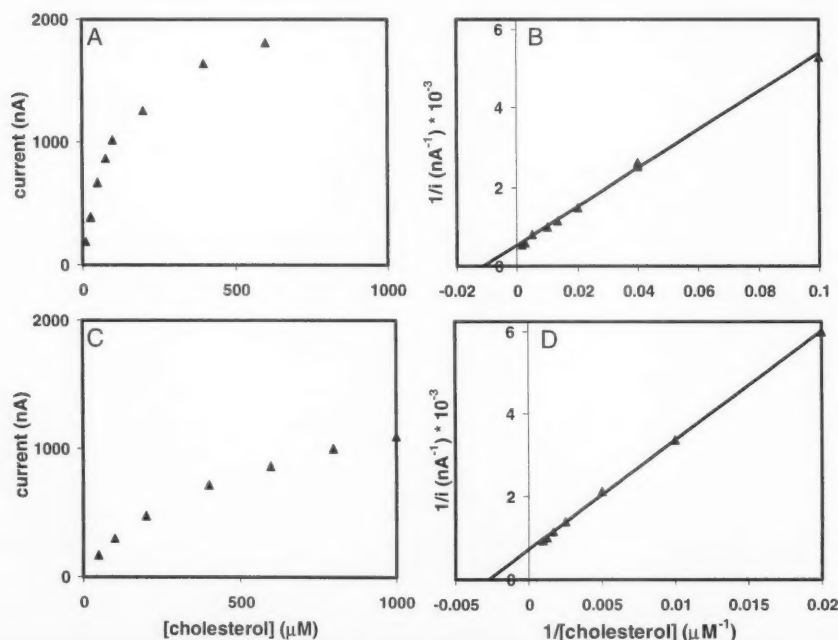


Fig. 8. (A) Plot of steady-state current vs. cholesterol concentration showing saturation behavior for an electrode on Day 2 of use. (B) Lineweaver-Burk plot of data in Fig. 8A. (C) Plot of steady-state current vs. cholesterol concentration showing saturation behavior for an electrode on Day 8 of use. (D) Lineweaver-Burk plot of data in Fig. 8C. All experiments were conducted using 50 mM CD.

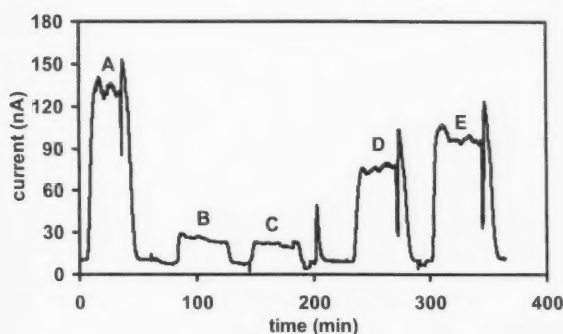


Fig. 9. Amperometric response at a cholesterol oxidase-modified electrode for exposure to 100 μ M cholesterol in buffered CD (A), buffered LDL solution (B and C), 100 μ M cholesterol (D), and buffered LDL solution containing 50 mM CD (E). The cholesterol concentration (not including cholesterol esters) of the LDL solutions is 100 μ M.

calculated from cyclic voltammograms recorded in buffer ($E = +420$ to $+620$ mV versus NHE, $v = 10$ mV/s).

2.3. Cholesterol solution preparation

Solutions of hydroxypropyl β -cyclodextrin (Cargill) in sodium phosphate buffer (50 mM, pH 6.5) were used to prepare all cholesterol solutions. Cyclodextrin (CD) is a large amphipathic molecule (molecular weight ca. 1400–1600 g/mol; 1600 g/mol was assumed in preparing CD solutions) that increases the solubility of cholesterol in aqueous solution [78]. A 20 mM ethanolic stock solution of 5-cholesten-3 β -ol (cholesterol) was prepared from powdered reagent (Sigma). The cholesterol stock was then dried under a stream of nitrogen and re-dissolved in 50 mM CD to a cholesterol concentration of 100 μ M.

For higher cholesterol concentrations, a 2 mM cholesterol solution was first prepared in 100 mM CD. This stock was then diluted to 1 mM cholesterol and 50 mM CD by adding an equal volume of buffer. Lower cholesterol concentrations were prepared by serial dilution from 100 μ M and 1 mM stocks. Buffered CD (50 mM) was used for all cholesterol dilutions. Human low density lipoprotein (LDL) was obtained from the Cleveland Clinic Foundation protein bank through collaboration with Dr. Guy Chisolm. LDL (6020 μ g/ml total cholesterol) was prepared in buffer and in buffered CD.

2.4. Amperometry

Two syringe pumps (Harvard Apparatus) were connected to the flow cell through a six-way valve to allow the flow to be alternated between buffer and cholesterol solution. One pump contained a given concentration of cholesterol in buffer. The other pump contained only buffer (no cholesterol). The flow rate for both pumps was calibrated to a true rate of 88 μ L/min, at which rate the volume of solution in the cell is exchanged over about 5 s. The working electrode was held at $+822$ mV versus NHE. This potential is suffi-

cient to oxidize H_2O_2 at a mass transfer controlled rate at platinum (data not shown).

Before each cholesterol exposure a baseline current was established by flowing cholesterol-free buffer through the cell. After a stable baseline was observed the flow was changed to cholesterol solution for a minimum of 12–15 min and then changed back to buffer. Cholesterol exposures were performed before (control) and after immobilization of cholesterol oxidase in the electrode-supported lipid membrane.

Electrode responses exhibited a rise to a steady-state plateau current for each cholesterol concentration. The reported numerical values for steady-state current were obtained by averaging data points in the plateau regions. The range of data averaged was consistent for all exposures and was defined as beginning at the first visible maximum (on a given plateau) and ending at the time when flow was changed back to buffer. Current traces were biased to set the lowest observed baseline current to zero for analysis (except for Figs. 6 and 9 which show raw data).

2.5. Cholesterol oxidase immobilization

Pseudomonas sp. cholesterol oxidase (activity of 4.8–5.3 units/mg) was obtained from Wako. A 4.0 mg/ml solution of enzyme was prepared in 50 mM phosphate buffer, pH 6.5. The cholesterol oxidase solution was injected into the flow cell and incubated overnight in order to immobilize the enzyme in the lipid bilayer membrane.

3. Results and discussion

Capacitance data indicate deposition of lipids on the platinum electrode surface. Formation of the thiolipid monolayer (inner lipid leaflet) results in a 90% decrease in capacitance from the bare platinum value. This decrease in capacitance is similar to that reported for deposition of a thiolipid monolayer on gold [79]. Alkanethiol monolayers formed on gold electrodes also result in comparable decreases in electrode capacitance [80].

The outer lipid leaflet is deposited by a vesicle fusion method [5]. Formation of the DPPC outer leaflet on the monolayer of thiolipid results in a further decrease (21%) in electrode capacitance. These data are comparable to decreases in capacitance that have been reported by other groups for deposition of outer lipid leaflets on covalently attached thiol monolayers on metal electrodes (ca. 40% decrease for deposition of a DPPC outer leaflet on a thiolipid monolayer on gold [79]). The capacitance data for deposition of both thiolipid and DPPC qualitatively indicate formation of a thiolipid/lipid bilayer membrane on the platinum electrode surface. It is noted that the structure of the membrane is not known and a lipid multi-bilayer structure could exist on regions of the electrode surface. Acoustic impedance data collected at platinum quartz crystal microbalance electrodes

indicate a mass increase roughly equal to that expected for deposition of a complete lipid bilayer membrane (data not shown). However, voltammetric studies at lipid membrane-modified platinum electrodes do not show complete blocking of ferricyanide reduction indicating the existence of defects in the membrane. The electrode surface may have regions containing a lipid multi-bilayer structure, regions of lipid bilayer, and regions of exposed bare platinum (e.g., membrane defects). In earlier work reporting immobilization of cholesterol oxidase in lipid bilayer membranes on tin-doped indium oxide electrodes [44], we hypothesized that unmodified regions of the electrode surface provided sites for electrochemical reduction of hydrogen peroxide generated by the enzyme-catalyzed reaction. The same speculation is offered here for electrochemical oxidation of hydrogen peroxide at the platinum electrode surface.

Electrodes have been prepared by exposing cholesterol oxidase to platinum electrodes modified with only a monolayer of thiolipid (i.e., no outer lipid leaflet). These electrodes did not show steady-state current for cholesterol exposures and the responses were relatively small. Additionally, electrodes were prepared using no thiolipid. In this case, bare platinum electrodes were treated with the vesicle solution for deposition of lipids and subsequently with cholesterol oxidase. Similarly, such electrodes did not show steady-state current for cholesterol exposure. Initial characterization studies for vesicle fusion on bare platinum quartz crystal microbalance electrodes suggest that a lipid multilayer is deposited. The data also suggest that initial treatment of electrodes with thiolipid allows subsequent deposition of a single outer lipid leaflet through vesicle fusion. Both steps are required to produce enzyme modified electrodes that exhibit steady-state current for exposure to cholesterol solution. The outer lipid layer provides polar lipid head groups at the membrane/solution interface that likely contribute to binding of the enzyme to the electrode-supported lipid bilayer membrane. Why the thiolipid modification step is required is not yet understood.

Anodic current is observed upon exposure of cholesterol to the cholesterol oxidase modified electrodes under continuous solution flow conditions. Fig. 4, trace A shows the current observed for changing the flow from buffer to a 100 μM cholesterol solution ($t = 7$ min) and for changing the flow back to buffer ($t = 125$ min). A current plateau (at 1350 nA) is observed during the time window (ca. 2 h) when cholesterol is exposed to the electrode (Fig. 4, trace A). The average current density for the plateau is 2.41 $\mu\text{A}/\text{cm}^2$ and the source of the low frequency noise in the current plateau is not known. The steady-state currents observed at all other electrode preparations under identical conditions are within $\pm 25\%$ of that shown in Fig. 4, trace A. Control exposures of cholesterol to electrodes modified with a lipid bilayer membrane containing no cholesterol oxidase show no response (Fig. 4, trace B). This control experiment was conducted at the same electrode used in Fig. 4, trace A, prior to immobilization of the enzyme. It is noted that cholesterol detection

limit is less than 1 μM for these electrodes. Clearly resolvable steady-state current plateaus are observed for exposures to 0.5 μM concentrations of cholesterol.

The current measured under cholesterol exposure is attributed to the electrochemical oxidation of hydrogen peroxide produced upon enzyme-catalyzed oxidation of cholesterol by molecular oxygen. Fig. 5 shows the balanced chemical equations for the oxidation of cholesterol in the membrane and for electrochemical oxidation of the generated hydrogen peroxide at the electrode surface. Note that electrochemical oxidation of hydrogen peroxide at the electrode surface regenerates molecular oxygen.

Experiments conducted under near anaerobic conditions (nitrogen purged solutions) show smaller responses (ca. 50%) compared with those observed using air saturated solutions. Fig. 6 shows the current for changing the flow from aerobic buffer to an aerobic cholesterol solution (A: 230 s) and for changing flow from aerobic cholesterol solution to anaerobic cholesterol solution (B: 900 s). The current for changing the flow back to aerobic cholesterol solution (C: 1800 s) and for changing the flow to buffer (D: 2450 s) is also shown. Exposure of anaerobic versus aerobic buffer (no cholesterol) to the cholesterol oxidase modified electrodes has no detectable effect on the baseline current (data not shown). The decrease in response for anaerobic cholesterol solution supports the electron transfer mechanism given in Fig. 5 above where oxygen is a reactant. A smaller response is expected because the concentration of oxygen (one of the reactants) in purged solution is significantly decreased.

The nonzero current observed for the nitrogen purged solution is likely due to residual oxygen (and thus electrochemical hydrogen peroxide oxidation). However, a second possibility is that the current observed for the nitrogen purged solutions reflects a contribution from direct electron transfer from the enzyme to the electrode. The idealized structural model (Fig. 1) suggests a separation distance between the FAD active site of the enzyme and the electrode surface of 30–40 Å. It is noted that electron transfer distances of up to 30 Å have been reported for zinc/ruthenium-modified myoglobins [81]. For a monolayer of enzyme on the electrode surface, the current measured under anaerobic conditions corresponds to an enzyme turnover rate of ca. 1 electron per second. Given this relatively low enzyme turnover rate (i.e., 1 electron per second), the current for nitrogen purged solutions could reflect slow direct electron transfer from the enzyme to the electrode via tunneling. It is also possible that some enzyme molecules are immobilized closer to the electrode surface than depicted by the idealized structural model (Fig. 1). However, direct electron transfer from the enzyme to the electrode is speculative and additional experiments are underway to test this hypothesis.

It is interesting to note that, upon changing the flow to anaerobic solution, the current approaches steady-state slower than for changing the flow back to aerobic solution (ca. 15 min anaerobic for versus ca. 8 min for aerobic). This could reflect depletion of oxygen in the electrode-supported

lipid bilayer membrane upon changing the flow to anaerobic solution.

Representative amperometric data for a series of cholesterol exposures (under aerobic conditions) in the range of 10–60 μM is shown in Fig. 7. The replicate cholesterol exposures (Fig. 5, responses A and G: 10 μM ; Fig. 5, responses B and H: 30 μM) indicated a slight increase in steady-state current (6–10 nA beyond the baseline drift) over the course of the experiment. Other electrodes have shown a decrease in response of similar magnitude over comparable time. Several factors may contribute to the limiting currents observed. The activity and amount of immobilized enzyme, along with the collection efficiency of hydrogen peroxide at the electrode surface, are major factors determining the steady-state currents observed in the linear cholesterol concentration range. It is not known if the rates of cholesterol partitioning into the membrane, and of lateral diffusion within the membrane, also significantly affect steady-state current.

3.1. Enzyme kinetics

The response of the cholesterol oxidase modified electrodes shows saturation behavior under higher cholesterol concentrations. The steady-state currents observed for higher cholesterol concentrations are shown for two different cholesterol oxidase-modified electrodes (up to 600 μM cholesterol for a freshly prepared electrode shown in Fig. 8A and 1000 μM for an aged electrode shown in Fig. 8C). The corresponding Lineweaver–Burk (double-reciprocal) plots are also shown (Fig. 8B and D, respectively). For both electrodes the plot of steady-state current versus cholesterol concentration is hyperbolic. At cholesterol concentrations in the range of 200–1000 μM the response deviates from linear and asymptotically approaches a limiting value.

This behavior is consistent with the Michaelis–Menten mechanism for enzyme-catalyzed reactions in which reversible binding of enzyme and substrate results in either product formation or dissociation. In this model, the rate of reaction becomes independent of substrate concentration (zero order) when all enzyme active sites are occupied by substrate. The extrapolated limiting current corresponds to the maximum velocity (V_m) that a reaction may attain under given conditions. The Michaelis constant (K_m) is the substrate concentration that yields a reaction rate that is equal to $1/2 V_m$. It is also an apparent dissociation constant for the enzyme–substrate complex.

Fig. 8A and B are for an electrode on Day 2 of study (fresh electrode) and are representative of the activity (V_m is 1820 nA and K_m is 90 μM) observed during the first few days for all electrodes. Fig. 8C and D show data for an electrode on Day 8 of study (aged electrode) and these data, compared to those in Fig. 8A and B, reflect the initial decrease in response that is observed at the cholesterol oxidase-modified electrodes (V_m is 1400 nA and K_m is 370 μM). That is, during the first week of study, K_m increases and V_m decreases. After aging, the electrodes exhibit K_m values that are in rea-

sonable agreement with the value reported for a cross-linked cholesterol oxidase film on gold (520 μM) [76].

The observed decrease in V_m (from 1820 to 1400 nA over 6 days) suggests a loss of enzyme molecules from the electrode surface and/or a decrease in activity for immobilized enzymes. The former is expected given that cholesterol oxidase has a measurable dissociation constant (K_D) of $57 \pm 21 \mu\text{M}$ for binding to mixed phospholipid/cholesterol vesicles [57]. The possibility that loss of electrode response (decreased V_m) reflects a decrease in enzyme activity is supported by the observed increase in K_m (e.g., from 90 μM for a fresh electrode on Day 2, to 370 μM for an aged electrode on Day 8), which suggests a decrease in activity for the enzyme molecules that remain immobilized on the electrode surface (it is noted that K_m is independent of enzyme concentration). The dissociation rate of enzyme from the membrane must become slow after extended exposure to buffer, given that electrodes have shown responses for up to 60 days. The electrodes retain about 5% of the original response after this time. Re-exposing aged electrodes to enzyme solution does not restore any electrode activity for amperometric cholesterol detection. The decrease in electrode response could be coupled to changes that occur in the structure of the lipid bilayer membrane (resulting in irreversible desorption of enzyme) and the conformation of the enzyme (the enzyme may denature over time). That is, the integrity of the lipid bilayer membrane structure upon electrode ageing is not known. It may be possible to minimize the loss of electrode activity that is observed over days by optimizing the storage conditions (e.g., storing the electrodes at 4 °C).

3.2. Lipoprotein experiments

Experiments have been conducted to evaluate the ability of the electrodes to detect cholesterol contained in LDL solutions. Fig. 9 shows the electrode response to 100 μM cholesterol in buffered CD (trace A), replicate exposures to buffered LDL solution (traces B and C), 100 μM cholesterol in buffered CD (trace D; replicate of A), and LDL in buffered CD (trace E). The responses for exposure to buffered LDL reflect detection of aqueous phase cholesterol (i.e., cholesterol not contained in the lipid monolayer sheath of LDL). The concentration of cholesterol (not including cholesterol esters) in the buffered LDL solution is 100 μM (including aqueous phase and LDL resident cholesterol). The smaller response for the LDL solution (traces B and C) compared to 100 μM cholesterol in buffered CD (trace A) is consistent with the notion that LDL resident cholesterol is not directly detected at the electrode. The equilibrium that exists between cholesterol contained in the lipid monolayer sheath of LDL and the aqueous phase lies largely towards LDL resident cholesterol. That is, much of the cholesterol in the LDL solution is contained within the LDL particles and this LDL resident cholesterol does not directly partition into the electrode-supported lipid bilayer membrane.

Electrode response to 100 μM cholesterol in buffered CD was measured before (trace A) and after (trace D) exposure of the electrode to LDL solution. These data indicate that exposure of the electrode to LDL results in a substantial decrease in electrode activity (ca. 50% for this experiment). The decrease in electrode activity may be due to adsorption of LDL on the electrode surface. It is also noted that the second LDL response (trace C) is slightly smaller than the first LDL response (trace B) indicating a decrease in electrode activity.

Data are also shown for electrode response to LDL in buffered CD (trace E). The increased response (ca. six times larger) compared to the response measured for the same LDL concentration in buffer containing no CD (traces B and C) reflects a higher aqueous phase cholesterol concentration due to the increased solubility of cholesterol in the aqueous phase of the buffered CD solution.

4. Conclusions

Platinum electrodes modified with thiolipid/lipid bilayer membranes have been prepared to immobilize cholesterol oxidase and to sequester cholesterol from solution. In this system the close proximity of cholesterol oxidase to the electrode surface facilitates electrochemical detection of hydrogen peroxide generated by the enzyme. Flow exposure of aerobic cholesterol solution to the cholesterol oxidase-modified electrodes indicates that the enzyme resides in a conformation capable of oxidizing cholesterol. The data indicate that the reaction follows the Michaelis–Menten kinetic model and that the enzymatic activity decreases over days. Importantly, this work provides a measure of the K_m for cholesterol oxidase associated with a supported lipid bilayer membrane that may be a better model for the natural environment of the enzyme, as compared with methods that involve detergents or covalent immobilization of the enzyme. Detection of cholesterol in lipoprotein solution suggests that this electrode architecture may be useful in clinical sensing applications.

Acknowledgements

A.D. acknowledges a student fellowship provided by Eveready Battery Company Inc. and the Ernest B. Yeager Center for Electrochemical Sciences at Case Western Reserve University. Helpful discussion with Professors Barry Miller, Daniel A. Scherson, and Morris Burke are acknowledged. Revisions and experiments done by Jonathan Ipsaro are acknowledged, along with experiments conducted by Latifa Odom and Carrie McDonough.

References

- [1] R. Guidelli, G. Aloisi, L. Becucci, A. Dolfi, M.R. Moncelli, F.T. Buoninsegni, *J. Electroanal. Chem.* 504 (2001) 1.
- [2] E.K. Sinner, W. Knoll, *Curr. Opin. Chem. Biol.* 5 (2001) 705.
- [3] E. Sackmann, *Science* 271 (1996) 43.
- [4] D.M. Tiede, *Biochim. Biophys. Acta* 811 (1985) 357.
- [5] A.L. Plant, *Langmuir* 15 (1999) 5128.
- [6] A.L. Plant, *Langmuir* 9 (1993) 2764.
- [7] H.T. Tien, Z. Salamon, *Biochem. Bioenerg.* 22 (1989) 211.
- [8] A.L. Ottova, H.T. Tien, *Bioelectrochem. Bioenerg.* 42 (1997) 141.
- [9] H.T. Tien, A.L. Ottova, *Electrochim. Acta* 43 (1998) 3587.
- [10] M.L. Wagner, L.K. Tamm, *Biophys. J.* 79 (2000) 1400.
- [11] C. Steinem, A. Janshoff, W.P. Ulrich, M. Sieber, H.J. Galla, *Biochim. Biophys. Acta* 1279 (1996) 169.
- [12] L. Ding, J. Li, S. Dong, E. Wang, *J. Electroanal. Chem.* 416 (1996) 105.
- [13] J.T. Groves, N. Ulman, S.G. Boxer, *Science* 275 (1997) 651.
- [14] A.L. Parikh, J.D. Beers, A. Shreve, B. Swanson, *Langmuir* 15 (1999) 5369.
- [15] E.E. Ross, B. Bondurant, T. Spratt, J.C. Conboy, D.F. O'Brien, S.S. Saavedra, *Langmuir* 17 (2001) 2305.
- [16] Y. Kanzaki, M. Hayashi, C. Minami, Y. Inoue, M. Kogure, Y. Watanabe, T. Tanaka, *Langmuir* 13 (1997) 3674.
- [17] Z. Wu, B. Wang, Z. Cheng, X. Yang, S. Dong, E. Wang, *Biosens. Bioelectron.* 16 (2001) 47.
- [18] H. Gao, G.A. Luo, J. Feng, A.L. Ottova, H.T. Tien, *J. Photochem. Photobiol. B* 59 (2000) 87.
- [19] H. Hillebrandt, G. Wiegand, M. Tanaka, E. Sackmann, *Langmuir* 15 (1999) 8451.
- [20] G. Wiegand, N.A. Layton, H. Hillebrandt, E. Sackmann, P. Wagner, *J. Phys. Chem. B* 106 (2002) 4245.
- [21] L. Huang, *Biochemistry* 24 (1985) 29.
- [22] Z. Salamon, H.A. Macleod, G. Tollin, *Biochim. Biophys. Acta* 1331 (1997) 131.
- [23] M. Nakanishi, *FEBS Lett.* 176 (1984) 385.
- [24] Z. Salamon, G. Tollin, *Bioelectrochem. Bioenerg.* 25 (1991) 447.
- [25] Z. Salamon, G. Tollin, *Arch. Biochem. Biophys.* 294 (1992) 382.
- [26] Z. Salamon, F.K. Gleason, G. Tollin, *Arch. Biochem. Biophys.* 299 (1992) 193.
- [27] Z. Salamon, J.T. Hazzard, G. Tollin, *Proc. Natl. Acad. Sci. USA* 90 (1993) 6420.
- [28] B. Fischer, S.P. Heyn, M. Egger, H.E. Gaub, *Langmuir* 9 (1993) 136.
- [29] P. Bianco, J. Haladjian, *J. Electroanal. Chem.* 367 (1994) 79.
- [30] P. Bianco, J. Haladjian, *Electrochim. Acta* 39 (1994) 911.
- [31] Z. Zhang, A.E.F. Nassar, Z. Lu, J.B. Schenkman, J.F. Rusling, *J. Chem. Soc. Faraday Trans.* 93 (1997) 1769.
- [32] O. Pierrat, N. Lechat, C. Bourdillon, J.M. Laval, *Langmuir* 13 (1997) 4112.
- [33] R. Naumann, A. Jonczyk, C. Hampel, H. Ringsdorf, W. Knoll, N. Bunjes, P. Graber, *Bioelectrochem. Bioenerg.* 42 (1997) 241.
- [34] J.K. Cullison, F.M. Hawkrige, N. Nakashima, S. Yoshikawa, *Langmuir* 10 (1994) 877.
- [35] J.D. Burgess, M.C. Rhoten, F.M. Hawkrige, *Langmuir* 14 (1998) 2467.
- [36] J.D. Burgess, V.W. Jones, M.D. Porter, M.C. Rhoten, F.M. Hawkrige, *Langmuir* 14 (1998) 6628.
- [37] P.L. Edmiston, S.S. Saavedra, *Biophys. J.* 74 (1998) 999.
- [38] P.L. Edmiston, S.S. Saavedra, *J. Am. Chem. Soc.* 120 (1998) 1665.
- [39] J.D. Burgess, M.C. Rhoten, F.M. Hawkrige, *J. Am. Chem. Soc.* 120 (1998) 4488.
- [40] M.C. Rhoten, J.D. Burgess, F.M. Hawkrige, *Electrochim. Acta* 45 (2000) 2855.
- [41] M.C. Rhoten, J.D. Burgess, F.M. Hawkrige, *J. Electroanal. Chem.* 534 (2002) 143.
- [42] J.D. Burgess, F.M. Hawkrige, in: A. Bajter-Toth, J.Q. Chambers, *Electroanalytical Methods of Biological Materials*, New York, NY, 2002, p. 109.
- [43] A. Dolfi, F.T. Buoninsegni, M.R. Moncelli, R. Guidelli, *Langmuir* 18 (2002) 6345.
- [44] A. Devadoss, J.D. Burgess, *Langmuir* 18 (2002) 9617.

- [45] I. Karube, K. Hara, H. Matsuoka, S. Suzuki, *Anal. Chim. Acta* 139 (1982) 127.
- [46] U. Wollenberger, M. Kuhn, F. Scheller, V. Deppmeyer, M. Janchen, *Bioelectrochem. Bioenerg.* 11 (1983) 307.
- [47] M. Masoom, A. Townshend, *Anal. Chim. Acta* 174 (1985) 293.
- [48] B.F.Y. Yon Hin, C.R. Lowe, *Sens. Actuators B* 7 (1992) 339.
- [49] J. Motonaka, L.R. Faulkner, *Anal. Chem.* 65 (1993) 3258.
- [50] H. Wang, S. Mu, *Sens. Actuators B* 56 (1999) 22.
- [51] J.-C. Vidal, E. Garcia-Ruiz, J.-R. Castillo, *Electroanalysis* 13 (2001) 229.
- [52] M.K. Ram, P. Bertoncello, H. Ding, S. Paddeu, C. Nicolini, *Biosens. Bioelectron.* 16 (2001) 849.
- [53] T. Abe, Y.Y. Lau, A.G. Ewing, *Anal. Chem.* 64 (1992) 2160.
- [54] J.B. Meyerhoff, M.A. Ewing, A.G. Ewing, *Electroanalysis* 11 (1999) 308.
- [55] N. Matsumoto, X. Chen, G.S. Wilson, *Anal. Chem.* 74 (2002) 362.
- [56] J. Li, A. Vrielink, P. Brick, D.M. Blow, *Biochemistry* 32 (1993) 11507.
- [57] N.S. Sampson, I.J. Kass, K.B. Ghoshroy, *Biochemistry* 37 (1998) 5770.
- [58] K.B. Ghoshroy, W. Zhu, N.S. Sampson, *Biochemistry* 36 (1997) 6133.
- [59] X. Chen, D.E. Wolfgang, N.S. Sampson, *Biochemistry* 39 (2000) 13383.
- [60] P.G. Atrat, B. Wagner, M. Wagner, J. Schumann, *J. Steroid Biochem. Mol. Biol.* 42 (1992) 193.
- [61] Y. Lange, *J. Lipid Res.* 33 (1992) 315.
- [62] M.C. Phillips, W.J. Johnson, G.H. Rothblat, *Biochim. Biophys. Acta* 906 (1987) 223.
- [63] G.H. Rothblat, M.L. Ilera-Moya, V. Afger, G. Kellner-Weibel, D.L. Williams, M.C. Phillips, *J. Lipid Res.* 40 (1999) 781.
- [64] P.F. Fahey, D.E. Koppel, L.S. Barak, D.E. Wolf, E.L. Elson, W.W. Webb, *Science* 195 (1977) 305.
- [65] P. Stroeve, I. Miller, *Biochim. Biophys. Acta* 401 (1975) 157.
- [66] E. Györfy, B. Wetzler, U.B. Sleytr, A. Sinner, A. Offenhausser, W. Knoll, *Langmuir* 15 (1999) 1337.
- [67] J. MacLachlan, A.T.L. Wotherspoon, R.O. Ansell, C.J.W. Brooks, *J. Steroid Biochem. Mol. Biol.* 72 (2000) 169.
- [68] J.I. Teng, L.L. Smith, *Steroids* 61 (1996) 627.
- [69] N. Doukyu, R. Aono, *Biochem. J.* 341 (1999) 621.
- [70] L. Pollegioni, G. Gadda, D. Ambrosius, S. Ghisla, M.S. Pilone, *Appl. Biochem.* 30 (1999) 27.
- [71] Y. Yin, N.S. Sampson, A. Vrielink, P.I. Lario, *Biochemistry* 40 (2001) 13779.
- [72] L. Pollegioni, G. Wels, M.S. Pilone, S. Ghisla, *Eur. J. Biochem.* 264 (1999) 140.
- [73] F. Cheillan, H. Lafont, E. Termine, F. Fernandez, P. Sauve, G. Lesgards, *Biochim. Biophys. Acta* 999 (1989) 233.
- [74] Y.A. Aleksandrovskii, V.N. Titov, *Biokhimiya* 58 (1993) 1408.
- [75] S. Lee, H. Rhee, W. Tae, J. Shin, B. Park, *Appl. Microbiol. Biotechnol.* 31 (1989) 542.
- [76] T. Nakaminami, S. Ito, S. Kuwabata, H. Yoneyama, *Anal. Chem.* 71 (1999) 1068.
- [77] E.L. Crockett, J.R. Hazel, *J. Exp. Zool.* 271 (1995) 190.
- [78] M.P. Haynes, M.C. Phillips, G.H. Rothblat, *Biochemistry* 39 (2000) 4508.
- [79] H. Lang, C. Duschl, H. Vogel, *Langmuir* 10 (1994) 197.
- [80] M.D. Porter, T.B. Bright, D. Allara, C.E.D. Chidsey, *J. Am. Chem. Soc.* 109 (1987) 3559.
- [81] A.W. Axup, M. Albin, S.L. Mayo, R.J. Crutchley, H.B. Gray, *J. Am. Chem. Soc.* 110 (1988) 435.

Simultaneous determination of nickel(II) and cobalt(II) by square wave adsorptive stripping voltammetry on a rotating-disc bismuth-film electrode

Manolis Morfobos, Anastasios Economou*, Anastasios Voulgaropoulos

Laboratory of Analytical Chemistry, Department of Chemistry, Aristotle University of Thessaloniki, 54124 Thessaloniki, Greece

Received 13 January 2004; received in revised form 13 May 2004; accepted 13 May 2004

Available online 13 July 2004

Abstract

This work reports the use of square-wave adsorptive stripping voltammetry (SWAdSV) for the simultaneous determination of Ni(II) and Co(II) on a rotating-disc bismuth-film electrode (BFE). The metal ions in the non-deoxygenated sample were complexed with dimethylglyoxime (DMG) and the complexes were accumulated by adsorption on the surface of the BFE. The stripping step was carried out by using a square-wave potential–time voltammetric excitation signal. Electrochemical cleaning of the bismuth film was employed, enabling the same bismuth film to be used for a series of measurements. The experimental variables (choice of the working electrode substrate, the presence of oxygen, the DMG concentration, the buffer concentration, the preconcentration potential, the accumulation time, the rotation speed and the SW parameters) as well as potential interferences were investigated and the figures of merit of the methods were established. Using the selected conditions, the 3σ limits of detection were 70 ng l^{-1} for Co(II) and 100 ng l^{-1} for Ni(II) (for 300 s of preconcentration) and the relative standard deviations were 2.3% for Co(II) and 3.9% for Ni(II) at the $2 \mu\text{g l}^{-1}$ level ($n = 8$). Finally, the method was applied to the determination of nickel and cobalt in real samples with satisfactory results.

© 2004 Elsevier B.V. All rights reserved.

Keywords: Nickel(II); Cobalt(II); Square-wave adsorptive stripping voltammetry; Bismuth-film electrode

1. Introduction

Adsorptive stripping voltammetry (AdSV) has been established as a reliable trace metal analysis technique applicable to different samples [1]. Traditionally the hanging mercury drop electrode (HMDE) has been used as the working electrode in AdSV but this electrode, despite its sensitivity, has many drawbacks that make it unsuitable for many applications [2]. Mercury film electrodes (MFE's), prepared by electroplating a thin film of mercury on a suitable substrate, have in many cases replaced the HMDE in AdSV with satisfactory results [2]. The advantages of MFE's over the HMDE are the precise mass-transfer of the analyte species to the electrode surface, their simplicity in terms of construction and maintenance, their mechanical stability and the scope for different cell configurations [3]. In particular,

it has been possible to determine Ni(II) and Co(II) by AdSV after complexation with different dioximes by employing MFE's in different batch and flow–cell configurations [4–8].

However, the increased risks associated with the use, manipulation and disposal of metallic mercury or mercury salts have led some countries to completely ban mercury [9], and, as a result, new electrode materials with properties comparable to those of mercury are sought. Recently, bismuth-film electrodes BFE's, consisting of a thin bismuth film deposited on a suitable substrate, have been shown to offer comparable performance to MFE's in anodic stripping voltammetry (ASV) [10–13]. It has been shown that BFE's maintain all the advantages of MFE's and, at the same time, are environmentally friendly as the toxicity of bismuth and its salts is negligible. So far, the area of AdSV on BFE's remains largely unexplored, since neither does a systematic study exist on the different parameters that affect the determination of metals (including Ni(II) and Co(II)) on BFE's by AdSV, neither have applications to real samples been reported. Three short communications that have pub-

* Corresponding author.

E-mail address: aeconomou@chem.auth.gr (A. Economou).

lished, investigating the feasibility of utilising BFE's in the determination of Ni(II) or Co(II) by adsorptive stripping analysis, only reported preliminary results [14–16].

In this work, the suitability of a rotating-disc BFE for square-wave AdSV (SWAdSV) has been investigated for the simultaneous trace determination of Ni(II) and Co(II) after complexation with dimethylglyoxime (DMG). All the relevant experimental parameters associated with the analysis were systematically investigated for the first time with the view to analyse samples with different Ni(II)–Co(II) concentration ratios. The utility of the method developed was demonstrated for the simultaneous determination of Ni(II) and Co(II) by SWAdSV on BFE's in different real samples for the first time.

2. Experimental

2.1. Instrumentation

Voltammetric measurements were performed with a home-made potentiostat interfaced to a PC through a 6025E PCI multi-purpose interface card (National Instruments, Austin, TX USA). The experimental sequence was fully automated and controlled by the PC using a control application developed in LabVIEW 5.1 (National Instruments) as reported previously [17].

The voltammetric cell was a standard 50 ml glass vial (Metrohm, Switzerland) equipped with a Ag/AgCl reference electrode and a Pt counter electrode. An electrode rotator (Metrohm 628-10) or a magnetic stirrer were used during the preconcentration and cleaning steps.

The glassy carbon (GC) working electrode (3 mm in diameter) was from Metrohm. Before use, the electrode was polished with a water slurry of 0.3 μm Al_2O_3 and rinsed with ethanol and water. A carbon paste (CP) electrode was prepared by mixing thoroughly 1.5 g of graphite powder with 1.2 ml of Nujol and filling a syringe-type holder with the resulting paste; the diameter of the active surface was 5 mm. A smooth surface was formed by gently rubbing the electrode on a clean filter paper. The impregnated graphite (IG) electrode (6 mm in diameter) was donated by M. Halama (University of Cosice, Slovakia) and was polished by rubbing on a clean filter paper before use.

2.2. Reagents and glassware

All the chemicals were of analytical grade and purchased from Merck (Darmstadt, Germany). De-ionised water was used throughout. Working metal ion solutions were prepared from 1000 mg l^{-1} atomic absorption standard solutions after appropriate dilution with de-ionised water. The stock supporting electrolyte was an ammonia buffer (1 mol l^{-1} in total ammonium species, pH 9.2). A 0.1 mol l^{-1} solution of dimethylglyoxime (DMG) was prepared by dissolving the appropriate amount of DMG in absolute ethanol. The

bismuth and mercury plating solutions were 100 mg l^{-1} Bi(III) or Hg(II) in acetate buffer (1 mol l^{-1} in total acetate species, pH 4.5). A 1000 mg l^{-1} stock solution of Triton X-100 (BDH, Poole, England) was prepared in water.

2.3. Procedure

2.3.1. Preparation of the samples

Iron ore and duraluminium were purchased from Hoepfner Gebr. (Hamburg, Germany); their certified nickel content was 0.14 and 0.10% (w/w), respectively. Iron ore or duraluminium (2.00 g) were dissolved in 10 ml of 6 mol l^{-1} HNO_3 under mild heating and this solution was diluted to 100 ml. For the voltammetric analysis, 100 μl of the sample were placed into 20 ml of 0.2 mol l^{-1} ammonia buffer (pH 9.2) and the determination was carried out as described in the following section.

The certified river water sample SLRS-2 (NIRC) was purchased from the LGC (Teddington, UK). For the voltammetric analysis, 2.0 ml of the 1 mol l^{-1} ammonia buffer and 18.0 ml of the sample were placed in the cell and the determination was carried out as described in the following section.

2.3.2. Determination of Ni(II) and Co(II)

The bismuth film was preplated from the 100 mg l^{-1} Bi(III) solutions for 5 min on the working electrode at -1.0 V. The electrodes were immersed into the sample solution (20.0 ml), the sample was spiked with the required volume of the DMG solution (to give the desired final DMG concentration) and the preconcentration was carried out at the selected preconcentration potential under stirring or rotation of the electrode. After accumulation, the solution was left to equilibrate for 10 s and a cathodic SW scan to a final potential of -1.3 V was applied on the working electrode while the voltammogram was recorded. After the scan, the bismuth film was cleaned of the remaining adsorbed complexes by keeping the potential of the electrode at -1.3 V for 10 s under rotation or stirring. After the cleaning step, standard additions of Ni(II) and/or Co(II) were made as required and the measurement procedure repeated on the same bismuth film. After a series of measurements the bismuth film was removed by wiping the electrode with a wet tissue.

3. Results and discussion

3.1. Cyclic voltammetry

Two successive cyclic voltammograms (in the range from -0.7 to -1.3 V) of a solution containing Ni(II) and Co(II) in the presence of DMG after preconcentration on a BFE are shown in Fig. 1. The first cathodic scan (Fig. 1 (1)) revealed two peaks, at -0.99 and -1.13 V arising from the

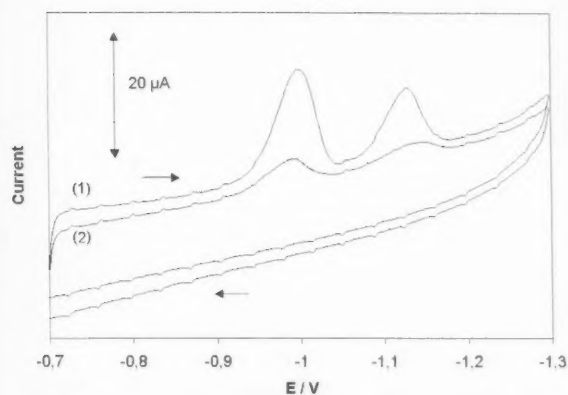


Fig. 1. Two successive cyclic voltammograms in a solution containing $10 \mu\text{g l}^{-1}$ of Ni(II) and Co(II) after preconcentration for 60 s on a BFE. DMG concentration: 0.08 mmol l^{-1} ; deposition potential: -0.7 V ; supporting electrolyte: ammonia buffer pH 9.2; potential scan rate: 50 mV s^{-1} ; electrode rotation speed: 500 rpm.

reduction of the Ni(II) and Co(II), respectively, in their complexes with DMG which were adsorbed on the BFE. No peaks were observed in the anodic scan, suggesting that the reduction of the complexes was an irreversible process. Fast desorption of the complexes from the electrode surface was indicated by the lower peaks obtained in the second cathodic scan (Fig. 1(2)) that immediately followed the first scan. Irreversibility of the reduction process was also implied by the shift of peak potentials to more negative values upon increasing the scan rate.

3.2. Choice of the working electrode—comparison between BFE and MFE in the presence of dissolved oxygen

Three carbon materials were studied as substrates for the bismuth film: GC, CP and IG. A comparison of the voltammograms of a solution containing Ni(II) and Co(II) obtained on these substrates, after preplating with a bismuth film, is illustrated in Fig. 2. The GC electrode (Fig. 2(a)) produced the flattest and less noisy baseline as well as the highest current density, followed by the IG electrode (Fig. 2(b)) and the CP electrode (Fig. 2(c)). As a result, the GC electrode was selected for further work.

The effect of dissolved oxygen was studied by performing AdSV analysis in a solution containing Ni(II) and Co(II) on both a BFE and a MFE without solution deoxygenation. As demonstrated in Fig. 2, while the BFE produced well defined and sharp peaks (Fig. 2(a)), the peaks on the MFE (Fig. 2(d)) (and especially the Ni peak) were distorted due to the underlying oxygen background. Moreover, there was no statistically significant difference between peak heights in deoxygenated and non-deoxygenated solutions on the BFE. The performance of the BFE in unpurged solutions was a significant advantage over the MFE since the time-consuming deoxygenation step was obsolete. Thus, for the rest of this

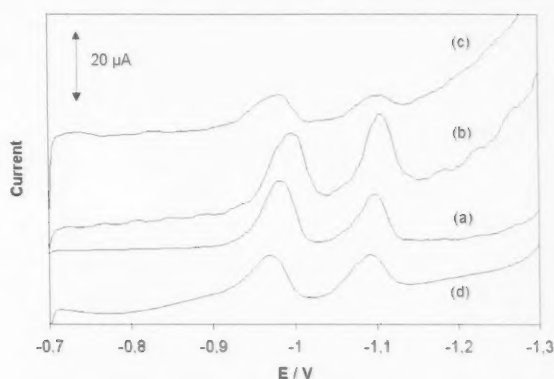


Fig. 2. SW voltammograms in a solution containing $10 \mu\text{g l}^{-1}$ of Ni(II) and Co(II) without deoxygenation after preconcentration for 120 s on: (a) a BFE plated on GC; (b) a BFE plated on IG; (c) a BFE plated on CP; and (d) an MFE plated on GC. SW frequency 25 Hz; scan increment: 2 mV; pulse height: 40 mV; other conditions as in Fig. 1.

work direct measurements of samples without solution purging was adopted.

3.3. Buffer concentration and DMG concentration

The effect of concentration of the ammonia buffer on the stripping responses in a solution containing Ni(II) and Co(II) was examined in the range $0.05\text{--}0.5 \text{ mol l}^{-1}$. It was found that this parameter had an effect on the resolution between the Ni and Co peaks and the absolute peak height of Ni while the Co peak height was not affected. In particular, the resolution between the Ni and Co peaks and the Ni peak height increased with increasing buffer concentration up to 0.2 mol l^{-1} and remained constant for higher concentrations. This general dependence was also observed for AdSV on mercury drop electrodes [18], but no similar study was conducted on MFE's. Indeed, the use of a low buffer concentration of 0.01 mol l^{-1} might account for the limited resolution between the Ni and Co peaks observed in previous work on BFE's [15]. Thus, a buffer concentration of 0.2 mol l^{-1} was adopted for subsequent experiments; higher concentrations were avoided to minimize the blank values.

The effect of the DMG concentration on the Ni and Co peak heights in a solution containing Ni(II) and Co(II) was investigated in the range $0.01\text{--}0.25 \text{ mmol l}^{-1}$ and is illustrated in Fig. 3(a). At low DMG concentrations, both the peaks increased with increasing DMG concentration. However, the Ni peak height essentially stabilized for DMG amount concentrations higher than 0.05 mmol l^{-1} . On the contrary, the Co peak height increased almost linearly up to a DMG concentration of 0.15 mmol l^{-1} and still continued to increase at higher DMG concentration but at a lower rate. This behaviour was similar to that observed in the case of MFE's [4]. This sharply differentiated response in the presence of varying concentrations of DMG could be exploited for the simultaneous determination of Ni and Co in cases

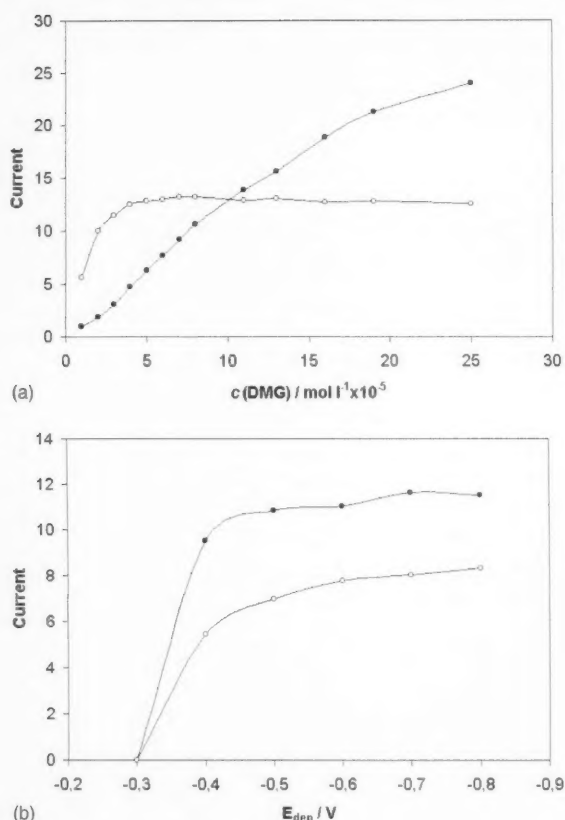


Fig. 3. Effect of: (a) the DMG concentration on the Ni (○) and Co (●) peak heights in a solution containing $10 \mu\text{g l}^{-1}$ of Ni(II) and Co(II); and (b) the preconcentration potential on the Ni (○) and Co (●) peak heights in a solution containing $5 \mu\text{g l}^{-1}$ of Ni(II) and Co(II), after preconcentration for 120 s on a BFE. DMG concentration: 0.15 mmol l^{-1} . Other conditions as in Figs. 1 and 2.

at greatly varying mass concentration ratio, as will be discussed below.

3.4. Deposition potential

The effect of the preconcentration potential on the peak heights on Ni and Co in a solution containing Ni(II) and Co(II) was studied in the range from -0.3 to -0.8 V and is shown in Fig. 3(b). The adsorption of the both metal–DMG complexes was negligible at -0.3 V ; this rather positive potential also marked the start of the reduction of the bismuth coating. The degree of adsorption increased as the potential became more negative than -0.3 V and the height of both peaks almost stabilized at potential more negative than -0.6 V . This observation contrast sharply with the observed behavior of the DMG complexes of the Ni and Co on the MFE where the Ni peak exhibited a relative insensitivity towards the preconcentration potential and the Co peak a strong increasing tendency at more negative potentials [4].

3.5. Preconcentration time and electrode rotation speed

For the linearised part of the Langmuir adsorption isotherm and for an adsorption step controlled by mass-transport of the adsorbate, it has been shown previously that the surface concentration of the adsorbate species (and consequently the peak current) will increase (though not linearly) with increasing preconcentration time and mass-transfer coefficient until the saturation surface concentration is gradually reached [19]. Thus, increasing the values of these parameters was expected to have an net enhancing effect on the stripping peak heights.

The effect of the preconcentration time on the stripping peak heights for Ni and Co heights in a solution containing 1 and $5 \mu\text{g l}^{-1}$ of Ni(II) and Co(II) in the range 0–520 s is illustrated in Fig. 4A (a and b). The peak currents increased initially almost linearly with increasing deposition time and at higher deposition times the plots for both metals started to level-off as the equilibrium surface concentration of the adsorbed complexes was approached. As expected for the linearised part of the Langmuir adsorption isotherm, the peak currents corresponding to the saturation surface concentration for both complexes were lower at lower solution concentrations of the metals. It was also interesting to note that the plot for Co exhibited a greater slope indicating that the use of longer deposition times caused a greater enhancement of the Co peak. The use of a rotating-disk electrode for the preconcentration step greatly enhances the mass-transfer efficiency during preconcentration and ensures more reproducible mass-transfer conditions than stirring of the solution. The effect of the electrode rotation speed on the stripping peak heights for Ni and Co heights in a solution containing 1 and $5 \mu\text{g l}^{-1}$ of Ni(II) and Co(II) in the range 500–3000 rpm is illustrated Fig. 4B (a and b). For the rotating disk electrode, as the electrode rotation speed increased, so did the mass-transfer coefficient as expected from theory [19,20] and a clear increase in the peak heights for Ni and Co was observed.

3.6. Square-wave parameters

The SW parameters that were investigated were the frequency, the pulse height and the pulse increment in a solution containing Ni(II) and Co(II). The effect of frequency and the scan increment was studied in the range 12.5–100 Hz and 1–16 mV, respectively. The peak heights for both Ni and Co increased with SW frequency due to the increase in the effective scan rate but at frequencies higher than 50 Hz the background slope deteriorated. This was attributed to the shorter pulse widths associated with higher frequencies that did not allow sufficient decay of the capacitive current. Increasing the scan increment caused an increase in the peak heights of both metals since the effective scan rate was increased. However, the resolution between the two peaks was compromised at higher scan increments. As the reduction of Ni and Co complexes with DMG was an irreversible process,

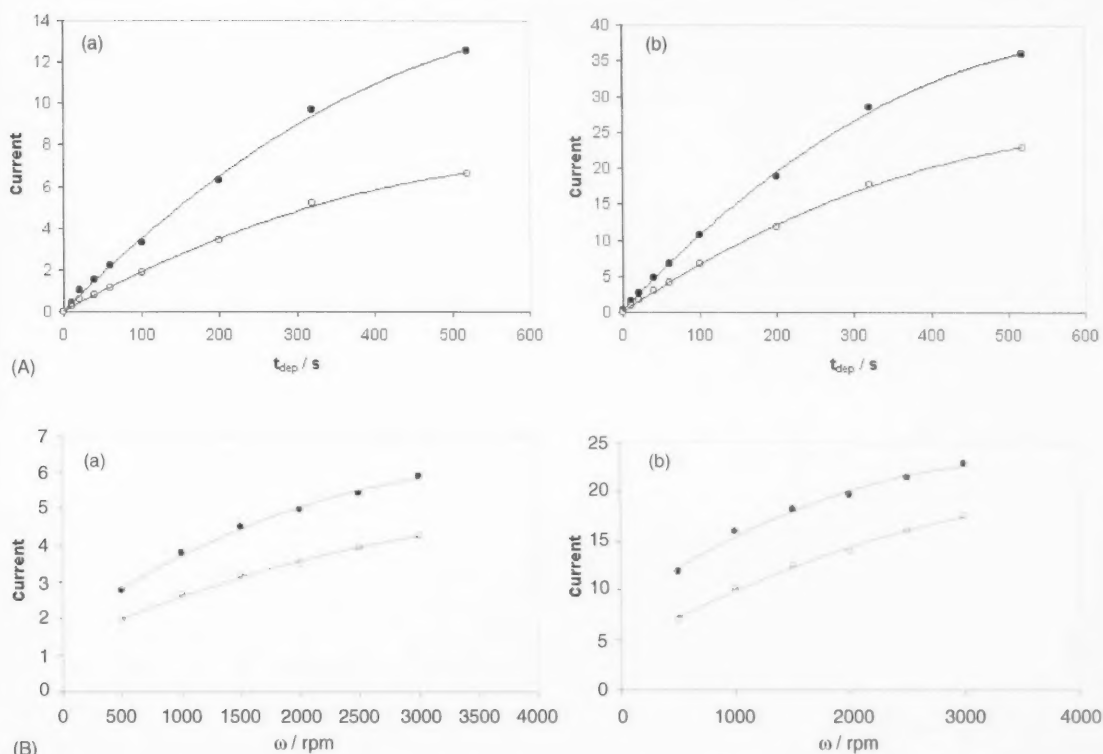


Fig. 4. Effect of (A) the preconcentration time, and; (B) the electrode rotation speed, on the Ni (○) and Co (●) peak heights in a solution containing: (a) $1 \mu\text{g l}^{-1}$ of Ni(II) and Co(II); and (b) $5 \mu\text{g l}^{-1}$ of Ni(II) and Co(II). Other conditions as in Fig. 3.

increase in the effective scan rate (caused by an increase in either the frequency or the scan increment) resulted in a shift of the peak potentials to the negative direction.

The effect of the pulse height was examined in the range 10–80 mV. The peaks for Ni and Co increased with increasing pulse height and, at the same time, were shifted to the positive direction.

3.7. Figures of merit

Calibration graphs for the simultaneous determination of Ni(II) and Co(II) were constructed for four concentration ranges ($0.5\text{--}5 \mu\text{g l}^{-1}$, $1\text{--}10 \mu\text{g l}^{-1}$, $2\text{--}20 \mu\text{g l}^{-1}$ and $5\text{--}50 \mu\text{g l}^{-1}$) at different preconcentration times. A series of voltammograms for the concentration range $1\text{--}14 \mu\text{g l}^{-1}$ of Ni(II) and Co(II) is illustrated in Fig. 5(a). The limits of detection were 100 ng l^{-1} for Ni(II) and 70 ng l^{-1} for Co(II) at the 3σ level (for 300 s accumulation time) and the relative standard deviations were 2.3% for Co(II) and 3.9% for Ni(II) at the $2 \mu\text{g l}^{-1}$ level ($n = 8$). The limit of detection for Ni(II) was dictated by the blank values resulting from impurities in the DMG and the ammonia buffer supporting electrolyte. These limits of detection were consistent with, or even better than, the ones obtained with MFE's [4,7].

As the relative concentrations of Ni(II) and Co(II) in real samples vary within a wide range, it is important to be able to determine both metals simultaneously even in samples in which one of the ions is found at a great excess with respect to the other. With the BFE, it was possible to control the adsorption process in order to achieve preferential adsorption of a particular DMG complex and thus facilitate the determination of a specific ion. The main variables that were involved were: the DMG concentration (DMG concentrations $> 0.1 \text{ mmol l}^{-1}$ resulted in an increased Co response); the preconcentration time (longer preconcentration times resulted in an enhanced Co peak height, and; the concentration of the ammonia buffer (at lower buffer concentrations a decreased response for Ni was observed). By using the appropriate conditions it was possible to determine one metal ion in the presence of a 20-fold excess of the other as shown in Fig. 5(b).

3.8. Plating, reproducibility, stability and cleaning of the bismuth film

The stability of the bismuth film was very important for the reliability of the results. It was found that the longer the bismuth plating time, the better was the between-film reproducibility (i.e. the reproducibility in the peak heights

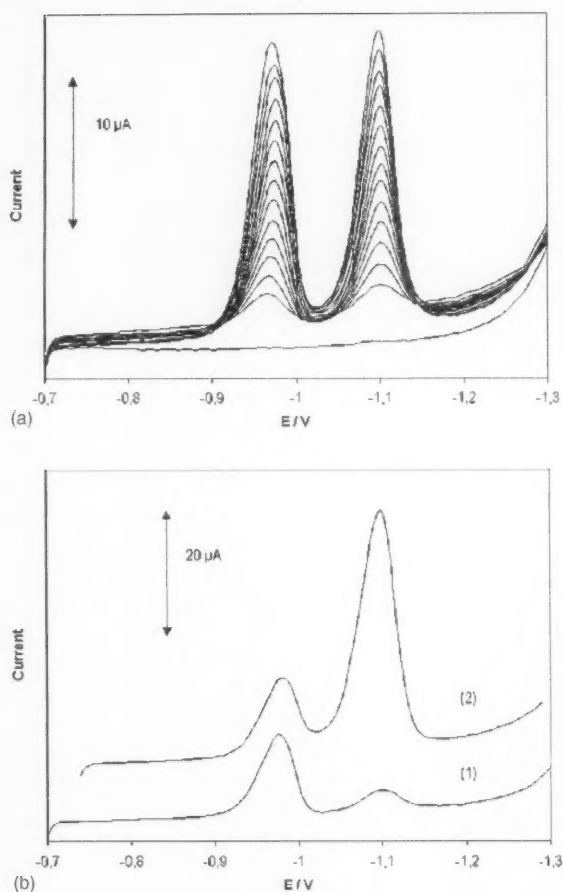


Fig. 5. (a) A series of 14 SW voltammograms in a solution containing increasing Ni(II) and Co(II) concentrations in steps of $1 \mu\text{g l}^{-1}$ (lower trace is the blank) after preconcentration for 120 s on a BFE. Scan increment: 4 mV; electrode rotation speed: 1000 rpm; DMG concentration: 0.1 mmol l^{-1} . Other conditions as in Figs. 1 and 2. (b) Simultaneous determination of Ni(II) and Co(II) at greatly varying mass-concentration ratios: (1) solution containing $5 \mu\text{g l}^{-1}$ of Ni(II) and $0.25 \mu\text{g l}^{-1}$ Co(II); DMG concentration: 0.8 mmol l^{-1} ; (2) solution containing $5 \mu\text{g l}^{-1}$ of Ni(II) and $100 \mu\text{g l}^{-1}$ Co(II). DMG concentration: 0.02 mmol l^{-1} , after preconcentration for 120 s on a BFE. Other conditions as in Figs. 1 and 2.

obtained at different BFE's). However, this parameter was not all that important since bismuth films would normally be stable for at least 2 h and a single film could be used for several tens of stripping cycles; thus, the within-film reproducibility (i.e. the reproducibility in the peak heights obtained on a single BFE), as discussed in the Section 3.7, was more important. Moreover, the mechanical stability of the bismuth film on the glassy carbon substrate was satisfactory since reproducible and well-defined peaks were obtained even at rotation speeds of 3000 rpm (the maximum rotation rate attainable with the Metrohm rotator).

Attempts to use an in-situ plated bismuth film (by spiking the sample solution with Bi(III) ions), were generally unsuccessful as the peaks for Ni and Co were distorted and

the reproducibility unacceptable and preplated bismuth films were used. It is important to note that a high buffer concentration (at least 1 mol l^{-1} in total acetate species) was necessary to ensure high buffering capacity during the bismuth plating step; at lower buffer concentrations hydrolysis of Bi(III) was visibly observed as clouding of the plating solution and this phenomenon was attributed to the hydroxyl ions produced during the potentiostatic step of the bismuth film formation.

Cleaning of the bismuth film was carried out by holding the potential of the electrode at -1.3 V after each voltammetric cycle. At this potential, traces of the remaining DMG complexes on the electrode surface were reduced and quickly desorbed. It was found that only a short cleaning period of 10 s was required to completely refresh the electrode surface.

3.9. Interference study

Two major sources of interference were investigated. First, surfactants present in most real samples are the more serious interference in stripping analysis and their effects on MFE's have been systematically studied in both ASV and AdSV [21] but similar studies on BFE's are very limited. Triton X-100 was used to simulate the effect of a typical non-ionic surfactant and Fig. 6(a) shows how the peak heights of Ni and Co heights are affected in the presence of different concentrations of Triton X-100.

In addition, metal ions can also interfere with the measurement by complexing competitively with DMG or by producing reduction peaks that overlap with, or even completely suppress, the Ni and Co peaks. A number of metal ions that could potentially interfere were examined: Pb(II), Hg(II), Cu(II), Fe(II), Al(III), Cd(II), Ti(IV), Ca(II) and Mn(II) added at a 1000-fold mass concentration excess over Ni(II) and Co(II) did not interfere (the criterion for interference was a $\pm 8\%$ error in the peak heights of Ni and Co). It is well known that excess Zn(II) is likely to interfere with the determination of Co(II) in AdSV by producing a diffusion-controlled peak at the cathodic side of the Co peak [22]. Indeed, a Zn(II) peak was observed at -1.24 V on the BFE but did not interfere even at a 1000-fold mass concentration excess of Zn(II) over Ni(II) and Co(II) (Fig. 6(b)). This was a marked improvement on analogous measurements on MFE's which could only tolerate a 100-fold mass concentration excess of Zn over Ni(II) and Co(II) [4]. This was attributed to the reduced sensitivity for Zn on the BFE compared to MFE's [10,13]. Even higher concentrations of Zn(II) could be tolerated by using a "medium-exchange" approach. In this case, after the preconcentration step in the sample solution containing a 10,000-fold mass concentration excess of Zn(II), the electrode was quickly transferred to a "medium-exchange" solution containing ammonia buffer at pH 9.2, in which the actual voltammogram was recorded: after "medium-exchange" the diffusion-related Zn peak was barely discernible (Fig 6(c)).

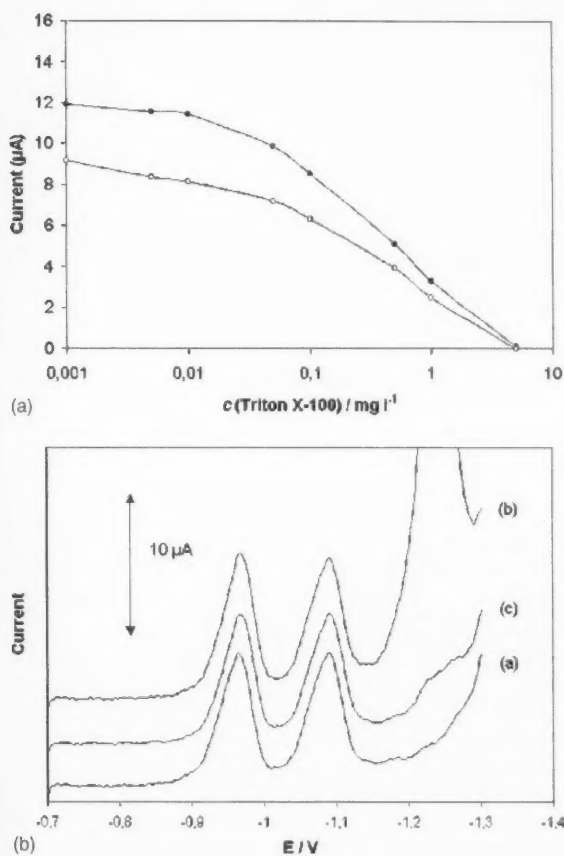


Fig. 6. (a) The effect of different concentrations of Triton X-100 on the Ni (○) and Co (●) peak heights in a solution containing $5 \mu\text{g l}^{-1}$ of Ni(II) and Co(II) after preconcentration for 120 s on a BFE. DMG concentration: 0.15 mmol l^{-1} ; other conditions as in Figs. 1 and 2 (b) SW voltammograms in: (1) a solution containing $10 \mu\text{g l}^{-1}$ of Ni(II) and Co(II) after preconcentration for 120 s on a BFE; (2) as in (1) but in the presence of 10 mg l^{-1} of Zn(II), and; (3) as in (1) but in the presence of 100 mg l^{-1} of Zn(II) and "medium-exchange" in pure ammonia buffer. DMG concentration: 0.1 mmol l^{-1} ; other conditions as in Figs. 1 and 2.

3.10. Applications

The accuracy of the method was assessed by determining nickel and cobalt in duraluminium, iron ore and a reference river water sample. The results are shown in Table 1. For both the iron ore and the duraluminium samples, the initially

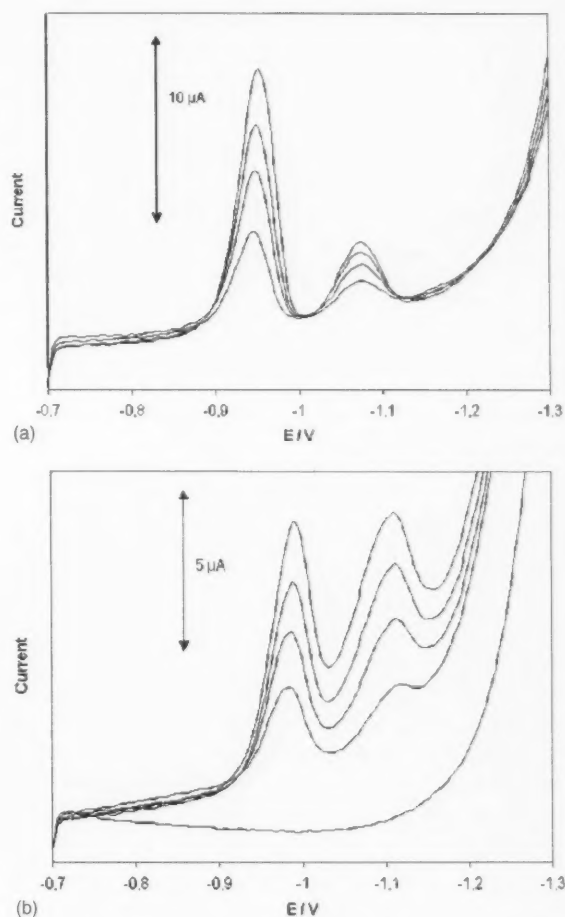


Fig. 7. (a) SW voltammograms after standard additions of Ni(II) and Co(II) in a digested iron ore sample after preconcentration for 60 s on a BFE. From below: sample and three successive standard additions of $8 \mu\text{g l}^{-1}$ Ni(II) and $1 \mu\text{g l}^{-1}$ Co(II). DMG concentration: 0.1 mmol l^{-1} . Other conditions as in Figs. 1 and 2. (b) SW voltammograms after standard additions of Ni(II) and Co(II) in a river water sample after preconcentration for 300 s on a BFE. DMG concentration: 0.25 mmol l^{-1} . From below: sample and three successive standard additions of $0.4 \mu\text{g l}^{-1}$ Ni(II) and $0.1 \mu\text{g l}^{-1}$ Co(II). Other conditions as in Fig. 5(a). NaNO_2 concentration = 0.2 mol l^{-1} .

digested sample was extensively diluted and no interference from matrix components was observed. A series of voltammograms after standard additions for the determination of nickel and cobalt in iron ore is illustrated in Fig. 7(a). In the

Table 1
Results for the determination of nickel and cobalt in different samples

	Found (% , w/w) ^a		Certified value (% , w/w)	
	Ni	Co	Ni	Co
Duraluminium	0.105 ± 0.005	Trace	0.10	–
Iron ore	0.136 ± 0.007	0.019 ± 0.001	0.14	–
Found ($\mu\text{g l}^{-1}$) ^a				
Certified value ($\mu\text{g l}^{-1}$)				
SLRS-2 river water	0.98 ± 0.06	0.075 ± 0.006	1.03	0.063

^a Mean of three determinations.

case of river water, lower concentrations exist, in particular for Co(II), and subtraction of the Ni blank was necessary. A series of voltammograms after standard additions for the determination of Ni(II) and Co(II) in a river water sample is illustrated in Fig. 7(a). The analysis of the water sample indicated that it was possible to determine Ni(II) and Co(II) at sub- $\mu\text{g l}^{-1}$ levels on the BFE using the proposed methodology despite the fact that the presence of potential ligands is to be expected in this matrix (in this sample the Co(II) concentration was close to the detection limit of the method but quantification was still possible after addition of NaNO_2 to increase the sensitivity [16].

4. Conclusions

In this work, a study was conducted on the determination of Ni(II) and Co(II) by SWAdSV on a rotating-disk BFE. The relevant chemical and instrumental parameters were investigated enabling the selection of the most appropriate conditions for the particular application in view of the variability of the nickel and cobalt contents in many samples. The BFE has been shown to possess some unique advantages compared to the MFE, namely its insensitivity to dissolved oxygen and its tolerance to the presence of large excess of Zn. In most other respects, the performance of the BFE was comparable to that of the MFE. The advantageous analytical properties of the BFE, combined with the minimal toxicity of metallic bismuth and bismuth salts, indicate that there is extended scope for the adoption of this type of electrode for alternative target analytes in the field of adsorptive stripping analysis.

References

- [1] J. Wang, in: A.J. Bard (Ed.), *Electroanal. Chem.*, Marcel Dekker, New York, vol. 16, 1988, pp. 1–86.
- [2] A. Economou, P.R. Fielden, *TrAC* 16 (1997) 286.
- [3] A. Economou, P.R. Fielden, *Analyst* 128 (2003) 205.
- [4] A. Economou, P.R. Fielden, *Analyst* 118 (1993) 47.
- [5] A. Economou, P.R. Fielden, *Talanta* 46 (1998) 1137.
- [6] C.M.A. Brett, A.M.C.F. Oliveira Brett, J.L.C. Pereira, *Electroanalysis* 3 (1991) 683.
- [7] H. Eskilsson, C. Haraldsson, D. Jagner, *Anal. Chem.* 175 (1985) 79.
- [8] H.J. Diederich, S. Meyer, F. Scholz, *Fresenius J. Anal. Chem.* 349 (1994) 670.
- [9] E. Gustafsson, *Water Air Soil Pollut.* 80 (1995) 99.
- [10] J. Wang, J.M. Lu, S.B. Hoocevar, P.A.M. Farias, B. Ogorevc, *Anal. Chem.* 72 (2000) 3218.
- [11] J. Wang, J.M. Lu, U.A. Kirgoz, S.B. Hoocevar, B. Ogorevc, *Anal. Chim. Acta* 434 (2001) 29.
- [12] K. Vytras, I. Svancara, R. Metelka, *Electroanalysis* 14 (2002) 1359.
- [13] G. Kefala, A. Economou, A. Voulgaropoulos, M. Sofoniou, *Talanta* 61 (2003) 603.
- [14] J. Wang, J.M. Lu, *Electrochem. Commun.* 2 (2000) 390.
- [15] E.A. Hutton, S.B. Hoocevar, B. Ogorevc, M.R. Smyth, *Electrochem. Commun.* 5 (2003) 765.
- [16] A. Krolicka, A. Bobrowski, K. Kalcher, J. Mocak, I. Svancara, K. Vytras, *Electroanalysis* 15 (2003) 1859.
- [17] A. Economou, S.D. Bolis, C.E. Efsthathiou, G. Volikakis, *Anal. Chim. Acta* 467 (2002) 179.
- [18] S.B. Adeloju, A.M. Bond, M.H. Briggs, *Anal. Chim. Acta* 164 (1984) 181.
- [19] P. Delahaye, I. Trachtenberg, *J. Am. Chem. Soc.* 79 (1957) 2355.
- [20] A.J. Bard, L.R. Faulkner, *Electrochemical Methods: Fundamentals and Applications*, John Wiley, NY, 1980, p. 288.
- [21] A. Economou, P.R. Fielden, *Analyst* 118 (1993) 1399.
- [22] A. Bobrowski, A.M. Bond, *Electroanalysis* 3 (1991) 157.

Determination of neutral and cationic herbicides in water by micellar electrokinetic capillary chromatography

María-Isabel Acedo-Valenzuela*, Teresa Galeano-Díaz¹, Nielene Mora-Díez, Antonio Silva-Rodríguez

Departamento de Química Analítica, Facultad de Ciencias, Universidad de Extremadura, Av. de Elvas s/n, 06071 Badajoz, Spain

Received 2 February 2004; received in revised form 24 May 2004; accepted 24 May 2004

Available online 15 July 2004

Abstract

The separation and determination of two *s*-triazines and two quats in water samples by MEKC was described. The influence of pH, type and concentration of buffer, concentration and type of surfactant, organic modifier and the added salt on the separation of the two neutral and the two cationic herbicides was studied. Simazine and atrazine (neutral compounds at the working pH) were little influenced by the chemical variables, while the cationic paraquat and diquat were more influenced. In the optimisation on the separation voltage, the total concentration of salt in the run buffer and the repeatability of the separation were taken into consideration. The composition of dissolution, in which the analytes were dissolved, was also studied.

A solid-phase extraction method to retain and to elute the four analytes in a single step was also developed. Recoveries between 80 and 95% and R.S.D. between 6 and 10% was obtained in the analysis of a well-water sample spiked with 2 and 5 ppb of triazines and quats, respectively. Detection limits were between 0.6 and 1.9 ppb.

© 2004 Elsevier B.V. All rights reserved.

Keywords: Pesticides; Water analysis; *s*-Triazines; Quaternary ammonium compounds; MEKC

1. Introduction

Modern agricultural production depends considerably on the use of herbicides to control weeds. Within this large number of compounds, triazines and quaternary ammonium compounds (quats) have been extensively used in recent years, mainly in the cultivation of the olive tree and vine in Spain, making their determination in environmental samples necessary. Due to their widespread usage, simazine, atrazine, paraquat and diquat, along with other herbicides, are included in a priority list of herbicides of potential concern established by the European Union for the Mediterranean countries [1]. Also, these herbicides are on the priority list of pesticides for a monitoring program in the USA's national pesticide survey [1,2]. In addition,

diquat and paraquat are extremely toxic and are often encountered in cases of poisoning.

Triazine herbicides have been determined by gas chromatography, HPLC, and their hyphenated techniques over the past decades [3,4]. In recent years, capillary electrophoresis (CE) in various modes, and its hyphenated technique CE-MS, are applied to separate several kinds of herbicides [5,6]. However, there are few reports on the separation of triazines by micellar electrokinetic capillary electrophoresis (MEKC) [5–8]. The most important application of these methods are in natural waters.

Quats, for example paraquat and diquat, have been analysed by diverse techniques as spectrophotometry, HPLC, using ion-pairing reagents, and more recently, by CE [9–12]. The mode used in CE is usually capillary zone electrophoresis (CZE) due to their ionic nature. Quats have been analysed in diverse matrices such as water, soil, plant material and biological samples.

To analyse these herbicides in water, a preconcentration step is necessary, due to the extremely low levels of these compounds to be determined. So, the United States

* Corresponding author. Fax: +34-924289375.

E-mail addresses: miacedo@unex.es (M.-I. Acedo-Valenzuela), tgaleano@unex.es (T. Galeano-Díaz).

¹ Tel.: +34-24-289-671; fax: +34-24-289-375.

Environmental Protection Agency has established maximum contaminant levels (MCLs) of 4 ppb of simazine, 3 ppb of atrazine, 3 ppb of paraquat and 20 ppb of diquat [12,13]. The European Union directive about the drinking water demands a maximum value of 0.1 ppb for a single pesticide, and 0.5 ppb for the sum of all pesticides, depending of their toxicological hazardous potential.

Only one paper has been found which carries out the analysis of triazines and quats together. The mode used is isotachopheresis and a derivation of the triazines is necessary [14].

In this work, the separation of two triazines (simazine and atrazine) and two quats (paraquat and diquat) was attempted by MEKC, using sodium dodecyl sulphate as surfactant. The influence of pH, the buffer nature and concentration, surfactant concentration, salt concentration and organic modifier, was evaluated. Also, a solid-phase extraction method, as a preconcentration step, is described in this paper. Due to the different nature of the analytes, this study was an analytical challenge. Finally, the determination of these herbicides in well-water was achieved with good results.

2. Materials and methods

2.1. Reagents and solutions

Atrazine (6-chloro-*N*²-ethyl-*N*⁴-isopropyl-1,3,5-triazine-2,4-diamine) (AT), simazine (6-chloro-*N*²,*N*⁴-diethyl-1,3,5-triazine-2,4-diamine) (SM), paraquat (1,1'-dimethyl-4,4'-bipyridinium dichloride) (PQ) and diquat (1,1'-ethylene-2,2'-bipyridinium dibromide) (DQ) (each 99%) were obtained from Riedel-de-Haën (Seelza, Germany). Stocks solutions (500 and 100 ppm) prepared by dissolution in methanol (for SM), in methanol–water 30% (v/v) (for AT) or in water (for PQ and DQ) were kept at 4 °C and used for studies and for preparation of spiked water samples.

Analytical-reagent grade boric acid, sodium tetraborate, disodium phosphate, sodium hydroxide, sodium perchlorate and trifluoroacetic acid (TFA) were purchased from Merck (Darmstadt, Germany). Sodium dodecyl sulphate (SDS) from Sigma-Aldrich (St. Louis, MO, USA) and HPLC-grade methanol and acetonitrile from Merck were also utilised. Ultrapure water was obtained from a Millipore Milli-Q system (Millipore, Bedford, MA, USA). All other chemicals were of analytical-reagent grade.

Polypropylene vials (Agilent Technologies, Madrid, Spain), of 1 mL and 300 µL, were used to place samples, buffers and other solutions in the electrophoretic system.

2.2. Apparatus

All experiments were conducted in a capillary electrophoresis system (Hewlett-Packard Española, model HP 3DCE; Madrid, Spain), equipped with a temperature control device, maintained at 25 °C by forced air, a diode array

detector, set at 220, 254 and 300 nm and the ChemStation Software package to control the instrument. The software package was supplied by the manufacturer for data acquisition and data analysis.

Fused-silica capillaries (Agilent Technologies, Madrid, Spain) with 48.5 cm total length, 40 cm effective length, 50 µm i.d., 375 µm o.d., and an extended optical path of 150 µm were utilised to perform the separations.

2.3. Procedures

2.3.1. Conditioning of the capillary and MEKC separation conditions

MEKC separations of the four analytes were performed with a 10 mM sodium tetraborate buffer containing 25 mM SDS, 40 mM sodium perchlorate and 15% (v/v) of acetonitrile at pH 9.3. At the beginning of each day, the capillary was rinsed 5 min with 0.5 M NaOH, followed by 5 min with water and 10 min with running buffer. Before each sample injection, the capillary was rinsed 2 min with NaOH 0.1 M, followed by 10 min with running buffer. After each injection to ensure a long life, high pressure water was passed through capillary for 5 min.

Standards/samples were injected in a solution composed by 8 mM disodium phosphate, 10 mM SDS and 3% (v/v) of methanol (pH adjusted to 8.5–9). Hydrodynamic injections were made by applying positive pressure in the sample vial (50 mbar) for 11 s (19 nL of injection volume and 9.8 mm of plug length) and the separation runs were carried out at normal polarity and constant voltage of 30 kV. The voltage of 30 kV was reached following a ramp of 0.2 min. The temperature of the capillary and the try of samples were adjusted at 25 °C. Triazine herbicides were monitored at 220 nm, paraquat at 254 nm and diquat at 300 nm. In all cases, corrected peak areas (CPA) were used as analytical signal, for the calculations. To obtain CPA, the peak area of each analyte was divided by its corresponding migration time.

2.3.2. Solid-phase extraction

For the preconcentration of 250 mL of water, two cartridges C₁₈ (360 mg; Waters Millipore, Mildford, Massachusetts) were used, conditioned differently because of the different nature of the analytes. One of them was conditioned with 10 mL of methanol, 10 mL of milli-Q water and passing air during 1 min. Through the other cartridge, 10 mL of methanol, 10 mL of milli-Q water and 15 mL of milli-Q water at pH 10.5–11, were passed. The two cartridges were united as indicated in Fig. 1. The sample water, fortified with the analytes and adjusted at pH 9 (with NaOH), was passed through the cartridges at 2 mL min⁻¹ using a house-made vacuum manifold. Later, the cartridges were dried with air for 1 min, and eluted with 10 mL of the 0.9% (v/v) TFA in methanol at 0.5 mL min⁻¹. The eluent was evaporated using a rotary evaporator at 40 °C. The residue was completely dried under a nitrogen stream at room temperature and re-dissolved by sonication, in 1 mL of buffer

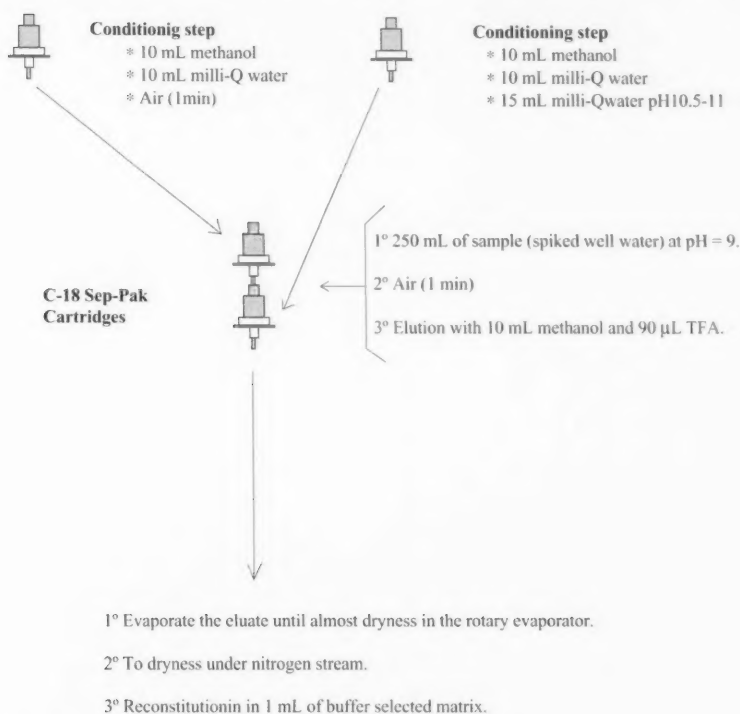


Fig. 1. Solid-phase extraction pathway.

consisting of 8 mM trisodium phosphate, 10 mM SDS and 3% (v/v) of methanol (pH adjusted to 8.5–9). The turbid samples were injected immediately in the electrophoretic system without filtration.

3. Results and discussion

3.1. MEKC separation performance

In the literature, the pK_a for simazine and atrazine was reported around 1.7 [7]. Therefore, very low pH values are needed for their separation by CZE. Paraquat and diquat are cationic. Their separation by CZE usually is in acidic medium [10,12] to avoid the adsorption to the capillary wall that happens in basic medium and the resulting broadening of signals. In these conditions separations take much time and because of it we have chosen the MEKC methodology to perform the separation of the four herbicides. An anionic surfactant, SDS, was preferred to perform the separation and a basic pH is necessary to provide strong cathodal EOF. Triazines peaks always appeared narrow and well resolved, but the quats peaks showed tailing. Therefore, optimisation of the process was focused to improve the form of these peaks.

For the preliminary studies, standards prepared in the same running buffer were injected hydrodynamically at 30 kV and applying 50 mbar for 5 s.

Slight changes were observed in the electropherograms when pH was varied between 8 and 10.2, using buffers consisting of 50 mM SDS and 20 mM tetraborate. The triazines were eluted well resolved and separated from the EOF, while the slightly retarded quats were eluted together. Buffer concentration was varied within the 10–80 mM range. A slight decrease in the EOF was observed when increasing buffer concentration, being almost constant the corrected migration times ($t'_m = t_m - t_{EOF}$, where t_m and t_{EOF} are the migration times of the analyte and the EOF) and the peak widths of the analytes. An increase in the concentration of the buffer did not improve the resolution of the quats peaks. When 25 mM of phosphate was used instead of borate, a slight improvement of the resolution of the peaks of the quats but longer migration times of all analytes and an increase in the current were observed. For further experiments, tetraborate buffer, which gives a pH of 9.3, was selected.

As it was expected, without the presence of SDS the quats gave rise to an only peak before the EOF, which is wide and poorly shaped probably due to the contribution of adsorption in the capillary [15], while the triazines eluted with the EOF. Above 20 mM of SDS, the peaks of the triazines appear separate and after the EOF while the quats eluted always together, in the whole studied range (0–100 mM). A constant value of the EOF and an increase in the corrected retention time for all analytes was also observed.

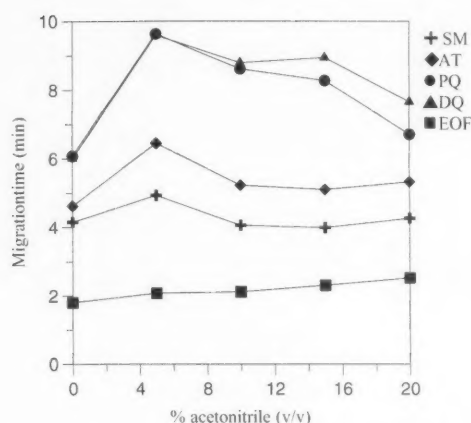


Fig. 2. Effect of the % (v/v) of acetonitrile in the migration times of analytes (25 ppm of each in run buffer). Run buffer: 20 mM sodium tetraborate, 50 mM SDS and variable percentage of acetonitrile.

When SDS was substituted by cholate, the peaks of the quats appeared before the EOF and the addition of cholate to SDS did not improve the selectivity.

We tried to improve selectivity by addition of an organic solvent. The presence of methanol or acetonitrile between 15 and 20% (v/v), produced the separation of the peaks of the quats at baseline. A decrease in the EOF was observed in both organics, while the influence on the migration times was different. In methanol, an increase of the proportion of the same one led to an increase of the times of migration of all analytes. The influence of the acetonitrile is quite different as it shown in Fig. 2. This behaviour can be explained as due to the different change that the electrophoretic mobility of micelles suffers with the increase of both solvents, as it has already been reported by Liu et al. [16]. For further experiments, we chose acetonitrile (AcCN) in the running buffer.

The injection of the analytes dissolved in an adequate sample matrix, produces electropherograms with more narrow peaks; therefore, greater volumes of sample to be injected. For this study, analytes were injected, dissolved in

aqueous solutions of different composition (matrix), and the peak widths and the corrected peak areas were compared. Hence, a dissolution composed by 8 mM disodium phosphate, 10 mM SDS and 3% (v/v) of methanol was chosen as optimum.

The ionic-strength of the running buffer influences, not only on the EOF and μ_{cp} (electrophoretic mobilities), but indirectly, on the viscosity of the medium. Thus, the addition of salts, such as sodium perchlorate, in concentrations between 0 and 50 mM was investigated. An increase in the concentration of perchlorate produced lower t_m of the quats and only a slight decrease in the EOF. No variation in the t_m of the triazines was observed. In presence of 40 mM of sodium perchlorate, a marked improvement in the t_m and the width of the peaks of the quats took place. This phenomenon can be the result of two effects: the formation of ion pairs between the perchlorate and the quat ions [17] and the reduction of adsorption of quat ions on the capillary surface [18]. We have observed a similar result in presence of 40 mM NaCl and therefore we attribute the improvement of electropherogram to the second of the cited effects. On the other hand, the effect of a possible field amplification was also discarded, since the improvement was also obtained even when NaClO₄ was added to the sample matrix to achieve the same conductivity of the running buffer. On the other hand, an increase in the current is obtained with the increase of the perchlorate concentration; hence, with 40 mM of sodium perchlorate and a voltage of separation of 30 kV, an intensity of 178 μ A was produced.

A representation of Ohm's law showed that we was in the nonlinear section. This last can affect to the repeatability. The solution could be, therefore, to decrease the concentration of salts or to diminish the applied voltage. To select the appropriate conditions for the separation, a study of the repeatability was made in different running buffers and separation voltages, which are detailed in Table 1. In the #2 conditions, bad results were obtained because after the sixth injection, two peaks appear together. Conditions 3 and 4 gave similar results of R.S.D., which were worse than in the conditions 1. Although the results from conditions 1 and 4 were both in the nonlinear section of Ohm's

Table 1
Repeatability values for different composition of the run buffer and separation voltages

Buffer composition	Voltage (kV)/ intensity (μ A)	CPA (%R.S.D.) ^a				t_m (%R.S.D.) ^a			
		SM	AT	PQ	DQ	SM	AT	PQ	DQ
(1) 20 mM tetraborate + 50 mM SDS + 15% AcCN + perchlorate 40 mM	30 ^b /178	4.03 (12)	3.49 (10)	3.74 (12)	1.92 (7)	4.12 (3.6)	5.01 (4.4)	3.09 (2.1)	3.50 (2.8)
(2) 20 mM tetraborate + 50 mM SDS + 15% AcCN + perchlorate 40 mM	20 ^c /80	—	—	—	—	—	—	—	—
(3) 10 mM tetraborate + 25 mM SDS + 15% AcCN + perchlorate 20 mM	30 ^c /75	7.33 (1.9)	6.68 (3.7)	12.3 (5.3)	4.39 (5)	2.60 (1.3)	3.02 (1.6)	4.55 (3.0)	5.07 (3.0)
(4) 10 mM tetraborate + 25 mM SDS + 15% AcCN + perchlorate 40 mM	30 ^b /125	7.52 (4.6)	7.60 (3.8)	17.7 (4.4)	9.93 (5)	2.48 (0.8)	2.89 (1.1)	3.46 (4.3)	3.89 (4.5)

^a For nine successive injections.

^b In the nonlinear section of the Ohm's law.

^c In the linear section of the Ohm's law.

law, the current produced in conditions 1 was higher, and repeatability in the corrected peak areas was worse. For further studies, we have chosen the conditions 4 because the peak shapes for paraquat and diquat are better than in condition 3. Therefore, a running buffer consisted of 10 mM sodium tetraborate, 25 mM SDS, 40 mM NaClO₄, 15% acetonitrile with a separation voltage of 30 kV, was used in the subsequent studies. The reduction of concentration of SDS produces lower t_m for triazines, and the increase of concentration of NaClO₄ gives rise to lower t_m for quats.

In these conditions, we can appreciate the influence of suppression of sodium perchlorate in the running buffer (Fig. 3).

Due to the increase of the current produced with temperature, we decided to maintain the temperature of the capillary and the try of samples at 25 °C for further studies.

A study over the influence of the injection time on the separation was performed while applying a constant pressure of

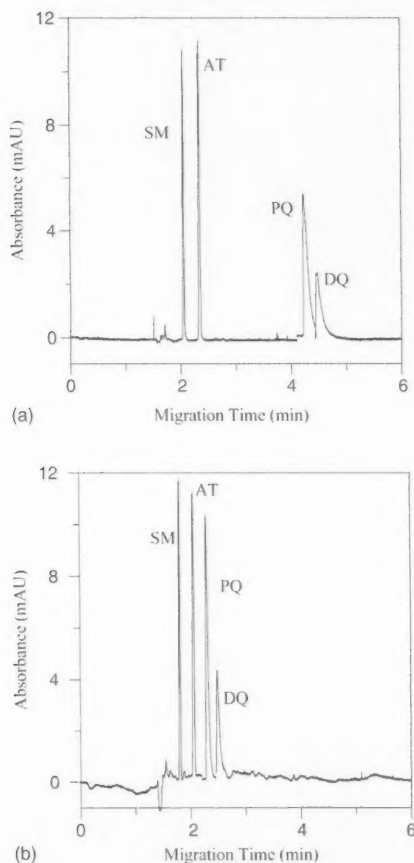


Fig. 3. Effect of concentration of sodium perchlorate in the separation of analytes (5 ppm of triazines and 15 ppm of quats). Run buffer: (a) 10 mM sodium tetraborate, 25 mM SDS, 15% (v/v) acetonitrile; (b) the same but also with 40 mM sodium perchlorate. Sample matrix: 8 mM disodium phosphate, 10 mM SDS, 3% (v/v) methanol.

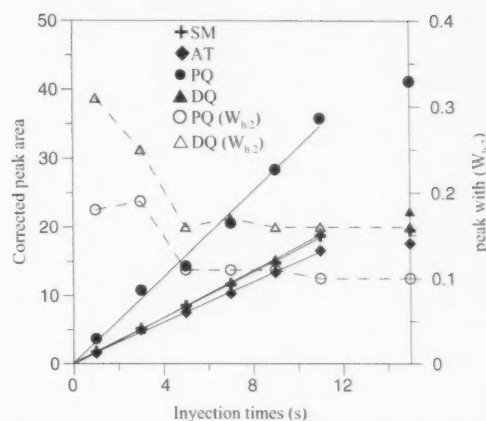


Fig. 4. Effect of injection times on the corrected peak areas of analytes (5 ppm of triazines and 25 ppm of quats dissolved in the selected matrix) and on the peak width ($w_{0.2}$) for paraquat and diquat (dashed lines). Run buffer as in Fig. 3b.

50 mbar in the sample vial (5 ppm of triazines and 25 ppm of quats dissolved in the selected matrix) and varying the time of this application (between 1 and 15 s). To avoid spontaneous extraneous injection of sample [19], the volumes in the two vials, that are at the ends of the capillary during the injection, were kept equal. From each electropherogram the corrected peak areas and the peak widths were obtained and represented regarding the injection time in Fig. 4. Linearity can be observed for injections up to 11 s. On the other hand, smaller injection volumes gave greater peak widths for the quats. Also, the migration times of these analytes were slightly affected. For the triazines the peak widths and migration times were almost constant. We selected an injection time of 11 s as optimum for further experiments.

3.2. Calibration and precision

Linearity was assessed by injection of solutions of the four analytes, dissolved in the optimum matrix, in the concentration range 0.5–8.0 ppm ($n = 7$) for triazines and 1.75–18 ppm ($n = 7$) for the quats. Each injection was performed in using the experimental conditions selected.

The regression equations were

$$\text{SM: } \text{CPA} = 0.45(\pm 0.24) + 3.07(\pm 0.05) \text{ ppm SM}; \\ R^2 = 0.999, s_{y/x} = 0.43 \quad (1)$$

$$\text{AT: } \text{CPA} = 0.57(\pm 0.19) + 3.10(\pm 0.04) \text{ ppm AT}; \\ R^2 = 0.999, s_{y/x} = 0.34 \quad (2)$$

$$\text{PQ: } \text{CPA} = 1.40(\pm 0.50) + 1.44(\pm 0.05) \text{ ppm PQ}; \\ R^2 = 0.996, s_{y/x} = 0.94 \quad (3)$$

$$\text{DQ: } \text{CPA} = 0.68(\pm 0.22) + 0.77(\pm 0.02) \text{ ppm DQ}; \\ R^2 = 0.997, s_{y/x} = 0.42 \quad (4)$$

The satisfactory determination coefficient values show that the responses of SM, AT, PQ and DQ were linear with the concentration in the ranges studied.

Limits of detection of 0.10, 0.13, 0.15 and 0.12 ppm for SM, AT, PQ and DQ were calculated from the standard deviation ($n = 5$) of the lowest level of concentration in the calibration graph [20].

Repeatability was evaluated by performing nine successive injections of the four analytes in concentration of 5 and 10 ppm for the triazines and quats, respectively, with the optimal experimental conditions. Acceptable precision, R.S.D. between 0.4 and 2.2% for t_m and between 1.8 and 4% R.S.D. for CPA, was obtained.

3.3. Solid-phase extraction

Due to the extremely low concentrations of the pesticides in environmental waters, a preconcentration procedure is necessary.

We utilised an SPE procedure, with C_{18} Sep-Pak cartridges, to extract the pesticides. Due to their different characteristics (atrazine and simazine are neutral compounds, and paraquat and diquat are ionic compounds), the retention and elution of them was an analytical challenge. An apolar phase is adequate for triazines retention, and quats are largely retained on silica sorbent, but also in apolar C_8 or C_{18} sorbents, by means of different mechanisms. The formation of ion pairs with adequate reagents is one of the possibilities but also it is possible to previously transform the sorbent in a weak cation-exchanger by passing an alkaline aqueous solution through the cartridges giving rise to free silanol groups [9]. There are some reports about the extraction of diquat and paraquat from river water samples, adjusting the pH of sample to 9.5–10 or pH 13 [21,22] and using conditioned C_{18} cartridges. One possible explanation for this behaviour could be that the retention of these herbicides was due to the interactions with silanol groups, present in the C_{18} solid-phase at these pH values. The solid-phase extraction method proposed in this paper is based on these references. In other paper that appears in the literature, the preconcentration on-line in a C_{18} precolumn, without previously conditioning this at pH alkaline, it gives rise to low recovery values, being necessary the addition of ion-pair reagent [23]. The importance of an adequate conditioning of the cartridges is deduced.

In our case, two cartridges (the upper, conditioned with methanol and water, for retaining triazines and the lower, conditioned also with water at pH 10.5–11, for quats) were employed, by using the procedure described in Section 2.3.2, which is shown in Fig. 1. In the retention stage, more basic media for the well-water sample were assayed. At pH 10, the turbid solution obtained gave low recoveries for triazines. At pH 12–13, following the Tsunoda method, well-water samples were so turbid that the C_{18} Sep-Pak cartridges become obstructed (the well-water used had 15 °F of hardness, which is considered medium hardness water). The best results were obtained with well-water samples at pH 9.

For the final dissolution of the residue, two different methods were assayed: the first one uses 3 mL of 10% methanol (v/v) and subsequent neutralisation with some drops of NaOH; and the second one uses 1 mL of the selected matrix but substituting disodium phosphate by trisodium phosphate, to get a final pH value between 8 and 9 (because after the elution with TFA in methanol and subsequent evaporation, a very acid dissolution is obtained). The selected method was the second due to the best recovery values, the greater sensitivity and the lower R.S.D. values obtained.

The final solution is also slightly turbid. However, we have proved that this has no effect on the injection of the sample. For this purpose, a standard addition method has been applied to these final solutions. The slope of straight lines obtained was statistically equal to the slope obtained with external standards. To avoid the obstruction of capillary, this was cleaned by passing water through at high pressure during 5 min.

Finally, we have analysed three different well-water samples, using the procedure of Fig. 1. The results are shown in Table 2. These values are acceptable and demonstrate the repeatability of the method. Fig. 5 shows one of the electropherograms obtained.

By applying the results obtained in the analysis of well-water samples with the lowest level of concentration (2 ppb for triazines and 5 ppb for quats), the detection limits of the developed method were calculated, according to US Environmental Protection Agency (EPA) method 549.2, revision 1.0 (determination of diquat and paraquat in drinking water). Four different samples were analysed using 99% confidence level. The detection limits were: 0.6 ppb for

Table 2
Recovery values and R.S.D. for 250 mL of well-water samples

Analyte	g/L added	%R ^a (%R.S.D.)	g/L added	%R ^a (%R.S.D.)	g/L added	%R ^b (%R.S.D.)
Simazine	15	92 (2)	7	87 (8)	2	87 (6)
Atrazine	15	88 (6)	7	94 (7)	2	90 (10)
Diquat	30	84 (2)	15	96 (2)	5	80 (8)
Paraquat	30	85 (2)	15	89 (1)	5	95 (7)

^a Average of three independent determinations.

^b Average of four independent determinations.

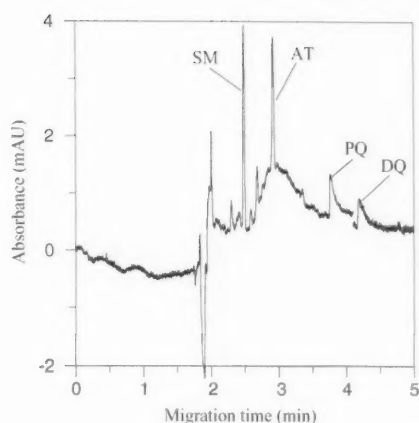


Fig. 5. Electropherogram obtained for well-water spiked with 2 ppb of triazines and 5 ppb of quats, after SPE onto two C_{18} cartridges (enrichment factor of 250). Run buffer as in Fig. 3b.

simazine; 1.0 ppb for atrazine; and 1.9 ppb for diquat and paraquat.

4. Conclusions

It has been demonstrated that MEKC allows baseline separation of triazines and quats in less than 5 min. Usually, given their ionic nature, the quats are separated by CZE. In this paper, we show that the methodology of MEKC is also appropriate to achieve their separation. The peaks of the triazines almost always appear narrow and very resolved. On the contrary, the peaks of the quats are more subject to the influence of additives like the organic modifier and sodium perchlorate. The addition of the salt, produces a narrowing in the peaks of the quats and an increase of the produced current. Optimum salt concentration and separation voltage were selected simultaneously, keeping in mind the repeatability of the separation.

The use of two C_{18} cartridges for SPE of water samples was demonstrated to be an easy and efficient preconcentration system for the four pesticides, including ionics and neutrals. The combination of this SPE method with MEKC allows the determination of these herbicides at the ppb lev-

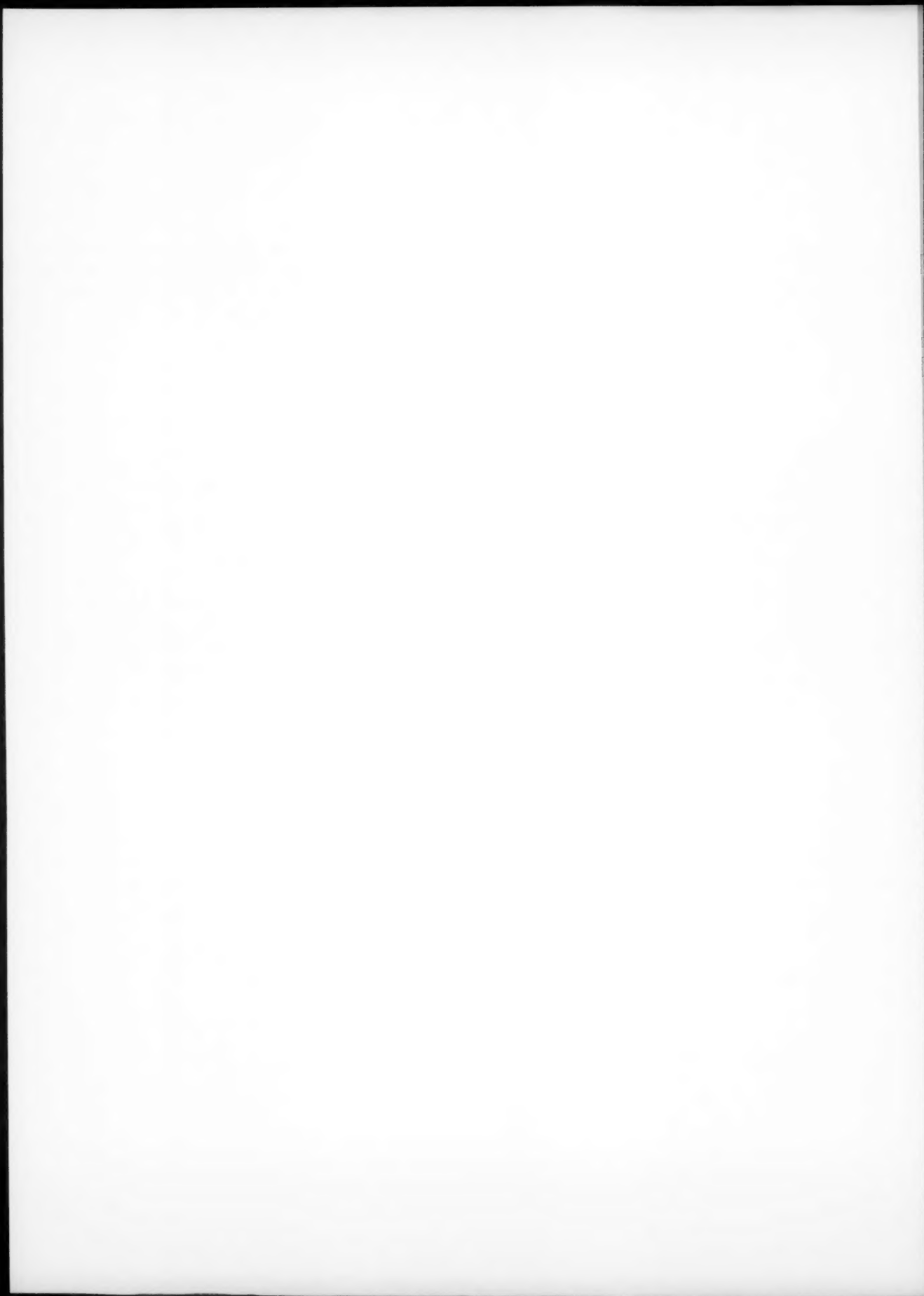
els, and below the limits established by the EPA of United States.

Acknowledgements

The authors wish to thank to Ministerio de Ciencias y Tecnología Español for the financial support (CAL00-034-C2-01 and BQU2002-00918). Antonio Silva Rodríguez acknowledges a fellowship from the Consejería de Educación, Ciencias y Tecnología-Junta de Extremadura.

References

- [1] D. Barceló, *J. Chromatogr. A* 643 (1993) 117.
- [2] J.R. Dean, G. Wade, I.J. Barnabas, *J. Chromatogr. A* 733 (1996) 295.
- [3] J. Sherma, *Anal. Chem.* 67 (1995) 1R.
- [4] A. Martín-Esteban, P. Fernández, A. Fernández-Alba, C. Cámara, *Quim. Anal.* 17 (1998) 51.
- [5] F. Menzinger, Ph. Schmitt-Kopplin, D. Freitag, A. Ketrup, *J. Chromatogr. A* 891 (2000) 45.
- [6] Y. Picó, R. Rodríguez, J. Mañes, *TrAC* 22 (2003) 133.
- [7] C.E. Lin, C.C. Hsueh, T.Z. Wang, T.C. Chiu, Y.C. Chen, *J. Chromatogr. A* 835 (1999) 197.
- [8] E. Turiel, P. Fernández, C. Pérez-Conde, C. Cámara, *J. Chromatogr. A* 872 (2000) 299.
- [9] Y. Picó, G. Font, J.C. Moltó, J. Mañes, *J. Chromatogr. A* 882 (2000) 251.
- [10] O. Núñez, E. Moyano, M.T. Galceran, *J. Chromatogr. A* 946 (2002) 275.
- [11] O. Núñez, E. Moyano, M.T. Galceran, *J. Chromatogr. A* 961 (2002) 65.
- [12] O. Núñez, E. Moyano, M.T. Galceran, *J. Chromatogr. A* 974 (2002) 243.
- [13] <http://www.epa.gov/safewater/mcl.htmlmcls>.
- [14] Z. Stránský, *J. Chromatogr.* 320 (1985) 219.
- [15] M.T. Galceran, M.C. Cameiro, L. Puignou, *Cromatographia* 39 (1994) 581.
- [16] Z. Liu, H. Zou, M. Ye, J. Ni, Y. Zhang, *Electrophoresis* 20 (1999) 2898.
- [17] W. Jiang, J.N. Awasum, K. Irgum, *Anal. Chem.* 75 (2003) 2768.
- [18] J.S. Green, J.W. Jorgenson, *J. Chromatogr.* 478 (1989) 63.
- [19] E.M. Gruska, R.M. McCormick, *J. Chromatogr.* 121 (1989) 421.
- [20] J.A. Glaser, D.L. Foerst, G.D. McKee, S.A. Quave, W.L. Budde, *Environ. Sci. Technol.* 15 (1981) 1427.
- [21] T. Galeano-Díaz, A. Guiberteau-Cabanillas, F. Salinas, *Electroanalysis* 12 (8) (2000) 616.
- [22] N. Tsunoda, *Eisei-Kagaku* 29 (4) (1983) 206.
- [23] R. Castro, E. Moyano, M.T. Galceran, *J. Chromatogr. A* 869 (2000) 441.



Separation and selectivity in micellar electrokinetic chromatography using sodium dodecyl sulfate micelles or Tween 20-modified mixed micelles

Miao Wang^a, Dan Wu^{a,*}, Qi Yao^a, Xueyou Shen^b

^a Zhejiang University, Center of Analysis and Measurement, Hangzhou 310027, PR China

^b Zhejiang University, Department of Environmental Science, Hangzhou 310027, PR China

Received 10 December 2003; received in revised form 19 May 2004; accepted 19 May 2004

Available online 13 July 2004

Abstract

The separation and selectivity of eight aromatic compounds ranging from hydrophilic to hydrophobic properties in micellar electrokinetic chromatography (MEKC) using sodium dodecyl sulfate (SDS) micelles or Tween 20-modified mixed micelles were investigated. The effect of different operation conditions such as SDS and Tween 20 modifier surfactant concentration, buffer pH, and applied voltage was studied. The resolution and selectivity of analytes could be markedly affected by changing the SDS micelle concentration or Tween 20 content in the mixed micelles. Applied voltage and pH of running buffers were used mainly to shorten the separation time. Complete separation of eight analytes could be achieved with an appropriate choice of the concentration of SDS micelles or Tween 20-modified mixed micelles. Quicker elution and better precision could be obtained with SDS–Tween 20 mixed micelles than with SDS micelles. The mechanisms that migration order of those analytes was mainly based on their structures and solute–micelle interactions, including hydrophobic, electrostatic, and hydrogen bonding interactions, were discussed.

© 2004 Elsevier B.V. All rights reserved.

Keywords: Micellar electrokinetic chromatography; Selectivity; Sodium dodecyl sulfate; Tween 20; Mixed micelles

1. Introduction

Micellar electrokinetic chromatography (MEKC) is one important branch of capillary electrophoresis (CE) techniques. Based on electrophoretic mobilities of the analytes when partitioned between the micellar and aqueous phases, MEKC has a high-resolution efficiency, which enables excellent separation of ionic analytes and also electrically neutral or nonionic analytes [1–5]. Therefore, separation and selectivity can be easily controlled by modifying the micellar phase or aqueous phase so that the interactions of analytes with both the phases can be deeply influenced [6–8]. To modify the aqueous phase, highly hydrophilic organic solvents, such as methanol [9], ethanol [10] or acetonitrile [11], etc., and electrolyte additives, for instance cyclodextrin [12,13], urea [14] are often used to enhance the solubility of hydrophobic analytes in the aqueous phase. On the other hand, the modification of the micellar phase has so far

been made to affect the separation in MEKC by the use of mixed micelles [15–18] or hydrophobic organic compounds solubilized in the micelles [19,20]. Especially, mixed surfactant systems in MEKC provide various analytical advantages, since some additional interactions can be introduced into the separation system to optimize the selectivity. Chiral compounds incorporated into ionic surfactant micelles offer chiral selectivity to MEKC [21–25], and some distributed surfactants, which change the charge density of micellar phases allowing novel selectivity owing to different electrostatic interaction [26–30]. Besides, solubilization of some substances with various polar groups can present hydrogen bonding or dipolar interaction to grant additional selectivity [31–33]. By a change in buffer pH, micellar concentration or ratio of mixed surfactants and additive compounds, the separation and selectivity in MEKC are easily optimized [21–29,33].

In this paper, the separation and selectivity of eight aromatic compounds ranging from hydrophilic to hydrophobic properties, as model analytes in MEKC using sodium dodecyl sulfate (SDS) micelles or Tween 20-modified mixed micelles, were investigated. Various parameters

* Corresponding author. Tel.: +86 571 8795 1968; fax: +86 571 8795 1995.

E-mail address: liif@mail.hz.zj.cn (D. Wu).

such as the concentration of SDS micelles and Tween 20-modified mixed micelles, buffer pH, and applied voltage were studied. Besides, the separation efficiency, the linearity, the detection limit, and the reproducibility of the separation methods in both SDS micelles and Tween 20-modified mixed micelles-based MEKC were compared. The results showed that the concentrations of both SDS micelles in single micelle-based MEKC and Tween 20 in mixed micelle-based MEKC could efficiently influence the separation selectivity. It revealed that not only the predominant hydrophobic interaction but also other important solute–micelle interactions could manipulate the separation.

2. Experimental

2.1. Apparatus

All separation experiments were carried out on a Waters Quanta 4000 CE system (Waters Chromatography Division of Milford, MA, USA) with a positive power supply. Untreated fused-silica capillary (Ruifeng Inc., Hebei, China) of 50 μm i.d. and 47 cm effective length (55 cm total length) was used from the injection end of the capillary to the detector. Direct UV detection for absorbance measurement was performed at 214 nm wavelength. The temperature was kept at 35 °C by additionally equipped temperature controller XMTA-2002 (Yuyao Telecommunicating Instrument Corp., Zhejiang, China). Sample was introduced from the anodic end of the capillary by hydrostatic injection, where the sample vial was raised by 9.8 cm above the other electrolyte vial for 30 s. Data acquisition was carried out with a C-R1B Chromatopac (Shimadzu Corp. Analytical Instruments Division, Kyoto, Japan). All pure water was deionized with a Millipore Milli-Q water purification system (Millipore Corp., Bedford, MA, USA). A Model pHs-W pH meter (Hangzhou Wanda Instrument Factory, Zhejiang, China) was employed for pH measurement.

2.2. Chemicals and reagents

SDS and Tween 20 (polyethylene (20) sorbitan monolaurate) were purchased from Shanghai Reagent Factory (China) and Longyou Chemical Plant (Zhejiang, China), respectively. As analytes, benzene (Hangzhou Chlorophyll Factory, Zhejiang, China), toluene (Hangzhou Chemical Reagent Ltd., Zhejiang, China), ethylbenzene (The First Plant of Shanghai Chemical Reagents, China), naphthalene (imported from Germany and purified), aniline (Wulian Chemical Plant, Shanghai, China), phenol (Suanglin Chemical Reagent Plant, Hangzhou, China), 2-chlorophenol (The Third Plant of Shanghai Chemical Reagents, China), and 4-nitrophenol (Shanghai Chemical Reagent Company, China) were of analytical grade. All other chemicals were of analytical reagent grade.

Standard stock solutions of benzene, toluene, ethylbenzene, and naphthalene were individually prepared in an aqueous solution containing 60% ethanol at concentrations of 10, 5, 5, and 1 g L^{-1} , and aniline, phenol, 2-chlorophenol, 4-nitrophenol of 1 g L^{-1} dissolved in pure water. Borax stock solution was prepared at a concentration of 100 mmol L^{-1} , and SDS, Tween 20 at 200 mmol L^{-1} . All stock solutions were stored in a 4 °C refrigerator.

2.3. Experimental procedures

Various concentrations of the needed running buffers were prepared from the stock solutions and degassed by ultrasonication for approximately 10 min before use. The capillary was daily conditioned by washing, in order, with 0.1 mol L^{-1} sodium hydroxide for 5 min, water for 5 min, ethanol for 5 min, water for 5 min, and the running buffer for 10 min. Between consecutive analyses, the capillary was purged with the running buffer for 3 min. The pH of the borate buffer solution was adjusted by mixing 0.1 mol L^{-1} HCl or 0.1 mol L^{-1} NaOH solution. The analytes in sample solution were appropriately diluted with 10 mmol L^{-1} SDS solution by mixing eight specific standard stock solutions before injection.

3. Results and discussion

3.1. MEKC separation with SDS micelles

The influence of the concentration of SDS micelles in the range of 25–150 mmol L^{-1} on the separation of the eight aromatic compounds in a 10 mmol L^{-1} borate buffer of pH 9.2 was investigated. As the concentration of SDS surfactant was increased, migration behaviors of most analytes were markedly influenced, as shown in Fig. 1. The migration velocities of all solutes decreased with increase in the concentration of SDS. And the migrations of benzene, toluene, ethylbenzene, and naphthalene changed greatly, but meanwhile those of aniline, phenol, 2-chlorophenol, and 4-nitrophenol were slightly influenced. As a result, the elution order and the retention behaviors of all solutes varied when the concentration of SDS increased. As the interior cores of SDS micelles are highly hydrophobic, the selectivity of solutes is mainly governed by hydrophobic interaction. But aniline, phenol, 2-chlorophenol, and 4-nitrophenol are derived from aromatic ring with hydrophilic groups, which moderated the hydrophobic interaction between the four analytes and micellar phase. Besides, the electrostatic repulsion was not ignorable between the anionic solutes, 2-chlorophenol (pK_a 8.56) and 4-nitrophenol (pK_a 7.15) [34], and anionic SDS micelles. It was observed that the selectivity of peaks between 2-chlorophenol and 4-nitrophenol decreased with increase in the concentration of SDS from 25 to 100 mmol L^{-1} , and then increased from 125 to 150 mmol L^{-1} . Consequently, the reversal of the

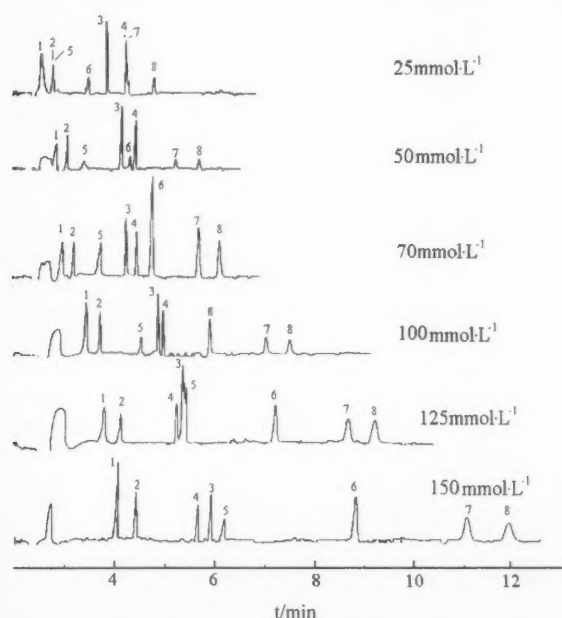


Fig. 1. The electropherogram of eight aromatic compounds in MEKC with different SDS concentrations. Separation conditions: a borax running buffer (10 mmol L^{-1}) at pH 9.2 containing $25\text{--}150 \text{ mmol L}^{-1}$ SDS; applied voltage, 25 kV ; temperature, 35°C . Peaks identification: 1, aniline; 2, phenol; 3, 2-chlorophenol; 4, 4-nitrophenol; 5, benzene; 6, toluene; 7, ethylbenzene; and 8, naphthalene.

migration order of the two analytes occurred between the concentrations of 100 and 125 mmol L^{-1} . The hydroxyl group in 2-chlorophenol can form intramolecular hydrogen bonds with chlorine at 2-position of the aromatic ring. SDS micellar phase, as the hydrogen bond donors, can form the hydrogen bonds with the nitril group in 4-nitrophenol. Therefore, 2-chlorophenol was eluted before 4-nitrophenol at low SDS concentration. However, the hydrogen bonds between SDS micelles and 2-chlorophenol could gradually form to substitute the intramolecular hydrogen bonds while the SDS concentration increased, so that the interaction between SDS and 2-chlorophenol was gradually enhanced. As a result, the peak of 2-chlorophenol approached that of 4-nitrophenol, and then the peak order of both reversed with the increase in SDS concentration from 25 to 150 mmol L^{-1} . Evidently, hydrogen bonding interaction also played a significant role in the selectivity of the solutes. Baseline separations for all sample standards were easily obtained by adjusting SDS content in running buffers, which reflected that a change in SDS concentration was able to affect not only the retention factor but also the selectivity for all analytes.

A borate buffer (10 mmol L^{-1}) containing 70 mmol L^{-1} SDS was undertaken to investigate the variations in retention behaviors of eight aromatic compounds as a function of buffer pH in the range 8.9–9.5, as shown in Fig. 2. It was observed that with the increasing pH value, from 8.9 to 9.2, the migration of all the solutes gradually increased and the peak

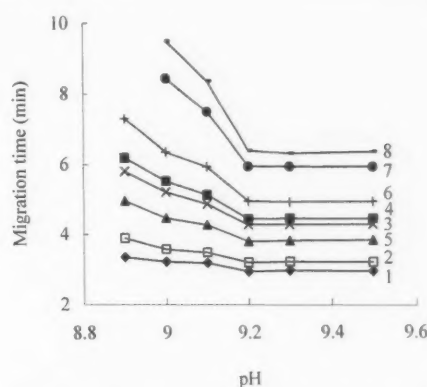


Fig. 2. Effect of buffer pH on the migration time of eight aromatic compounds. Buffer: 10 mmol L^{-1} borate buffer containing 70 mmol L^{-1} SDS. Other conditions were same in Fig. 1.

shapes of the last two analytes (ethylbenzene and naphthalene) obviously improved at the same time, for the elution of both was not detected at pH value 8.9. However, the separation of all the solutes was scarcely effected when pH increased from 9.2 to 9.5. Their retention behaviors were also investigated at pH 10.8, and their migration time was nearly same as it was at pH 9.5. Variation in pH, between 8.9 and 9.5, slightly changed the electro-osmotic flow (EOF) of the aqueous phase and the migration of the solutes. As the pH value increased, the velocity of EOF increased slightly and the migration time of the solutes decreased. Moreover, the variation of pH value significantly influenced the hydrolysis of borate, and the effect of the molecules of boric acid on SDS micelles was gradually moderated with the increase in pH. Consequently, the interaction between the solutes and SDS micelles was weakened. At low pH value, the interaction between solutes and micelles increased, and the longitudinal diffusion enhanced. An optimum baseline separation was achieved in 6.5 min with a 10 mmol L^{-1} borax buffer of pH 9.2 without adjusting the pH value of the solution by acid or base.

The effect of applied voltage on the aromatic compounds' migration was also examined with a 10 mmol L^{-1} borate buffer containing 70 mmol L^{-1} SDS. As the separation voltage increased from 20 to 30 kV , the total migration time of the eight analytes was shortened from 12 to 6 min and the separation selectivity was not changed. At lower voltage, the peaks were broadened due to the longitudinal diffusion. Higher voltage increased the baseline noise and produced more Joule heat, resulting in poorer detection limits and lower separation efficiency. Therefore, 25 kV was selected as the run voltage to accomplish a good compromise.

3.2. MEKC separation with SDS–Tween 20 mixed micelles

It has been reported that the selectivity of analytes could be improved and the elution range could be adjusted with the use of mixed micelles in MEKC [15–18,27–29]. In this

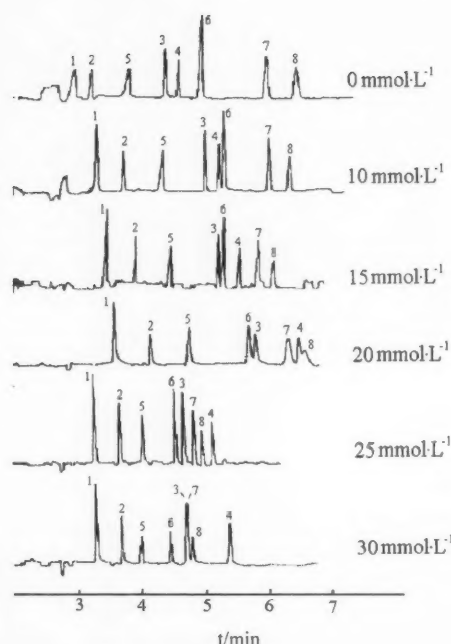


Fig. 3. The electropherogram of eight aromatic compounds in mixed SDS-Tween 20-based MEKC with different Tween 20 concentrations. Separation conditions: a borax running buffer (10 mmol L^{-1}) at pH 9.2 containing 70 mmol L^{-1} SDS with $0\text{--}30 \text{ mmol L}^{-1}$ Tween 20. All other separation conditions were same as in Fig. 1.

study, a nonionic surfactant Tween 20 was chosen to form SDS-Tween 20 mixed micelles so that the baseline separation could be achieved in less time.

The influence of the concentration of Tween 20, with 70 mmol L^{-1} SDS in a 10 mmol L^{-1} borax buffer of pH 9.2, on the separation of the eight aromatic compounds was investigated. The results showed that the separation and selectivity of the analytes were greatly affected with the use of Tween 20 when its concentration ranged from 0 to 30 mmol L^{-1} , as shown in Fig. 3. It was observed that the separation window was narrowed as the concentration of Tween 20 varied from 0 to 30 mmol L^{-1} because the addition of Tween 20 led to the reduction of the negative charge density of the micellar phases and the net migration of the micelles to cathode was expedited. Moreover, the velocity of EOF decreased with the increase in the Tween 20 content due to the increase in the electrolyte viscosity. The migration of all solutes, except ethylbenzene and naphthalene, slowed in the beginning and quickened later, as the concentration of Tween 20 increased. The addition of Tween 20 improved the solubilization of solutes into micelles [35] and could form hydrogen bonds with the hydrogen bond-donating solutes, such as aniline, phenol, 2-chlorophenol, and 4-nitrophenol. As a result, the solutes interacted more strongly with the mixed micelles. Therefore, the expediting micellar phase led to the irregular variation of the elution of the solutes. As to the selectivity of all analytes,

2-chlorophenol and 4-nitrophenol, which moved slower at the higher concentration of Tween 20, behaved differently from the other analytes and caused the lagging elution of both. It could be explained that the formation of the mixed micelles introduced a decrease in the repulsive ionic interactions between the anionic analytes, 2-chlorophenol and 4-nitrophenol, and SDS by the polyether chains of Tween 20 and benefited the solubilization of the two analytes into the micellar phases. Tween 20 has long polyether chains as hydrophilic groups and the polyether chains must be stuck out of the surfaces of the mixed micelles. The projecting polyether moiety may partly cover the sulfate group of SDS, resulting in the reduction of the ionic repulsion. In addition, the nonionic surfactant possesses hydrogen bond acceptor characteristic in the polyether chain and hydrogen bond donor characteristic in the hydroxyl groups, which was expected to interact with 2-chlorophenol and 4-nitrophenol. The results indicated that a suitable concentration of Tween 20 modifier could effectively control the separation selectivity and shorten the separation time. An optimum baseline separation was achieved within 5.1 min, when a running buffer contained 25 mmol L^{-1} Tween 20 with 70 mmol L^{-1} SDS mixed micelles. Further research on the analysis of the chlorophenols and nitrophenols, under various experimental conditions, will be reported later.

A borate buffer (10 mmol L^{-1}) with 70 mmol L^{-1} SDS and 25 mmol L^{-1} Tween 20 mixed micelles was used as a background electrolyte to study the influences of buffer pH in the range of 8.8–9.4 and applied voltage from 20 to 30 kV on the separation of eight aromatic compounds, respectively. The migration velocities of the analytes increased gradually and the elution order was not significantly affected with increasing buffer pH value or increasing separation voltage. In lower pH value buffer, the prolonged separation time caused the peaks to broaden and the resolution between ethylbenzene and naphthalene could not achieve baseline separation. At higher applied voltage, the baseline noise was not obviously increased and the thermal diffusion of all the solutes was not aroused. Therefore, excellent separation efficiency could be achieved in less elution time. But, pH 9.2 and 25 kV separation voltage were also chosen in order to compare the separation results in SDS-based MEKC with those in SDS-Tween 20 mixed-based MEKC under the same operation conditions.

3.3. Validation of the methods

So far, the optimum separation condition, where all eight aromatic compounds were completely separated, was achieved with a 10 mmol L^{-1} borate buffer (pH 9.2) containing 70 mmol L^{-1} SDS in the absence or presence of 25 mmol L^{-1} Tween 20. However, further comparison of the performances of both SDS-based MEKC and mixed SDS-Tween 20-based MEKC on the method validation was also needed. Under the respective selective condition, a series of mixed eight aromatic compounds standards

Table 1
Theoretical plate number, linear range, detection limits, reproducibility, and correlation coefficients of regression equations of eight aromatic compounds standards in SDS-based MEKC and mixed SDS–Tween 20-based MEKC methods

Analyte	Theoretical plate numbers (N/m)		Retention time reproducibility R.S.D. (%)		Peak area reproducibility R.S.D. (%)		Correlation coefficient		Linear range (g L ⁻¹)		Detection limits (g L ⁻¹ , S/N = 3)	
	SDS ^a	SDS–Tween 20 ^b	SDS	SDS–Tween 20	SDS	SDS–Tween 20	SDS	SDS–Tween 20	SDS	SDS–Tween 20	SDS	SDS–Tween 20
Aniline	15374	87829	0.17	0.23	2.08	1.45	0.9936	0.9973	60–320	40–400	60	15
Phenol	66087	154181	0.30	0.14	9.42	2.63	0.9962	0.9971	15–100	12.5–200	15	8
2-Chlorophenol	212292	263513	0.24	0.16	1.07	4.41	0.9958	0.9994	15–100	15–400	15	6
4-Nitrophenol	85386	122204	0.48	0.20	1.83	2.21	0.9943	0.9994	15–250	15–1300	15	12
Benzene	29793	116718	0.27	0.15	2.21	2.31	0.9916	0.9974	500–7000	400–5000	400	250
Toluene	48939	208870	0.37	0.25	3.36	5.00	0.9929	0.9957	100–2000	100–5000	100	50
Ethylbenzene	50970	175337	0.49	0.15	3.29	3.53	0.9942	0.9998	100–2000	100–5000	100	60
Naphthalene	49670	225278	0.61	0.21	3.98	1.75	0.9955	0.9964	5–60	4–200	5	4

^a SDS-based MEKC system, separation condition: a borax running buffer (pH 9.2) contained 70 mmol L⁻¹ SDS; 25 kV voltage; and 35 °C column temperature were applied.

^b Mixed SDS–Tween 20-based MEKC system, separation condition: a borax running buffer (pH 9.2) contained 70 mmol L⁻¹ SDS and 25 mmol L⁻¹ Tween 20 mixed micelles; 25 kV voltage; and 35 °C column temperature were applied.

at different concentration were injected to investigate the theoretical plate numbers, the linear ranges of the calibration curves, and the detection limits defined as the analyte concentration that gives a signal-to-noise ratio of 3:1. The reproducibility of the proposed methods was validated by six intra-day replicated injection. The results were listed in Table 1. Overall, the validated results of two MEKC methods indicated that mixed SDS–Tween 20-based MEKC had higher separation efficiency, better reproducible sample injection, higher linear calibration curves, wider linear range, and lower detection limit than SDS-based MEKC. Because the addition of the nonionic Tween 20 could significantly alter the surface structure of the micelles and improve the interactions of the micelles with the analytes, and at the same time there was no increase in the current and in Joule heat, high-separation efficiency and precision were produced.

4. Conclusion

The baseline separation of eight aromatic compounds was effectively achieved by MEKC with the use of either SDS micelles or SDS–Tween 20 mixed micelles. Various separation parameters were optimized. The selectivity could be mediated by manipulation of SDS micelle concentration and Tween 20 modifier concentration. The mixed SDS–Tween 20 micellar system could achieve the complete separation in a shorter time and offer higher separation efficiency and precision than the SDS micellar system. Moreover, the migration order of those analytes depended predominately on the hydrophobic interactions between each analyte and the micellar phases, but electrostatic interactions and hydrogen bonding interactions also played significant roles in the separation.

Acknowledgements

This work is supported by National Natural Science Foundation of China (Grant No. 20277032).

References

- [1] S. Terabe, K. Otsuka, K. Ichikawa, A. Tsuchiya, T. Ando, *Anal. Chem.* 56 (1984) 111.
- [2] S. Terabe, K. Otsuka, T. Ando, *Anal. Chem.* 57 (1985) 834.
- [3] S. Fujiwara, S. Honda, *Anal. Chem.* 59 (1987) 2773.
- [4] X. Fu, J. Lü, *Capillary Electrophoresis*, Zhejiang University Press, Hangzhou, China, 1997.
- [5] C.-H. Kuo, S.-W. Sun, *Anal. Chim. Acta* 482 (2003) 47.
- [6] J. Lü, X. Xu, X. Fu, *Chem. J. Chin. Univ.* 19 (1998) 1752.
- [7] J.S. Fritz, *Electrophoresis* 24 (2003) 1530.
- [8] X. Shang, Z. Yuan, *Anal. Chim. Acta* 456 (2002) 183.
- [9] R. Rodríguez, Y. Picó, G. Font, J. Manes, *J. Chromatogr. A* 924 (2001) 387.
- [10] M. Wang, J. Yan, Y. Lin, J. Lü, X. Fu, *Chin. Chem. Lett.* 13 (2002) 1203.

- [11] H. Stěrbová, P. Sevcíková, L. Kvasnicková, Z. Glatz, J. Slanina, *Electrophoresis* 23 (2002) 253.
- [12] R. Gotti, J. Fiori, M. Hudaib, V. Cavrini, *Electrophoresis* 23 (2002) 3084.
- [13] P.J.S. Filho, A. Rios, M. Valcárcel, E.B. Caramao, *Water Res.* 37 (2003) 3837.
- [14] C. Lin, B. Gulbis, E. Delobbe, F. Catton, F. Vertongen, *J. Chromatogr. B* 719 (1998) 47.
- [15] M.C. Boyce, P.R. Haddad, T. Sostaric, *Anal. Chim. Acta* 485 (2003) 179.
- [16] J. Kang, G.D. Reymaeker, A.V. Schepdael, E. Roets, J. Hoogmartens, *Electrophoresis* 22 (2001) 1356.
- [17] Y. Esaka, K. Tanaka, B. Uno, M. Goto, K. Kano, *Anal. Chem.* 69 (1997) 1332.
- [18] C. Lin, C. Chen, H. Chen, H. Huang, C. Lin, Y. Liu, *J. Chromatogr. A* 910 (2001) 165.
- [19] J. Lü, W. Yuan, X. Fu, *Proceedings of the 4th Symposium of Capillary Electrophoresis*, Guangzhou, 2000, p. 47.
- [20] W.E. Wall, D.J. Allen, K.D. Denson, G.I. Love, J.T. Smith, *Electrophoresis* 20 (1999) 2390.
- [21] S.P. Méndez, E.B. González, A. Sanz-Medel, *Anal. Chim. Acta* 416 (2000) 1.
- [22] R.J. Pascoe, A.G. Peterson, J.P. Foley, *Electrophoresis* 21 (2000) 2033.
- [23] G. Thorsén, J. Bergquist, *J. Chromatogr. B* 745 (2000) 389.
- [24] A.L. Crego, M.A. Garca, M.L. Marina, *J. Microcolumn Sep.* 12 (2000) 33.
- [25] C.D. Tran, J. Kang, *J. Chromatogr. A* 978 (2002) 221.
- [26] E.L. Hult, A. Emmer, J. Roeraade, *J. Chromatogr. A* 757 (1997) 255.
- [27] M. Wang, J. Yan, Y. Wang, J. Lü, X. Fu, *Acta Chim. Sinica* 61 (2003) 1980.
- [28] Y.C. Chen, C.E. Lin, *J. Chromatogr. A* 802 (1998) 95.
- [29] J. Manuel, H. Martínez, C. Ràfols, M. Rosés, J.L. Torres, E. Bosch, *Electrophoresis* 24 (2003) 707.
- [30] M.R.N. Monton, K. Otsuka, S. Terabe, *J. Chromatogr. A* 985 (2003) 435.
- [31] M.S. Leonard, M.G. Khaledi, *J. Sep. Sci.* 25 (2002) 1019.
- [32] M.G. Khaledi, J.G. Bumgarner, M. Hadumohammadi, *J. Chromatogr. A* 802 (1998) 35.
- [33] M.C. Boyce, E.E. Spickett, *J. Agric. Food Chem.* 47 (1999) 1970.
- [34] D.R. Lide (Ed.), *Handbook of Chemistry and Physics*, 84th ed., CRC Press, Boca Raton, FL, 2003.
- [35] H. Zhang, G. Hu, *Surfactant Chemistry*, Zhejiang University Press, Hangzhou, China, 1996.

Certification measurement of the cadmium, copper and lead contents in rice using isotope dilution inductively coupled plasma mass spectrometry

Emilia Vassileva, Christophe. R. Quétel*

*Isotope Measurements Unit, Institute for Reference Materials and Measurements, Joint Research Center,
European Commission, Retieseweg, B-2440 Geel, Belgium*

Received 10 March 2004; received in revised form 13 May 2004; accepted 13 May 2004

Available online 14 July 2004

Abstract

This paper describes the certification of the Cd, Cu and Pb amount contents in a rice material, that were used as reference values for round 19 of the international measurement evaluation programme (IMEP).

The protocol developed in this study was based on isotope dilution associated to inductively coupled plasma mass spectrometry (ID-ICP-MS). A multiple spiking approach was applied to reduce significantly the number of analytical steps. For the decomposition of the sample, three different microwave assisted digestion procedures were tested and compared. The use of hydrofluoric acid was found necessary to ensure full solubilisation and complete isotopic equilibration. Estimation of the combined uncertainty attached to the measurement results was performed according to the ISO guidelines. Contributions from the correction for moisture content, sample homogeneity, procedural blank, spike impurities, spectral interferences, instrumental background and dead-time effects were evaluated.

SI-traceable values with less than 2% combined uncertainty ($k = 2$) were obtained for Cd, Cu and Pb, respectively, $(14.39 \pm 0.21) \times 10^{-6} \text{ mol kg}^{-1}$, $(44.31 \pm 0.42) \times 10^{-6} \text{ mol kg}^{-1}$ and $(2.034 \pm 0.034) \times 10^{-6} \text{ mol kg}^{-1}$.

The rice powder was observed to be highly hygroscopic and a second series of isotope dilution mass spectrometry measurements was carried out on samples in equilibrium with the ambient moisture conditions ('saturated' samples). The Comité Consultatif pour la Quantité de Matière (CCQM) requested this approach for the participation to the key comparison 24 on the same rice test material. The excellent agreement for Cd between the IMEP-19 reference value, the value submitted by the institute for reference materials and measurements (IRMM) to CCQM-K24 and the corresponding reference value obtained as the arithmetic mean from the results of the 11 participating National Measurement Institutes (less than 0.27% difference) further validated this work. Eventually, this series of results on 'saturated' samples was submitted, for the 3 elements, as the IRMM contribution to the certification of the IRMM-804 rice candidate certified reference material (CRM).

© 2004 Elsevier B.V. All rights reserved.

Keywords: IDMS; ICP-MS; Cd, Cu and Pb in rice; Food matrix; Moisture determination; Uncertainty in chemical measurements; Metrology in chemistry; IMEP; BIPM-CCQM; Rice CRM

1. Introduction

Rice is the main foodstuff for about half of the world's population. For the last decades rice consumption has been expanding beyond the traditional rice-grown areas, particularly in Europe. In most countries, surveillance measures are taken regarding the presence of contaminants in important

foodstuff such as rice to protect the public health. Cd and Pb maximum levels in foodstuff are set in relevant regulation such as the EC Directive 466/2001 [1].

Cadmium may induce dysfunction and reproductive deficiencies in humans and is suspected to act as a human carcinogen [2]. Lead can cause brain damage, kidney failure, seizures and anaemia [3]. Accurate measurement of trace levels of essential elements like Cu in foodstuffs is also of crucial importance to estimate dietary uptake rates required for normal human growth.

* Corresponding author. Tel.: +32 14 571 658; fax: +32 14 571 863.
E-mail address: christophe.quetel@cec.eu.int (C.R. Quétel).

Risk assessment, on the one hand, provides a tool for making decisions to ensure the protection of the consumer and, on the other hand it may also have repercussions on international trade (e.g. stop of import/export). Important conclusions and decisions linked to the customer protection sphere derive from measurement results that have to be based on reliable data of good quality (e.g. sufficiently small uncertainty). To be comparable, measurement results must be traceable to the same system of reference, preferably to SI.

Comparison 19 of the international measurement evaluation programme (IMEP) [4] was organised in support of the area of measurements covered by the above mentioned EC Directive. It focused on the evaluation of the measurement performance for the determination of the Cd, Cu and Pb mass fractions in rice. IMEP is owned and co-ordinated by the institute for reference materials and measurements (IRMM). It is one of the few inter-laboratory comparison programmes world-wide that do not evaluate measurement performance against consensus values (i.e. derived from the participants' results). Test samples with undisclosed values are sent to interested participants who can have their results (claimed performance) compared to a certified 'reference value' with stated uncertainty and traceable to the SI whenever possible.

In parallel to IMEP-19 identical samples were offered to the Comité Consultatif pour la Quantité de Matière (CCQM) [5] for its key comparison K-24. This corresponds to a need for increasing the awareness of food quality issues, and other CCQM inter-comparisons were also organised recently on the same topic (CCQM-P12 on Pb in wine [6]; CCQM-P13 on Ca, Cu, and Cd in artificial food digests [7]). Proposed EU legislation setting limits on levels of toxic elements in food have led to the publication of several papers dealing with analytical determination of metal contaminants in a range of foodstuff. This is often a difficult topic because of the low concentrations and the complexity of the sample matrices. Hence, very sensitive analytical techniques are required. Graphite furnace atomic absorption, preferably with Zeeman background correction, is commonly used to determine Cd, Pb and Cu in different food matrices [8,9]. In recent years inductively coupled plasma mass spectrometry (ICP-MS) has been increasingly applied to the determination of trace elements in food samples, because of its low detection limits, multi-element capability, large dynamic range and rapid analysis time [6,7,10–14]. Some of these studies were dedicated to rice and grain samples in particular [12–14]. And only two involved a procedure based on isotope dilution mass spectrometry (IDMS), one on a diluted microwave digest [13] and the other on matrix separated (silica-immobilised 8-hydroxyquinoline column) samples [14].

IDMS is a powerful strategy capable of highly accurate (small combined uncertainty) results. The CCQM recognised it as a potentially primary method of measurement, i.e. a method "having the highest metrological qualities, whose operation can be completely described and understood, for which a complete uncertainty statement can be written down

in term of SI units" [15]. The CCQM also stated that 'measurements of amount of substance, to be considered primary, must be made using a method for which the values of all parameters, or corrections which depend on other species or the matrix, are known or can be calculated with appropriate uncertainty' [15].

IDMS is based on the measurements of isotope amount ratios. This is often advantageous in the case of samples with strong matrix effects [16], such as food products. Digesting the rice sample following the spike addition ensures the isotope equilibration and drastically reduces the matrix effects during the isotope ratio measurements. Measuring isotope amount ratios has the additional advantage of making the procedure independent of other possible sources of uncertainties, such as analyte loss occurring during the sample treatment [17].

The objectives of this work were to demonstrate the application of IDMS to SI-traceable certification measurements of the Cd, Cu and Pb mass fractions in rice. An analytical procedure, using a microwave digestion method and multiple spiking of the replicate samples was developed for this purpose.

2. Experimental

2.1. Rice, chemicals and materials

The rice powder used in IMEP-19 was provided by the National Metrology Institute of Japan and originates from rice grown in cadmium contaminated water. The cadmium amount content in this rice material was envisaged to be close to the upper limit as stated in Japanese regulation.

The test material was prepared at IRMM following standard procedures, including milling, drying, storage under dry conditions, reprocessing into units of 15 g and bottling in glass containers [18].

High quality deionised water from Milli-Q system (Millipore, Bedford, MA, USA) was used throughout this work. Ultra pure nitric acid (Ultrex[®], T.T. Baker, Phillipsburg, NJ, USA) and in-house sub-boiled hydrofluoric acid, HF (originally p.a. from Merck, Darmstadt, Germany) were used for sample digestion. Hydrogenperoxide (p.a. from Merck) was also used in preliminary investigations.

The Isotopic Certified Reference Materials (ICRM) used for IDMS purposes for the 3 elements are listed in Table 1.

Only new labware material (bottles, vessels, tips, syringes, etc.) was employed and it was cleaned thoroughly following a procedure described elsewhere in detail [7]. In order to avoid risks of memory effects from previous experiments, digestion vessels were submitted to a supplementary hot cleaning procedure—first addition of approximately 10 g concentrated HNO₃ to each vessel; second microwave treatment at 350 W for 10 min; third the vessels were thoroughly rinsed with Milli-Q water.

Table 1
Certified reference materials used in the measurement process

Element	CRM	Main characteristic isotopic composition	Use
Cd	IRMM-622	^{111}Cd enriched	Isotope dilution spike
Cu	IRMM-632	^{65}Cu enriched	Isotope dilution spike
	IRMM-633	Natural	Correction for mass-discrimination
Pb	NIST SRM 991	^{206}Pb enriched	Isotope dilution spike
	NIST SRM 981	Natural like	Correction for mass-discrimination
	NIST SRM 982	Equal-atom between ^{206}Pb and ^{208}Pb	Correction for mass-discrimination

All sample processing steps were performed at the ultra-clean chemical laboratory, a clean room environment for sample preparation available at IRMM.

2.2. Instrumentation

Microwave assisted digestion of the rice material was performed using a Milestone Microwave System MLS 1200 (Milestone Laboratory Systems, Bergamo, Italy) equipped with a carousel holding 6 teflon digestion vessels.

All isotope ratio measurements were carried out with an Elan 6000 ICP-MS (Perkin Elmer Sciex, Ontario, Canada), equipped with a low flow Meinhard type nebulizer (Glass Expansion, Australia) and a Cinnabar Spray Chamber (Glass Expansion, Australia). The system parameters and the measurement method (Table 2) were adjusted for optimum repeatability of the isotope ratio measurements. The signal intensities per replicate were corrected for dead-time, instrumental blank and possible interferences prior to calculating an average ratio and RSD. The Elan 6000 was also used to carry out semi-quantitative measurements ('total quant' routine) for the survey of the sample composition.

The presence of isobaric interference on Cu masses was investigated at medium mass resolution with an Element 2 single collector magnetic sector ICP-MS (ThermoFinnigan, Bremen, Germany). The instrument was equipped with a PFA nebulizer and a cyclonic spray chamber.

The dead-time value and its associated standard uncertainty were determined according to corrected methods described by Nelms et al. [19].

2.3. Analytical protocols

The complete protocol deployed for the certification of the Cd, Cu and Pb amount content in rice is schematically represented on Fig. 1. It combined a sample decomposition stage by microwave digestion with 'direct' IDMS measurements (Eq. (1)). In order to reduce significantly the number of analytical steps and intermediate samples a multiple spiking approach was applied [20].

$$c_X = c_Y \frac{m_Y}{m_X} \left(\frac{R_Y - (K_B R_B)}{(K_B R_B) - R_X} \right) \frac{\sum(R_i)_X}{\sum(R_i)_Y} - \frac{(a_{\text{blank}} + a_{\text{impurity}})}{m_X} \quad (1)$$

X , Y and B indices denote the sample, the spike and the blend solutions, respectively; c , m , individual R and $\sum(R_i)$ indicate successively element amount contents, masses, the same working isotope ratio in the three solutions and the sums of all ratios (all the ratios are referenced to the same isotope of the element).

The blend isotope ratios were corrected externally for mass-discrimination by measuring, immediately before and immediately after, the ratio of interest in the material used as reference (comparison between the known ratio and the measured ratio, $K_B = R_{\text{Known}}/R_{\text{Meas}}$).

Table 2
Experimental setting for the Elan 6000 ICP-MS

Parameter	Cd	Cu	Pb
Plasma gas flow (L min^{-1})	14.8	14.8	14.8
Auxiliary gas flow (L min^{-1})	0.850	0.850	0.850
Nebulizer gas flow (L min^{-1})	0.940	0.935	0.935
Plasma power (W)	1100	1100	1100
Sensitivity for 1 ng g^{-1} (cps)	200,000	150,000	190,000
Background on mass 220 (cps)	<10	<10	<10
Dead-time (ns)	55 ± 6 ($k=2$)	51 ± 6 ($k=2$)	61 ± 6 ($k=2$)
Lens voltage (autolens off) (V)	9.32	8.5	11
Number of sweeps/replicate	250	250	300
Number of replicate	6	6	6
Dwell time per isotope (ms)	20 for ^{110}Cd , ^{111}Cd , ^{112}Cd , ^{113}Cd , ^{114}Cd , 10 for ^{98}Mo , ^{117}Sn , ^{105}Pd	20 for ^{63}Cu , ^{65}Cu	20 for ^{204}Pb , ^{206}Pb , ^{207}Pb , ^{208}Pb , 10 for ^{201}Hg
Short settling time enabled	Yes	No	Yes
Total analysis time /sample (s)	212.7	103.5	207

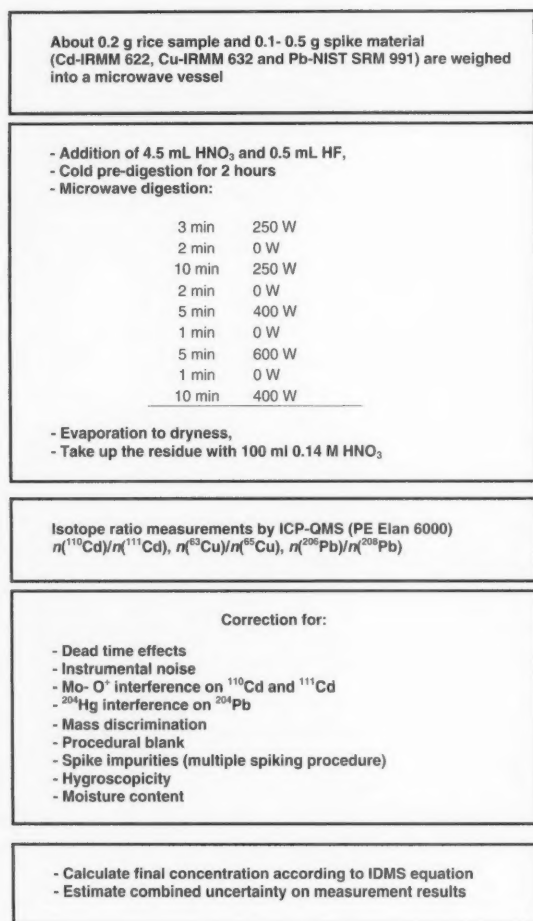


Fig. 1. Analytical protocol applied for the determination of Cd, Cu and Pb amount contents in rice sample, using IDMS.

The absolute amount of the element measured in the procedural blank, a_{blank} , was obtained by adding identical chemical reagents in similar proportions to separate bottles and submitting them to identical treatment than those of the IMEP-19 sample. The absolute amount of the element measured, introduced in the blends with spike solutions of other elements, because of the multiple spiking approach, is called a_{impurity} .

The evaluation of the amount of spike to add resulted from a compromise between factors including the results from preliminary semi-quantitative measurements, the characteristics of the spike materials themselves (certificate data), the calculation of the lowest error magnification factor [21], sufficiently high counting rate, the detector range and the minimisation of dead-time effects. Within these conditions, the optimum $n(^{63}\text{Cu})/n(^{65}\text{Cu})$ blend ratio was calculated to be 0.3 for a corresponding error magnification factor of 1.16, whereas the optimum $n(^{110}\text{Cd})/n(^{111}\text{Cd})$ blend ratio was calculated to be 0.105 for a corresponding error magnification

factor of 1.16. In the case of lead the optimum blend ratio $n(^{206}\text{Pb})/n(^{208}\text{Pb})$ was 0.2, for a corresponding error magnification factor of 1.10.

A comparison was made between two series of IDMS experiments. The first series corresponded to 'non-saturated' samples (i.e. samples spiked immediately after opening of the rice bottles), and 15 blends (three sub-samples per bottle) were prepared. The second series corresponded to 'saturated' samples (i.e. samples spiked after having attained a moisture equilibrium with the laboratory ambient atmosphere), and 10 blends (two sub-samples per bottle) were prepared. Weighing of the reference materials and addition of the spike aliquots were performed exclusively through metrological gravimetry principles in a humidity-controlled area using substitution measurements against operational mass standards. Sub-samples of rice were taken for the determination of their water content.

Typically, ~0.2 g of the rice material was blended directly into a microwave vessel with ~0.33 g of the IRMM-622 ^{111}Cd , ~0.22 g of the NIST SRM-991 ^{206}Pb and ~0.132 g of the IRMM-632 ^{65}Cu spike solutions.

2.4. Determination of the water content

Two methods were investigated and compared for the determination of the water content in the rice material. The Karl Fisher titration [22] was carried out on two samples of 0.2 g samples from five bottles (10 samples in total). The second method consisted in drying approximately 1 g test samples for 18 h at $85 \pm 2^\circ\text{C}$ in a ventilated oven under atmospheric pressure, and weighing the samples every 6 h until a difference not exceeding 0.001 g with the previous attempt would be achieved. This method was applied to 15 samples (three samples/bottle) taken from the same five bottles used for the 'saturated' samples experiments.

Rice material was found to take up moisture under normal laboratory condition. The hygroscopicity of the 'non-saturated' samples from three different bottles was evaluated by weighing 0.2 g rice samples at regular time intervals during 150 min from the opening of the sample bottle. Hygroscopicity was estimated under the same environmental conditions, as weighing the samples and measuring the increase in mass of one typical blend sample. Based on the repeated measurements of moisture pick-up isotherms, the correction for hygroscopicity was evaluated. The rate of water absorption used to calculate the change in mass of blend samples was calculated from the equations describing the water absorption versus the time.

2.5. ICP-MS isotope ratio measurements

Dilution of all samples was adjusted to achieve intensities ranging between 30,000 and 300,000 counts s^{-1} (minimisation of the uncertainty propagation associated with the correction for dead-time and instrumental background). Cd and

Pb isotope ratio in blend solutions were measured without dilution whereas, for Cu isotope ratio measurements, blend samples were further diluted by a factor 5.

The isotopic composition of Cu and Cd in the rice material was assumed natural and taken from column nine in the IUPAC table [23]. As for Pb it was measured.

The selection of the isotopes to be measured in the blend samples was done with respect to availability of spike materials, abundance of the isotopes and possible spectral interferences during measurement by ICP–MS.

For correction of these interferences, the equation 2 was used:

$$I_{a1}^{\text{cor}} = I_{a1}^{\text{tot}} - I_{b2} \cdot \frac{A_{b1}^{\text{IUPAC}}}{A_{b2}^{\text{IUPAC}}} \quad (2)$$

In this equation $a1$ represents the interfered isotope of the element a , $b1$ represents the interfering isotope of element b and $b2$ represents the isotope of element b used to extrapolate the magnitude of the interference from $b1$. The abundance values A are taken from column nine of the IUPAC table [23].

The Cd isotopes ^{110}Cd , ^{111}Cd , ^{112}Cd , ^{113}Cd and ^{114}Cd were measured simultaneously in the blends, as the comparison of the results of the IDMS calculations using different pairs of isotopes can help revealing the presence of biases due to spectroscopic interferences. The $n(^{206}\text{Pb})/n(^{208}\text{Pb})$ ratio was selected for Pb as both isotopes were free of significant spectral interferences.

Careful rinsing followed by a check of the instrumental background was performed prior to every sample measurement in order to monitor sample to sample memory effects and correct for them, if necessary.

The ICP–MS measurement sequence was as follows: first a 0.14 mol L^{-1} HNO_3 solution to evaluate the instrumental background, then a calibration solution for the K-factor determination, third another 0.14 mol L^{-1} HNO_3 solution, and finally two blend solutions.

2.6. Uncertainty estimation

All uncertainties indicated are expanded uncertainty $U_c = k u_c$ where u_c is a combined standard uncertainty and k is a coverage factor equal to 2. Combined standard uncertainties on the certified results were obtained by propagating together individual uncertainty components according to the ISO/GUM guide [24]. In practice, a dedicated software program [25] was used, based on the numerical method of differentiation described by Kragten [26]. Commonly, there are ‘additive’ corrections applied to the individual isotope signal intensities such as those for the instrumental background, the isobaric interferences and to some extent, the dead-time effect. These factors cannot be neglected. However, propagating these uncertainties directly with the repeatability of the measurements of the individual isotope signal intensities can lead to a gross overestimation of the resulting combined uncertainty. To avoid this risk and for the combined uncer-

tainty calculations only, ‘additive’ corrections on intensities were translated into multiplicative correction factors on ratios following a method described elsewhere [27].

3. Results and discussion

3.1. Rice decomposition method

Several methods of rice decomposition involving various combinations of acids and microwave digestion have been described [13,14,28–31]. The main drawback with these methods, apart from the complexity, is the risk of producing very high and possibly not reproducible procedural blanks. Comparatively, the method we developed involved smaller amounts of chemical reagents relative to the amount of rice being digested in order to reduce this problem of contamination.

Rice is a complex mixture of carbohydrates, proteins, fats, fibres and mineral silicates that requires particular methods to ensure completeness of the decomposition [32]. For some trace elements, poor recovery rates can be observed due to incomplete digestion of silicon bound phases [10,33,34]. The use of hydrofluoric acid followed by an evaporation to dryness step can be essential for the decomposition of silica compounds (and, volatilisation of the silicon as SiF_4). Beside the improvement in solubilisation, this also results into less solid residues in the digests, which is advantageous for ICP–MS measurements.

With respect to the above mentioned considerations three different digestion procedures for rice were evaluated—digestion with HNO_3 only, digestion with $\text{HNO}_3\text{--H}_2\text{O}_2$ and with $\text{HNO}_3\text{--HF}$.

As it can be seen from Fig. 2, sample dissolution was more complete with the $\text{HNO}_3\text{--HF}$ digestion mixture than with the first two others, particularly for Cu and Cd. Thus, the third digestion strategy was retained for these certifications.

3.2. Selection of the isotopes and interference correction

Medium mass resolution spectra demonstrated that none of the Cu isotopes were significantly affected by possible Ar--Na^+ , Ba^{++} or Si--Cl^+ interferences and thus, could be measured by Q-ICP–MS in the blend samples without further corrections.

Cd measurements by ICP–MS can easily suffer from spectral interference [7]. The isotopes ^{112}Cd , ^{114}Cd and ^{116}Cd suffer from interference by tin. ^{110}Cd is interfered by ^{110}Pd . The MoO^+ interference affects all Cd isotopes except ^{106}Cd , which is not suitable as a reference isotope for IDMS, because of its low abundance (1.25%). In the present study the signal on ^{98}Mo was 20,000–26,000 cps and the possibility of MoO^+ interferences was investigated more particularly. Using the same experimental parameters as for the blend measurements, the oxide formation rate for several Mo isotopes was measured by means of a Mo solution at 100 ng g^{-1} , and

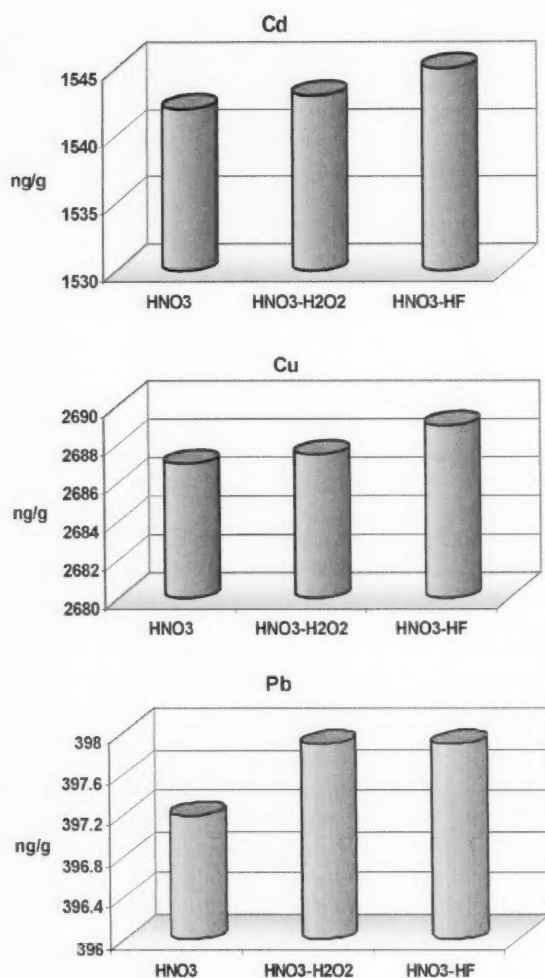


Fig. 2. Comparative study of three procedures, applied for the digestion of rice sample.

was found to be $\sim 0.25\%$. This interference, which was corrected for on all five isotopes, contributed very little to the signals measured (less than 0.01% for ^{110}Cd and ^{111}Cd). An excellent agreement, within uncertainty, was found between the IDMS results obtained using the different pairs of Cd isotopes. This was probably a good indication that no major problem of interference had been left behind following the various corrections, and that complete isotopic equilibration had been achieved during the sample digestion step. The $n(^{110}\text{Cd})/n(^{111}\text{Cd})$ ratio was selected for the final certification calculations as it corresponded to the combination of the less interfered isotopes.

The Pb isotopic composition in the sample was determined from three independent measurements of the isotope ratios $n(^{204}\text{Pb})/n(^{206}\text{Pb})$, $n(^{207}\text{Pb})/n(^{206}\text{Pb})$ and $n(^{208}\text{Pb})/n(^{206}\text{Pb})$. The ^{201}Hg signal was monitored to correct for ^{204}Hg on ^{204}Pb ($\sim 0.5\%$ of the signal). The derived isotopic composition of lead in the sample is listed in

Table 3

Lead isotopic composition of the rice material

Isotope (%)	Abundance ($\pm U$, $k = 2$)
^{204}Pb	1.3740 ± 0.0076
^{206}Pb	24.960 ± 0.042
^{207}Pb	21.330 ± 0.059
^{208}Pb	52.336 ± 0.081

Table 3. From this data, the atomic weight of lead in the rice material was calculated to be $M_{\text{Pb sample}} = (207.2084 \pm 0.0012) \text{ g mol}^{-1}$.

3.3. Amount content determination and uncertainty estimation

The Cu, Cd and Pb amount contents were corrected principally for contamination effects and moisture content. The individual uncertainty components associated to these corrections, but also to those of the isotope ratio measurement results (spectral interferences, instrumental background and dead-time effects) were propagated together. This way, the combined uncertainty statements (as detailed in Table 4) that arise go far beyond the simple repeatability calculations and reflect our understanding of the measurement process. Very importantly they ensure the comparability of our results with others.

The contamination effects accounted for (Table 5) included those occurring during sample preparation (six procedural blank measurements) and those arising from the multiple spiking approach chosen (three replicate measurements per spike material).

Two methods for correcting for dry mass were compared. Additionally, this correction needed to be addressed differently whether the samples would be allowed to equilibrate with the laboratory ambient moisture conditions or not before addition of the IDMS spike. In the later case, measuring the sample hygroscopicity was necessary to account for moisture pick-up during IDMS blend sample preparation. These experiments are described in detail in a separate paper [35]. Water content determination remains an important source of discussions. Under given experimental drying conditions, mainly water but also other volatile substances present in the sample are evaporated. Also, the determination of water in food matrices leads to discussions about the different binding forms of water, and only the Karl Fisher titration method provides results which can be attributed to the total water content, a defined physical property [22,36]. Although, from the above, moisture could easily be seen as an operationally defined parameter our results show that, for this rice sample and under our experimental conditions, this was not necessarily the case.

Considering that usual practice in field laboratories probably consists in performing their measurements on non moisture-equilibrated samples, the certified values for IMEP-19 were established from the series of 'non-saturated'

Table 4

Typical uncertainty budget for the determination of Cd, Cu and Pb in 'non-saturated' samples (IMEP-19 rice sample)

	Cd; $U_c = 1.5\%$; $k = 2$	Cu; $U_c = 1.0\%$; $k = 2$	Pb; $U_c = 1.6\%$; $k = 2$
Main uncertainty contributions (%)			
s.u. on the correction for dead-time effect on isotope signal intensities during individual blend ratio measurements	13.4	10.3	1.1
s.u. on the correction factor for hygroscopicity	24.8	59.4	6.6
s.u. on IUPAC isotopic composition data	49.3	–	–
s.u. on certified ratio value of the spike R_Y	9.3	0.5	–
s.u. on spike concentration C_Y	1.4	18.9	0.5
s.u. on the correction factor for moisture	0.9	2.2	0.7
s.u. on the correction for procedural blank and impurity	–	–	88.7
s.u. on the correction for dead-time effect on isotope signal intensities during individual K factor measurements	–	7.4	–
Other	0.9	1.3	2.4

s.u.: standard uncertainty; U_c : combined uncertainty.

Table 5

Procedural blanks ($n = 6$) and impurity content of spike materials

	Cd	Cu	Pb
Procedural blank (nmol)	$0.00026 \pm 130\%$	$0.01235 \pm 79\%$	$0.00380 \pm 89\%$
Procedural blank (ng)	$0.0288 \pm 134\%$	$0.7851 \pm 78\%$	$0.782 \pm 90\%$
Impurity content Pb SRM 991 nmol g^{-1}	$6.776 \times 10^{-5} \pm 50\%$	$1.481 \times 10^{-3} \pm 50\%$	–
Impurity content Cu IRMM-632 nmol g^{-1}	$3.716 \times 10^{-3} \pm 50\%$	–	$1.348 \times 10^{-3} \pm 50\%$
Impurity content Cd IRMM-622 nmol g^{-1}	–	$5.349 \times 10^{-2} \pm 50\%$	$1.733 \times 10^{-2} \pm 50\%$

The relative standard uncertainties include a coverage factor $k = 2$. Molar masses used: Cd $112.411(8) \text{ g mol}^{-1}$ [38]; Cu $63.5456(40) \text{ g mol}^{-1}$ [39]; Pb $207.2084 (12) \text{ g mol}^{-1}$.

samples using Karl Fisher titration for moisture determination. The obtained result for water content in rice on 10 measurement replicates was 4.53% of the sample weight with 0.13% expanded uncertainty ($k = 2$) of the sample weight. A factor accounting for progressive moisture pick-up, obtained from simulation experiments over 2.5 h (Fig. 3), was added to this correction. Considering that 1 min was approximately the duration for the preparation of an IDMS blend sample, the correction factor for hygroscopicity was evaluated to be 0 with 0.70% expanded uncertainty ($k = 2$).

For the CCQM-K24 comparison exercise an approach based on 'saturated samples' and the use of a drying method based on oven treatment was prescribed to ensure comparability of the results obtained by the different participants [37]. As drying methods do not allow to distinguish between water and other volatile substances, the choice of our experimental parameters required a careful investigation. The

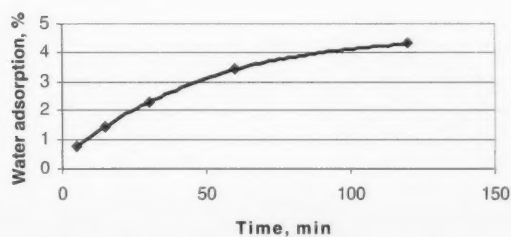


Fig. 3. Water adsorption (%) from 0.2 g rice sample.

moisture determination was eventually performed at 85°C on 15 samples and led to a average water content in rice of 4.37% of the sample weight with 0.11% expanded uncertainty ($k = 2$). There is a significant difference with the value obtained using Karl Fisher titration, which is not surprising considering the fact that these results have been obtained from 'saturated' and 'non-saturated' samples, respectively.

However, the IDMS results achieved from the two series of samples mentioned above were in excellent agreement within uncertainty, irrespective of the method used to correct for moisture content. This was also the case between our contribution for Cd and the corresponding CCQM-K24 reference value obtained as the arithmetic mean from the results of all participants (less than 0.27% difference) [37]. All our results and contributions to the various applications described are reported in Table 6. It must be noted that, from the results available for the 'saturated' samples series (10 replicates from five bottles), we only reported as our CCQM-K24 value the average of the two replicates from only one bottle as only one bottle had been distributed to each participant. Similarly, the IRMM contribution to the certification of the IRMM-804 rice candidate CRM was based also and for the three elements on the average of the two replicates from only one bottle. This was considered to be the way to avoid that our contribution cover, even partially, for between bottle homogeneity as this will be taken into consideration at a later stage by the certification body.

As can be seen from Table 4, for the three elements the correction for hygroscopicity represented a major contribu-

Table 6

IRMM contribution to IMEP-19 (used as reference values), CCQM-K24 and the certification of the IRMM-804 rice candidate CRM

	Cd		Cu		Pb	
	mg kg ⁻¹	μmol kg ⁻¹	mg kg ⁻¹	μmol kg ⁻¹	mg kg ⁻¹	μmol kg ⁻¹
IMEP-19 ('non-saturated' samples; 5 bottles; 15 replicates)	1.618 (24)	14.39 (21)	2.816 (27)	44.31(42)	0.4214 (69)	2.034 (34)
CCQM-K24 ('saturated' samples; 1 bottle; 2 replicates)	1.626 (24)	14.46 (22)	—	—	—	—
IRMM-804 Rice Candidate RM ('saturated' samples; 1 bottle; 2 replicates)	1.626 (21)	14.46 (19)	2.813 (20)	44.27 (32)	0.418 (14)	2.018 (66)

The combined uncertainties are given in parentheses and include a coverage factor $k = 2$. They apply to the last two digits of the value. Molar masses used: Cd 112.411(8) g mol⁻¹ [38]; Cu 63.5456(40) g mol⁻¹ [39]; Pb 207.2084 (12) g mol⁻¹.

tion to the combined uncertainty statements, and was even the first one for Cu (nearly 60%). The largest uncertainty contributors for Cd (nearly 50%) were the IUPAC data used as R_X values in the IDMS equation, and for Pb, by far (nearly 90%) the uncertainty on the correction for contamination during the sample preparation (procedural blank).

A relative expanded uncertainty ($k = 2$) below 2% was achieved for all three certified amount contents (Cd, Cu and Pb) used as reference values for the IMEP-19 comparison. The transparency provided throughout this paper associated to the thorough estimation of realistic combined uncertainties contribute strongly to the validation of the analytical protocols developed for this certification exercise.

Acknowledgements

The metrological weighing performed by Mrs. B. Dyckmans (IRMM, Geel, Belgium) is gratefully acknowledged. The authors thank Dr. Ph. Taylor and Dr. J. Diemer for fruitful discussions during the certification work.

References

- [1] Commission Regulation (EC) N 466/2001 of 8 March 2001 setting maximum levels for certain contaminants in foodstuff, Official Journal of the European Communities L077, 16/03/2001, 0001–0013.
- [2] H. Boiteau, A. Pineau, Cadmium in: H.A. Mc Kenzie, L.E. Smythe, Quantitative Trace Analysis of Biological Materials, Elsevier Science Publishers B.V., 1988, p. 543.
- [3] T.R. Daher, Anal. Chem. 67 (1995) 405R.
- [4] <http://www.irmm.jrc.be/>.
- [5] <http://www.bipm.fr/>.
- [6] C.R. Quétel, S. Nelms, L. Van Nevel, I. Papadakis, P.D.P. Taylor, J. Anal. At. Spectrom. 16 (2001) 1091.
- [7] E. Vassileva, C.R. Quétel, I. Petrov, Spectrochim. Acta Part B 58 (2003) 1553.
- [8] D. Santos Jr., F. Barbosa Jr., A.C. Tomazelli, F.J. Krug, J.A. Norbega, M.A.Z. Arruda, Anal. Bioanal. Chem. 373 (2002) 183.
- [9] A. Taylor, S. Branch, A. Fisher, D. Halls, M. White, J. Anal. At. Spectrom. 16 (2001) 421.
- [10] X. Feng, S. Wu, A. Wharmby, A. Wittmer, J. Anal. At. Spectrom. 14 (1999) 939.
- [11] E. Larsen, G. Pedersen, J. Mc Laren, J. Anal. At. Spectrom. 12 (1997) 963.
- [12] S. D'Ilio, M. Alessandrelli, R. Cresti, G. Forte, S. Caroli, Microchim. J. 73 (2002) 195.
- [13] K. Okamoto, Sci. Total Environ. 107 (1991) 29.
- [14] X. Park, J.K. Sun, J. Anal. At. Spectrom. 12 (1997) 573.
- [15] Comité consultatif pour la quantité de Matière, Rapport de la 1^{ère} session, BIMP, Sèvres, France, 1995.
- [16] H. Falk, R. Geerling, B. Hattendorf, K. Krenzel-Rothensee, K.P. Schmidt, Fresenius J. Anal. Chem. 359 (1997) 352.
- [17] K.G. Heumann, Isotope dilution mass spectrometry (IDMS) of the elements, Mass Spectrom. Rev. 11 (1992) 41.
- [18] Y. Aregbe, C. Harper, J. Norgaard, M. De Smet, L. Van Nevel, P. Smeyers, P. D. P. Taylor, IMEP-19 Trace Elements in Rice EUR 20551 EN Report to Participants, 2003, p. 5.
- [19] S. Nelms, C.R. Quétel, T. Prohaska, M. Hamester, W. Kerl, P. Taylor, J. Anal. At. Spectrom. 16 (2001) 333.
- [20] T. Prohaska, C.R. Quétel, C. Hennessy, D. Liesegang, I. Papadakis, P.D.P. Taylor, C. Latkoczy, S. Ham, G. Stinger, J. Environ. Monitoring 2 (2000) 613.
- [21] P. De Bièvre, Trace Element Analysis in Biological Specimens, in: R.F. Herber, M. Stoepller (Eds.), Isotope Dilution Mass Spectrometry (IDMS), Elsevier, Amsterdam, 1994, p. 169.
- [22] K. Schmit, H.D. Isengard, Anal. Bioanal. Chem. 360 (1998) 465.
- [23] International union of pure and applied chemistry, isotopic composition of the elements 1997, Pure Appl. Chem. 70 (1998) 217.
- [24] International Standards Organisation, Guide to Expression of Uncertainty in Measurement, ISBN 92-67-10188-9, ISO, Geneva, 1995.
- [25] GUM Workbench, The Software Tool for the Expression of Uncertainty in Measurement, Metrodata GmbH, D-79639, Grenzach-Wyhlen, Germany.
- [26] J. Kragten, The Analyst 119 (1994) 2161.
- [27] C.R. Quétel, T. Prohaska, S. Nelms, J. Diemer, P. Taylor, in: G. Holland, S. Tanner (Eds.), Proceeding of the 7th Durham Conference, Plasma Source Mass Spectrometry: The New Millennium, Royal Society of Chemistry, Cambridge, 2001, p. 257.
- [28] G. Schelkoph, B.D. Milne, Anal. Chem. 60 (1988) 2060.
- [29] S. Wu, Y.H. Zhao, X. Feng, A. Wittmeier, J. Anal. At. Spectrom. 12 (1994) 797.
- [30] E. Beary, P. Paulsen, J. Fassett, J. Anal. At. Spectrom. 9 (1997) 1363.
- [31] T.D. Phuong, P.V. Chuong, D.T. Khiem, S. Kokot, The Analyst 124 (1999) 553.
- [32] D.T. Khiem, S. Kokot, The Analyst 124 (1999) 561.
- [33] M. Hoenig, Talanta 54 (2001) 1021.
- [34] S. Wu, Y.H. Zhao, X. Feng, J. Anal. At. Spectrom. 11 (1996) 287.
- [35] E. Vassileva, C.R. Quétel, Influence of the Correction for Moisture Content on the Quality of the Certification of Cd, Cu and Pb Mass Fractions in Rice (in preparation).
- [36] H.D. Isengard, Trends Food Sci. Technol. 6 (1995) 155.
- [37] Y. Aregbe, P. Taylor, in: CCQM-K24 key comparison—Cd amount content in rice, GE/R/IM/37/02, EC JRC IRMM, Geel, Belgium, 2002.
- [38] International Union of Pure and Applied Chemistry, Atomic Weights of The Elements 1995, Pure Appl. Chem. 68 (1996) 2339.
- [39] IRMM Certificate Spike Isotopic Reference Material IRMM 633.

Determination of bismuth and cadmium after solid-phase extraction with chromosorb-107 in a syringe

Nilgun Tokman, Suleyman Akman*

Fen-Edebiyat Fakultesi, Istanbul Teknik Universitesi, Kimya Bolumu, 34469 Maslak-Istanbul, Turkey

Received 14 April 2004; received in revised form 28 May 2004; accepted 28 May 2004

Available online 10 July 2004

Abstract

The determination of bismuth and cadmium by graphite furnace atomic absorption spectrometry (GFAAS) after solid-phase extraction (SPE) on Chromosorb-107 filled in a syringe was described. To retain the analytes, the sample solution treated with and without ammonium pyrolidine dithiocarbamate (APDC) was drawn into the syringe filled with Chromosorb-107 and discharged back manually. Bismuth and cadmium were quantitatively sorbed at $\text{pH} \geq 6$ irrespective of whether the analyte was complexed with APDC prior to passing through the Chromosorb-107. Analyte elements sorbed on the resin were quantitatively eluted with 3.0 M of HNO_3 again drawing and discharging the eluent into the syringe and ejected it back. Optimum flow rates of sample or eluent for sorption and elution processes were 20 ml min^{-1} for drawing and 20 ml min^{-1} for discharging in all cases. Bismuth and cadmium were analyzed by graphite furnace atomic absorption spectrometry. The elements could be concentrated by drawing and discharging several portions of sample successively but eluting only one time. The validity of the proposed method was checked with standard reference materials (NIST SRM 1515 Apple-Leaves, CWW-TM-E Waste Water and CRM-SW Sea Water). The analyte elements were quantitatively (>95%) recovered from different matrices irrespective of treated samples with APDC. Detection limits (δ) were 0.8 and $1.2 \mu\text{g l}^{-1}$ for Bi and Cd, respectively. The method can be characterized with fastness, simplicity, quantitative recovery and high reproducibility.

© 2004 Elsevier B.V. All rights reserved.

Keywords: Solid-phase extraction; Syringe technique; Bismuth and cadmium; Graphite furnace atomic absorption spectrometry

1. Introduction

Cd is one of the chief elements studied in AAS studies because even its ultratrace concentration is not desirable because of its high toxicity and fairly long biological half-life should be determined in all matrices. Bismuth is not an essential element for plants and animals. It has been used in antiacids, peptic ulcer treatments, some kinds of gastritis treatments and tropical dermatological creams. As the use of bismuth in medicine increased, it has spread in the environment and the chance of exposure of organisms to bismuth has increased. A number of toxic effects in humans have been attributed to bismuth compounds, such as nephrotoxic, neurotoxic, kidney damage symptoms nephropathy, osteoarthritis, hepatitis and neuropathology. Thus, determination of bismuth at ultra-trace levels in biological fluids

such as serum, whole blood or urine and body tissues are important. In addition, the presence of trace amounts of bismuth may influence physical, mechanical and magnetic properties of metallurgical materials.

The use of an enrichment and separation technique has become an essential part of spectrometric analysis if the concentrations of analyte elements are too low to be determined and/or matrix interferences cannot be controlled. In order to solve this problem, a lot of enrichment and separation techniques including liquid–liquid extraction [1,2], ion exchange [3], solid-phase extraction [4,5] have been used. Solid-phase extraction techniques for the preconcentration and separation of the trace elements have become increasingly popular. Polymeric resins, silica and activated carbon with or without chelating groups, Amborsorb 563, Diaion HP-20 have been used for this purpose [6–11].

Yalcin and Le have developed two methods, which are based on the use of inexpensive solid-phase extraction (SPE) cartridges as low pressure chromatographic columns

* Corresponding author. Tel.: +90 212 285 3160.

E-mail address: akmans@itu.edu.tr (S. Akman).

for separation and hydride generation atomic absorption spectrometry (HGAAS) and hydride generation atomic fluorescence spectrometry (HGAAS) for detection of arsenic [12]. Tangen et al. used different types of solid-phase extraction cartridges, based on cation exchange, anion exchange, and chelation for the fractionation of Al and Fe in soil water [13]. Chromosorb is a well-known stationary phase support material in gas-chromatographic (GC) separation of organic compounds and has hydrophilic properties. It has recently been used in column for the separation and enrichment of trace elements by solid-phase extraction. Saracoglu and Elci [14] used Chromosorb-102 resin for the sorption and preconcentration of Bi, Cd, Cu, Co, Fe, Ni and Pb from drinking water, seawater by FAAS. Elci et al. [15] investigated solid-phase extraction of lead in soil oil water using Chromosorb-102 by FAAS.

The use of a syringe filled with amino modified silica was proved a useful technique in the separation and concentration of Bi, Cd and Ni [16]. The syringe technique proposed in this study is absolutely different from commercial ready-in use SEP-PAK devices (various adsorbents within a plastic syringe) because SEP-PAK devices are used only for the separation of anions, i.e. a kind of filters for matrix but they are not being used for the concentration of analytes. In previous paper, for the first time it was shown that Chromosorb-107 could be successfully used in the syringe for the separation/enrichment of Pb and Ni [17]. In this study, a syringe again filled with Chromosorb-107 was used for the solid-phase extraction of bismuth and cadmium from different matrices prior to their determination by graphite furnace atomic absorption spectrometry (GFAAS).

2. Experimental

2.1. Apparatus and chemicals

Trace concentrations of bismuth and cadmium were determined by a Perkin Elmer 3030 Zeeman Atomic Absorption Spectrometry equipped with an HGA-600 Graphite Furnace. Pyrolytic graphite coated tubes with pyrolytic L'vov platforms were used throughout this work. Instrumental parameters were adjusted according to the manufacturer's recommendations. Bismuth and cadmium hollow cathode lamps were used as the spectral radiation sources. The resonance wavelengths of 223.1 and 228.8 nm for Bi and Cd were used, respectively.

All chemicals were of analytical reagent grade (Merck). Stock solutions (1000 mg l^{-1}) of Bi and Cd were prepared from Titrisol standards (Merck) and further diluted with distilled-deionized water daily to prepare reference solutions.

The pH adjustments were made by adding 0.1 M of HCl or 0.1 M of NaOH and controlled using WTW pH-340-A/SET 2 pHmeter.

Chromosorb-107 resin (Phase separation Inc., Norwalk, CT) was used as the solid-phase extractant. Its surface area is in the range of $400\text{--}500 \text{ m}^2 \text{ g}^{-1}$; particle size is 80–100 mesh; density is 0.30 g cm^{-3} and porous size is $0.008 \mu\text{m}$.

The following standard references materials were used in this study: NIST SRM 1515 Apple-Leaves, CWW-TM-E Waste Water and CRM-SW Sea Water. In order to dissolve Apple-Leaves (NIST SRM 1515), 0.1 g of dried sample was weighed exactly into the vessel of Mars 5 Microwave furnace. Then 5.0 ml of 32.5% (m/v) nitric acid was added and the vessel was inserted into the microwave digestion furnace and treated according to the manufacturer's recommendation. After adding 20 ml of water, the solution in the vessel was transferred into a beaker and evaporated almost to dryness on a hot plate. The residue was diluted to 25 ml with distilled-deionized water for the determination of Bi and Cd. Other standard references materials (CWW-TM-E Waste Water and CRM-SW Sea Water) were not treated any further and used as bought.

Sea-water samples were collected from Marmara Sea-Istanbul. After filtering through a $0.45 \mu\text{m}$ Millipore cellulose membrane, coastal sea-water samples were preserved by adding of 5 ml l^{-1} nitric acid, and finally stored in acid-washed polyethylene bottles.

2.2. Procedure for sorbent—in syringe

First, porous disk filters were washed with 3.0 M of HNO_3 , distilled-deionized water, 1.0 M of NaOH and distilled-deionized water, respectively. Cleaned porous disk filters were placed on the bottom and the top of a 5 ml of syringe. The syringe was filled with 0.3 g of Chromosorb-107 (1 ml of syringe). Before using the Chromosorb-107 was washed successively with 3.0 M of HNO_3 , distilled-deionized water, 1.0 M of NaOH and distilled-deionized water, respectively. The pH of the sample was adjusted to the desired value with 0.1 M of HCl or 0.1 M of NaOH solutions. Ionic strength was not adjusted. Whenever necessary, 1 ml of 0.1% ammonium pyrrolidine dithiocarbamate (APDC) was added in the sample. 25 ml of sample (five times 5 ml of sample, $\text{pH} \geq 6$) was drawn into the syringe in about 15 s and then discharged passing back through the syringe in about 15 s again. Then, 2.5 ml of 3.0 M of HNO_3 as the eluent was drawn into the syringe and ejected back to desorb the analyte elements at the same drawing and discharging rates. The analyte elements in the discharge were determined by GFAAS and recoveries were calculated. The results were given as the average of five independent analyses. Standard solutions, blanks, standard references materials and sea-water samples were treated in the same manner except that sea-water samples were filtered from $0.45 \mu\text{m}$ membran filter. To re-use the syringe in a subsequent analysis, it was regenerated by passing 5 ml of 3.0 M HNO_3 and then distilled-deionized water until the pH of the washings was above 6.

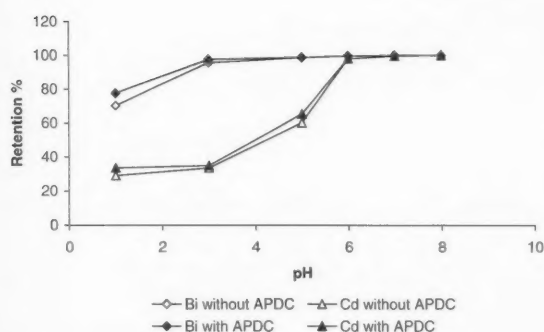


Fig. 1. The effect of the pH of sample on the sorption of bismuth and cadmium with/without APDC.

3. Results and discussion

3.1. Effect of pH on Sorption

The sample was drawn into the syringe passing through the sorbent and discharged passing through the again one more time. We called this drawing and discharging process as one cycle. During this procedure, the analyte elements were sorbed by the sorbent.

The effects of sample pH on the sorption of analytes on Chromosorb-107 by adding or without adding APDC prior to passing through the resin were shown in Fig. 1. The effect of salts on the sorption pH was not taken into account. If 5 ml of sample was drawn in 15 s and discharged again in 15 s, which corresponds to flow rates of 20 ml min^{-1} for drawing and 20 ml min^{-1} for discharging, bismuth and cadmium were quantitatively sorbed at $\text{pH} \geq 6$ irrespective of whether the analytes were complexed with APDC or not. Solid-phase extraction process (sorption and elution) took 1–2 min excluding enrichment which needs a few times drawing and discharging for sorption process and needs longer extraction times.

If the samples are not highly acidic ($\text{pH} \geq 6$), the analyte elements could be quantitatively sorbed on Chromosorb-107 without needing any pH adjustment, which makes the process even much faster and easier. The addition of reagents into the sample for the adjustment of pH causes high and maybe irreproducible contaminations, which increase the relative standard deviation (R.S.D.) values. If there is no need pH adjustment step, R.S.D. and consequently, LOD values would be lower.

3.2. Flow rate

The flow rate (drawing and discharging rates of sample or eluent) depends on the pulling and pushing forces applied manually to syringe piston. Since the forces applied to syringe piston could not be adjusted precisely, quantitative sorption and elution yield should not change in a wide range of flow rate. Otherwise recoveries could not be repro-

Table 1

The effect of different eluents on the recoveries of bismuth and cadmium: analyte concentration = 0.1 mg l^{-1} ; pH 6; sample and eluent volume 5 ml ($N = 5$)

Eluent	Bi		Cd	
	Without APDC	With APDC	Without APDC	With APDC
2.0 M HNO_3	88	90	82	88
3.0 M HNO_3	99	100	99	100
2.0 M HCl	42	46	52	57
3.0 M HCl	54	53	63	68
2.0 M CH_3COOH	^a	^a	^a	^a

^a Recovery is less than %30.

ducible due to the small changes of flow rates. From a series of experiments, (not shown in this paper) it was found that quantitative recoveries were obtained if sample or eluent was drawn or ejected back at flow rate slower than 30 ml min^{-1} which means 5 ml of sample or eluent should be drawn at least in 10 s and ejected back again in 10 s. This is much faster than our manual pulling and pushing rates of samples because we never reached to 30 ml min^{-1} . In all our experiments, 5 ml of sample was drawn or ejected in around 15 s which corresponds to 20 ml min^{-1} . Thus, flow rate was not a critical parameter at least for this resin and studied elements and at optimum conditions quantitative recoveries with low R.S.D. were obtained.

3.3. Elution

The eluent was drawn into the syringe and discharged to desorb the analyte elements. The effects of different acids on desorption of bismuth and cadmium was shown in Table 1. As can be seen from the results, the analyte elements retained by the sorbent could be quantitatively desorbed with 3.0 M of HNO_3 irrespective of whether they were retained on the sorbent as their chelates with APDC or not prior to passing through the Chromosorb-107 in the syringe. It is likely that not only an acidity effect but oxidizing power of HNO_3 plays a role in the elution because HCl was not as effective as HNO_3 .

Table 2

Analytical results for bismuth in standard references materials without APDC ($N = 5$)

Standard references materials	Certified	Added	Found ^a
NIST SRM 1515	ND	0.250 ^{b,c}	0.244 ± 0.020
Apple-Leaves ($\mu\text{g g}^{-1}$)			
CWW-TM-E Waste Water ($\mu\text{g ml}^{-1}$)	ND	0.0100 ^c	0.0096 ± 0.0002
CRM-SW Sea Water (mg kg^{-1})	ND	0.250 ^{b,c}	0.242 ± 0.005

ND: not detected.

^a Mean ± 95% confidence limits.

^b The analyte concentration added in sample solution is converted to that in original sample as $\mu\text{g g}^{-1}$.

^c The analyte concentration in sample solution before enrichment.

Table 3

Analytical results for cadmium in standard references materials without APDC ($N = 5$)

Standard references materials	Certified	Added	Found ^a
NIST SRM 1515 Apple-Leaves ($\mu\text{g g}^{-1}$)	0.013 ± 0.002	$0.1250^{\text{b,c}}$	0.1260 ± 0.0004
CWW-TM-E Waste Water ($\mu\text{g ml}^{-1}$)	0.025	—	0.0024 ± 0.0001
CRM-SW Sea Water (mg kg^{-1})	0.0001	0.00200^{c}	0.00204 ± 0.00020

^a Mean \pm 95% confidence limits.^b The analyte concentration added into sample solution is converted to that in original sample as $\mu\text{g g}^{-1}$.^c The analyte concentration in sample solution before enrichment.

3.4. Enrichment

The ratio of total sample/eluent volumes depends on the concentration factor needed. In order to obtain 10 times of concentration five times of 5 ml sample were drawn and ejected back but 2.5 ml of 3.0 M HNO_3 as the eluent was drawn and ejected only one time. The both analytes were recovered quantitatively with low R.S.D. values (around +2%).

Since the graphite furnace is a very sensitive technique, generally very high concentration factors are not needed except ultra-trace elements but the separation of matrix is much more important to eliminate interferences because absorption signals are highly influenced from matrix interferences. Thus, we did not make an effort to reach very high concentration factors. Ten-fold of concentration was enough for our aim. The use of small syringe was more handy, practical and fast. For the sake of simplicity and handiness, we preferred a small syringe with relatively lower concentration factors. On the other hand, if higher concentration factors are needed, syringes with larger volumes could be used.

3.5. The validation of the method

In order to show the validity of method in various complicated matrices, Bi and Cd were determined, with or without APDC, in standard reference materials (NIST SRM 1515 Apple-Leaves, CWW-TM-E Waste Water, CRM-SW Sea Water). Tables 2 and 3 show the recoveries of analytes added to different certified references materials as the average of five independent determinations. The analyte elements were enriched (concentrated) 10-fold. If the analyte elements is not present in the sample, we added the analyte element in the sample. This situation is different from spike addition to any non-certified sample because some constant errors may cause errors in the concentration of analyte in the sample but recovery of spike seems to be quantitative. This is due to same errors made for the determination of analyte in the sample with and without spike (Table 2).

On the other hand, since the concentration of analyte in the certified sample is known, the recovery of spike is really an indication of validation of the method in the matrix chosen.

The added amount concentration in the table are those after 10-fold of enrichment. As can be seen from the results, in the absence of APDC the bismuth and cadmium added to the samples were recovered 95–101%. If the samples

Table 4

Analytical results for the determination of bismuth and cadmium in spiked sea-water sample (sample volume = 25 ml (five times of 5 ml); pH 6; eluent 2.5 ml; 3.0 M of HNO_3 ($N = 5$))

	Bi	Cd
Sea-Water (mg l^{-1}) ^a	0.053 ± 0.002	0.022 ± 0.002
Added (mg l^{-1})	0.100	0.100
Found (mg l^{-1}) ^a	0.151 ± 0.001	0.121 ± 0.002
Recovery (%) ^b	99 ± 2	99 ± 2

^a Mean \pm 95 % confidence limits.^b Mean \pm R.S.D.

were treated with APDC, the recoveries were in the same level.

Since recoveries obtained with or without APDC were quantitative and almost the same, it is advisable to carry out the experiments in the absence of APDC which is faster and more economic.

The results in Tables 2 and 3 show that described syringe procedure using Chromosorb-107 as a sorbent can be successfully applied to different matrices for the separation and preconcentration of bismuth and cadmium prior to their determination by GFAAS.

Finally Table 4 shows the cadmium and bismuth concentration in a surface sea water sample taken from Marmara Sea near to Istanbul which is known to be heavily polluted due to industry and civilization.

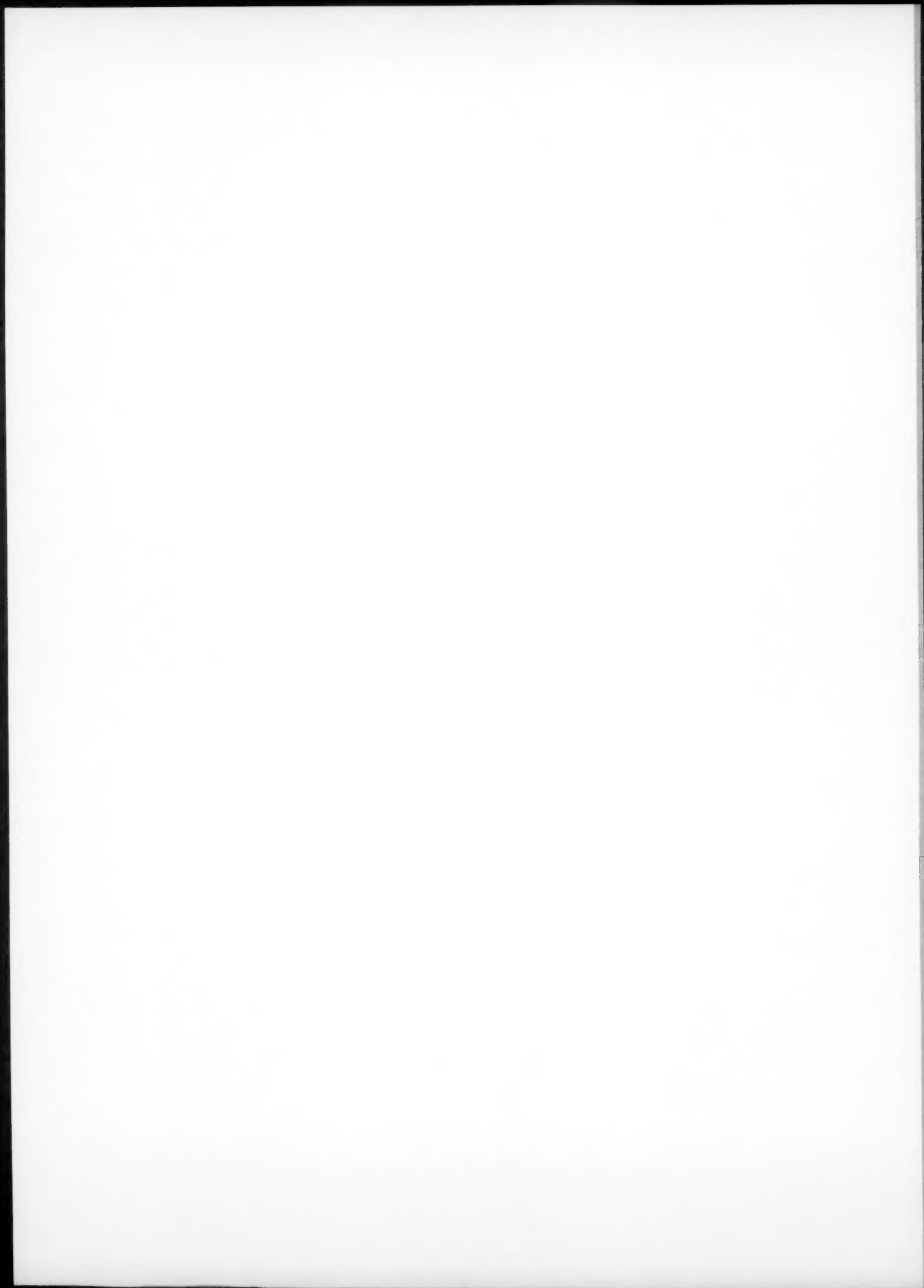
4. Conclusion

Syringe filled with Chromosorb-107 perfectly applied for the separation and preconcentration of bismuth and cadmium in seawater prior to their analysis by GFAAS. This technique is more handy, practical, faster and easier than column technique. The risk of contamination from reagents, apparatus and the laboratory atmosphere is much lower. This is a very important factor for ultratrace analyses. It is possible to make sorption process even in the source of sample with only condition that the sample is not highly acidic.

References

- [1] A.R.K. Dapaah, A. Ayame, *Anal. Chim. Acta* 360 (1998) 43.
- [2] M.A. Rodriguez, J.A.B. Zambrano, A.A. Ordaz, R.N. Mendoza, T.I.S. Medina, *Talanta* 45 (1998) 875.

- [3] I.M.M. Kenawy, M.A.H. Hafez, M.A. Akl, R.R. Lashein, *Anal. Sci.* 16 (2000) 493.
- [4] R.G. Wuilloud, J.A. Salonia, J.A. Gasquez, R.A. Olsina, L.D. Martinez, *Anal. Chim. Acta* 420 (2000) 73.
- [5] A. Takahashi, S. Igarashi, *Anal. Sci.* 16 (2000) 433.
- [6] Y. Cai, G.B. Jiang, J.F. Liu, *Analyst* 126 (2001) 1678.
- [7] R.G. Wuilloud, G.M. Wuilloud, J.C.A. de Wuilloud, R.A. Olsina, L.D. Martinez, *At. Spectrosc.* 23 (2002) 44.
- [8] M. Ozcan, S. Akman, C. Ozeroglu, *Anal. Lett.* 35 (2002) 1075.
- [9] S. Samal, S. Acharya, R.K. Dey, A.R. Ray, *Talanta* 57 (2002) 1075.
- [10] M. Soylak, L. Elci, Y. Akkaya, M. Dogan, *Anal. Lett.* 35 (2002) 487.
- [11] T. Prasada Rao, J.M. Gladis, *Rev. Anal. Chem.* 20 (2001) 145.
- [12] S. Yalcin, C. Le, *Talanta* 47 (1998) 787.
- [13] G. Tangen, T. Wickstrom, S. Lierhagen, R. Vogt, W. Lund, *Environ. Sci. Technol.* 36 (2002) 5421.
- [14] S. Saracoglu, L. Elci, *Anal. Chim. Acta* 452 (2002) 77.
- [15] L. Elci, Z. Arslan, J.F. Tyson, *Spectrochim. Acta B: At. Spectrosc.* 55 (2000) 1109.
- [16] N. Tokman, S. Akman, M. Ozcan, *Talanta* 59 (2003) 201.
- [17] S. Akman, N. Tokman, *Talanta* 60 (2003) 199.



Micro-solid phase extraction with helical-solid-sorbent in the presence of organic solvent for gas chromatography–mass spectrometry analysis of per-*O*-methylated mono- and disaccharides

Ionel Ciucanu^{a,*}, Kathleen C. Swallow^{a,1}, Rodica Căpriță^b

^a Department of Chemistry, West University of Timisoara, Strada Pestalozzi 16, RO-300115 Timisoara, Romania

^b Department of Biochemistry, University of Agriculture Sciences, Calea Aradului 118, RO-300298 Timisoara, Romania

Received 4 March 2004; received in revised form 11 May 2004; accepted 11 May 2004

Available online 17 July 2004

Abstract

A new method for the analysis of mono- and disaccharides by gas chromatography–mass spectrometry (GC–MS) has been developed. The analysis uses per-*O*-methylation of analytes and dynamic micro-solid phase extraction with helical sorbent as sample preparation steps. The two-phase (solid–liquid) extraction rate of per-*O*-methylated carbohydrates was not affected by the stirring rate of the sample solution. The rate-limiting process was the diffusion of per-*O*-methylated carbohydrates in polydimethylsiloxane (PDMS) sorbent. The amount of per-*O*-methylated carbohydrates extracted was significantly increased by the addition of a few drops of a solvent such as dimethyl sulfoxide, benzene, or chloroform. A new three-phase (solid–liquid–liquid) extraction technique, which increased the efficiency of extraction by more than 50 times, was developed. The micro-solid phase extraction with a helical sorbent was examined for its applicability to the analysis of mono- and disaccharides from a synthetic mixture and from orange juice. The reproducibility was found to be approximately 2% when the extraction and injection were performed with a special helical sorbent holder device. The linearity was found to be very good up to 0.3 mg/mL. The limit of detection (LOD) was up to nanograms per milliliter, depending on the organic solvent present in solution.

© 2004 Elsevier B.V. All rights reserved.

Keywords: Helical-solid-sorbent; Micro-solid phase extraction; Three-phase (solid–liquid–liquid) extraction; Solid phase microextraction; Liquid–liquid extraction; Per-*O*-methylated carbohydrates; Gas chromatography–mass spectrometry analysis

1. Introduction

In the last decade there has been a revolution in attitudes toward carbohydrates due to their biological importance. The analysis of carbohydrates can be done by either classical or instrumental techniques, but one of the most important techniques for carbohydrate structural determination is gas chromatography–mass spectrometry (GC–MS). The first application of gas chromatography (GC) to carbohydrates was reported in 1958 and described the separation of fully methylated monosaccharides [1]. Since then, carbohydrates have been analyzed by GC using a variety of derivatives such as trimethylsilyl, acetyl, trifluoroacetyl, methanoboronate,

acetal, or a combination [2]. The GC–MS analysis of carbohydrate derivatives has some limitations due to the low volatility of these derivatives, and is useful only for mono-, di-, and trisaccharides. However, the technique has the advantage of separating these carbohydrate derivatives before mass spectrometry (MS) analysis. Moreover, GC itself is adequate for determining the anomeric and absolute configuration of the monosaccharides by comparison with standards.

Per-*O*-methylation became the major derivatization reaction for carbohydrates because it is an essential step for determining the position of the glycosidic attachment of all monosaccharide units in the carbohydrate polymer. It also confirms the identity and ring form of each of the sugar components and provides a means for determining the points of attachment of noncarbohydrate moieties [3]. There are many methods for making per-*O*-methylated carbohydrates [3], but the most common method is the Ciucanu per-*O*-methylation [4,5], which uses methyl io-

* Corresponding author. Fax: +40 256190293.

E-mail address: ciucanu@cbg.uvt.ro (I. Ciucanu).

¹ Present address: Department of Chemistry, Merrimack College, North Andover, MA 01845, USA.

dide and sodium hydroxide in polar aprotic solvents. The method gives complete *O*-methylation with high yields, no by-products, and a very short reaction time. The isolation of the per-*O*-methylated carbohydrate from the reaction mixture is carried out by extraction with organic solvents, followed by washing of the organic phase with water. For small sample quantities, the extraction step can result in loss and degradation of the analytes [5]. The liquid–liquid extraction is time and labor intensive, requires relatively large amounts of high-purity solvents, multiple extractions, and purification of the combined extracts. The solvents are toxic, flammable, and relatively expensive. Moreover, the purification of the organic extract by washing with water can reduce the recovery to 90%. Many of these disadvantages of the liquid–liquid extraction method can be overcome using solid phase extraction for isolation of the per-*O*-methylated carbohydrate.

The isolation of organic compounds from a sample matrix by sorption on a solid sorbent and their desorption by the introduction of the sorbent into a GC injector for analysis was invented in 1971 by E. Palm [6]. The sorbent material was deposited on the surface of a transportable body such as a small rod or tube. In 1989, Pawliszyn [7] used the Palm technique for the analysis of pollutants from water. Later [8], he changed the name of small rod, tube, and sample collection with fiber, hollow fiber, and solid phase microextraction, respectively. In 2002, Ciucanu [12] introduced a helical solid sorbent for solid phase dynamic extraction, which reduced the extraction time to seconds for volatile organic compounds and improved the GC resolution. With a small volume of sorbent, the amount of analytes extracted is too low for dilute samples, reducing the sensitivity of the analysis. An increase in the coating thickness, using rods [9] or magnetic rods [10] coated with a thicker polydimethylsiloxane (PDMS) coating, improved the sensitivity, but required an additional cryofocusing step prior to the introduction of analytes into the capillary column. Moreover, the extraction time necessary to reach equilibrium with the PDMS fiber and the PDMS rod are in the order of hours, especially for semi-volatile organic compounds [11].

This paper presents a study of the extraction of per-*O*-methylated mono- and disaccharides by micro-solid phase extraction with a helical sorbent. A new three-phase (solid–liquid–liquid) extraction technique increases the amount of analyte extracted by more than 50 times.

2. Experimental

2.1. Reagents and materials

Sucrose, maltose, D-glucitol, D-glucose, D-fructose, 2,3,4,6-tetra-*O*-methyl-D-glucose, sodium hydroxide (pellets), methyl iodide (stabilized by copper), and dimethyl sulfoxide (DMSO) (99.9%) were of the highest grade available from Sigma-Aldrich (Milwaukee, WI). Sodium iodide (NaI), benzene, and chloroform were analytical grade from

Merck (Darmstadt, Germany). The solvents and the methylation agent are toxic and must be handled carefully in fume hood. The 30- μ m non-bonded PDMS fiber was from Supelco (Bellefonte, PA, USA). PDMS used for the helical sorbent was the OV-1 stationary phase (Alltech, Hoogeveen, The Netherlands).

2.2. Apparatus and methods

Gas chromatography analysis was carried out with an HP 6890 gas chromatograph (Hewlett-Packard, Avondale, PA) equipped with flame ionization detector (FID). GC–MS analyses were performed using a HRGCC 5300 gas chromatograph (Carlo Erba, Milan, Italy) coupled with a QMD 1000 quadrupole mass spectrometer (Fisons Instruments, East Sussex, England). High-purity helium was used as carrier gas at a constant flow rate of 1 mL/min. All GC separations were performed on a DB-5MS fused silica capillary column (30 m \times 0.25 mm i.d.) with 0.25- μ m polydimethylsiloxane cross-bonded film (J&W Scientific). The GC oven temperature was maintained at 100 °C for 5 min after sample injection, increased to 240 °C at 6 °C/min, and maintained at 240 °C for 10 min. The mass spectra were recorded in the positive-ion electron ionization (EI) mode over the scan range m/z 40–750. The filament emission current was 20 μ A at 200 °C and it was turned off for the first 6 min. The transfer line temperature was 270 °C.

The identification of the peaks was performed by interpretation of fragmentation patterns in the EI mass spectra as well as by comparing the spectra with mass spectra of standards in MS libraries or published in the literature. The quantitative evaluation of the permethylated carbohydrates was carried out by integration of the peak areas.

The methylation reactions were performed at room temperature (22 °C) in 2-mL glass vials having a V shape and equipped with silicone septa lined screw caps and a magnetic stirrer (VWR Scientific, Malboro, MA). The carbohydrate sample (4–6 mg) was introduced into the vial, and dimethyl sulfoxide (1 mL) was added without using special drying conditions or an inert gas atmosphere [4,5]. The sodium hydroxide pellets were ground with a pestle in a dry mortar to get a fine powder. A weighed amount of powdered sodium hydroxide (3 equivalents per mol of replaceable H) (~30 mg) was added to the sample solution and stirred at room temperature for 5 min to get a suspension. Methyl iodide (3 equivalents per mol of replaceable H) (~60 μ L) was added with a syringe, and the mixture was stirred vigorously for 10 min. The methylation reaction was quenched with water and carefully neutralized with 1M hydrochloric acid solution. The permethylated products were extracted at least five times by adding 1.0 mL of organic solvent (benzene, or chloroform), shaking the mixture, and separating the layers by centrifugation. The combined organic layers were washed at least three times with water and dried over night under vacuum at 40 °C. The dried residue was dissolved in water for the preparation of stock solutions of individ-

ual permethylated carbohydrates. Standard solutions were prepared from stock solution by dilution with appropriate solvents.

Details of the preparation of the helical solid sorbent have already been described [12,13]. The helical solid sorbent can be a solid material with any geometrical form in cross-section, arranged in any type of helical line, having sorption properties as such or coated physically or chemically with a sorbent material. The solid sorbent used in these experiments was actually a soft solid consisting of PDMS rubber. This soft solid sorbent was coated on a helical support made by wrapping a wire around a straight wire with the same diameter at a constant pitch. The wire was made from chromium–aluminum alloy (AB Kanthal, Hallstahammer, Sweden) and had 0.07 mm diameter. When the wrapping was completed, the straight wire was removed and the helical support was cut to an appropriate length. One end was straightened (~5-mm) and fixed with an epoxy resin to an elongation arm. After cleaning with water, acetone and dichloromethane, the surface of the helical support was coated with several layers of PDMS by immersion of the helical support in a concentrated solution of PDMS in dichloromethane. PDMS cross-linking was accomplished by adding 0.8% dicumyl peroxide to the coating solution. After each coating, the solvent was evaporated by heating the helical sorbent at 150 °C for 30 min. The thickness of the final coating polymer depended on the concentration of PDMS solutions and the number of coatings. The helical sorbent was weighed after each coating in order to obtain an ~30- μ m thickness. The final length of the helical sorbent was adjusted to give the same amount of PDMS as that on a 30- μ m Supelco PDMS fiber. The helical solid sorbent fixed to the elongation arm was introduced into a stainless steel tube for protection. The protection tube with the helical solid sorbent inside was attached to a holder device [12], which can effect longitudinal movement of the helical solid

sorbent. The helical sorbent attached to the holder device was introduced into a GC injector with a nitrogen flow of 3 mL/min and was heated from 150 to 200 °C at 0.3 °C/min for final cross-linking, and then was heated to 300 °C for 6 h for conditioning.

The micro-solid phase extraction was performed in 8-mL vials with screw cap and septum containing different solutions of per-*O*-methylated carbohydrates. A magnetic stirrer with a speed upto 1200 rpm was used to agitate the analytes solution. The vials were thermostated at 22 °C and the stirring of the sample was started before sampling. The extractions with helical solid sorbent process were performed in all the experiments with the helical sorbent holder device and involved a few simple steps that can avoid the penetration of analytes and solution between the elongation arm and the protection tube. In the first step (Fig. 1A), the tip of the protection tube with the helical sorbent retracted was adjusted inside of the guide plate hole using nuts or a guide connector. The guide plate was laid on the top of the vial screw cap. In the second step (Fig. 1B), the barrel was pushed down, the spring of the guide rods was compressed and the vial septum was pierced by the protection tube containing the helical sorbent. The length of the protection tube in the vial was adjusted with a limitation nut to avoid contact with the surface of solution. In the third step (Fig. 1C), the plunger stopper was pushed, releasing the plunger spring, and the helical solid sorbent was moved down from the protection tube into the solution. In the fourth step (Fig. 1D), the spring of the guide rod was released and the protection tube was immediately retracted from vial. This position, with the protection tube outside of vial, was used during the extraction. When the extraction was finished, the barrel was pushed down and the protection tube was inserted again into vial. The plunger was pulled upto the stopper position, and the helical solid sorbent was retracted into protection tube. Stopping to push down the barrel, the protection tube containing the retracted

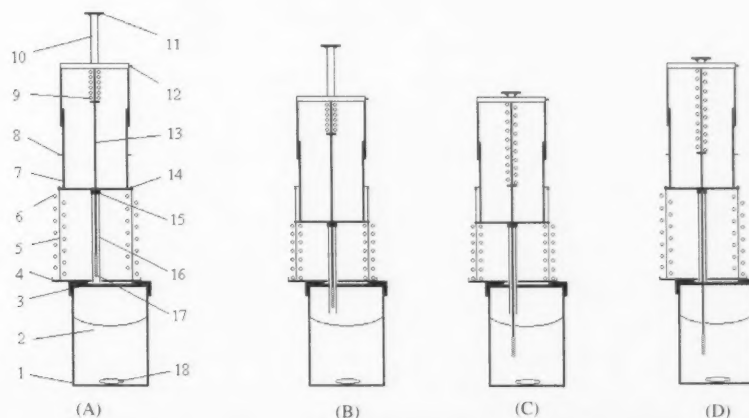


Fig. 1. Schematic diagram of the introduction of helical sorbent into the liquid sample for micro-solid phase extraction: (1) Vial; (2) sample solution; (3) septum; (4) guide plate; (5) guide rod; (6) guide rod spring; (7) barrel; (8) limitation nut; (9) plunger spring; (10) plunger; (11) handle; (12) plunger stopper; (13) elongation arm; (14) adjustable nut; (15) sealing material; (16) protection tube; (17) helical sorbent; (18) magnetic stirring bar.

helical sorbent was completely removed from the vial. Similar steps were used for the introduction and removal of the helical sorbent into the GC injector port.

3. Results and discussion

3.1. Two-phase (solid–liquid) extraction

Solid–liquid extraction of the per-*O*-methylated carbohydrates is a selective distribution process based on the mass transfer of the analytes from the liquid solution to the solid sorbent. The number of moles of analyte extracted at equilibrium in the solid–liquid extraction can be evaluated taking into account the mass balance before and at equilibrium and the distribution equilibrium of the analytes between the two phases, using the equation:

$$M_a = \frac{K_{sl} V_{sol} V_{ep} C_{sol}^0}{K_{sl} V_{ep} + V_{sol}} \quad (1)$$

where C_{sol}^0 is the initial concentration of analyte in solution, V_{sol} and V_{ep} are the volumes of solution and extraction phase, respectively, and K_{sl} is the solid–liquid distribution constant.

Usually, the ratio between the volume of the sample matrix and solid phase is at least 10^4 . Because only the solid phase is small, micro-solid phase extraction is a more appropriate name for this process instead of solid phase microextraction. When the volume of the solid phase is significantly lower than that of the sample matrix, Eq. (1) can be simplified to:

$$M_a = K_{sl} V_{ep} C_{sol}^0 \quad (2)$$

With a very small volume of solid phase, the steady-state distribution equilibrium can be reached in a certain time and the amount extracted in one stage cannot be exhaustive, compared to solid phase extraction in a cartridge [14].

Fig. 2 shows the variation of the amount of the per-*O*-methylated glucose and per-*O*-methylated gulcitol extracted with 30- μ m cross-linked PDMS helical sorbent as a function of the extraction time. The per-*O*-methylation reaction mixtures were neutralized, and the resulting solutions contained water, dimethyl sulfoxide, and alkaline salts. Therefore, this mixture was used as the matrix for these experiments. A similar curve was obtained for per-*O*-methylated sucrose. The amount extracted by helical sorbent was directly proportional to the peak area. The extraction time was measured from the insertion of the solid sorbent into sample solution until it was retracted into the protection tube. The time required to reach the extraction equilibrium can be determined from the extraction profile curves when the steady state is reached. Using the assumption that equilibration is reached when 95% of the equilibrium amount of an analyte is extracted from the sample [15] can reduce the extraction time by more than one-half [11], inducing alterations in the interpretation of the results.

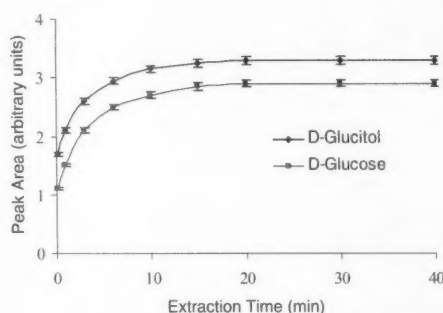


Fig. 2. Extraction profile of the per-*O*-methylated-D-glucose and per-*O*-methylated glucitol from a neutralized matrix by micro-solid phase extraction with 30- μ m cross-linked PDMS helical sorbent. Extractions were performed from a 5 ml solution of water: dimethyl sulfoxide (2:1) with 150 mg NaI/mL at 22 °C, 1.0 mg/mL per-*O*-methyl-D-glucose and 1.5 mg/mL per-*O*-methyl glucitol using magnetic stirring at 600 rpm.

The distribution between the liquid and solid phases involves the following steps: (1) mass transport of analytes from the bulk of the liquid phase to the interface; (2) mass transport of analytes through the interface, also called the boundary layer; (3) adsorption of the analytes on the surface of the sorbent; and (4) mass transport of analytes into the layer of sorbent. The rate of mass transfer of analytes in a given phase and through the interface is governed by molecular diffusion and turbulent diffusion. The increase of the magnetic stirrer speed up to 1200 rpm resulted in no change of the extraction rate with 30- μ m PDMS helical sorbent. This indicates that, in this speed range, the rate-controlling step of the mass transport is not steps (1) and (2), which are affected by agitation, but rather step (3) or (4).

According to Eq. (1), the amount of analyte extracted by the PDMS helical sorbent is linearly proportional to the concentration of analyte in the experimental solution. This linearity is limited by the low solubility of the per-*O*-methylated mono- and disaccharides in water. The solubility of the per-*O*-methylated carbohydrates in water was checked by weighing. All per-*O*-methylated mono- and disaccharides from this study were soluble in water up to 3 mg/mL. The addition of dimethyl sulfoxide improved the solubility of per-*O*-methylated carbohydrates. Experiments with standard 2,3,4,6-tetra-*O*-methyl-D-glucose, which contains a free hydroxyl group, showed a higher solubility in water than per-*O*-methylated glucose. However, the 2,3,4,6-tetra-*O*-methyl-D-glucose gave no chromatographic peak, which indicated that it could not be retained by the PDMS helical sorbent.

Fig. 3 shows the influence of the various sample matrices on the amount of per-*O*-methylated glucose extracted by the PDMS helical sorbent. The graphs were constructed over a range of 0.01–3 mg/mL in water, water with 150 mg NaI/mL, water:dimethyl sulfoxide (2:1), and water:dimethyl sulfoxide (2:1) with 150 mg NaI/mL. Excellent linearity was observed for all solutions. The detection limit ($S/N = 3$) for

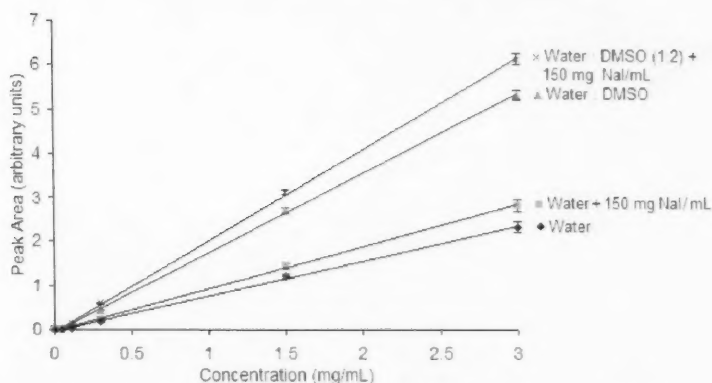


Fig. 3. The effect of the sample matrix on the amount of per-*O*-methylated glucose extracted by micro-solid phase extraction with 30- μ m cross-linked PDMS helical sorbent. Extractions were performed for 30 min from 5 mL solution using magnetic stirring at 600 rpm.

per-*O*-methyl glucose using a flame ionization detector was 10 μ g/mL for aqueous solutions and 3 μ g/mL when dimethyl sulfoxide was added. The addition of salt in solution resulted in a small increase in the amount extracted by helical sorbent, because the per-*O*-methylated glucose has a very low capability for electrostatic interactions with the salt ions in solution. Dimethyl sulfoxide had a more important influence on the extraction efficiency. The addition of one part of dimethyl sulfoxide to two parts of water increased the amount extracted up to three times. Dimethyl sulfoxide is a dipolar aprotic solvent that is miscible with water and can interact with polar as well as non-polar compounds [16]. Dimethyl sulfoxide can be also extracted by the PDMS helical sorbent. Once extracted by PDMS, dimethyl sulfoxide will improve the solubility of per-*O*-methylated carbohydrates in the PDMS sorbent because per-*O*-methylated carbohydrates are very soluble in dimethyl sulfoxide. The volume of dimethyl sulfoxide present in the sample vial was high and small

variations ($\sim 10\%$) did not affect the amount of analyte extracted, when the concentration of the analyte was kept constant.

3.2. Three-phase (solid-liquid-liquid) extraction

Fig. 4 shows the influence of an additional immiscible solvent added as 1% (v/v) to the per-*O*-methylated carbohydrate standard solution. The addition of an immiscible organic solvent such as benzene increased the amount extracted of per-*O*-methylated glucose up to 10 times and the addition of chloroform increased it more than 50 times. These organic solvents are not miscible with water, but they solvate the per-*O*-methylated carbohydrates very well. A three-phase (solid-liquid-liquid) extraction system is developed by adding a few drops of immiscible solvent to the sample matrix [17]. The per-*O*-methylated carbohydrates are extracted by the PDMS solid sorbent from the ben-

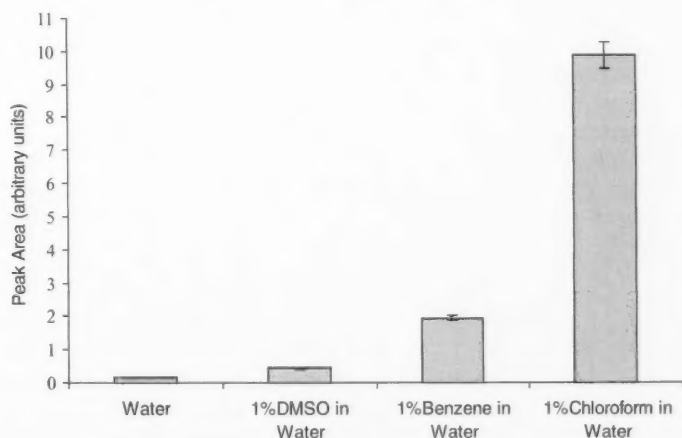


Fig. 4. The extracted amount of per-*O*-methylated glucose as a function of the solvent added to aqueous matrix. The micro-solid phase extractions were performed with 30- μ m cross-linked PDMS helical sorbent for 30 min from 5 mL aqueous solution using magnetic stirring at 600 rpm. The concentration of per-*O*-methylated glucose was 300 μ g/mL and the amount of solvent added to matrix was 1% (v/v).

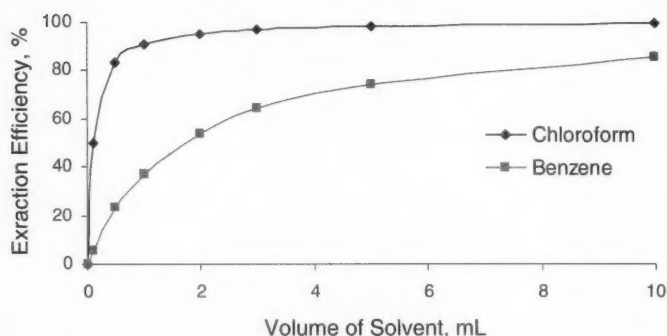


Fig. 5. Liquid-liquid extraction efficiency of per-*O*-methylated-D-glucose as a function of the volume of immiscible organic solvent. Each extraction was performed from 3 mL neutralized derivatization mixture containing ~ 10 mg/mL of analyte.

zene or chloroform phase where the concentration of the per-*O*-methylated carbohydrates has been increased several times by this liquid-liquid pre-extraction. Consequently, the amount of analytes extracted by the PDMS sorbent is increased in accordance with Eq. (2). The concentration of analyte in immiscible solvent (C_{is}) is given by equation:

$$C_{is} = K_{ll} C_{sol}^0 \quad (3)$$

and depends on the concentration of analyte in matrix (C_{sol}^0) and the parameters that affect the liquid-liquid distribution constant (K_{ll}).

Fig. 5 shows that increasing of the volume of immiscible solvent increases the amount of analyte extracted by solvent, but the volume variations do not affect the concentration of analyte in the immiscible solvent. Consequently, the volume of immiscible solvent does not influence, in accordance with Eq. (2), the amount of analyte extracted by PDMS sorbent. In addition to effecting the liquid-liquid extraction, the immiscible solvents introduced into the matrix solution were also extracted by the solid sorbent as a function of their solubility in PDMS. The presence of these organic solvents in the PDMS sorbent improves the diffusion coefficient of the per-*O*-methylated carbohydrate as a function of the organic solvent retained by PDMS. Moreover, the organic solvent retained by PDMS may increase the volume of the extraction phase and, according to Eq. (2) can increase directly proportionally the amount of per-*O*-methylated carbohydrates extracted. Holding all of the parameters that affect liquid-liquid extraction and solid-liquid extraction constant is essential for good reproducibility of the technique.

3.3. Reproducibility, linearity, and limits of detection

In micro-solid phase extraction with both helical sorbent and fiber, the analytes can easily diffuse and condense into the gap between the elongation arm of the sorbent and the protection needle. With a liquid sample, small amounts of sample can also be introduced into this gap during stirring. The presence of the analytes or of the solution in this gap

can generate errors in quantitative evaluations and carryover for analytes with low volatility and high thermal sensitivity. This effect was obvious for longer extraction times used for semivolatile compounds with a Supelco fiber where the range of standard deviation was large [11]. The only solution is to avoid a prolonged contact between the sample matrix and the needle gap. Recently [12], a helical sorbent holder device was introduced that totally avoids these undesirable effects. The device can be used for both manual and automatic extraction in GC injection. Extraction and injection with this device requires several steps (Fig. 1). After piercing the vial septum, the protection needle releases the helical sorbent and the protection needle can be withdrawn from the sample matrix with a spring system. Consequently, the protection needle remains outside the sampling vial during extraction. The introduction of the helical sorbent into the sample matrix and into the GC injector was done at constant speed due to the plunger spring, making it highly reproducible. The precision of extraction and injection obtained with this helical sorbent holder device was very good. The relative standard deviation (R.S.D.) did not exceed 2% (Table 1). Extraction with a helical sorbent can be repeated more than 100 times without loss of extraction capacity, because of the cross-linking of the PDMS helical sorbent. The inherent differences among hand-made helical sorbents will be smaller with commercially available helical sorbents. The Supelco fiber used in these experiments had non-bonded PDMS and was not stable in the presence of organic solvents. Consequently, the reproducibility with Supelco fiber was very poor, and the extraction capacity was reduced with $\sim 50\%$ after three consecutive extractions in the presence of chloroform.

Table 1 gives the linear range for per-*O*-methylated glucose and sucrose. The linearity was investigated using standard samples containing per-*O*-methylated analyte in concentrations ranging from 0.01 to 0.3 mg/mL and was found to be very good.

The limit of detection (LOD) was evaluated on the basis of $S/N = 3$ and can be regarded as an indication of the sensitivity of this technique. For many analytical techniques,

Table 1

Reproducibility, linearity, and limit of detection for solid–liquid extraction and solid–liquid–liquid extraction followed by GC analysis for per-*O*-methylated glucose and sucrose

	Solid–liquid extraction ^a		Solid–liquid–liquid extraction ^b	
	Glucose	Sucrose	Glucose	Sucrose
RSD ($n = 7$), %	1.8	1.9	1.9	2.0
Regression coefficient	0.9991	0.9988	0.9989	0.9986
LOD ($S/N = 3$)	3 $\mu\text{g/mL}$	3.3 $\mu\text{g/mL}$	183 ng/mL	191 ng/mL

^a Extraction at 22 °C for 30 min with magnetic stirring at 600 rpm from 5 mL solution of water:dimethyl sulfoxide (2:1) containing the same amount of each analyte.

^b Similar conditions, but from 5 mL solution of water with 50 μL chloroform.

the LOD is determined by a sample preparation step and not by the instrumental detection power. The addition to the sample matrix of an immiscible solvent in which the per-*O*-methylated analytes are soluble increased the sensitivity of the technique and pushed the LOD for the flame ionization detector into the nanograms per milliliter range (Table 1).

3.4. Applications

Fig. 6 shows the gas chromatogram of a mixture of five per-*O*-methylated mono- and disaccharides isolated from the neutralized derivatization mixture by micro-solid phase extraction with the PDMS helical sorbent. The per-*O*-methylation of carbohydrates with a free hemiacetal

group such as D-glucose, D-fructose, and maltose gave several isomers resulting from the two cyclic forms and the presence of anomeric centers. All these isomers were separated by GC generating multiple peaks for one compound. Sucrose and D-glucitol do not have hemiacetal groups and thus gave only one peak. The helical sorbent generated a very good peak shape improving the resolution significantly. The chromatograms with the Supelco PDMS fiber had peaks 1 and 2 only partially separated and peaks 5 and 6 overlapping. This difference between the PDMS helical sorbent and the Supelco PDMS fiber was the consequence of a faster thermal desorption from the PDMS helical sorbent. The fast heat transfer from the hot carrier gas to the cold sorbent as a result of the turbulent rotational flow on the surface of the helical sorbent in GC injector produces

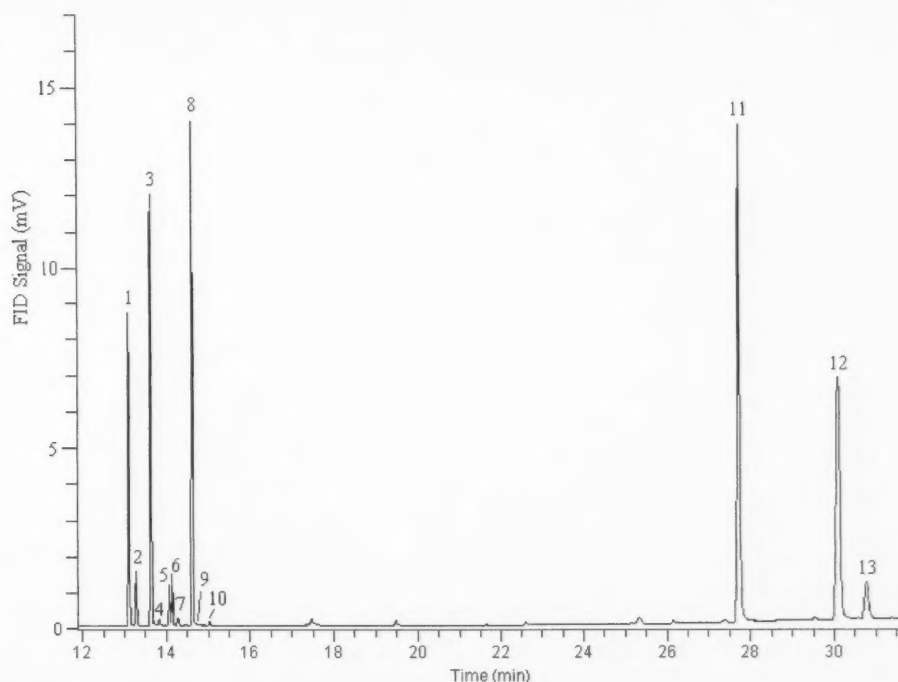


Fig. 6. Gas chromatogram of the five per-*O*-methylated carbohydrates extracted by PDMS helical sorbent. The concentration of the per-*O*-methylated carbohydrates in neutralized derivatization mixture was in the range 100–150 $\mu\text{g/mL}$. Numbered peaks: (1, 6, 7, 9) D-glucose; (2, 3, 4, 5, 10) D-fructose; (8) D-glucitol; (11) Sucrose; (12, 13) Maltose. For chromatographic conditions, see Section 2.

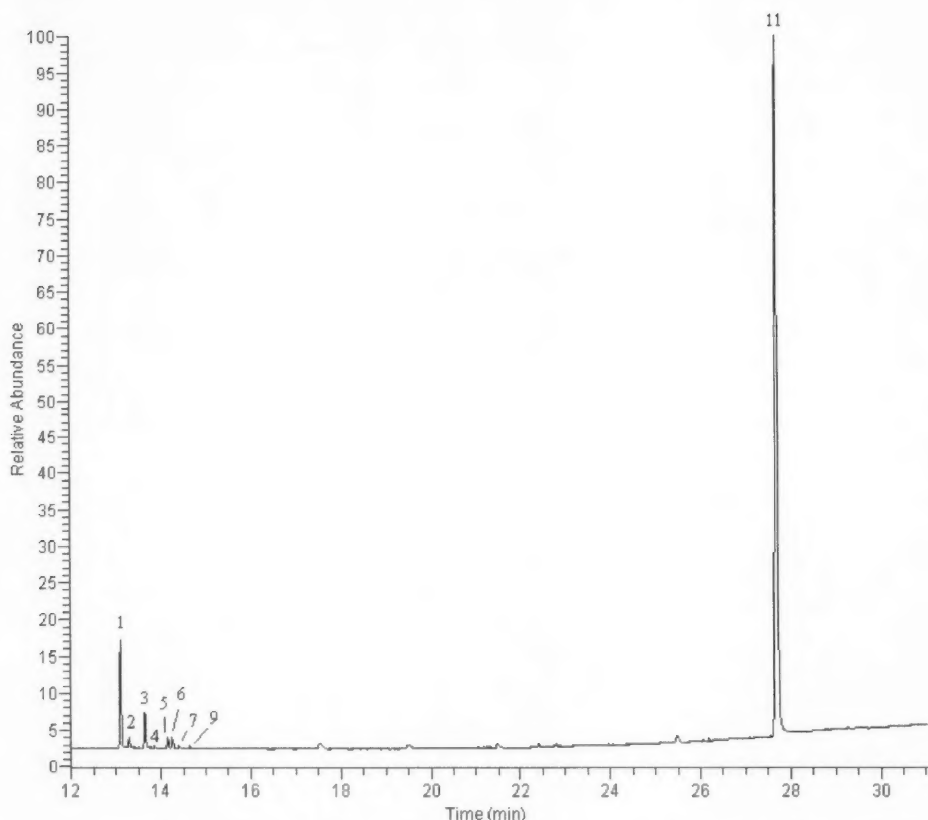


Fig. 7. GC–MS total ion chromatogram of the per-*O*-methylated carbohydrates from orange juice. For numbered peaks and chromatographic conditions, see Fig. 6.

this effect [12]. With this fast thermal desorption, no cryofocusing is required for the introduction of analytes with the helical sorbent into the capillary column. The small peaks eluted after the per-*O*-methylated monosaccharides peaks were identified by mass spectrometry as PDMS oligomers desorbed from the PDMS sorbent due to the presence of dimethyl sulfoxide in the extraction matrix. The PDMS peaks did not interfere with the sample peaks, were easily detected by MS, and were minimized by conditioning of the PDMS helical sorbent at 250 °C over night under nitrogen flow. Dimethyl sulfoxide, benzene, and chloroform each gave a large peak, which eluted at the beginning of the chromatogram, and did not interfere with per-*O*-methylated carbohydrates peaks.

Fig. 7 shows the GC–MS total ion chromatogram of per-*O*-methylated mono- and disaccharides from orange juice. The fresh fruits were squeezed and 40 μ L of juice without additional purification was introduced into a conical-glass vial with a syringe. The per-*O*-methylation was performed without drying the sample, and an additional amount of 150 mg solid sodium hydroxide was added to the derivatization mixture to retain the water introduced in the system by the juice [5]. The per-*O*-methylated carbohydrates were isolated from the neutralized derivatization

mixture by the micro-solid phase extraction with the PDMS helical sorbent. The extracted samples were introduced into GC capillary column with helical sorbent using the steps shown in Fig. 1, with the special holder device. The peaks generated by per-*O*-methylated mono- and disaccharides were identified using standards and mass spectra. The isomers corresponding to per-*O*-methylated D-glucose and D-fructose were first identified using the retention times, because their mass spectra were very similar. Peak 10, a small isomer of fructose, was not detected. Orange juice is a complex mixture of organic compounds, but using methylation and micro-solid phase extraction as sample preparation steps, the chromatogram was very clean and contained only per-*O*-methylated mono- and disaccharides.

4. Conclusions

The results of this study clearly show that micro-solid phase extraction with the PDMS helical sorbent is a very good solution for the isolation of per-*O*-methylated carbohydrates directly from a neutralized derivatization mixture. The only requirement prior to extraction is the neutralization of the excess base from the derivatization mixture. The

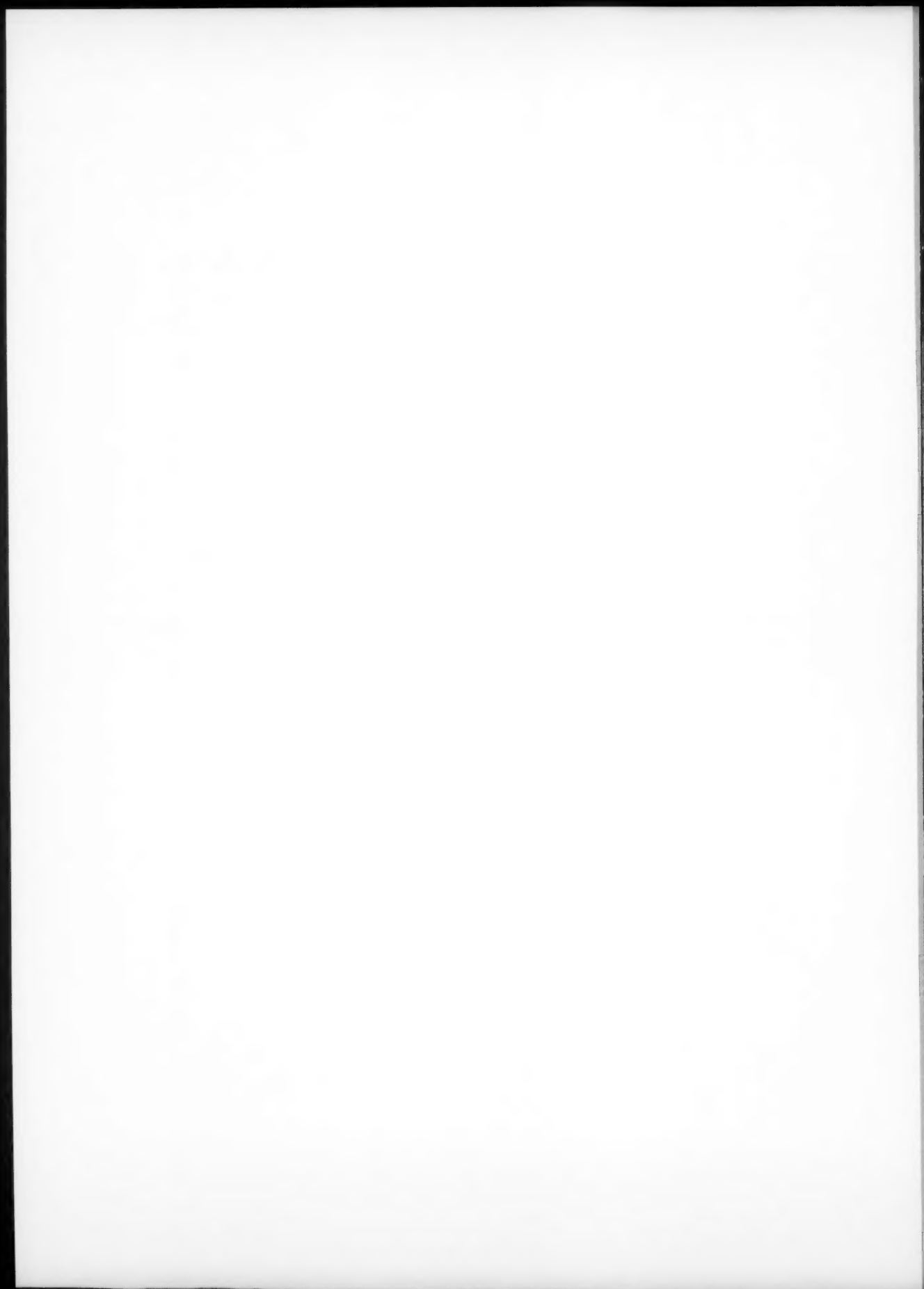
per-*O*-methylated carbohydrates have a low solubility in the PDMS sorbent, but the presence of the dimethyl sulfoxide in the extraction solution improves their solubility and extraction efficiency. The results show that the addition of immiscible organic solvents such as benzene and chloroform can generate a three-phase extraction system and can increase the extraction efficiency by more than 50 times. The helical configuration of the sorbent improved the thermal desorption and no additional cryofocusing was used for introduction of analytes into GC capillary column. Future work will investigate the three-phase extraction technique using different cross-linked sorbents. This work is the first attempt of isolation of compounds with very low volatility by micro-solid phase extraction for GC–MS analysis, but it can be also used for LC–MS analysis [17].

Acknowledgements

Dr. K.C. Swallow thanks the Fulbright Foundation for a Senior Specialist Grant.

References

- [1] A.G. McInnes, D.H. Ball, F.P. Copper, C.T. Bishop, *J. Chromatogr.* 1 (1958) 556.
- [2] D.R. Knapp, *Handbook of Analytical Derivatization Reactions*, Wiley & Sons, New York, 1979, pp. 539–598.
- [3] S.B. Lavery, In D.G. Large, C.D. Warren, (Eds.), *Glycopeptides and Related Compounds*, Marcel Dekker, New York, 1997, pp. 541–592.
- [4] I. Ciucanu, F. Kerek, *Carbohydr. Res.* 131 (1984) 209.
- [5] I. Ciucanu, E.C. Costello, *J. Am. Chem. Soc.* 125 (2003) 16213.
- [6] (a) Palm, E. DE Patent 2,139,992, 19971;
(b) Palm, E. US Patent 3,797,318, 1974.
- [7] R.G. Belardi, J. Pawliszyn, *J. Water Pollut. Res. Can.* 224 (1989) 179.
- [8] (a) J. Pawliszyn, GB Patent 9,007,356, 1990;
(b) J. Pawliszyn, US Patent 5,691,206, 1997.
- [9] L. Montero, P. Popp, A. Paschke, J. Pawliszyn, *J. Chromatogr. A* 1025 (2004) 17.
- [10] E. Baltussen, P. Sandra, F. David, C.A. Cramers, *J. Microcolumn Sep.* 11 (1999) 737.
- [11] I. Bruheim, L. Xiaochuan, J. Pawliszyn, *Anal. Chem.* 75 (2003) 1002.
- [12] I. Ciucanu, *Anal. Chem.* 74 (2002) 5501.
- [13] I. Ciucanu, A. Caprita, A. Chiriac, R. Barna, *Anal. Chem.* 75 (2003) 736–741.
- [14] N.J.K. Simpson, (Ed.) *Solid phase Extraction: principles, techniques and applications*, Marcel Dekker, New York, 2000.
- [15] J. Pawliszyn, *Solid phase Microextraction: Theory and Practice*, Wiley-VCH, New York, 1997.
- [16] D. Martin, H.G. Hauthal, *Dimethyl Sulphoxide*, Wiley, New York, 1975, pp. 61–103.
- [17] I. Ciucanu, Patent Application, RO/ 00050, 2004.



Study and characterization of the ancient bricks of monastery of “San Filippo di Fragalà” in Frazzanò (Sicily)

Paola Cardiano^{a,*}, Salvatore Ioppolo^b, Concetta De Stefano^a,
Antonello Pettignano^c, Sergio Sergi^a, Pasquale Piraino^a

^a Dipartimento di Chimica Inorganica, Chimica Analitica e Chimica Fisica, University of Messina,
Salita Sperone 31 S. Agata, 98166 Messina, Italy

^b Dipartimento di Scienze Geologiche, Sezione di Mineralogia, Petrografia, Vulcanologia e Geochemica,
University of Catania, Corso Italia 55, 95129 Catania, Italy

^c Soprintendenza ai Beni Culturali e Ambientali di Messina, Viale Boccetta 38, 98100 Messina, Italy

Received 20 January 2004; received in revised form 18 May 2004; accepted 18 May 2004

Available online 13 July 2004

Abstract

The ancient bricks of the monastery of Fragalà in Frazzanò, the first Basilian-Norman center in Sicily and symbol of 15 centuries of cultural life, were studied and characterized by a combination of techniques (INAA, ICP, porosimetry, HPLC, TG-DTA and XRD). Chemical analysis shows that the Byzantine samples were mainly manufactured by calcareous clay while medieval ones were made of limeless clay. The combined results of TG-DTA and XRD analyses, based on the presence of high-T Ca silicate phases, suggest that the firing temperature was not exceeding 900 °C while HPLC investigations evidence that the building does not suffer from decay phenomena due to the presence of soluble salts.

© 2004 Elsevier B.V. All rights reserved.

Keywords: Brick analysis; Thermal analysis; Mercury porosimetry; Major oxides; Rare-earth elements; Soluble salts; X-ray diffraction

1. Introduction

Among the remarkable ancient monuments featuring the Nebrodi's (northern Sicily) geographic area, the monastery of San Filippo di Fragalà in Frazzanò (Messina) (Fig. 1), the first Basilian-Norman center in Sicily, symbol of 15 centuries of cultural life, is one of the most representative [1]. The most ancient part of the monument was built in the eighth century, while the monastery and the Church were established in 1090, following the Basilian architecture. The cloister, the kitchens and the friars' small rooms, still legible, belong to this period. Inside the Norman church there is a “fresco” wall painting (11th and 12th centuries) featured by the Comnenian style. During the middle age the monastery was among the most important Sicilian religious centers; its prestige is evidenced by a plenty of historical documents

collected in the Palermo library “Archivio di Stato”. During the 17th century the building was restored and some ancient parts of the Medieval Church were changed according to the baroque style. After a period of decadence (from the beginning of 19th century) the monastery was classified as an important national monument so that in the 1930 some restoration activities were carried out. Although some parts of the monastery show at the moment a poor state of conservation and the whole building underwent considerable transformations over the time, several original characteristics are still recognizable, like, for instance, the pilasters of the apse made of red brick.

Aim of the present work is two-fold: (a) to gain further knowledge of the building history of the monastery of Frazzanò through an extensive investigation on plasters, mortars, bricks and frescoes; (b) to determine the overall state of conservation of the building and to provide useful information thus allowing correct restoration activities to be planned. The knowledge of the raw materials, the building materials production processes and local techniques has an important

* Corresponding author. Tel.: +39 90 6765716; fax: +39 90 393756.
E-mail address: cardiano@chem.unime.it (P. Cardiano).



Fig. 1. The monastery of "San Filippo di Fragalà".

bearing on the conservation technology. Today in fact historical buildings are restored using plasters, mortars and bricks made according to contemporary standards, neglecting that the preservation of the original appearance of an historical building as well as the physico-chemical compatibility with the old materials require individual solutions. The paper also remarks the central role played by the analytical chemists, among the other scientists, in the diagnosis of the conservation state of artworks as well as in the chemical characterization of artifacts of great historical and artistic value.

We report here on the characterization and classification of the bricks of Frazzanò Monastery according to their chemical (major and trace elements) and mineralogical features. X-ray and TG-DTA analyses were also carried out to obtain information about the raw materials used as well as qualitative indications about firing temperatures. The characterization of the raw materials may be a source of information on the technology of bricks production in Sicily, the identification of the production centers and the periods in which they were manufactured. The raw materials to produce bricks in fact were usually outcropped within a relatively short dis-

tance from the kiln and some times excavated and fired on the side of the building itself. The overall conservation state of the bricks was investigated through mercury intrusion porosimetry, that provides data on the microstructure of the samples, and by means of HPLC to determine the soluble salts content, that is related to the action of marine aerosol and to the migration of salts solution from the ground.

2. Experimental

The sampling was accomplished in conjunction with archaeologists of "Soprintendenza ai Beni Culturali e Ambientali" of Messina and performed on the basis of historical and architectonic considerations. Information regarding sampling location and historical periods are provided in Table 1 and Fig. 2. After removal of the external part in order to analyse only non-altered material, the samples, taken with a chisel, were studied by a combination of techniques. Major and rare-earth elements analyses were accomplished by inductively coupled plasma atomic emission spectrometry

Table 1
Sampling

Samples	Sampling area	Height (m)	Sampling point
BO1	NE corner, outside, Byzantine church	2.5	Central apse, arched lintel
BI2	NE corner, inside, Byzantine church	2	Left apse, inner arched lintel
BI3	NE corner, inside, Byzantine church	2	Central apse, left side, inner arched lintel
BI4	NE corner, inside, Byzantine church	2	Central apse, left side, superior arched lintel
BI5	NE corner, inside, Byzantine church	1	Right apse, arched lintel
NO1	NW corner, outside	0.3	Main portal, left side
NO2	NW corner, outside	2	Main portal, left side
NI3	Norman church, inside	1	Main arch, right pier
NI4	Norman church, inside	1	Main arch, right pier
NO5	E wall, outside, Norman church	1	Central apse, right pilaster strip
NO6	E wall, outside, Norman church	1	Central apse, left pilaster strip
MO1	N wall, outside	0.3	Under a balcony dated 1937

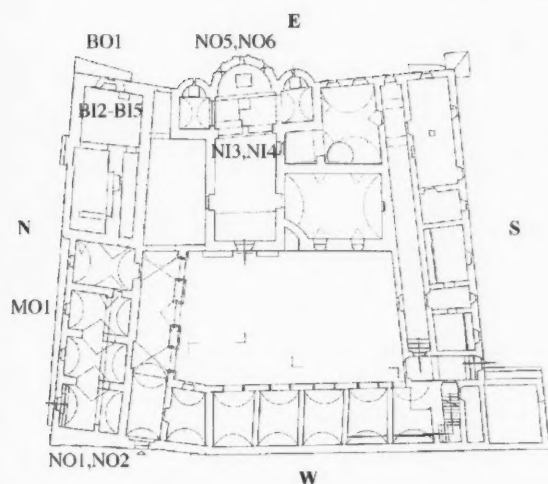


Fig. 2. Plan of the monastery and sampling points. B, Byzantine; N, Norman; M, Modern; I, Inside; O, Outside.

(ICP) and instrumental neutron activation analysis (INAA) by Activation Laboratories Ltd., Ancaster, Ont., Canada. Mercury intrusion porosimetry measurements have been performed with low-pressure (400 kPa) Pascal 140 and high-pressure (200 MPa) Pascal 240 porosimeters by Fisons Instruments according to Normal recommendation 4/80 [2]. Soluble salts determination (Normal recommendation 13/83 [3]) has been carried out by treating finely ground samples with a fixed volume of ultrapure water. The quantitative determination of the most representative ions in the aqueous extract has been performed by means of a Dionex Chromatographer equipped with the ED40 conductometric detector and isocratic pump. The data acquisition and elaboration was performed with the software package PeakNet 5.1. The conductometric investigations have been carried out with an InoLab CondLevel1 conductometer. Thermogravimetric analyses were performed by means of Perkin-Elmer Pyris Diamond TG-DTA in the temperature range between 25 and 1000 °C, under dynamic air (50 ml/min) and heating rate of 10 °C/min. XRD investigations were carried out on Siemens D5000 diffractometer equipped with vertical goniometer and Cu K α radiation filtered by Ni, with experimental conditions of 40 kV, 20 mA, 2 mm aperture diaphragm, 1 mm scattered radiation diaphragm and 0.2 detector diaphragm, CT: 1 s, steps: 0.017° 2 θ /s.

3. Results and discussion

The bricks have been characterized by a combination of techniques (INAA, ICP, MIP, HPLC, TG-DTA and XRD) that are among the most employed to investigate stone artworks. Each of the above techniques provides useful information only when complemented by the others. Otherwise incomplete or misleading conclusions may be obtained.

For instance, high porosity materials (with total porosity > 20%) are usually associated to high soluble salt content on the basis of porosimetric or HPLC investigations only. But this relationship is not straight, as we have found by performing both analyses on each sample. In addition INAA or ICP data on bricks may be misinterpreted when not corroborated by XRD; at the same time the latter must be used in combination with TG-DTA experiments to recover indications on the brick firing temperature. In this context this paper reports the most complete characterization of ancient bricks and provides supported suggestions on all the complementary techniques to be used for an accurate study of bricks.

3.1. Bricks

Bricks are ceramic materials obtained by firing raw clay at temperatures ranging between 650 and 1000 °C [4]. Color, composition and mechanical properties are dependent on the nature of the clay (kaolinite, illite, smectite), kiln environment (oxidative or reductive), kiln operator, temperature and firing process, nature and amount of the temper (quartz, carbonates, shards, grounded fired clays). Although, in proper conditions primary clay minerals may survive, calcite tempered clays are subjected to two main thermal processes: clay dehydroxylation (ca. 400–600 °C) and decarbonation of the calcareous materials (750–850 °C) [5–7]. Higher firing temperatures lead the calcite decomposition products to react with fired clays to form new calcium silicates phases such as gehlenite, anorthite or diopside (wollastonite) [6–8]. The thermal modifications following Ca-poor clays firing are simpler since the original raw materials mineralogy is mainly preserved.

From a visual inspection samples BO1–BI5 were crumbly, although their core was still featured by good aggregation and consistency while NO1–NO6 and MO1 appear more compact and in a better state of conservation. No formation of salt efflorescence was observed. It is worth to mention that the main stress cause for bricks may be identified in the migration and crystallization of soluble salts that can originate from the material itself and from the environment (marine spray, underground, air pollution).

3.2. ICP and INAA analyses

The concentration of major and traces elements was determined by ICP and INAA analyses. The outcomes of the ICP analysis (Figs. 3–5) allow grouping the bricks into three groups by considering the CaO content. Samples NO1, NO2, MO1 and BI5, featured by a low CaO content, belongs to group I (Fig. 3) while NO5 and NO6, featured by a medium CaO content (4.3–7.1%) may be placed in set II (Fig. 4). Samples BO1, BI2, BI3 and BI4, NI3 and NI4, characterized by a high CaO percentage (ranging from 10.01 to 12.01%), may be grouped in set III (Fig. 5). This classification is also supported by SiO₂ and Fe₂O₃ contents. The ratio

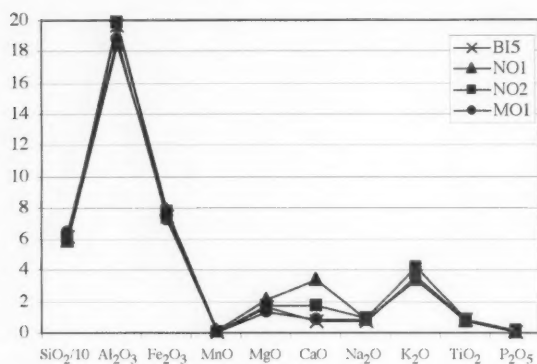


Fig. 3. Major oxides (%): samples with low CaO content.

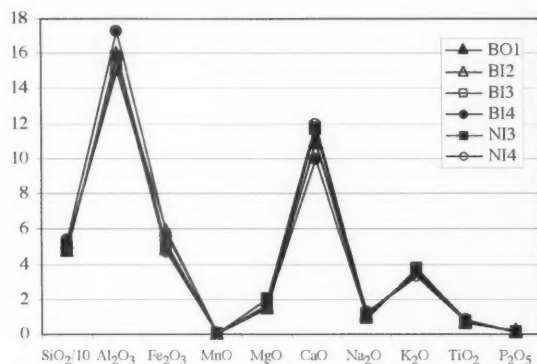


Fig. 5. Major oxides (%): samples with high CaO content.

$\text{SiO}_2/\text{Al}_2\text{O}_3$ ranges from 3 to 3.4 for all the samples while the $\text{SiO}_2/\text{Fe}_2\text{O}_3$ ratio covers a wider range which goes from 7.4 to 10.5. It is to note that BI5, dated back to the eighth century, NO1 and NO2, dated back to 1090, and MO1, dated back to 1930, show a very similar composition included a higher Fe_2O_3 content and the lowest CaO content. Furthermore, samples NO5 and NO6, dated back to 1090, are the only species with a medium CaO content but a different MgO and LOI. Samples BO1, BI2, BI3 and BI4, dated back to 700, show similar composition except the LOI.

INAA, a technique that gives qualitative and quantitative information about rare-earth elements, represents the preferred analytical technique to address questions such as composition of raw, cooked and aged materials. As a consequence it is a very useful tool to understand if the raw materials used for the production of bricks originated from the same geological area. Current methods used in archaeometry to establish raw material source involve in fact the analytical content of rare-earths as well as oligoelements such as Ni and Cr [9]. The relative abundance of rare-earths elements is peculiar of the geological history of a material and represents the fingerprint of an archeological material [10,11]. Analysis of the graph of Fig. 6 shows that all the samples are

featured by a very similar pattern concerning rare-earth elements, suggesting that the raw materials employed in manufacturing the bricks of the monastery of Frazzanò have a local, common geological source.

3.3. Mercury porosimetry

We particularly focused our attention on porosimetric investigations since the pores represent the sites where most of the physico-chemical processes associated to weathering and biological phenomena occurs [12,13]. It seems well established in fact that meso- and especially micropores are the major responsible ones of stone decay since they are mainly involved in water transport mechanism and then in salt crystallization processes. Furthermore, since the pore space represents also the site where the materials used to consolidate decayed bricks accumulate, the investigation of the pore system allows to detect the modification of the original internal porous structure following consolidating treatment and to measure the effectiveness of the conservation treatments. Partial filling of the macropores and their transformation into smaller pores could cause further deterioration of the stone material.

In Fig. 7 a typical porosimetric distribution graph is shown (sample BI5). The curve is obtained by plotting cumulative volume data versus radius during intrusion experiments. It represents the specific volume of mercury penetrated into pores having a definite radius. The histograms heights corresponds to the percentages of pores having radius included between fixed values, as shown in Table 2.

The porosimetric findings allow revealing further differences or similarities among the samples (Table 2). The porosity values of the samples NO1, NO2, MO1 and BI5, namely the samples featured by the lowest calcite content, range from 22.3 to 39.4%. The pore size distribution curves of the samples NO1, NO2 and surprisingly BI5 are similar: both exhibit an average pore radius ranging from 0.80 to $0.83\ \mu\text{m}$ while the maxima lie between 1 and $0.5\ \mu\text{m}$, namely at the border-line between macro- and mesopore region (according to IUPAC classification). The only no-

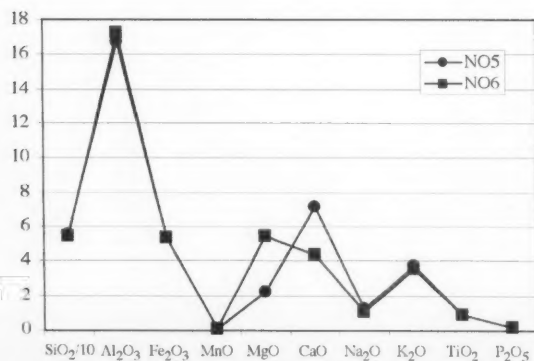


Fig. 4. Major oxides (%): samples with medium CaO content.

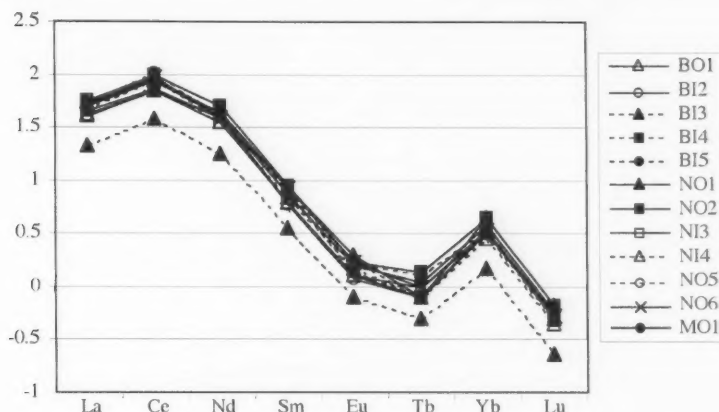


Fig. 6. Rare-earth elements (log ppm).

ticeable difference lies in the percentage of the voids corresponding to the maxima. On the contrary MO1 appears very different either in porosity as in the pore size distribution. The pore size distribution of MO1, the less porous (22.3%) among all the analysed samples, is mainly concentrated in the range 0.3–0.003 μm (85%), dramatically shifted towards the micropore region. This means that MO1, the newest sample, will show lower resistance to water and soluble salt migration.

The samples taken from the Byzantine church BI2 (internal part of the church) and BI3 (arched lintel of sacred arch) are characterized by comparable values of porosity, while BO1 (external part of the church) differs for the average pore radius and the pore size distribution. It is to note that sample BI4, taken from the arched lintel as well, is featured by a very different texture. While BI3 shows a total porosity of 31.4%, with an average pore radius of 0.21 μm , BI4 is much more porous (42.6%) and exhibits an average pore radius of 0.64 μm . They also considerably differ in the pore size distribution: while the greatest percentage of pores of BI4 (70%) is detected in the range 1–0.4 μm (58.91% in the

range 1–0.5 μm), the pore size distribution of BI3 is mainly concentrated in the range 0.3–0.05 μm .

Among the six middle age samples: NI3 and NI4 exhibit comparable parameters while NO5 and NO6, expected to be very similar as sampled in the two pilaster strips of the apse, according to analytical and thermogravimetric analyses (see later) show significant differences above all in the pore size distribution which for NO6 includes pores ranging from 1 to 0.05 μm while for NO5 it is mainly concentrated between 0.4 and 0.1 μm .

3.4. Thermogravimetric analysis

Thermogravimetric and thermal analyses are often used as a tool for the characterization and classification, in combination with other techniques, of historical mortars and bricks [14]. Temperature range and weight loss allow identification and semiquantitative determination of calcite, lime, magnesite, hydromagnesite and gypsum, the detection of organic compounds and clay dehydroxylation phenomena [15]. Dehydroxylation–rehydroxylation of clay mineral is a

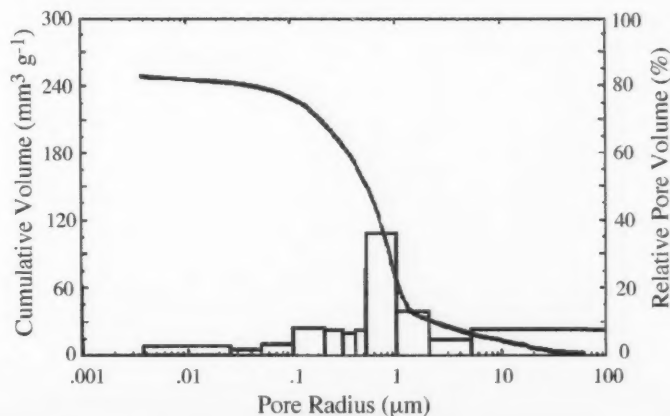


Fig. 7. Porosimetric distribution of sample BI5.

Table 2
Bricks porosimetric data

	BO1	BI2	BI3	BI4	BI5	NO1	NO2	NI3	NI4	NO5	NO6	MO1
Total porosity (%)	32.9	32.5	31.4	42.6	39.4	35.5	37.9	35.3	35.4	32.2	22.3	
Bulk density (g cm ⁻³)	1.64	1.69	1.72	1.52	1.58	1.62	1.64	1.64	1.59	1.54	1.83	1.84
Average pore radius (μm)	0.32	0.20	0.21	0.64	0.83	0.80	0.81	0.38	0.36	0.38	0.47	0.27
Relative volume (%)												
Pore radius ranges (μm)												
>5	2.72	2.58	2.08	2.13	7.88	6.02	8.68	1.25	1.75	1.11	5.72	4.16
5–2	1.2	0.17	1.55	0.13	4.94	4.11	5.41	0	0.08	2.23	4.13	1.08
2–1	1.14	0.3	0.96	0.79	13.19	7.2	12.9	0.47	0.58	3.95	1.78	0.98
1–0.5	3.84	0.53	0.89	58.91	35.88	47.87	35.36	3.88	2.16	1.22	13.37	1.66
0.5–0.4	6.32	0.45	0.36	11.51	7.38	6.46	6.82	31	28.26	1.93	14.07	0.91
0.4–0.3	23.61	1.97	1.01	7.37	6.89	6.46	6.54	31.44	31.83	41.34	15.13	6.15
0.3–0.2	18.73	34.12	23.22	6.7	7.57	6.75	7.94	11.8	13.46	18.24	16.98	19.93
0.2–0.1	16.49	35.11	44.83	4.57	8.43	8.52	9.12	6.83	8.48	14.18	17.24	18.43
0.1–0.05	9.6	11.53	11.73	2.98	3.58	3.38	3.59	4.66	4.49	7.5	6.6	11.17
0.05–0.025	6.47	5.98	6.18	2.13	1.63	1.91	1.76	3.7	3.99	3.83	2.62	9.82
0.025–0.003	9.89	7.26	7.18	2.77	2.63	1.32	1.87	4.97	4.92	4.48	2.36	25.7

reversible process. Clay fired at temperature below 800 °C may slowly rehydroxylate partially restoring the original material. Above this temperature the process becomes irreversible [16,17] and the mineral clay undergoes structural and/or compositional modifications. Suggestions on raw material composition and provenance as well as information on the baking temperature may be also available based on simultaneous TGA/DTA investigations.

According to the porosimetric findings, the TG and DTA analysis of samples falling in set I, namely NO1, NO2, MO1 and BI5, allows to detect some differences that would lead to a further grouping of the above bricks. Samples NO1 and NO2 show similar featureless curves with less than 2% of total weight loss at 1000 °C (Table 3). Most of the weight loss (1.2%) appears in the range 200–400 °C, very likely due to loss of interlayer water. The total weight loss of BI5, one of the oldest brick sampled, is quite low (ca. 2%) in the whole range of temperature. Only two small inflections centered at 217 and 299 °C were detected. In contrast the derivative curve (DTG) of the scan of MO1 (total loss of 12.4%) shows four peaks, endothermic in nature, corre-

sponding to the four inflections observed at 78, 342, 432 and 570 °C. The partially superimposed weight losses falling in the temperature range 342–500 and 500–650 °C represent the main processes and are ascribed to interlayer water loss and clay dehydroxylation, respectively [18]. A small peak at 806 °C and a not negligible amount of imbibition water was also observed. It is worth to remember that MO1, the less porous brick sample, was taken in the northern side of the monastery that has been restored in the 1930.

The curves of NO5 and NO6 are a little surprising. To confirm the differences found by ICP in the MgO and CaO content, despite their sampling points in the pilaster strips are very close, their thermogravimetric behaviour shows similar total weight loss but significant differences in the location of the inflections. The thermograms of NO6 are featured by three processes, endothermic in nature: two partially superimposed weight losses falling in the range 200–550 °C, very likely due to interlayer water escape and clay dehydroxylation, and a small peak at 139 °C (peak at 7.64 Å in the X-ray diffractogram of NO6), assigned to gypsum dehydration. The paragenesis of CaSO₄ may be due to residual mortar joints traces or, alternatively, may be found in the sulphur oxide rich kiln environment. Burning of sulphureous coal or decomposition of sulphur compounds, such as pyrite, present in the raw material, may generate a sulphur trioxide atmosphere which easily reacts with CaO leading to CaSO₄. On the contrary sample NO5 shows, as a major process, a weight loss (3.5%) at 659 °C assigned to calcareous material decomposition. These differences, also supported by XRD investigations, suggest that the raw material used to manufacture NO5 and NO6, was recovered from different sources.

The DTG and DTA analysis of samples NI3, NI4 and BO1–BI4, the latter set sampled in the Byzantine church, show similar features: total weight loss in the whole range of temperature lying between 12 and 4% and a main inflection falling in the range 600–750 °C, due to calcareous decomposition. The decomposition temperature of calcitic mate-

Table 3
Weight loss (%)

	<200 °C	200–600 °C	600–850 °C	25–1000 °C
BO1	1.5	2.7	7.4	11.6
BI2	1.4	2.2	5.0	8.6
BI3	1.5	2.3	4.6	8.4
BI4	0.4	0.9	2.7	4.0
BI5	0.2	1.7	–	1.9
NO1	–	1.3	0.4	1.7
NO2	–	1.4	–	1.4
NI3	1.4	3.1	3.4	7.9
NI4	2.0	3.1	3.9	9.0
NO5	1.6	1.8	3.5	6.9
NO6	3.6	3.6	0.8	8.0
MO1	2.8	4.3	5.3	12.4

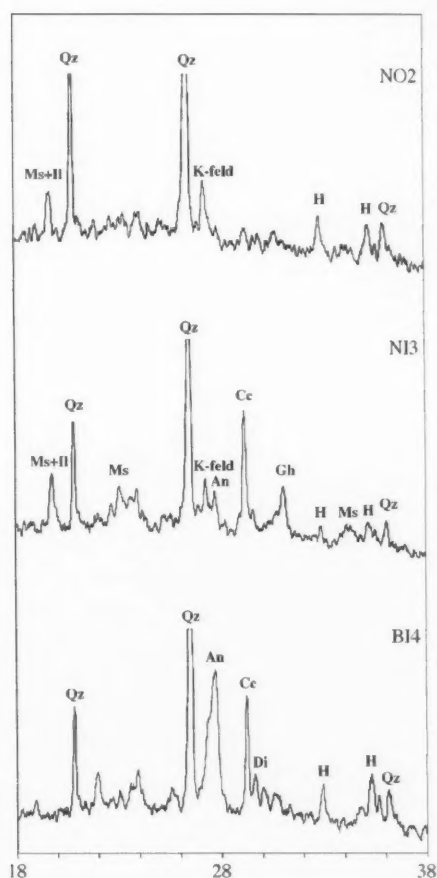


Fig. 8. Representative XRD spectra (2θ) of samples NO2, NI3, BI4 (Qz, quartz; Cc, calcite; K-feld, K-feldspar; Ms, muscovite; Il, illite; H, hematite; An, anorthite; Di, diopside; Gh, gehlenite).

rials may vary in a large temperature range (600–850 °C) as a function of the experimental conditions and the degree of crystallinity of the material. Shoval et al. [19] clearly showed that while monocrystalline calcite undergoes complete decarbonation at temperatures higher than 750 °C, polycrystalline materials, such as limestone or chalk, start to decompose at temperatures lower than 650 °C. On these basis a temperature range for calcite decomposition may be defined rather than a specific temperature. Furthermore,

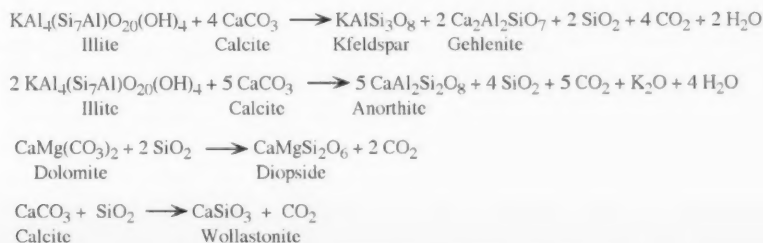
since calcareous temper disappears on firing at 650–850 °C, the calcite still present is recarbonated lime. The amount of CaCO_3 , as found by thermogravimetric and calcimetry (Fruhling method), does not correspond to the CaO content as determined by chemical analysis, indicating that the exceeding CaO content arises from other Ca containing mineral phases such as hydrated silicoalluminates. The curves of NI3, NI4 and BO1–BI4 also show small hygroscopic water loss under 100 °C as well as broad absorptions between 300 and 600 °C due to the phenomena associated to clay decomposition. Samples NI3 and NI4 show, as a well detectable difference with respect to BO1–BI4, a small loss of interlayer water at ca. 200 °C while the phenomena associated to clay decomposition are less evident.

3.5. X-ray analysis

The powder X-ray data (Fig. 8) are fully in agreement with the porosimetric and thermogravimetric findings and confirm that different typologies of bricks are present. They clearly show the mineral assemblage of the raw materials (quartz, calcite, muscovite, chlorite) and the high temperature mineral phases (plagioclase, gehlenite, diopside or wollastonite, hematite). The 12 samples are featured by at least five different mineral assemblages mainly arising from the bulk composition of the clay and the firing temperature. The relevant reactions that occur when raw clay is fired is strongly dependent, as before stated, on the nature of the temper. In Ca-rich clay gehlenite, anorthite and diopside are the most important new phases which grow up when the carbonatic mixture is baked at higher temperatures. Gehlenite starts to form when illite and calcite react at temperature of ca. 800 °C while anorthite forms, also at expense of gehlenite, not below 850 °C. Diopside (or wollastonite) is the product of the reaction of quartz and dolomite in the temperature range of 900–1050 °C (Scheme 1) [5–7].

On the contrary, firing of Ca-poor clays induces textural modifications only without major compositional changes. The presence of hematite, which appears at ca. 850 °C, is the most valuable indicator of their firing temperature. So, the mineral assemblage after baking is a good help to make suggestions on the bricks firing temperature.

Quartz, calcite, Kfeldspar and hematite are the mineral phases common to almost all the bricks while muscovite



Scheme 1. Reactions occurring when Ca-rich clays are fired.

Table 4
Soluble salts content (%)

	Cl ⁻	NO ₂ ⁻	NO ₃ ⁻	SO ₄ ²⁻	PO ₄ ³⁻	Na ⁺	NH ₄ ⁺	K ⁺	Mg ²⁺	Ca ²⁺
BO1	0.56	–	0.52	0.04	–	0.46	0.03	0.31	0.05	0.64
BI2	0.20	–	0.20	0.14	0.01	0.26	0.01	0.67	0.04	0.65
BI3	0.09	–	0.06	0.12	–	0.12	–	0.11	0.02	0.14
BI4	0.31	–	0.12	0.06	–	0.59	0.05	0.12	0.02	0.13
BI5	0.12	–	0.51	0.07	–	0.24	0.03	0.31	0.03	0.22
NO1	0.11	0.01	0.06	0.04	–	0.34	0.03	0.05	0.01	0.31
NO2	0.11	–	0.03	0.03	–	0.14	0.03	0.14	0.01	0.10
NI3	0.35	–	1.00	0.10	–	0.41	0.01	0.35	0.09	0.66
NI4	0.30	–	0.97	0.05	0.01	0.38	0.02	0.38	0.07	0.57
NO5	0.74	–	0.07	0.06	–	0.15	0.02	0.17	0.03	0.32
NO6	0.58	–	0.09	0.04	–	0.17	0.01	0.15	0.02	0.34
MO1	1.04	–	1.19	0.06	–	0.60	0.03	0.42	0.06	0.78

(peaks at 10 and 4.499 Å) is present, with different abundance, in all the samples except NO1, NO6, BI4. Independently from age and composition, diffractometric data suggest that the possible baking temperature for most of the samples lies in the range of 800–900 °C, except for MO1 and BI4 which appear baked at higher temperatures.

The low CaO-content samples NO1, NO2, MO1 and BI5 clearly show the peaks at 2.51 and 2.69 Å of hematite which, as before stated, starts to form at ca. 850 °C. In addition optical microscopy analysis (results not reported) shows extended vitrification for sample MO1 only, suggesting that this sample was fired at higher temperature or baked for a longer time. The Norman samples NI3, NI4, NO5, NO6 and the eighth century sample BI2 exhibit, well detectable, the peaks of the high-temperature Ca-silicate phases gehlenite and anorthite that in NO5 and NO6 appear with different abundance. BO1 and BI3 besides, a large amount of muscovite, shows only traces of gehlenite and hematite suggesting they have been baked at lower temperature. BI4, although sampled very close to BI3, is featured by a comparatively large amount of anorthite as well as evident traces of diopside, indicative of a higher baking temperature.

3.6. Soluble salts analysis

The determination of soluble salts in building materials is one of the tests recommended by the Normal Commission in order to verify the degradation phenomena occurring on lithic samples and to determine their state of conservation. In fact the amount of soluble salts can be related to specific decay phenomena such as atmospheric pollution, acid rain or effects concerning marine spray. They cause weakening and degradation of the materials with formation of crusts or efflorescence as visible effects.

According to the low conductivity values (not reported), a first sight analysis of the data reported in Table 4 clearly shows that all the samples are featured by a low total salts content thus indicating that the building is not affected by appreciable decay phenomena. The low sulphate content, as confirmed by mineralogical-petrographic analysis, rules

also out sulphatation phenomena. Furthermore, the low salt content detected can be referred to the original composition of the raw clay rather than a specific alteration. The only notable data concern NI3, NI4 and MO1. Samples NI3 and NI4 show a nitrate content which approximates to 1%. They have been sampled inside the Norman Church that has been employed for a long time both as a stable and as a warehouse, and then, the nitrates can be confidently explained by this kind of activities. Brick MO1, sampled at ca. 30 cm from the ground in the northern part of the building, exhibits a chloride and nitrate content of ca. 1%. Taking into account the distance of the monument from the sea and the evidence of the low chloride content in all samples taken in the same area, probably the presence of above ions can be ascribed to capillary phenomena rather than marine aerosols transport [20,21].

4. Conclusions

Although the low number of bricks analysed does not allow a statistical treatment by hierarchical cluster analysis, the outcomes of the investigations carried out on brick samples taken from the monastery of San Filippo di Fragalà allows us to draw some preliminary conclusions. Independently from chemical composition, production technology and conservation state, all the raw materials used in brick manufacturing originate from the same geological source. Furthermore, the chemical analysis findings suggest that raw clay was excavated from different local sources. In fact, differently from Norman samples, made of limeless clay, the oldest samples were mainly manufactured by using calcareous raw material. Samples NO1, NO2, MO1 and BI5 (set I), although featured by a low percentage of CaO, can be distinguished by means of porosimetric, thermogravimetric and mineralogical investigations. In fact the bricks NO1 and NO2, both taken from the north-western side of the building near the main entrance (at different heights), show a unique weight loss (ca. 2%), mainly due to interlayer water escape, while X-ray analysis suggests a firing temperature

reaching up at least 850 °C. Furthermore, soluble salts investigations do not show differences between them, despite they have been taken, as already stated, at different heights (sample NO1 at about 30 cm from the ground, while NO2 at ca. 3 m), meaning that in this part of the building there are not degradation phenomena caused by rising damp.

Sample MO1, taken from the northern side in a zone that was restored during the thirties, is characterized by the lowest CaO content and is very different from all the others. It is the less porous (22.3%) with the pore size distribution considerably shifted towards the micropores region. TG experiments lead to a considerable weight loss mainly due to phenomena typical of clay, namely interlayer water loss and clay dehydroxylation while the groundmass shows isotropic feature, as if it has been fired at a relatively low temperature for a long time. BI5 is doubtless the more mysterious brick. Although, sampled in the arched lintel of the right apse of the Byzantine church, a few meters from the main arch were samples BO1–BI4 were taken, BI5 greatly differs from the analytical, porosimetric and thermogravimetric point of view and, as a consequence, it shows a different mineral assemblage.

The samples BO1, BI2 and BI3, taken in the Byzantine church, are characterized by comparable values of chemical composition, total porosity and TG response. Based on X-ray powder findings, which evidence the presence of anorthite in BI2, BO1 and BI3 appear fired at lower temperature. Nevertheless, we suggest that the different mineral assemblage may be due to different baking procedures more than to a different firing temperature. In contrast, the diffractogram of brick BI4, similar to the above samples for sampling location, chemical composition, textural and thermal properties, unequivocally shows the presence of diopside which is indicative of a baking temperature of at least 900 °C. This peculiarity too may be explained in terms of unhomogeneous kiln temperature rather than different raw clay composition. Samples NI3 and NI4, taken inside the Norman church, should be very similar to bricks NO1 and NO2 (taken in the main entrance of the monastery), NO5 and NO6 (taken from the apse of the Norman church), although these parts of the building were restored during the 17th century. Bricks NI3 and NI4, as already stated, are featured by a CaO content of ca. 11% and a porosimetric distribution very different from that of all the other samples. These findings are very different from those of NO1, NO2, NO5 and NO6. Samples NO5 and NO6, exhibiting medium CaO content, are intriguing too. Although sampled at the same height in the two pilaster strips of the central apse, which are quite close, they appear different, for chemical composition and TG response, from them as well as from the other medieval samples. A possible explanation lies in the nature of the pi-

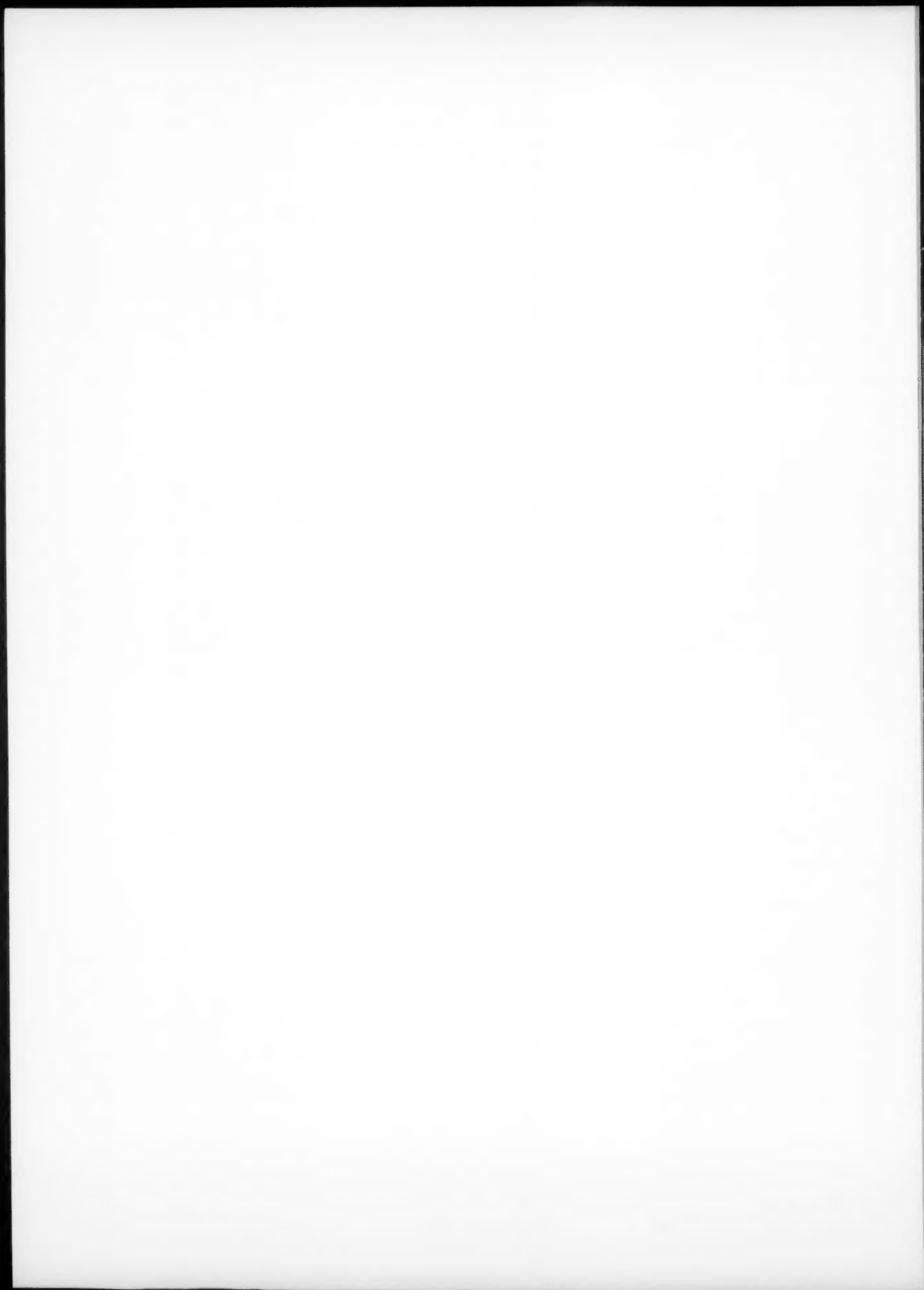
laster strip which is decorative only. So this decorative motif could be added later or alternatively it was restored later in time. The combined data concerning NO1–NO2, NI3–NI4, and NO5–NO6 suggest that, although dated back to 12th century, the Norman church and the main entrance of the monastery were built at different times or with different raw material.

Finally, the low amount of soluble salts detected in all the samples lead us to suggest that, independently from the location, in contrast with the high porosity values, the building does not suffer from decay phenomena due to rising damp, acid rain or marine spray.

All these findings must be considered as being of preliminary significance only since investigations on a large number of plasters and mortars are in due course.

References

- [1] C. Filangeri, *Monasteri Basiliani di Sicilia*, Messina, 1979.
- [2] Normal protocol 4/80, Distribuzione del volume dei pori in funzione del loro diametro, CNR-ICR, Rome, 1981.
- [3] Normal protocol 13/83, Dosaggio dei sali solubili, CNR-ICR, Rome, 1983.
- [4] J. Warren, *Conservation of Brick*, Butterworths/Heinemann, Oxford, 1999.
- [5] P. Dominuco, B. Messiga, M.P. Riccardi, *Thermochim. Acta* 321 (1998) 185.
- [6] J. Capel, F. Huertas, J. Linares, *Miner. Petrogr. Acta* 29-A (1985) 563.
- [7] P. Duminuco, M.P. Riccardi, B. Messiga, M. Setti, *Ceramurgia* 5 (1996) 281.
- [8] S. Shoval, *J. Thermal Anal.* 42 (1994) 175.
- [9] R. Vigil de la Villa, R. Garcia Giménez, J. Cuevas Rodriguez, D. Bernal Casasola, *Thermochim. Acta* 322 (1998) 9.
- [10] M.A. Bello, A. Martín, *Archaeometry* 34 (1992) 21.
- [11] H. Mommsen, *J. Radioanal. Nucl. Chem.* 247 (2001) 657.
- [12] G.C. Robinson, *Am. Cer. Soc. Bull.* 63 (1984) 295.
- [13] C. Cardell, T. Rivas, M.J. Mosquera, J.M. Birginie, A. Moropoulou, B. Prieto, B. Silva, R. Van Grieken, *Earth Surf. Process. Landforms* 28 (2003) 1.
- [14] P. Maravelaki-Kakaitzaki, A. Bakolas, A. Moropoulou, *Cement Concrete Res.* 33 (2003) 651.
- [15] A. Moropoulou, A. Bakolas, K. Bisbikou, *Thermochim. Acta* 269 (1995) 743.
- [16] C.R. Enriquez, J. Danon, M. da C.M.C. Beltrao, *Archaeometry* 21 (1979) 183.
- [17] S. Shoval, P. Beck, Y. Kirsh, D. Levy, M. Gaft, E. Yadin, *J. Thermal Anal.* 37 (1991) 1579.
- [18] A. Moropoulou, A. Bakolas, K. Bisbikou, *Thermochim. Acta* 269 (1995) 779.
- [19] S. Shoval, M. Gaft, P. Beck, Y. Kirsh, *J. Thermal Anal.* 40 (1993) 263.
- [20] G. Alessandrini, R. Bugini, R. Negrotti, L. Toniolo, *Eur. J. Miner.* 3 (1991) 619.
- [21] C. Riontino, C. Sabbioni, N. Ghedini, G. Zappia, G. Gobbi, O. Favoni, *Thermochim. Acta* 321 (1998) 215.



New flow-multicommutation method for the photo-chemiluminometric determination of the carbamate pesticide asulam

A. Chivulescu^a, M. Catalá-Icardo^b, J.V. García Mateo^c, J. Martínez Calatayud^{a,*}

^a Department of Analytical Chemistry, University of Valencia, Dr. Moliner 50, Burjassot 46100, Valencia, Spain

^b Department of Chemistry, Polytechnic University of Valencia, Valencia, Spain

^c Department of Chemistry, Biochemistry and Molecular Biology, University Cardenal Herrera CEU, Moncada, Valencia, Spain

Received 31 December 2003; received in revised form 29 April 2004; accepted 14 May 2004

Available online 10 July 2004

Abstract

This paper deals with a straightforward automated method for the determination of asulam in water based on the use of a flow manifold including three computer-controlled solenoid valves. The method involves irradiating on an aqueous solution of asulam in glycine buffer at pH 8.3 with UV light during 90 s, then follows the oxidation with potassium permanganate in a sulphuric medium and chemiluminescence-based detection of the resulting photoproducts. The limit of detection thus achieved is $40 \mu\text{g l}^{-1}$. The detector response is linear up to a 5 mg l^{-1} asulam concentration and the throughput is $30 \text{ samples h}^{-1}$. In parallel tests, oxidation with alkaline ferricyanide was also assessed and the results compared (sensitivity, selectivity and reproducibility) with those from oxidation with potassium permanganate in acidic medium. The use of a flow based on solenoid valves results in substantial reagent savings and constitutes a further extension of clean chemistry procedures. To the authors' knowledge, this is the first chemiluminescence-based determination of asulam and also the first based on multicommutation analysis.

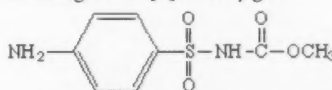
© 2004 Elsevier B.V. All rights reserved.

Keywords: Asulam; Multicommutation; Solenoid valves; Chemiluminescence; Photodegradation

1. Introduction

Asulam (methyl-4-aminobenzenesulphonyl carbamate), the molecular structure of which is shown below, is a carbamate pesticide with a broad spectrum of biological activity; thus, it is used as an insecticide, herbicide and fungicide, among others. Most often, however, it is used as a post-emergency herbicide for controlling deciduous and perennial grasses, as well as the fern *Pteridium aquilinum* L. Asulam acts by stopping cell division and growth of plant tissues. The maximum allowed residual concentration of asulam in crops for human consumption in Spain is 0.05 mg l^{-1} (or mg kg^{-1}) [1]. Asulam can accumulate and remain in soil for more than one season. However, it exhibits a high mobility by virtue of the high water solubility of its sodium salt and is therefore a potential water

pollutant. This justifies its control in both ground and underground water, which requires the use of accurate, sensitive, selective methods for its determination allowing its rapid in situ quantitation. The current guideline value for asulam in drinking water [2] is $0.1 \mu\text{g l}^{-1}$.



Asulam is most often determined by diazotization of its amino group and subsequent coupling with Marshall's reagent [*N*-(1-naphthyl)ethylenediamine] [3]. This method is poorly selective, however. Synchronous fluorimetry [4] allows asulam to be determined following derivatization of the primary amino group with fluorescamine. This method has been used to determine the analyte in peaches. Asulam has also been quantified electrochemically (using a glassy carbon electrode) [5] and by square-wave voltammetry and amperometry. The voltammetric determination, allowed the mechanism behind the electro-oxidation of asulam to be elucidated; the use of the amperometric technique in

* Corresponding author. Tel.: +34 96 354 40 62; fax: +34 96 354 40 62.

E-mail address: jose.martinez@uv.es (J. Martínez Calatayud).

combination with FIA substantially reduced analysis times. However, the quantitation range afforded by both methods only allows the determination of relative large amounts of the herbicide.

Ensuring the sensitivity required for water analyses usually entails using a preconcentration and separation step that frequently involves the use of a solid phase reactor [6–10].

Most analyses for asulam, however, rely on chromatographic or electrophoretic separation. The following techniques have so far been used for this purpose: thin-layer chromatography (in soil) [6], HPLC–UV absorption (in citrus fruits and sugarcane [11], water [12–14] and peaches [15]), HPLC–fluorescence detection in combination with pre-column derivatization with fluorescamine [16,17], gas chromatography–mass spectrometry (in water) [8], capillary zone electrophoresis–fibre optic-coupled diode array detection [18], capillary isotachopheresis–HPLC [19,20], and electrokinetic capillary chromatography with simultaneous UV and electrochemical detection (in tap water) [10].

The aim of this work was to develop an automated method for the determination of the pesticide asulam in water samples. The optimized continuous-flow manifold is based on the emergent multicommutation methodology; a methodology consisting in a set of solenoid valves for the insertion of microvolumes of sample and reagents [21–23]. This methodology provides a highly flexible, easy to alter and to miniaturize manifolds, reduction of the sample and reagent consumption, and increase of reproducibility due to the reduced operator intervention. Some shortcomings can be reported of the multicommutation: namely, the necessary synchronization propulsion system and solenoid valves to insert very small volumes, the need to aspirate the solution, and at the present, the limited commercial availability of the equipment for controlling solenoid valves.

The asulam do not provides a chemiluminescence response with the common strong oxidants. However, after their irradiation with UV light, it undergoes structural changes and the resulting photoproducts supply the light emission by oxidation.

2. Experimental

2.1. Reagents

All reagents used were analytically pure unless stated otherwise and prepared in deionised water (18 M Ω cm) with a Sybron/Barnstead Nanopure II water purification system provided with a fiber filter of 0.2 μ m pore size. Asulam (94% purity) was from Dr. Ehrenstorfer. Other reagents used were: KMnO₄, K₃Fe(CN)₆, NaCl, acetone, Triton X-100, NH₄Cl and Na₂B₄O₇·10H₂O from Panreac; Ce(NH₄)₂(NO₃)₆, NH₃, KH₂PO₄, Fe(NO₃)₃·9H₂O and sodium acetate from Probus; H₂SO₄, H₂O₂, ethanol and acetonitrile from Merck; NaOH, HCl, H₂SO₄ and acetic acid from J.T. Baker; FeSO₄·7H₂O, sodium dodecyl sulfate

and hexadecylpyridinium chloride from Fluka; glycine and NaH₂PO₄·2H₂O from Scharlau; dimethylformamide from Roche; quinine sulfate from Guinama; Rhodamine B and Rhodamine 6G from Sigma. Cations tested as potential inorganic interferences were prepared from chloride (Na⁺ and K⁺ (Panreac), Ca²⁺ (Probus), Mg²⁺ (Prolabo), Zn²⁺ (Scharlau), Mn²⁺ (D'Hernio)) or sulfate (Cu²⁺ (Probus)). Anions were obtained from sodium salts (CH₃COO[−] and NO₂[−] (Probus), SO₄^{2−} (Panreac), HCO₃[−] (Guinama)) or potassium salts (H₂PO₄[−] (Panreac) and NO₃[−] (Probus)).

2.2. Apparatus

The flow manifold is depicted in Fig. 1 and consisted of a PTFE coil of 0.8 mm i.d.; a Gilson (Worthington, OH, USA) Minipuls 2 peristaltic pump provided with pump tubing from Omnifit; and, three Model 161T031 solenoid valves (NResearch, Northboro, MA, USA). The photoreactor consisted of a 173 cm length and 0.8 mm i.d. PTFE tubing helically coiled around a 15 W low-pressure mercury lamp (Sylvania) for germicidal use. The flow cell was a flat-spiral quartz tube of 1 mm i.d. and 3 cm total diameter backed by a mirror for maximum light collection. The photodetector package was a P30CWAD5F-29 Type 9125 photomultiplier tube (PMT) supplied by Electron Tubes operating at 1280 V; it was located in a laboratory-made light-tight box. The output was fed to a computer equipped with a counter-timer, also supplied by Electron Tubes.

2.3. Stock solution preparation

Stock solutions of asulam (100 mg l^{−1}) were prepared by exactly weighing and dissolving the pesticide in deionised water. This solution was stable for 1 week in the fridge and protected against light. The working standard solutions were freshly prepared by diluting the stock solution in the appropriate volume of deionised water. All solutions of pesticides were protected against light.

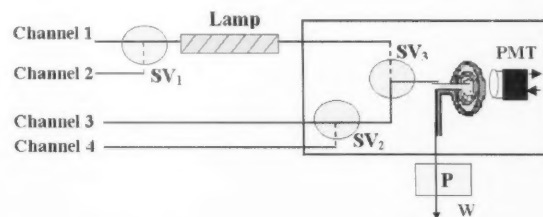


Fig. 1. Flow assembly optimized. Channel 1: photodegradation medium (glycine buffer at pH 8.3); Channel 2: aqueous solution of asulam; Channel 3: carrier (water); Channel 4: oxidant (K₃Fe(CN)₆ 0.1 mol l^{−1} in NaOH 1 mol l^{−1} or KMnO₄ 10^{−4} mol l^{−1} in H₂SO₄ 1.2 mol l^{−1}). Flow-rate: 9 and 10 ml min^{−1} for Fe(CN)₆^{3−} and MnO₄[−] system, respectively. P: peristaltic pump; W: waste; PMT: photomultiplier tube; SV: solenoid valve; Lamp: a 15 W low-pressure mercury lamp for germicidal use. The photoreactor consisted of a 173 cm length and 0.8 mm i.d. PTFE tubing helically coiled around the lamp.

2.4. Flow manifold

The manifold used with both alkaline $\text{Fe}(\text{CN})_6^{3-}$ and acid MnO_4^- is depicted in Fig. 1. It comprised three solenoid valves each of which acted as a stand-alone commutator with two positions, ON and OFF and represented in Fig. 1 as discontinuous or continuous lines, respectively. Valve operation was characterized in terms of $N(t_1, t_2)$, where t_1 and t_2 are the times during which the valve was ON and OFF, respectively, and N was the number of times the ON/OFF cycle was repeated. The flow system was operated identically throughout, the sole variations being those in the number of pulses and their length (times t_1 and t_2). The peristaltic pump was placed behind the reactor in order to aspirate the sample and reagents into the flow-cell at an overall flow-rate of 10 ml min^{-1} for the carrier (water). The individual flow-rate used for each stream varied with the reactor length and the number of solenoid valves encountered on its way by effect of the differential flow resistance. This departure from the typical location of the propulsion system in the manifold was intended to prevent the flow from stopping immediately upon insertion as the valve was actuated. With high temperatures, a water bath was used between the detection system and peristaltic pump in order to avoid overheating on the pump tubes and irreproducibility in the flow-rate as a result.

The optimum insertion profile for each oxidant system is depicted in Fig. 2. Thus, with the permanganate system, an overall 20 alternate microinsertions of pesticide and photodegradation medium were performed. During each microinsertion, valve SV_1 was kept ON for 0.3 s to aspirate asulam and OFF for 0.1 s to aspirate the buffer used as photodegradation medium. Valve V_3 was kept on to have the peristaltic pump aspirate asulam and the buffered medium throughout the duration of the process (8 s). This loading time allowed the inner walls of the photoreactor to be efficiently flushed in order to avoid sample carry-over. All valves were kept OFF for the next 90 s, time during which the sample/medium mixture was stopped in front of the lamp for irradiation with UV light. Next, valve SV_2 was switched ON for 17 s to allow the oxidant to flow and SV_3 was used to alternately microinsert photodegraded asulam (0.7 s segments) and the oxidant (0.2 s segments) in 17 ON/OFF cycles. The chemiluminescent signal was detected by the photomultiplier tube and transduced into a transient analytical signal. Once the baseline was restored, a new cycle was started. The overall analysis time was 120 s.

2.5. Sample preparation

For analytical application, water samples from different origins, namely: irrigation water, tap water and spring water, were freshly collected in plastic flasks and used within 24 h. For the determination, the water samples were spiked with asulam standard solution of 100 mg l^{-1} , to obtain solutions containing asulam between 70 and $100 \mu\text{g l}^{-1}$. Irriga-

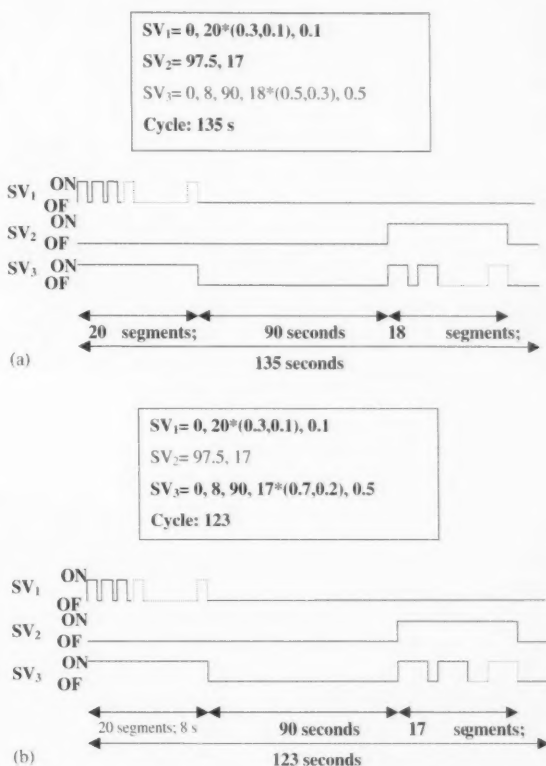


Fig. 2. Optimized insertion profile for obtaining a typical transient analytical signal for the two oxidant systems employed: (a) $\text{Fe}(\text{CN})_6^{3-}/\text{NaOH}$; (b) $\text{MnO}_4^-/\text{H}_2\text{SO}_4$. ON position corresponds to flow through discontinuous line in solenoid valve in Fig. 1. OFF position correspond to flow through continuous line in solenoid valve in Fig. 1.

tion water was filtered with a nylon filter of $0.45 \mu\text{m}$ to remove the suspended solid matter.

3. Results and discussion

3.1. Selection of the oxidation system

The photodegradation of asulam had previously been studied; to the authors' knowledge, however, neither the pesticide nor its photodegradation products had ever been determined with chemiluminescence-based detection. In order to establish the feasibility of such a determination, we tested three strong oxidants, namely: acid potassium permanganate and cerium(IV), and alkaline hexacyanoferrate(III). Asulam photodegradation was conducted in four different media, namely: NaOH, Fe(II) and H_2O_2 employed in the catalytic photo-Fenton reaction for the complete destruction (mineralization) of several pesticides [24,25]; and Fe(III) aqua complexes which has been reported as an efficient photocatalytic system for the mineralization of asulam upon irradiation with sunlight [26]. Blank signals for pure water and

analytical signals for a solution containing 25 mg l^{-1} asulam were obtained with the lamp ON and OFF, in the different photodegradation media [viz. water, 0.1 mol l^{-1} NaOH, $0.05\% \text{ H}_2\text{O}_2$, $3 \times 10^{-5} \text{ mol l}^{-1}$ Fe(III) and $3 \times 10^{-5} \text{ mol l}^{-1}$ Fe(II)]. To this end, SV_1 was actuated to merge the sample and photodegradation medium in a 13(0.5,0.2) sequence; after 150 s of stopped flow, SV_2 was switched ON and SV_3 used in a 16(0.6,0.2) sequence. A flow-rate of 10 ml min^{-1} was employed. The strongest signals were those obtained with acid potassium permanganate and alkaline hexacyanoferrate(III). These two oxidants provided similar signal intensities in all media except H_2O_2 and NaOH. Thus, the analytical signal was 80–100% smaller for both oxidants in H_2O_2 , and about 85% smaller for hexacyanoferrate(III) in NaOH.

In order to identify the oxidant providing the best analytical signal, permanganate concentrations from 2×10^{-4} to $10^{-3} \text{ mol l}^{-1}$ in an acid medium and hexacyanoferrate(III) concentrations from 5×10^{-4} to $10^{-1} \text{ mol l}^{-1}$ [in the presence of both Fe(II), Fe(III) and NaOH] were tested. Acid permanganate was found to provide a chemiluminescent signal with the lamp OFF, which, however, grew by a factor of 10 upon irradiation. On the other hand, hexacyanoferrate(III) provided no signal with the lamp OFF and signals 30% greater than those obtained with permanganate with the lamp ON. Therefore, although the differences suggested some superiority in hexacyanoferrate(III) as oxidant, we chose to use it at a 0.075 mol l^{-1} concentration in 1 mol l^{-1} NaOH to examine the photodegradation of asulam but continued to employ both oxidants in parallel.

3.2. Selection of the photodegradation medium

The tests performed to this end involved both aqueous solutions at a variable pH and potential photosensitizers and/or chemiluminescence enhancers in addition to Fe(II) and Fe(III). The media used included $2 \times 10^{-3} \text{ mol l}^{-1}$ H_2SO_4 and NaOH, glycine buffer at pH 2.8 and 8.5, acetic/acetate buffer at pH 4.7, phosphate buffer at pH 6.9, borax buffer at pH 9.7 and $\text{NH}_3/\text{NH}_4^+$ buffer at pH 10.4. Only the glycine buffer resulted in a significantly increased signal relative to pure water as photodegradation medium. The sensitizers and surfactants studied included 20% ethanol, 5% dimethylformamide, 20% 2-propanol, 20% acetonitrile, 1.2% sodium dodecylsulfate, 0.05% Triton X-100, 1.2% β -cyclodextrin and $5 \times 10^{-5} \text{ mol l}^{-1}$ quinine sulfate. The following substances were also tested but discarded because they precipitated with hexacyanoferrate(III): 0.2% hexadecylpyridinium chloride, 0.6% benzalkonium chloride and 0.2% *N*-cetyl-*N,N,N*-trimethyl ammonium bromide. Only quinine was found to enhance the analytical signal relative to pure water—at the expense of an also substantial increase in the blank signal, however.

We then examined the effect of the pH of the glycine buffer over the range 8.3–10.2. The signal was found to decrease with increasing buffer pH; however, a pH lower than

8.3 was avoided in order not to detract from the buffering capacity of glycine. The influence of the quinine concentration was examined over the range 5×10^{-5} to $3 \times 10^{-4} \text{ mol l}^{-1}$ and a $9 \times 10^{-5} \text{ mol l}^{-1}$ quinine solution found to provide the strongest signal. In the buffered solution, however, quinine provided a weaker signal than that obtained with the buffer alone. This, together with the strong blank signals obtained with quinine, led us to discard its use. The final choice as optimal medium (buffer and pH) was therefore a glycine buffer at pH 8.3.

3.3. Optimization of the flow-rate

The influence of the flow-rate was studied over the range $7\text{--}11 \text{ ml min}^{-1}$. Except at the lowest level (7 ml min^{-1}), where the signal was weaker owing to the fast kinetics of the reaction, the flow-rates tested provided a plateau, so an aspiration flow-rate of 9 ml min^{-1} was adopted.

3.4. Optimization of the insertion sequence for the sample and photodegradation medium

The insertion profile was optimized by identifying the $N(t_1, t_2)$ combination for each solenoid valve that ensured optimal software-controlled mixing of the sample and reagents. The procedure was as follows: in the first step, t_1 (the size of the asulam solution segment) was varied (from 0.4 to 0.8 s) at a constant t_2 (0.2 s) value; in the second, t_2 (the size of the glycine buffer segment) was changed (from 0.1 to 0.3 s) at a constant t_1 (0.7 s) value; in the third, t_1 and t_2 were varied simultaneously at a constant t_1/t_2 ratio. In every case, N was kept constant at a large enough value to ensure that the volumes of asulam and photodegradation medium would fill up the photoreaction zone. A (0.3,0.1) aspiration sequence (viz. sample insertion for 0.3 s and photodegradation medium insertion for 0.1 s) was selected in terms of sensitivity and reproducibility.

Because the absence of glycine segments would avoid dilution of the sample, the signal obtained with the previous insertion sequence was compared with that provided by a single segment of asulam of the same size. The difference was only 7%. However, we chose not to discard the buffer until its potential effect on the kinetics of the photoreaction had been examined.

3.5. Optimization of the photodegradation time

The influence of the UV irradiation time was examined over the range 30–240 s. The photodegradation medium might affect the kinetics of the photoreaction, so photodegradation would be maximal after a shorter or longer time depending on the particular medium. We used a 1 mg l^{-1} solution of asulam in glycine buffer in the above-described insertion sequence, as well as a single segment of the same size containing 1 mg l^{-1} asulam in pure water. As can be seen from Fig. 3, the photodegradation of asulam was faster

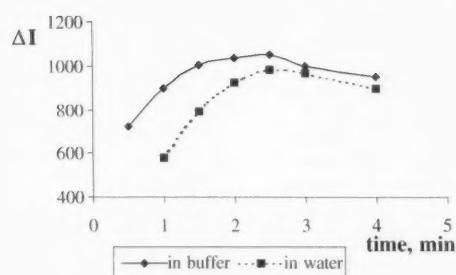


Fig. 3. Effect of the irradiation time on the chemiluminescent signal of 1 mg l^{-1} of asulam when the photoreaction medium is water or glycine buffer at pH 8.3.

in the glycine buffer (a plateau was obtained between 90 and 150 s); achieving the same extent of photodegradation in pure water took 150 s. In order to ensure an adequate insertion rate and, because the use of a buffer would allow pH oscillations caused by the sample matrix and altering the photodegradation kinetics to be absorbed, we chose to continue to use the buffer in conjunction with an irradiation time of 90 s.

3.6. Photodegradation of asulam

Photochemical studies have aroused much interest as a clean, cheap and reproducible analytical tool in different fields. The sunlight-based photocatalytic photodegradation processes have been recently proposed as a straightforward, affordable and cost-effective method for the *in situ* control of environmental pollutants [27,28].

Iron (III) aqua complexes are effective catalysts for the photodegradation and mineralization of dissolved asulam using UV light (365 nm) or sunlight [26]. The mechanism of the catalytic functioning of the Fe ions through the Fenton reaction has been questioned at times for different authors [29]. For many authors probably the process is driven by hydroxyl radicals produced upon excitation of $\text{Fe}(\text{OH})^{2+}$ ions. Once Fe(III) has been completely photo-reduced to Fe(II), asulam continues to be degraded in the presence of oxygen; therefore, the herbicide requires the presence of Fe(III), Fe(II) and molecular oxygen for its complete mineralization. A recent paper [29] discussed different pathways and reporting empirical evidence of Fe intermediate complexes [30] in which the reaction proceed via a ferryl ion (+IV) formed by a two-electron inner-sphere electron transfer.

Titanium dioxide has been used in the catalytic photodegradation for more than 100 organochlorine, organophosphorus, triazine, thiocarbamate and carbamate pesticides (asulam included) [31] for water purification purposes.

Chib and co-workers [32] have study of the photolysis of asulam in soil, and the influence of the moisture in their half-life.

Up to the author's knowledge, there is not previous information about the nature of the photoproducts obtained after

the irradiation with UV light of a aqueous solution of asulam. To assessment the molecular structure changes on the irradiation step, were obtained the UV-Vis and fluorimetric spectra of asulam in the glycine buffer selected as the suitable medium for the photodegradacion, both, with lamp ON and OFF. A simple flow assembly consisting in two merging channels with the aid of a PTFE "T" piece nesting close to the photoreactor was used; an aqueous solution containing 10 mg l^{-1} of asulam flowed through one channel and the selected solution for the photodegradacion medium (glycine buffer at pH 8.3) flowed through the second. The flow-rate pesticide/glycine ratio was 3:1 to reproduce the same conditions as the obtained in the multicommution assembly by switching SV_1 (0.3,0.1). And the global flow-rate trough the photoreactor was the necessary to obtain the same irradiation time (90 s). Spectra of emerging mixture were recorded for with lamp ON and lamp OFF, respectively.

Fig. 4 shows the UV-Vis spectral differences when the mixture is irradiated. As can be seen, the asulam maximum at 256 nm disappears with the irradiation, whereas a shoulder about 305 nm appears. The fluorimetric measurements also resulted in changes by irradiation. A fluorimetric emission was observed for the asulam in glycine buffer medium, with a intensity of 4283, at $\lambda_{\text{exc}} = 258 \text{ nm}$ and $\lambda_{\text{em}} = 361 \text{ nm}$ ($\text{Slit}_{\text{ex}} = 5 \text{ nm}$ and $\text{Slit}_{\text{em}} = 2.5 \text{ nm}$). However, a decrease of the fluorescence intensity was observed after the irradiation, with emission at 412 nm and excitation at 258 and 324 nm, providing intensities of 1971 and 2893, respectively (both at $\text{Slit}_{\text{ex}} = 5 \text{ nm}$ and $\text{Slit}_{\text{em}} = 5 \text{ nm}$).

3.7. Optimization of the chemiluminescent system based on $\text{Fe}(\text{CN})_6^{3-}$ as oxidant

The influence of parameters involving the oxidation reaction between photoproducts and ferricyanide in basic medium were studied. The NaOH concentration resulted in a plateau between 0.75 and 1 mol l^{-1} being the chosen concentration 0.8 mol l^{-1} . The effect of surfactants and β -cyclodextrin was definitively discarded. The assays on the insertion sequence for the photodegraded sample and oxidant was also optimized; a (0.5,0.3) sequence (*viz.* one

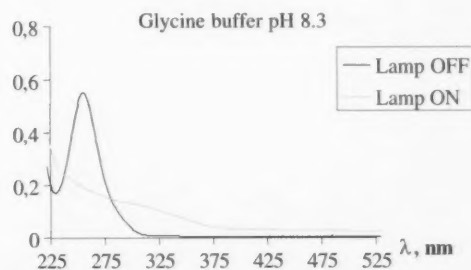


Fig. 4. UV-Vis spectra of asulam in glycine buffer at pH 8.3, without and with previous irradiation with the UV light provided for a low-pressure mercury lamp during 90 s.

involving aspiration of the photodegraded pesticide for 0.5 s and the oxidant for 0.3 s) was finally selected. The study of the influence of temperature for photodegradation and chemiluminescence by separated assays revealed in room temperature (20 °C) as the most suitable. Finally, the influence of the concentrations of the oxidant and oxidizing medium was re-examined and a chemiluminescence emission maximum was obtained with $0.10 \text{ mol l}^{-1} \text{ Fe(CN)}_6^{3-}$ in $1.0 \text{ mol l}^{-1} \text{ NaOH}$.

3.8. Optimization of the chemiluminescent system using permanganate as oxidant

Because the optimum system for the previous oxidant provided inadequate sensitivity and, as noted earlier, the differences initially observed from the permanganate/acid medium system were fairly small, we chose to also optimize this oxidant system for the determination of photodegraded asulam. To this end, we started from the optimum conditions for the previous system. Because the optimum medium, time and insertion sequence for the photodegradation reaction were independent of the particular chemiluminescent reaction, they were not re-optimized here. Only the influence of the presence of surfactants or sensitizers was re-examined as it would affect both the photoreaction and the chemiluminescence emission. The specific substances studied were 0.60 and 0.06% sodium dodecylsulfate, 0.06 and 0.02% Triton X-100, 0.20 and 0.02% hexadecyl pyridinium, 0.60 and 0.06% benzalkonium chloride and 3×10^{-4} and $3 \times 10^{-5} \text{ mol l}^{-1}$ quinine. All were used either in the glycine buffer or in the oxidant solution, so their influence reached the photodegradation and chemiluminescent reaction in the former case and only the chemiluminescent process in the latter. The use of the surfactants in the glycine buffer resulted in large blank signals, whichever the concentration, so it was discarded.

The influence of the permanganate and sulphuric acid concentrations was examined over the ranges 0.73×10^{-4} – $2.57 \times 10^{-4} \text{ mol l}^{-1}$ and 0.5 – 2.0 mol l^{-1} , respectively. Based on the results, a permanganate concentration of $10^{-4} \text{ mol l}^{-1}$ and an H_2SO_4 concentration of 1.5 mol l^{-1} were adopted.

At that point, the insertion sequence for the photodegraded sample and oxidant via SV_3 was optimized. The optimum sequence was found to be (0.7,0.2), i.e. one involving aspiration of the sample for 0.7 s and the medium for 0.2 s.

The effect of temperature on the chemiluminescent reaction was then re-examined by immersing the oxidant and the water carrier in a thermostated water bath. The temperatures studied were 20 °C (room level), 40, 60 and 80 °C. Unlike the previous tests, the signal increased virtually linearly with increasing temperature. A temperature of 80 °C was chosen as higher levels might result in bubble formation. The signal was found not to differ whether the carrier and oxidant or only the carrier were immersed in the water bath. We therefore chose to thermostat the carrier only in order to avoid potential degradation of the oxidant solution at the high temperature used.

The influence of the flow-rate was studied over the range 8–11 ml min^{-1} . Although the signal increased throughout it, the reproducibility degraded above 10 ml min^{-1} , which was adopted for subsequent work.

Finally, the permanganate and sulphuric acid concentrations were re-optimized at 10^{-4} and 1.2 mol l^{-1} , respectively.

4. Analytical figures of merit

The two oxidant systems studied were compared in terms of sensitivity, repeatability, reproducibility and selectivity. Table 1 lists the signal-concentration ratios obtained, the RSD for repeated insertions of the same solution, the limit of detection for each system (calculated as the lowest concentration of asulam yielding a signal equal to the blank signal plus three times its standard deviation), the insertion rate (throughput) and the volume of sample and reagent required to obtain a peak. Because the signal was not linearly related to the asulam concentration with the $\text{Fe(CN)}_6^{3-}/\text{NaOH}$ system, the experimental data were fitted to a second-order polynomial equation over the studied range (up to 5 mg l^{-1}). With the $\text{MnO}_4^-/\text{H}_2\text{SO}_4$ system, the response was linear up to an asulam concentration of 5 ppm; the relative standard deviation for the slope of five curves recorded for freshly

Table 1
Analytical performance characteristics for the proposed methods using $\text{sMnO}_4^-/\text{H}_2\text{SO}_4$ or $\text{Fe(CN)}_6^{3-}/\text{NaOH}$ as oxidative system

	Acid—permanganate	Alkaline—ferricyanide
Limit of detection ($\mu\text{g l}^{-1}$)	40	500
RSD (%)	4.1 (0.5 mg l^{-1}); 5.8 (2 mg l^{-1})	11.2 (2 mg l^{-1}); 8.9 (4 mg l^{-1})
Throughput (h^{-1})	30	30
Relation between emission intensity (corrected by the blank) (I_c) and concentration (C) in mg l^{-1}	Linear ^a : $I_c = (7800 \pm 300)C - (600 \pm 160)$, $r^2: 0.9990$	Second degree ^a : $I_c = (520 \pm 30)C^2 + (350 \pm 170)C - (360 \pm 180)$, $r^2: 0.998$
Sample volume ($\mu\text{l/peak}$)	610	530
Reactive volume ($\mu\text{l/peak}$)	767	1125

^a Average of five independent assays. Dynamic interval, up to 5 mg l^{-1} .

Table 2

Study of interfering compounds, for 0.25 or 2 mg l⁻¹ of asulam for MnO₄⁻/H₂SO₄ or Fe(CN)₆³⁻/NaOH system, respectively

Interferent	MnO ₄ ⁻ /H ₂ SO ₄		Fe(CN) ₆ ³⁻ /NaOH	
	Concentration (mg l ⁻¹)	Er (%)	Concentration (mg l ⁻¹)	Er (%)
K ⁺	500 ^a	+0.91	500 ^a	-1.26
Na ⁺	500 ^a	+0.22	500 ^a	+3.32
Ca ²⁺	500 ^a	-2.50	30	+2.99
NH ₄ ⁺	100 ^a	-3.93	100 ^a	+1.63
Mg ²⁺	100 ^a	+2.37	100 ^a	-2.60
Mn ²⁺	100 ^a	-3.35	0.2	-3.50
Cu ²⁺	0.03	+5.00	0.1	-4.02
Zn ²⁺	100 ^a	-4.16	15	+5.00
Cl ⁻	770 ^a	+0.22	770 ^a	+3.32
SO ₄ ²⁻	500 ^a	+2.29	500 ^a	+3.76
CH ₃ COO ⁻	500 ^a	+1.12	350	-0.39
HCO ₃ ⁻	500 ^a	+4.47	350	-3.08
NO ₃ ⁻	10	-5.00	3	-4.50
NO ₂ ⁻	0.1	-4.92	0.7	-3.09
H ₂ PO ₄ ⁻	500 ^a	+4.94	250	-4.69

^a Maximum assayed concentration.

made solutions on different days was 3.8%. As can be seen in the table, the RSD for series of 11 insertions of two concentrations within the operating range was lower for the MnO₄⁻/H₂SO₄ system, and so was the detection limit. This is a "clean" chemical procedure as the reagent uptake is very low in both cases (only 716 µl for permanganate and 1125 µl for ferricyanide).

Table 2 compares the selectivity of the two oxidant systems. Tests were performed with an asulam concentration of 0.25 mg l⁻¹ for the MnO₄⁻/H₂SO₄ system and 2 mg l⁻¹ for the Fe(CN)₆³⁻/NaOH system. The relative errors in the table represent the differences between the signals provided by insertions of this solution (or one of asulam also containing the specified amount of the species concerned). When the error exceeded 5%, a lower concentration of the potential interferent was studied. As can be seen, the MnO₄⁻/H₂SO₄ system proved more selective. Specially strong was the interference of calcium with the Fe(CN)₆³⁻/NaOH system. The most severe interference with the MnO₄⁻/H₂SO₄ system resulted from the photodegradation of nitrate to nitrite (which reacted with the permanganate) and from copper (which gave a strong chemiluminescent signal, even at low concentrations). This may require the prior removal of copper from some types of sample with an appropriate ion-exchange resin. There were, however, no substantial errors. Asulam is formulated as sodium salt and it is the single active chemical present in commercially available formulations; on the other hand, there are two published chemiluminescent procedures [33,34] dealing with carbamates and chemiluminescent detection and based on Ru compounds. On the other hand, a paper is devoted to the carbamate aldicarb which responds to an analytical procedure similar to the presented [35] but in a very different photodegradation medium.

Table 3

Determination of asulam in water samples

	Error (%)
Irrigation water 1	-2
Irrigation water 2	30.0
Tap water 1	14.6
Tap water 2	3.3
Spring water	-9.7

The depicted result is the average of four assays spiking the water with different concentrations of asulam between 70 and 100 µg l⁻¹. The RSD is also presented.

In the absence of irradiation, asulam provided no signal—at least up to a concentration of 25 mg l⁻¹—with ferricyanide as the oxidant. On the other hand, underivatized asulam exhibited chemiluminescence with acid permanganate as the oxidant. The signal was linearly related to the asulam concentration from 3 (the LOD) to 20 mg l⁻¹ asulam; the equation relating the two was $I = 110.42 (\text{mg l}^{-1}) - 214.84$ ($r^2 = 0.9926$). A comparison with the data in Table 1 reveals that the slope of the curve was 71 times smaller and the LOD 75 times greater; it is therefore advisable to previously derivatize asulam by UV irradiation.

The applicability of the proposed method to water samples was checked by using the optimized system based on acid permanganate to analyze tap, irrigation and spring water. Samples were spiked with four asulam concentrations, 70, 80, 90 and 100 µg l⁻¹. Table 3 shows their origin and the mean relative errors obtained at each asulam concentration, and the RSD of the series of replicates.

No sample pre-treatment—an usual requirement with asulam analyses—was needed. As can be seen from the results, the proposed method allows the determination of the herbicide asulam in water samples in a straightforward, expeditious manner (the insertion rate is 30 samples h⁻¹).

5. Conclusions

For the first time is proposed a chemiluminescent-based determination of asulam and also for the first time a multi-commutation system is used.

The proposed method is an effective choice for the determination of asulam at concentrations over the range 70–100 µg l⁻¹ in water samples without the need for labour-intensive extraction–preconcentration sample treatments. Derivatizing asulam in the sample by irradiation with a low-pressure Hg lamp enables the direct chemiluminescence-based determination of the herbicide over a wide concentration range (40–5000 µg l⁻¹) by oxidation of the products of its photodegradation in glycine buffer at pH 8.3.

Two oxidant systems (viz. acid permanganate and alkaline ferricyanide) were compared in terms of sensitivity and selectivity, and the former was found to provide better results than the latter. The use of solenoid valves in the manifold

allows the process to be fully automated and waste generation to be minimized, thereby providing a clean, simple, expeditious analytical system.

A comparison of the proposed method with previously reported non-chromatographic methods for the determination of asulam exposed its clear advantages. A batch method based on light emission (specifically, synchronous fluorescence) [4] following derivatization of the primary amino group with fluorecamine previously developed for the determination of asulam provides a similar LOD ($40 \mu\text{g l}^{-1}$); however, its application range is much narrower as it only reaches 0.214 mg l^{-1} (versus 5 mg l^{-1} in the proposed method).

To the authors' knowledge, the sole non-chromatographic continuous-flow method for the determination of asulam reported to date uses amperometric detection [5] and was applied to the determination of the herbicide in river and lake water. Its quantitation range, however, is $2.3\text{--}20.7 \text{ mg l}^{-1}$, which clearly excludes the typical concentrations of the herbicide in these types of sample. Its RSD is similar to that of the proposed method. Finally, it has a higher insertion rate but can be more difficult to automate than our method.

References

- [1] Boletín Oficial del Estado (BOE), Madrid, April, first, 2002.
- [2] EEC Drinking Water Guidelines, 80/779/EEC, EEC No. L229/11-29, EEC, Brussels, 1980.
- [3] C.H. Brockelsby, D.F. Muggleton, in: J. Sherma, G. Zweig (Eds.), *Analytical Methods for Pesticides and Plant Growth Regulators*, vol. VII, Academic Press, New York, 1973, Chapter 29, p. 497.
- [4] F. García Sánchez, A. Aguilar Gallardo, C. Cruces Blanco, *Talanta* 39 (1992) 1195.
- [5] H.P.A. Nouws, C. Delerue-Matos, J.L.F.C. Lima, E.M. Garrido, P. Vincke, N.A. Maes, *Int. J. Environ. Anal. Chem.* 82 (2002) 69.
- [6] M. Moder, P. Popp, R. Eisert, J. Pawliszyn, *Fresenius' J. Anal. Chem.* 363 (1999) 680.
- [7] J.Y. Hu, T. Aizawam, Y. Magara, *Wat. Res.* 33 (1999) 417.
- [8] H. Tsuji, N. Henmi, Y. Kaneda, *Jpn. J. Toxicol. Environ. Health* 41 (1995) 292.
- [9] H. Ohno, T. Aoyama, *Jpn. J. Toxicol. Environ. Health* 38 (1992) 202.
- [10] M. Chicharro, A. Zapardiel, E. Bermejo, A. Sanchez, *Anal. Chim. Acta* 469 (2002) 243.
- [11] A.E. Smith, L.J. Milward, *J. Chromatogr.* 265 (1983) 378.
- [12] T.L. Li, W.C. Lee, P.C. Chang, S.S. Chou, *Yaowu Shipin Fenxi* 9 (2001) 40.
- [13] M.C. Gennaro, C. Abrigo, D. Giacosa, L. Rigotti, A. Liberatori, *J. Chromatogr. A* 718 (1995) 81.
- [14] Y.P. Pan, T.G. Hiroo, C.L. Chen, *Sepu* 11 (1993) 302.
- [15] R.T. Kon, L. Geissel, R.A. Leavitt, *Food Addit. Contam.* 1 (1984) 67.
- [16] F. García-Sánchez, A. Navas-Díaz, A. García-Pareja, V. Bracho, *J. Liq. Chromatogr. Relat. Technol.* 20 (1997) 603.
- [17] J. Lochtmann, T. Gernikeites, R. Hueskes, *Gewaesserschutz Wasser Abwasser* 125 (1991) 576.
- [18] S. Strasik, M. Dankova, M. Molnarova, E. Olvecka, D. Kaniansky, *J. Chromatogr. A* 990 (2003) 23.
- [19] M. Hutta, D. Kaniansky, E. Kovalcikova, J. Marak, M. Chalanyova, V. Madajova, E. Simunicova, *J. Chromatogr. A* 689 (1995) 123.
- [20] D. Kaniansky, V. Madajova, M. Hutta, I. Zilkova, *J. Chromatogr.* 286 (1984) 395.
- [21] M. Catalá-Icardo, J.V. García-Mateo, J. Martínez-Calatayud, *Trends Anal. Chem.* 21 (2002) 366.
- [22] <http://www.uv.es/~martinej/Flow-Analysis/>
- [23] R.P.R. Rocha, B.F. Reis, E.A.G. Zagatto, J.L.F.C. Lima, R.A.S. Lapa, J.L.M. Santos, *Anal. Chim. Acta* 468 (2002) 119.
- [24] R. Bauer, H. Fallmann, *Res. Chem. Intermed.* 23 (1997) 341.
- [25] P.L. Huston, J.J. Pignatello, *Wat. Res.* 33 (5) (1999) 1238.
- [26] C. Catastini, M. Sarakha, G. Mailhot, M. Bolte, *Sci. Total Environ.* 298 (2002) 219.
- [27] Y. Hirahara, Y. Sayoto, K. Nakamuro, *Jpn. J. Toxicol. Environ. Health* 44 (1998) 451.
- [28] J.A. Arjona, A. Vidal, *Solar Energy* 68 (2000) 109.
- [29] H. Feng, L.L. Cheng, J. Zhejiang Univ. *SCI* 5 (2) (2004) 198.
- [30] S.H. Bossman, E. Oliveros, S. Göb, M. Kantor, A. Goepfert, A.M. Braun, L. Lei, P.L. Yue, *Prog. React. Kinet. Mex* 26 (2) (2001) 113.
- [31] K. Tanaka, K. Abe, C.Y. Sheng, T. Hisanaga, *Environ. Sci. Technol.* 26 (1992) 2534.
- [32] P. Graebing, M.P. Frank, J.S. Chib, *J. Agric. Food Chem.* 51 (15) (2003) 4331.
- [33] T. Pérez Ruiz, C. Martínez Lozano, V. Tomás, J. Martin, *Analyst* 127 (11) (2002) 1526.
- [34] T. Pérez Ruiz, C. Martínez Lozano, V. Tomás, J. Martin, *Anal. Chim. Acta* 476 (1) (2003) 141.
- [35] M. Palomeque, J.A. García Bautista, M. Catalá Icardo, J.V. García Mateo, J. Martínez Calatayud, *Anal. Chim. Acta* 512 (2004) 149.

Improved micro-flame detection method for gas chromatography

Kevin B. Thurbide*, Taylor C. Hayward

Department of Chemistry, University of Calgary, 2500 University Drive, N.W., Calgary, Alta., Canada T2N 1N4

Received 14 October 2003; received in revised form 10 May 2004; accepted 17 May 2004

Abstract

A previously developed micro-counter-current flame method is modified to provide both sensitive photometric and ionization detection for gas chromatography (GC). A stainless steel capillary (0.254 mm i.d.) supplying oxygen functions as a burner, which supports a compact flame that burns in a counter-flowing excess of hydrogen. In the “micro-flame photometric detector” (μ FPD) response mode, the background emission level is reduced by over an order of magnitude compared to previous experiments using a fused silica capillary burner, resulting in greatly improved detection limits. Chemiluminescent sulfur response in the μ FPD is quadratic over 3.5 orders of magnitude, yielding a detection limit of 3×10^{-11} gS/s, while that of phosphorus is linear over 5 orders of magnitude down to a minimum detectable limit of 3×10^{-12} gP/s. Tin response is examined for the first time in the μ FPD and yields a blue luminescence (ascribed to SnO^*) on the surface of the quartz flame enclosure. Although this emission provides a sensitive detection limit near 6×10^{-15} gSn/s, due to the limited surface area within the detector cell it only produces a linear response range of one order of magnitude. Ionization response toward hydrocarbons is also obtained from the hydrogen-rich micro-counter-current flame. A linear response is produced over five orders of magnitude, yielding a detection limit toward carbon of 2×10^{-10} gC/s. Analysis of a simple gasoline sample is used to demonstrate that the device can successfully operate as both a selective and universal GC detector. Results indicate that this micro-counter-current flame method yields comparable performance to conventional flame photometric and flame ionization detectors, making it potentially useful for adaptation to micro-analytical devices and portable GC units.

© 2004 Elsevier B.V. All rights reserved.

Keywords: Micro-flame detection; Chemiluminescence; Ionization; Counter-current flame

1. Introduction

An area of increasing development in the field of gas chromatography (GC) is instrument miniaturization [1–3]. Notable examples of such advances include portable field GC units [4,5] and GC separations achieved on a micro-analytical chip [6–8]. In conjunction with these efforts, there is also a growing interest in developing sensitive miniaturized detection methods that can be incorporated into micro-analytical devices. A number of such miniaturized or ‘micro’-detection methods have been reported based on a variety of principals including surface acoustic wave transmission [7], thermal conductivity [9], and plasma-based optical emission [10–14]. Although flame-based detectors are prevalent in many conventional GC applications [1,2], relatively few have been adapted to micro-analytical for-

mats. Since the latter tend to utilize very small (nL range) channels [10], this may be partly attributed to difficulties encountered in operating a stable flame within these dimensions. In this regard, however, a very interesting and useful system has been successfully demonstrated. The method employs low gas flows to support a high energy premixed flame (about 3 mm tall \times 1 mm wide) that can perform atomic emission/hydrocarbon ionization detection on the surface of a micro-analytical chip [15–18].

The flame photometric detector (FPD) is a widely used GC sensor for determining sulfur, phosphorus, tin, and other elements in volatile organic compounds based on their chemiluminescence within a low-temperature, hydrogen-rich flame [19–25]. Very recently, we introduced a novel method of generating a similar flame environment using counter-flowing streams of gas [26]. This ‘counter-current’ FPD was demonstrated to provide similar sensitivity and response characteristics to that of a conventional FPD when operated in the hydrogen-rich mode. As well, it was also found to yield useful flame ionization

* Corresponding author. Tel.: +1 403 220 5370; fax: +1 403 289 9488.
E-mail address: thurbide@ucalgary.ca (K.B. Thurbide).

detector (FID) signals when operated in the air-rich mode. Most notably, unlike a conventional FPD, this method produced remarkably stable flames at relatively low and high gas flows of varying stoichiometry. In fact, this aspect of the detector was employed in the primary focus of the study, which explored changes in transition metal response as a function of flame size derived from gas flows that differed by several hundred mL/min [26].

Subsequent to this work (but actually reported earlier) we exploited the great stability of counter-current flames in a new way by using them to create an enclosed hydrogen-rich micro-flame [27]. The flame was supported on a fused silica capillary by only a few mL/min of gas flow and encompassed a very small volume of 30 nL. As well, it produced qualitatively similar response characteristics toward sulfur and phosphorus-containing analytes as that of a conventional FPD [27]. The method was employed in a novel micro-flame photometric detector (μ FPD) which was operated either inside the end of a capillary gas chromatography column (on-column) or within a length of capillary quartz tubing after the separation column (post-column), with each mode displaying similar characteristics.

In general, the dimensions and qualities of the micro-counter-current flame indicated that it could be a potentially useful method of producing chemiluminescent molecular emission, similar to a conventional FPD, within small channels and analytical devices of reduced proportions. However, unlike the larger counter-current flame [26], the primary disadvantage to the micro-flame method was the relatively large detection limits that it produced for sulfur and phosphorus due to an elevated background emission [27]. The spectrum, intensity, and orange appearance of the emission indicated that the fused silica capillary burner was glowing from contact with the flame [27]. Despite efforts to prevent this it was observed under all conditions investigated.

Thus, it would be beneficial to examine the extent to which μ FPD response might be enhanced by removing this interference. For instance, it would be interesting to establish if the μ FPD flame could in fact also yield the same performance of a conventional FPD flame, even though the two differ in size by about three orders of magnitude [27]. Additionally, it would be useful to further study other potential response modes of the micro-counter-current flame, such as photometric tin response and flame ionization response, neither of which has yet been investigated for this method.

This paper describes an improved μ FPD response that is obtained by using a stainless steel capillary burner to support the micro-counter-current flame. The response characteristics of the μ FPD toward sulfur, phosphorus, and for the first time tin, will be presented and compared to those of a conventional FPD. Additionally, as a result of polarizing the burner, the ability of the micro-counter-current flame to produce ionization response toward carbon will also be evaluated and compared with conventional FID methods and the larger counter-current flame.

2. Experimental

Fig. 1 presents a schematic illustration of the micro-counter-current flame arrangement. A detailed description of the μ FPD construction has been reported earlier [27]. Briefly, a stainless steel 6.35 mm cross-union (Swagelok) acts as a prototype detector housing to enclose and monitor the micro-flame. The bottom of the cross is connected to a 10 cm length of stainless steel tubing (1.5875 mm o.d.) welded to a tube stub (6.35 mm o.d.) that fits the original FID base of the GC instrument (Shimadzu model GC-8A), and through which hydrogen is introduced. Vespel ferrules are used to connect this tubing to, but prevent its direct contact with, the GC instrument or detector housing in order to maintain proper FID operation. One of the horizontal ports of the cross is used to visually align and monitor the micro-flame. Directly opposite to this, the other horizontal port is adapted with a threaded stainless steel tube that encases a quartz light guide (150 mm \times 6 mm o.d.) which directs the flame emission to a photomultiplier tube (R 268 with wavelength range 300–650 nm; Hamamatsu, Bridgewater, NJ, USA).

Extending vertically throughout the housing is a quartz capillary sleeve (0.9 mm i.d.) which conducts the hydrogen and column effluent, entering through the bottom port, towards the flame front. Through a septum in the top port, a length of stainless steel capillary tubing (0.254 mm i.d. \times

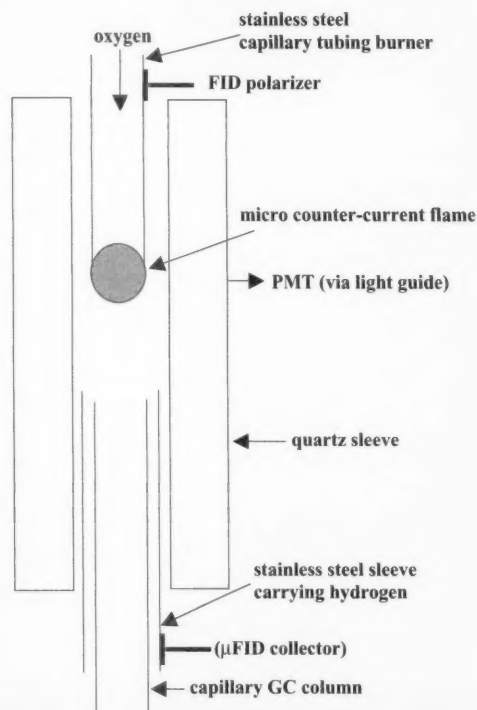


Fig. 1. A schematic diagram of the micro-counter-current flame arrangement used to collect the μ FPD and μ FID signals.

0.4572 mm o.d.) carrying oxygen extends downward into the quartz sleeve to the center of the union, directly in front of both the light guide port and the viewing port. Under typical operating conditions, the micro-flame is situated on the end of this oxygen capillary burning 'upside down' within a counter-flowing stream of hydrogen and column effluent from the bottom.

The separation column employed is an EC-5 [(5% phenyl)–95% methylpolysiloxane] megabore column (30 m \times 0.53 mm i.d.; 1.00 μ m thickness; Alltech, Deerfield, IL, USA) that extends vertically upward from the instrument and into the detector housing through the connecting stainless steel tube carrying the hydrogen. Typical separations employ 5 mL/min of helium as the carrier gas. Normally, about 2–3 mm separates the end of the column from the oxygen burner. For μ FID experiments, the original Shimadzu electrical leads are used such that the polarizer is connected to the stainless steel oxygen burner and the collector is connected to the stainless steel hydrogen tube surrounding the separation column.

High-purity helium, hydrogen, and oxygen are obtained from Praxair. Tetrahydrothiophene (99%), trimethyl phosphite (99%), benzene (99%), decane (99%), and tetramethyltin (95%) are obtained from Aldrich. Variations on burner dimensions, gas flows, and all other details are described in the text.

3. Results and discussion

3.1. Burner characteristics

Stainless steel capillary tubing of both 0.254 mm i.d. and 0.127 mm i.d. was investigated for its properties as a μ FPD burner. Respectively, these dimensions are the same as and smaller than the fused silica tubing i.d. used previously [27]. It was found that both tubing sizes were able to support a stable flame. However, the 0.127 mm i.d. (0.2286 mm o.d.) tubing was observed to glow considerably, yielding a similar background emission to that noted earlier for the fused silica burner [27]. In terms of relative wall thickness, this capillary burner (0.0508 mm) was slightly smaller compared to the fused silica tubing (0.0762 mm) used originally.

In contrast to this, when trials were run using the 0.254 mm i.d. (0.4572 mm o.d.) tubing as a burner, the orange glow was observed to disappear and the background emission was much less intense compared to that obtained with fused silica. This tubing has a wall thickness of 0.1016 mm. It therefore seems advantageous to have a wall thickness greater than 0.0508 mm under typical conditions in order to avoid any glowing of the stainless steel burner. In routine comparisons with fused silica burners, it was found that the thicker walled stainless steel capillary tubing readily reduced the background emission observed by over an order of magnitude. Also in general, the size, stability, chemiluminescent properties, and gas flow operating re-

gions of the flame itself did not differ between stainless steel and fused silica burners of 0.254 mm i.d. under the same conditions. Therefore, this stainless steel capillary tubing provides a more effective burner for the μ FPD and was used throughout the remaining experiments.

3.2. Photometric response of sulfur and phosphorus

Similar to earlier efforts using a fused silica burner, the best μ FPD signal-to-noise ratios in this study are also generally found at lower flows of oxygen and hydrogen, the former having a much more significant impact on the background emission [27]. Using stainless steel the optimum μ FPD response for sulfur was obtained with 7 mL/min of oxygen and 45 mL/min of hydrogen, while that for phosphorus was obtained when using 9 mL/min of oxygen and 58 mL/min of hydrogen. While these oxygen flows agree within 3–5 mL/min of those used in the 'post-column' detection mode of the previous μ FPD experiments, the hydrogen flows used are 30–40 mL/min smaller [27]. However, as demonstrated in that study, the latter is directly proportional to the inner diameter of the quartz capillary sleeve used. Since the sleeve used currently is narrower by comparison, smaller optimum hydrogen flows are to be expected.

As a result of the diminished background emission obtained using stainless steel, the signal-to-noise ratios realized for sulfur and phosphorus are about 100 times larger than those reported earlier for the μ FPD [27]. Fig. 2 demonstrates this with the μ FPD response towards increasing amounts of sulfur and phosphorus test analytes under

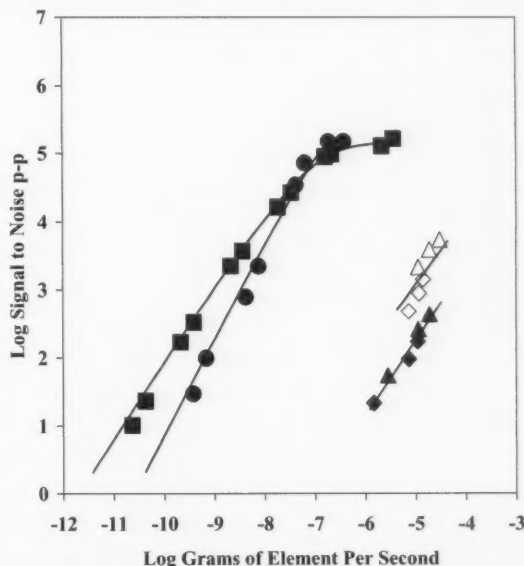


Fig. 2. μ FPD calibration curves for sulfur as tetrahydrothiophene (●) and phosphorus as trimethyl phosphite (■) under their respective optimal conditions. The response to carbon as decane (◆) and benzene (▲) is also shown under optimum sulfur (hollow symbols) and phosphorus (filled symbols) conditions. Gas flows are listed in the text.

their respective optimum conditions. As can be seen the quadratic response toward sulfur (as tetrahydrothiophene) spans over 3.5 orders of magnitude down to a minimum detectable limit of 3×10^{-11} gS/s. This value is determined at the conventional signal-to-noise ratio of 2, where noise is measured as the peak to peak fluctuations of the baseline over at least 10 analyte peak base widths. For phosphorus (as trimethyl phosphite) the μ FPD response is linear over five orders of magnitude down to a minimum detectable elemental flow of 3×10^{-12} gP/s. Overall, these values are greatly improved compared to the initial μ FPD study using a fused silica capillary burner [27]. In fact, similar to the larger counter-current flame [26], they now agree very well (within a factor of 2) to those produced by the much larger flame of a conventional FPD [28].

Fig. 2 also includes the response toward different flows of carbon (as both decane and benzene) obtained under optimal sulfur and phosphorus conditions in the μ FPD. As can be seen, the sensitivity between benzene and decane differs very little in each mode. While this is reasonable, it is necessary to examine since it has been demonstrated previously that aromatic compounds can respond considerably stronger than aliphatic compounds under certain FPD conditions [25]. As a result of the different optimal gas flows used, the carbon response displayed in Fig. 2 increases by a factor of 6 from the phosphorus to the sulfur mode. Therefore, phosphorus in the μ FPD yields a molar selectivity over carbon (i.e. mol P/mol C that yield the same response within the linear range) of five orders of magnitude. Conversely, owing to its quadratic response, sulfur produces a molar selectivity over carbon of 3.5 orders of magnitude near the upper response limit, which narrows as analyte amounts decrease. These values, obtained in the 'open' mode without any wavelength discrimination, are also improved relative to the earlier μ FPD study [27]. Further, they resemble those reported for a conventional FPD [28] and the larger counter-current flame [26].

Narrow band interference filters are often used to selectively monitor sulfur or phosphorus response in the conventional FPD [28], although this practice is known to decrease sensitivity [29]. Since these methods were equally effective in the μ FPD with a fused silica capillary burner [27], no differences in behavior were anticipated or observed from using stainless steel instead. For example, when the S_2^* emission of sulfur is isolated and monitored near 400 nm, the μ FPD sensitivity for this element typically decreases by a factor of 2–10 times depending on the filter used. Comparable results are also obtained when observing the HPO^* emission of phosphorus near 526 nm. Selective monitoring of sulfur and phosphorus using suitable interference filters with the μ FPD is demonstrated later in this study.

3.3. Photometric response of tin

Tin is another element commonly monitored by a conventional FPD, normally producing a red and/or blue chemi-

luminescence in the detector [24,28,30]. Thus far, tin response has not been examined in the μ FPD or in the larger counter-current flame. However, during the course of this study, quartz sleeves contaminated with traces of tin were visually observed to yield an intense blue emission on the surface of the enclosure surrounding the flame. This same luminescence is also observed in the form of tailing peaks when picogram quantities of tetramethyl tin are introduced into the detector equipped with a regular clean quartz capillary sleeve. This is consistent with the emission of SnO^* on a quartz surface, which is well known to yield a very sensitive response toward tin compounds in a conventional FPD [30]. Incidentally, the much less sensitive red emission in the gas phase (ascribed to SnH^*) was not observed here. Therefore, considering its intensity, the blue tin emission was further examined in the μ FPD.

Optimum signal-to-noise ratios for tin were obtained using 10 mL/min of oxygen and 25 mL/min of hydrogen. These μ FPD conditions provide sensitive response yielding a detection limit near 6×10^{-15} gSn/s. However, increasing amounts of tin were only found to linearly increase the response over an order of magnitude. For instance, with tetramethyl tin this is observed between approximately 0.1 and 1 pg of the injected compound. This narrow linear range also reproduces with other calibration standards such as tetrabutyl tin, and under a variety of gas flows investigated. Fig. 3 illustrates this for 0.1, 1, 10, 100, and 1000 pg injection of tetramethyl tin under the same optimal μ FPD condi-

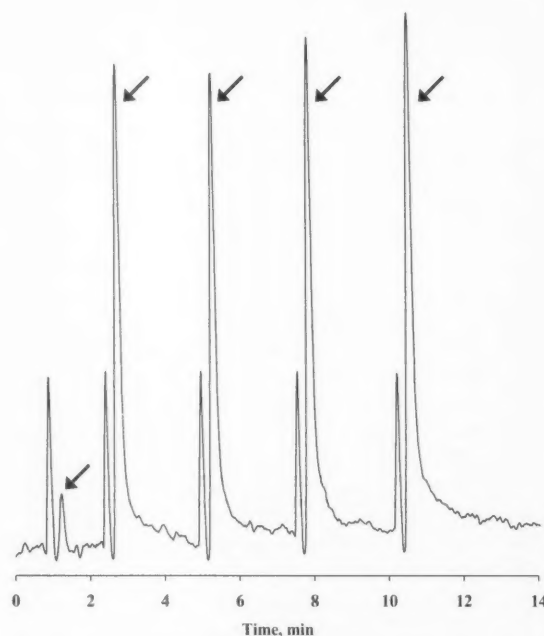


Fig. 3. Chromatogram illustrating the μ FPD response toward tin as tetramethyl tin. From left to right the amounts injected are 0.1, 1, 10, 100, and 1000 pg, respectively, which correspond to the peaks indicated by the arrows.

tion. As can be seen for the larger amounts, even though the mass of analyte increases 1000 times, very similar signals are produced. Additionally, while peak heights do not appreciably increase for this mass range, it is observed occasionally that the peak widths sometimes do. These factors are indicative of detector saturation near the upper limit of response, which has been noted for nanogram quantities of tin compounds in conventional FPD studies [30]. Since tin emission in the μ FPD stems from the quartz surface of the enclosure, attempts were made to increase the available surface area by using a larger diameter tube and packing quartz wool into the detector cell. While these alterations have shown positive effects on tin response in a conventional FPD, they were not effective in the μ FPD. It should be noted, however, that less peak tailing was observed when using the larger tubing. Thus, the μ FPD appears capable of yielding quartz surface emission that is sensitive toward picogram quantities of tin compounds. However, it is unclear why the detector currently displays saturation at such low analyte levels. Regardless, until further improvements can be realized, the narrow linear range of tin response offered by the μ FPD makes it impractical as a tool for routine organo-tin analysis.

3.4. Ionization response

By using a stainless steel capillary burner in the μ FPD, it has been demonstrated that the micro-counter-current flame yields chemiluminescent response that is very similar to that found in much larger conventional or counter-current FPD flames [26,28]. Earlier, it was also briefly noted that the larger counter-current flame was observed to provide highly sensitive FID response toward an aliphatic and an aromatic test analyte [26]. However, more comprehensive aspects such as the relative sensitivity toward these analytes or the linearity of these responses were not investigated in the primarily photometric study. Since the micro-counter-current flame provides photometric response that is similar to its larger analogue, it was somewhat anticipated that it too might also deliver useful ionization response toward carbon. However, the fuel-rich hydrogen radical flame chemistry that supports photometric signals is unique from the air-rich oxygen radical flame chemistry that promotes hydrocarbon ionization [28,31]. Since the effect of reducing counter-current flame size on these processes remains unclear, it is therefore necessary to establish and investigate the extent of FID response that can be derived from the μ FPD flame. This information is also potentially beneficial since such a feature could be useful in applications where both universal and selective detection of samples is desired.

Fortunately, this is facilitated by using a stainless steel capillary burner in the μ FPD, which makes it very convenient to apply a potential across the flame. Using the existing FID electrical leads of the GC, this mode of response was examined by applying the polarizer to the capillary burner and the collector to the stainless steel sleeve surrounding the end of the separation column. This arrangement most closely re-

sembles the polarized flame burner situated below the collector of a conventional FID [31]. While other variations such as reversing the polarizer and collector connections were explored, these were not found to yield as favorable a response.

Several gas flows were examined for their impact on the ionization response of the flame. Initially, when the capillary burner was new, about 12 mL/min of oxygen was found to provide the best sensitivity. However, after a few hours of conditioning, this value decreased and stabilized at lower flows. Ultimately, the optimum gas flows for the " μ FID" response mode of this flame toward carbon were obtained using 7 mL/min of oxygen and 40 mL/min of hydrogen. It is interesting to note that this flame stoichiometry is considerably rich in hydrogen compared to that of a conventional FID, which commonly yields optimal response when operated under leaner oxygen-rich conditions [31]. However, the flames used in the two devices are significantly different, particularly with respect to their structure.

For instance, the FID flame normally operates in a diffusion mode where hydrogen and column effluent are introduced through a central burner supporting the flame, which is concentrically surrounded by an excess of oxygen [31]. In contrast to this, the μ FID flame operates in the unique counter-current mode, where it is supported on a capillary delivering oxygen, and burns in a counter-flowing excess of hydrogen mixed with column effluent. In this fashion the analyte, immersed in hydrogen, is directed toward the counter-current flame's oxygen-rich inner cone through its hydrogen-rich outer mantle. This is opposed to the conventional FID where analytes, also immersed in hydrogen, enter the oxygen-rich outer mantle of the flame through its hydrogen-rich inner cone region.

Considering these structural differences then, they could possibly play an important role in the strong ionization response observed in the fuel-rich μ FID flame. For example, if more effective mixing were to occur in the micro-counter-current flame, despite its richer stoichiometry, it might still efficiently produce oxygenated carbon species such as CHO similar to the air-rich diffusion flame of a conventional FID [31]. Note that this species is believed responsible for the sensitive signal of the FID, even though it is only produced by about 1 in 10^6 carbon atoms [32]. Unfortunately, the actual extent of mixing in these two detectors, or their relative yields of flame species such as CHO is not presently established. However, it is interesting to point out that the above scenario is consistent with earlier reports of strong FID sensitivity being obtained from a premixed, fuel-rich, hydrogen/oxygen flame [33], and an even more turbulent oscillating FID flame [34].

Fig. 4 demonstrates the μ FID sensitivity towards carbon as both decane and benzene under optimum conditions. As can be seen, the response of the two compounds agrees within a factor of 2, and increases linearly over five orders of magnitude yielding a detection limit of 2×10^{-10} gC/s. In terms of absolute sensitivity, under typical operating con-

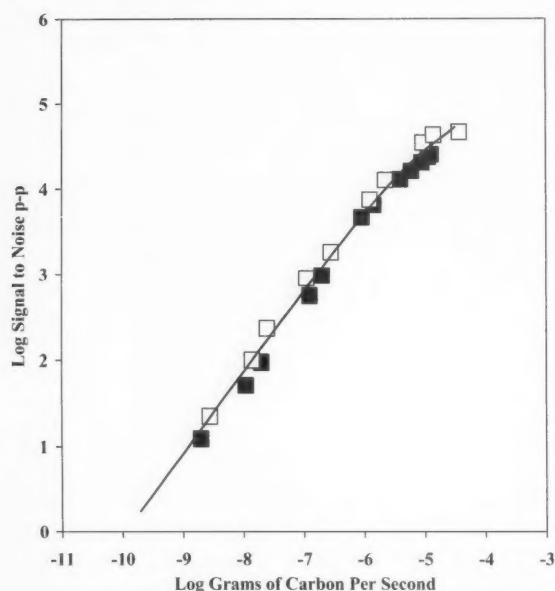


Fig. 4. μ FID response of the micro-counter-current flame toward carbon as decane (■) and benzene (□). The gas flows used are 7 mL/min oxygen and 40 mL/min hydrogen.

ditions the μ FID produces a response of about 5 mC/gC. The same values were also obtained from carbon measurements performed with the original GC-FID instrument adapted for use in these experiments. Further, they agree within a factor of 10 to those reported in the literature for a fully optimized commercial FID [31]. It should be noted that the larger counter-current flame was earlier observed to provide a greater FID sensitivity than that found in this study [26]. However, the optimal flame conditions established were air-rich, similar to a conventional FID [31]. This is opposed to the optimal hydrogen-rich flame conditions realized currently. Although leaner, oxygen-rich operating ranges were explored in the μ FID, it was found that the resulting flames were less stable and more difficult to manage under the conditions examined. Nonetheless, the performance of the prototype μ FID still compares well to a conventional FID, especially considering that it is obtained from a relatively simple apparatus. As such, better response may still be possible upon continued optimization of the flame, burner, and detector housing design.

Previously the larger counter-current flame was found to provide optimal ionization and optimal photometric response using respective air flows that were similar and hydrogen flows that differed by about 2–5 times [26]. In this way the detector appeared flexible for dual channel operation. However, since FID response was not primarily examined in that study, the effect on sensitivity of changing the gas flow settings was not investigated. What is interesting about the optimum hydrogen-rich gas flows for ionization

response in the current study, is that they are now much closer to those employed for optimal photometric response than was the case for the larger counter-current flame. Thus, it should be possible to utilize a common set of conditions that would provide both optimal, or near optimal μ FPD and μ FID response. This would be very useful in allowing the simultaneous screening of samples by both detection modes since conventionally one derives optimal response using an entirely different flame stoichiometry than the other. Therefore, it would be useful to know how the μ FPD sensitivity for sulfur and phosphorus may be influenced by changing the gas flows between the various optimum μ FPD and μ FID settings.

Table 1 illustrates the relative change in the μ FPD sulfur signal when using gas flows optimized for obtaining photometric sulfur, photometric phosphorus, and hydrocarbon ionization response from the flame. Also included is a similar set of data illustrating the relative change in the μ FPD phosphorus signal in each of these three operating modes. As can be seen from the table, the μ FPD sensitivity for sulfur and phosphorus changes relatively little amongst the different settings. The sulfur signal is decreased by only 4% when operated in the photometric phosphorus mode, and by 10% when operated in the hydrocarbon ionization mode. By comparison, the phosphorus signal is decreased by 15% when operated in the photometric sulfur mode. Furthermore, under μ FID optimized conditions where the largest change is observed, the μ FPD phosphorus signal still maintains about 70% of its optimal sensitivity.

3.5. Sample analysis

Given that significant ionization and chemiluminescent signals can both be obtained from the same micro-counter-current flame, it would be useful to investigate how the detector performs when analyzing an organic sample matrix. In order to demonstrate this, a quantity of unleaded gasoline (purchased from a local vendor) was spiked with both tetrahydrothiophene and trimethyl phosphite prior to analysis. Since gasoline typically contains a moderate variety of hydrocarbon compounds, this simple sample provides a good illustration of the detector's ability to screen a multi-component mixture for its carbon, sulfur, and phosphorus content.

Fig. 5 displays the chromatographic profile of the gasoline sample as monitored (from top to bottom) by the μ FID

Table 1
Effect of different operating modes on μ FPD sensitivity

	Operating mode ^a		
	μ FPD (S)	μ FPD (P)	μ FID (C)
Sulfur	1.00	0.96	0.90
Phosphorus	0.85	1.00	0.72

^a Each mode is optimized for the element shown in brackets. Conditions are listed in the text.

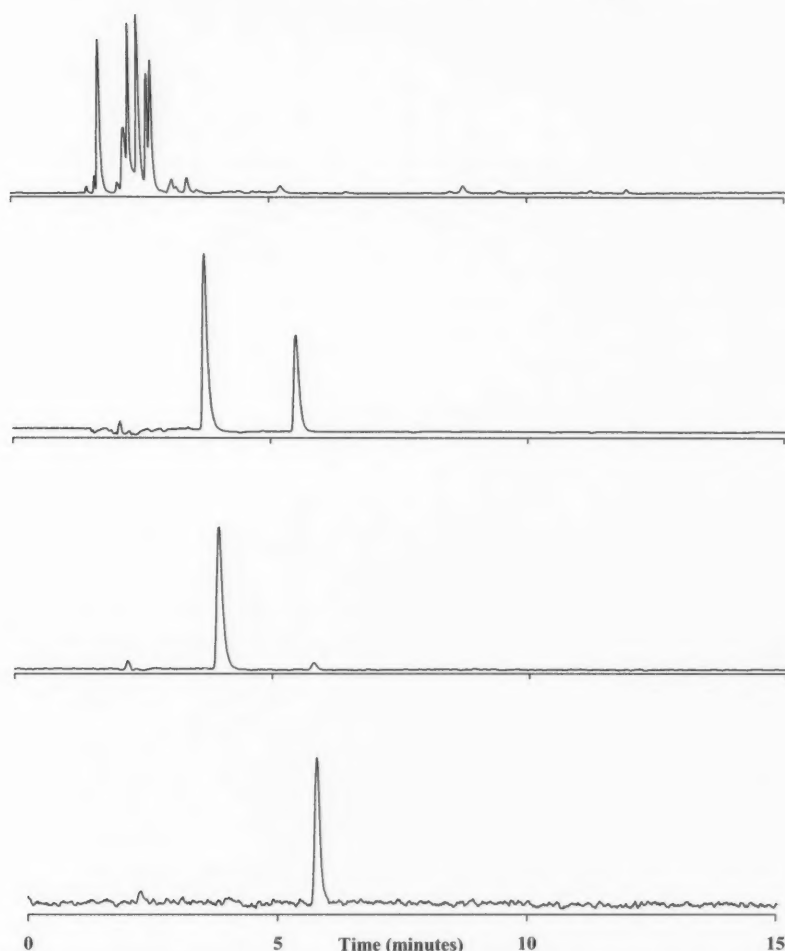


Fig. 5. Chromatograms of an unleaded gasoline as monitored (from top to bottom) in the μ FID mode, the μ FPD mode without an interference filter, the μ FPD phosphorus mode using a 520 nm (11 nm b.p.) interference filter, and the μ FPD sulfur mode using a 393 nm (11 nm b.p.) interference filter. The sample is diluted 1:10 in hexane. Injection volume is 0.5 μ L and also contains 500 ng each of tetrahydrothiophene and trimethyl phosphite. The gas flows used are 7 mL/min oxygen and 45 mL/min hydrogen.

response toward carbon, the μ FPD response without an interference filter, the μ FPD response toward phosphorus at 520 nm, and the μ FPD response toward sulfur at 393 nm. These were performed under a common set of conditions (i.e. those of optimal μ FPD sulfur response) chosen to yield the best possible sensitivity within all three detection modes. Incidentally, under these conditions, the μ FID response was found to be the least compromised and maintained 90% of its optimal sensitivity. As observed in the figure, the μ FID trace shows several partially separated peaks illustrating the primary hydrocarbon components of the sample, while in the μ FPD trace below only those peaks containing sulfur and phosphorus are dominant. It should be mentioned that while other sulfur or phosphorus peaks may have been present amongst the main hydrocarbon components of the sample, it is possible that quenching of their μ FPD emissions may have

occurred. For instance, emission quenching by co-eluting hydrocarbons is widely observed in the conventional FPD [28]. Similarly, it has also been shown to reduce μ FPD response by nearly 70 % when carbon flows of 60 μ g/s or greater are present in the detector [27].

Fig. 5 also demonstrates the μ FPD traces which selectively monitor the HPO^* emission of phosphorus, and the S_2^* emission of sulfur at specific wavelengths using an appropriate interference filter. Note that the peak for trimethyl phosphite appears somewhat sharper than in the earlier work, which was performed 'on-column' at lower temperatures when using hydrogen as the carrier gas [27]. Similar to previous studies, the phosphorus trace additionally yields a minor contribution from sulfur due to the well-known extension of S_2^* emission bands above 500 nm [27,28]. Thus, as anticipated, Fig. 5 shows that information quali-

tatively similar to a conventional FID and a conventional FPD can also be obtained in two dimensions from the same micro-counter-current flame.

4. Conclusions

In all, the attributes of this method demonstrate that the hydrogen-rich micro-counter-current flame is indeed capable of delivering useful, sensitive response toward organic analytes. In spite of its very small size, it yields selective chemiluminescent and universal hydrocarbon ionization response that is similar in quantity and quality to those of conventional flame-based detectors. As well, since it can deliver this as a multi-dimensional response under a common set of conditions, the micro-counter-current flame method allows for more information to be obtained from a sample analysis. The properties and dimensions of the micro-counter-current flame may therefore be potentially useful for application to analytical devices of reduced proportions. For instance, since the method can support a stable hydrogen-rich micro-flame within a small channel, it may be beneficial for portable or miniature GC methods where the performance of a conventional FPD and/or FID in an enclosed micro-format is desirable. Finally, other elements such as transition metals are also known to respond in the conventional FPD [25] and in the larger counter-current flame [26]. Therefore, it would be potentially interesting to examine the extent to which these elements may also respond in the μ FPD.

Acknowledgements

The authors are grateful to the Natural Sciences and Engineering Research Council of Canada for an operating grant in support of this research.

References

- [1] G.A. Eiceman, H.H. Hill, J. Gardea-Torresdey, *Anal. Chem.* 70 (1998) 321.
- [2] G.A. Eiceman, J. Gardea-Torresdey, E. Overton, K. Carney, F. Dorman, *Anal. Chem.* 74 (2002) 2771.
- [3] D.R. Reyes, D. Iossifidis, P.-A. Auroux, A. Manz, *Anal. Chem.* 74 (2002) 2623.
- [4] R.R. Reston, E.S. Kolesar Jr., *J. Microelectromech. Syst.* 3 (1994) 134.
- [5] E.B. Overton, K.R. Carney, N. Rouques, H.P. Dharmasena, *Field Anal. Chem. Technol.* 5 (2001) 97.
- [6] S.C. Terry, J.H. Jerman, J.B. Angell, *IEEE Trans. Electron. Dev.* ED-26 (1979) 1880.
- [7] G.C. Frye-Mason, R.J. Kottenstette, E.J. Heller, C.M. Matzke, S.A. Casalnuovo, P.R. Lewis, R.P. Manginell, W.K. Schubert, V.M. Hietala, R.J. Shul, in: D.J. Harrison, A. van den Berg (Eds.), *Micro Total Analysis Systems'98* Kluwer Academic Publishers, Dordrecht, 1998, p. 477.
- [8] S. Hannoe, I. Sugimoto, T. Katoh, in: D.J. Harrison, A. van den Berg (Eds.), *Micro Total Analysis Systems'98* Kluwer Academic Publishers, Dordrecht, 1998, p. 145.
- [9] J.V. Dam, P.J. Daenens, *Forensic Sci.* 39 (1994) 473.
- [10] J.C.T. Eijkel, H. Stoeri, A. Manz, *Anal. Chem.* 71 (1999) 2600.
- [11] J.C.T. Eijkel, H. Stoeri, A. Manz, *Anal. Chem.* 72 (2000) 2547.
- [12] R. Guchardi, P.C. Hauser, *J. Anal. Atom. Spectrom.* 18 (2003) 1056.
- [13] O.B. Minayeva, J.A. Hopwood, *J. Anal. Atom. Spectrom.* 18 (2003) 856.
- [14] S. Pedersen-Bjergaard, T. Greibrokk, *J. Microcol. Sep.* 6 (1994) 11.
- [15] S. Zimmerman, B. Riepenhusen, J. Müller, in: D.J. Harrison, A. van den Berg (Eds.), *Micro Total Analysis Systems'98* Kluwer Academic Publishers, Dordrecht, 1998, p. 473.
- [16] S. Zimmerman, S. Wischhusen, J. Müller, *Sens. Actuators B* 63 (2000) 159.
- [17] S. Zimmerman, J. Müller, *Microsyst. Technol.* 6 (2000) 241.
- [18] S. Zimmerman, P. Krippner, A. Vogel, J. Müller, *Sens. Actuators B* 83 (2002) 285.
- [19] C.H. Wang, S.S. Lin, W.U. Hwang, H.S. Weng, *Ind. Eng. Chem. Res.* 41 (2002) 666.
- [20] A. Maccone, M. Nardini, A. Antonucci, A. Maggio, R.M. Matarese, *J. Agric. Food Chem.* 50 (2002) 2169.
- [21] S. Otsuki, T. Nonaka, N. Takashima, W. Qian, A. Ishihara, T. Imai, T. Kabe, *Energy Fuels* 14 (2000) 1232.
- [22] E. Mochizuki, T. Yamamoto, Y. Komiyama, H. Nakazawa, *J. Agric. Food Chem.* 46 (1998) 5170.
- [23] T. Otake, J. Yoshinaga, Y. Yanagisawa, *Environ. Sci. Technol.* 35 (2001) 3099.
- [24] J. Gui-bin, Z. Qun-fang, H. Bin, *Environ. Sci. Technol.* 34 (2000) 2697.
- [25] X.-Y. Sun, B. Millier, W.A. Aue, *Can. J. Chem.* 70 (1992) 1129.
- [26] K.B. Thurbide, B.W. Cooke, W.A. Aue, *J. Chromatogr.* 1029 (2004) 193.
- [27] K.B. Thurbide, C.D. Anderson, *Analyst* 128 (2003) 616.
- [28] M. Dressler, *Selective Gas Chromatographic Detectors* (Journal of Chromatography Library, vol. 36), Elsevier, Amsterdam, 1986, p. 133.
- [29] C.R. Hastings, D.R. Younker, W.A. Aue, *Trace Subst. Environ. Health* 8 (1974) 265.
- [30] C.G. Flinn, W.A. Aue, *Can. J. Spectrosc.* 25 (1980) 141.
- [31] H.H. Hill, D.G. McMinn (Eds.), *Detectors for Capillary Chromatography*, Wiley, New York, 1992, p. 7.
- [32] T. Holm, J.O. Madsen, *Anal. Chem.* 68 (1996) 3607.
- [33] P.A. Rodriguez, C.L. Eddy, in: *Proceedings of the 15th ACS Central Regional Meeting Joint with the Ohio Valley Chromatography Symposium*, Abstract 65, Miami University, Oxford, OH, May 1983.
- [34] L.B. Graiff, *Nature* 203 (1964) 856.

Calendar of forthcoming meetings

15–20 August 2004

Montreal, Canada

ICORS 2004: 19th International Conference on Raman Spectroscopy.

URL: <http://icors2004.ubishops.ca>

5–10 September 2004

Salamanca, Spain

Euroanalysis XIII: European Conference on Analytical Chemistry. The Role of Analytical Chemistry in the protection of the Citizens. Viajes Iberia Congresos, C/Tetuán, 24, 41001 Sevilla, Spain.

Tel.: +34-95-4224095;

Fax: +34-95-4210215;

E-mail: congresos.sevilla@viajesiberia.com;

URL: <http://www.euroanalysis13.com>

11–12 September 2004

Rome, Italy

Eurosensors XVIII.

Contact: <http://www.eurosensors.it>

20–23 September 2004

Lisbon, Portugal

9th Chemometrics in Analytical Chemistry Conference. Contact: Dr Jose Menezes, AC-2004 Chair, Centre for Biological and Chemical Engineering, IST, Technical University Lisbon, Av. Rovisco Pais 1049-001, Lisbon, Portugal.

E-mail: cac2004@ist.utl.pt

28 September–1 October 2004

Torremolinos, Spain

3rd International Conference on Laser Induced Plasma Spectroscopy and Applications. Contact: Prof. J.J. Laserna, Department of Analytical Chemistry,

University of Málaga, E29071, Málaga, Spain.

E-mail: laserna@uma.es;

http://www.uma.es/libs_2004

29 September–3 October 2004

Kusadasi/Aydin, Turkey

AACD 2004: 4th Aegean Analytical Chemistry Days. Contact: Prof. Dr. Mustafa DEMÝR;

Tel.: +90-256-2128498/119;

Fax: +90-256-2135379;

E-mail: aacd2004@adu.edu.tr;

URL: <http://aacd2004.adu.edu.tr/>

6–8 October 2004

Amsterdam, The Netherlands

3rd Gas Analysis Symposium & Exhibition: ISO/TC 158. Contact:

E-mail: anja.jansen@nen.nl;

URL: <http://www.nen.nl/cgi-bin/index.pl?http://www.nen.nl/nl/act/agen/>

20041006_gasanalysis/

8–12 October 2004

Rome, Italy

6th Workshop on Biosensors and Bio-Analytical μ -Techniques in Environmental and Clinical Analysis. Contact:

E-mail: rome@biosensing.net;

URL: www.biosensing.net/iaeac.html

17–19 November 2004

Barcelona, Spain

3rd International Symposium on Food Packaging Ensuring the Safety, Quality and Traceability of Foods. Contact: Ir. Bernard Bottex- ILSI Europe, Avenue E. Mounier 83 - Bo 6, B-1200 Brussels, Belgium.

Tel.: (+32-2) 771-0014;

Fax: (+32-2) 762-0044;

E-mail: packaging.sympo@ilsieurope.be;

URL: <http://europe.ilsil.org>

2–4 February 2005

Amsterdam, The Netherlands

SCM-2: Second International Symposium on the Separation and Characterization of natural and Synthetic Macromolecules. Contact: Ordibo bvba, Edenlaan 26, B-2610 Wilrijk, Belgium.

Tel.: 0032 58 523116;

Fax: 0032 58 514575;

E-mail: scm@ordibo.be;

URL: <http://www.ordibo.be/scm>

8–11 May 2005

Philadelphia, PA, USA

PREP 2005: 18th International Symposium, Exhibit and Workshops on Preparative/Process Chromatography, Ion Exchange, Adsorption/Desorption Processes & Related Separation Techniques. Contact: Janet Cunningham, Barr Enterprises, PO Box 279, Walkersville, MD 21793, USA.

Tel.: (+1-301) 668-6001;

Fax: (+1-301) 668-4312;

E-mail: Janetbarr@aol.com;

URL: www.prepsymposium.org

22–25 May 2005

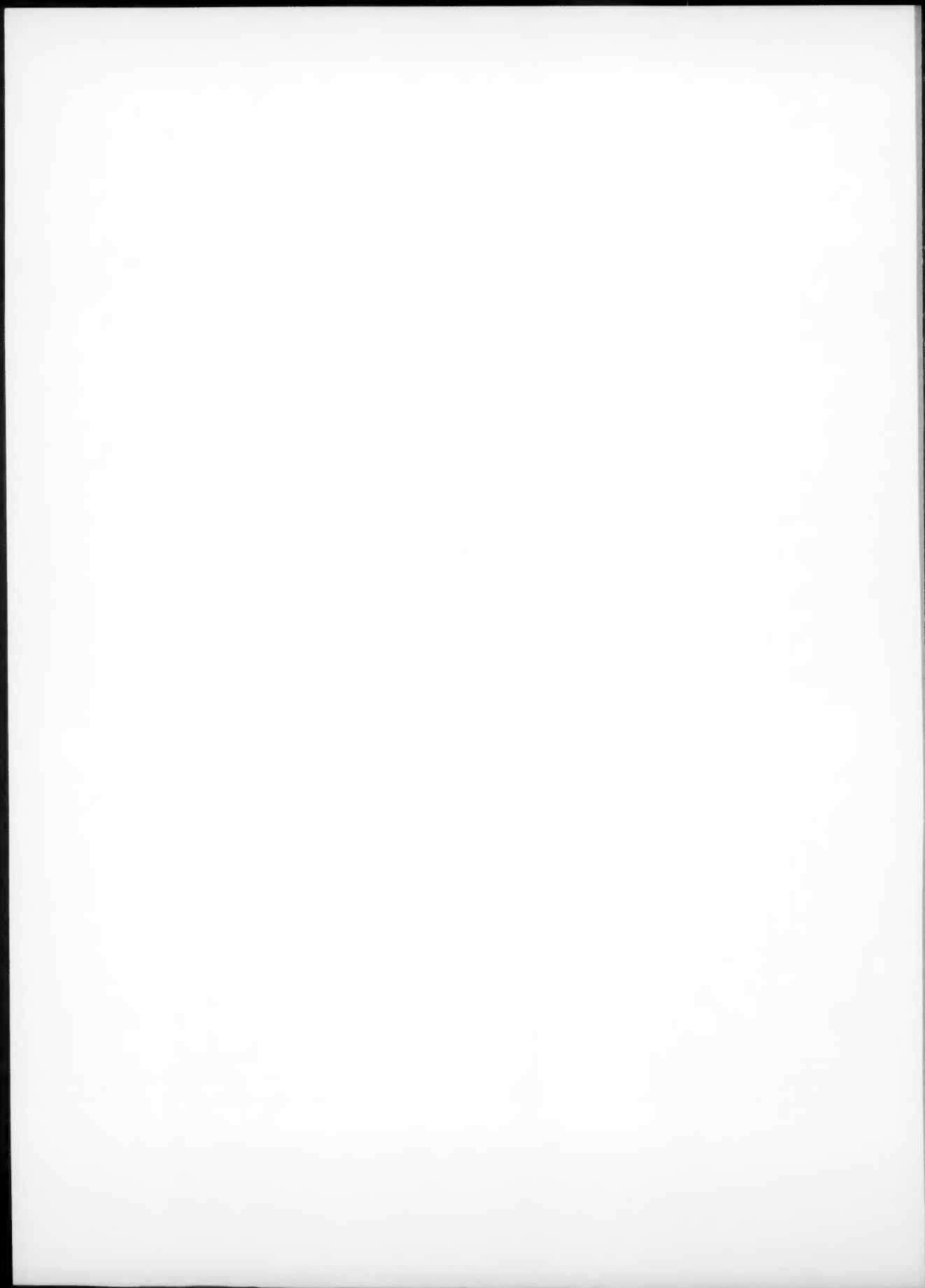
Las Vegas, Nevada, USA

ISCCE 2005: 28th International Symposium on Capillary Chromatography & Electrophoresis, Symposium Coordinator - Liz Hanson.

Tel.: 1 801 856 4240;

E-mail: liza_h_cce@yahoo.com;

URL: <http://www.casss.org>



INFORMATION FOR AUTHORS

Manuscripts. The language of the journal is English. Authors should submit four copies of the manuscript in clear double-spaced typing on one side of the paper only. *Vibrational Spectroscopy* also accepts papers in English only.

Rapid publication letters. Letters are short papers that describe innovative research. Criteria for letters are novelty, quality, significance, urgency and brevity. Submission data: max. of 2 printed pages (incl. Figs., Tables, Abstr., Refs.); short abstract (e.g., 3 lines); no proofs will be sent to the authors; submission on floppy disc; no revision will be possible.

Abstract. All papers, reviews and letters begin with an Abstract (50–250 words) which should comprise a factual account of the contents of the paper, with emphasis on new information.

Figures. Figures should be suitable for direct reproduction and as rich in contrast as possible. One original (or sharp glossy print) and two photostat (or other) copies are required. Attention should be given to line thickness, lettering (which should be kept to a minimum) and spacing on axes of graphs, to ensure suitability for reduction in size on printing. Axes of a graph should be clearly labelled, along the axes, outside the graph itself.

All figures should be numbered with Arabic numerals, and require descriptive legends which should be typed on a separate sheet of paper. Simple straight-line graphs are not acceptable, because they can readily be described in the text by means of an equation or a sentence. Claims of linearity should be supported by regression data that include slope, intercept, standard deviations of the slope and intercept, standard error and the number of data points; correlation coefficients are optional.

Photographs should be glossy prints and be as rich in contrast as possible; colour photographs cannot be accepted. Line diagrams are generally preferred to photographs of equipment. Computer outputs for reproduction as figures must be good quality on blank paper, and should preferably be submitted as glossy prints.

Nomenclature, abbreviations and symbols. In general, the recommendations of IUPAC should be followed, and attention should be given to the recommendations of the Analytical Chemistry Division in the Journal *Pure and Applied Chemistry* (see also *IUPAC Compendium of Analytical Nomenclature, Definitive Rules*, 1987).

References. The references should be collected at the end of the paper, numbered in the order of their appearance in the text (not alphabetically) and typed on a separate sheet.

Reprints. Twenty five reprints will be supplied free of charge. Additional reprints (minimum 100) can be ordered. An order form containing price quotations will be sent to the authors after acceptance of their article.

Papers dealing with vibrational spectroscopy should be sent to: Professor Dr. M. Diem, Department of Chemistry and Biochemistry, City University of New York, Hunter College, 695 Park Avenue, New York, NY 10021, U.S.A., Tel.: +212 772 5359; Fax: +1 212 772 5332; email: mdiem@hunter.cuny.edu or Professor J.H. van der Maas, Department of Vibrational Spectroscopy, Faculty of Chemistry, Utrecht University, Sorbonnelaan 16, 3584 CA Utrecht, The Netherlands, Tel.: +31 30253 7500; Fax: +31 30251 8219; email: j.h.vandermass@chem.uu.nl.

Special regulations for readers in the U.S.A. – This journal has been registered with the Copyright Clearance Center, Inc. Consent is given for copying of articles for personal or internal use, or for the personal use of specific clients. This consent is given on the condition that the copier pays through the Center the per-copy fee stated in the code on the first page of each article for copying beyond that permitted by Sections 107 or 108 of the US Copyright Law. The appropriate fee should be forwarded with a copy of the first page of the article to the Copyright Clearance Center, Inc., 222 Rosewood Drive, Danvers, MA 01923, U.S.A. If no code appears in an article, the author has not given broad consent to copy and permission to copy must be obtained directly from the author. The fee indicated on the first page of an article in this issue will apply retroactively to all articles in the journal, regardless of the year of publication. This consent does not extend to other copying, such as for general distribution, resale, advertising and promotion purposes, or for creating new collective works. Special written permission must be obtained from the publisher for such copying.

For a full updated Instructions to Authors, please refer to *Analytica Chimica Acta*, Volume 518 issues 1–2 pp. 199–200. The Instructions can also be found on the World Wide Web: access under <http://www.elsevier.com/locate/aca>

Advertising information: Advertising orders and enquiries can be sent to: **USA, Canada and South America:** Mr Tino DeCarlo, The Advertising Department, Elsevier Inc., 360 Park Avenue South, New York, NY 10010-1710, USA; phone: (+1) (212) 633 3815; fax: (+1) (212) 633 3820; e-mail: t.decarlo@elsevier.com. **Japan:** The Advertising Department, Elsevier K.K., 4F Higashi-Azabu, 1-Chome Bldg, 1-9-15 Higashi-Azabu, Minato-ku, Tokyo 106-0044, Japan; phone: (+81) (3) 5561 5037; fax: (+81) (3) 5561 5047; e-mail: jp.info@elsevier.com. **Europe and ROW:** Commercial Sales Department, Elsevier Ltd., The Boulevard, Langford Lane, Kidlington, Oxford OX5 1GB, UK; phone: (+44) 1865 843016; fax: (+44) 1865 843976; e-mail: media@elsevier.com

USA mailing notice: *Analytica Chimica Acta* (ISSN 0003-2670) is published 3 times a month by Elsevier B.V. (P.O. Box 211, 1000 AE Amsterdam, The Netherlands). Annual subscription price in the USA US\$ 8,081 (valid in North, Central and South America), including air speed delivery. Periodical postage rate paid at Jamaica, NY 11431.

USA POSTMASTER: Send address changes to *Analytica Chimica Acta*, Publications Expediting Inc., 200 Meacham Avenue, Elmont, NY 11003. **AIRFREIGHT AND MAILING** in the USA by Publications Expediting Inc., 200 Meacham Avenue, Elmont, NY 11003.

PRINTED IN THE NETHERLANDS

**FROM ELSEVIER SCIENCE...
SCIENCE PUBLISHER TO THE WORLD**



A FREE alerting service by E-mail for Elsevier Science journals.

ContentsDirect allows you unrivalled access to the tables of contents pages of Elsevier Science journals in the following subject areas:

- Chemistry and Chemical Engineering
- Clinical Medicine
- Computer Science
- Earth and Planetary Sciences
- Economics, Business and Management Science
- Engineering, Energy and Technology
- Environmental Science and Technology
- Life Sciences
- Materials Science
- Mathematics
- Physics and Astronomy
- Social Sciences
- Multidiscipline

What does ContentsDirect provide?

- Journal title
- Volume and issue number
- Title of paper
- Names of authors
- Page details
- Anticipated publication date
- News and offers

Why register to ContentsDirect?

- Provides via E-mail advance notice of forthcoming papers, allowing you to reserve the issue at your library.
- Provides an invaluable information resource to scientists and researchers requiring the very latest information on soon-to-be published papers.
- Keeps you at the forefront of current research.
- Enables you to create a personal archive of key journal contents in your field of interest.

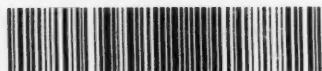
How to register for ContentsDirect:

- The quickest way to register for ContentsDirect is via Elsevier Science home page on the world wide web.
- Registration is simple and the selection of titles is provided by access to drop down menus of all subject classifications with a complete listing of all titles available.
- If you wish to select new titles or amend your existing selection - simply re-visit the web site and personally make your changes.

Register Now!

<http://contentsdirect.elsevier.com>

NB If you can't access the web - please note that you can still register by sending an E-mail to cdsubs@elsevier.co.uk



0003-2670(20040809)519:1;1-E

ContentsDirect



